STUDIES IN BIOINORGANIC CHEMISTRY:

SYNTHESIS AND REACTIVITY OF

NICKEL AND VANADYL N_XS_Y COMPLEXES

A Dissertation

by

ROXANNE MICHELLE JENKINS

Submitted to the Office of Graduate Studies of
Texas A&M University
in partial fulfillment of the requirements for the degree of

DOCTOR OF PHILOSOPHY

May 2010

Major Subject: Chemistry

STUDIES IN BIOINORGANIC CHEMISTRY:

SYNTHESIS AND REACTIVITY OF

NICKEL AND VANADYL N_XS_Y COMPLEXES

A Dissertation

by

ROXANNE MICHELLE JENKINS

Submitted to the Office of Graduate Studies of
Texas A&M University
in partial fulfillment of the requirements for the degree of

DOCTOR OF PHILOSOPHY

Approved by:

Chair of Committee,	Marcetta Y. Darensbourg
Committee Members,	David P. Barondeau
	Michael B. Hall
	Paul A. Lindahl
	Siegfried Musser
Head of Department,	David H. Russell

May 2010

Major Subject: Chemistry

ABSTRACT

Studies in Bioinorganic Chemistry:

Synthesis and Reactivity of Nickel and Vanadyl N_xS_y Complexes. (May 2010)

Roxanne Michelle Jenkins, B.S., University of Texas as San Antonio

Chair of Advisory Committee: Prof. Marcetta Y. Darensbourg

As inspired by the coordination environment of nickel in NikR and NiSOD, imidazole ligands were incorporated into N_2SNi^{II} square planar complexes in order to investigate the electronic and structural features of Ni^{II} species containing both imidazole and thiolate ligation. Rare examples of nickel complexes containing such ligand sets in continuous tetradentate ($N_2N'S$) and discontinuous (N_2S---N') coordination were synthesized and characterized. A significant finding in these studies is that the plane of the imidazole ligand is oriented perpendicular to the N_2SNi plane. Further investigations addressed the orientational preference and stereodynamic nature of flat monodentate ligands (L = imidazoles, pyridine and an N-heterocyclic carbene) bound to planar N_2SNi moieties. The solid state molecular structures of planar $[N_2SNiL]^{n+}$ complexes accessed through bridge-splitting reactions of dimeric, thiolate-S bridged $[N_2SNi]_2$ complexes, reveal that the plane of the added monodentate ligand orients largely orthogonal to the N_2SNiL square plane. Variable temperature ^1H NMR characterization of dynamic processes and ground state isomeric ratios of imidazole complexes in their stopped exchange limiting spectra, readily correlate with DFT-guided interpretation of Ni-L rotational activation barriers. Full DFT characterization relates the orientation mainly to

steric hindrance derived both from ligand and binding pocket. In the case of the imidazole ligands a minor electronic contribution derives from intramolecular electrostatic interactions (imidazole C-2 C-$H^{\delta+}$- - $S^{\delta-}$ interaction).

Our group has firmly established the versatility of the $(bme\text{-}daco)^{2-}$, $(bme\text{-}dach)^{2-}$, and $(ema)^{4-}$ ligands to accommodate a number of metals (M = Ni, Zn, Cu, and Fe), and have demonstrated reactivity of such N_2S_2M complexes occurs predominately at the S-thiolate sites. As vanadium is of interest for its biological, pharmacological and spectroscopic/analytical probe abilities, vanadyl analogues were explored as mimics of possible chelates formed from Cys-X-Cys binding sites *in vivo*. The structural and electronic changes from the incorporation of $V{=}O^{2+}$ in such dianionic and tetraanionic N_2S_2 binding pockets is investigated and compared to Ni^{2+} and Zn^{2+} in similar N_2S_2 environments. The nucleophilicity of the S-thiolate in these systems is explored with alkylating agents and $W(CO)_x$. Furthermore, the vanadyl interaction with the CGC peptide, the biological analogue of the tetraanionic N_2S_2 ligand, was produced and characterized by EPR; its $W(CO)_x$ adducts were indentified by υ(CO) infrared spectroscopy.

DEDICATION

This work is dedicated to my precious Amelia, who spent many hours with me in the lab; my sweet husband Scott, we always worked as a team; my encouraging family, their love and support always lifted me up; and my Lord and Savior Jesus Christ, through Him I found my strength.

ACKNOWLEDGEMENTS

I would first like to thank my research advisor Marcetta Darensbourg for all that she taught me about science and about myself, and I am grateful for her guidance and mentorship. Marcetta has always challenged me, and I believe challenge is the pathway to new understandings and new possibilities. Her embrace of science, her commitment and passion, has and will always be an inspiration.

I acknowledge my committee members David P. Barondeau, Paul A. Lindahl and Siegfried Musser, with special thanks to Michael B. Hall for his insight into the theoretical aspect of the imidazole orientational studies. I thank Dr. Joseph H. Reibenspies and Dr. Nattamai Bhuvanesh for their endless support in the X-ray Diffraction Laboratory, and gratefully acknowledge Dr. Joe Reibenspies in solving many of the structures presented here in this work.

I am grateful for the opportunity I was given to participate in the Chemistry-Biology Interface (CBI) Program, and I would like to acknowledge the funding I received from the National Institutes of Health (NIH) to be part of this program. Much gratitude goes to both Dr. Burgess and Dr. J. Martin Schotlz for allowing me to learn techniques in their laboratories during my CBI rotations. The knowledge I took from each rotation along with the relationships I developed have been tremendously valuable during my graduate career. I would especially like to thank Dr. Lindahl for his passion and dedication to keeping this program funded, and his hard work at making it exciting and beneficial for all the students involved.

I want to express my deepest gratitude to Dr. Toran Isom, Dr. Robert Swindell and Dr. Judith Walmsley. Each has had a positive impact on molding my career aspirations, and they have been personally instrumental in helping me achieve my goals. My heart felt thanks go to both Dr. Toran Isom and Dr. Robert Swindell, who both exemplify the true definition of a mentor. Thank you both for your continuous support and encouragement! Dr. Swindell's guidance and mentoring during my years at the University of Arkansas at Little Rock (UALR) played a key role in establishing my desire to do research, and I will always be grateful to him as he has deeply inspired my life. The methodical teaching and passion of Dr. Judith Walmsley inspired me to become an inorganic chemist. She encouraged me to apply to the graduate program at Texas A&M University (TAMU), and I am truly grateful that she did. I am indebted to each of these mentors; I appreciate that they have truly cared for my success, and they will forever share a special part of my education and life accomplishments.

I would like to acknowledge the Women in Science and Engineering (WISE) organization, and all the countless friendships I made with women across the campus through this awesome organization. Much gratitude goes to Bonnie Schriller, Dr. Nancy Magnussem, and Dr. Marian Hyman for their leadership and continuous support. My participation in this organization has enriched my life, and I am grateful for the skills I have gained while serving the TAMU College of Science and the community.

As part of the DJD and MYD family, I would like to acknowledge the past and present members of both groups. In particular, Dr. Jesse Tye, Dr. Stephen Jeffery, Dr. Elky Almaraz, Dr. Tianbiao "Leo" Liu, Dr. Adriana Moncada, Osit "Pop" Karroonnirun, Michael Singleton, Bin Li, and Tiffany Pinder have all been a special part of my life

throughout my time at TAMU. Many thanks go to my collaborator and friend, Michael Singleton. Thank you Mike for always believing in me, and I still think our imidazole rotation will eventually bring about world peace. Thank you Tiffany for your sincere friendship and for always having confidence in me. It has been so much fun working with both of you in the lab and I will really miss our trips to Starbucks. To my special friend, Adriana Moncada, thank you for your continuous friendship, support, and encouragement throughout the years. Thank you Pop for your sweet friendship and always willing to discuss research with me. I have learned so much from each of you and I will miss you all! I would also like to acknowledge the undergraduate students that I had the opportunity to work with: Mike Jones, Boram Lee, and Lauren Leamer. Many thanks to Lauren for her incredible hard work and dedication during the summer she spent working with me in the lab.

Most importantly, I would like to express my gratitude to my wonderful family for their unwavering support, love, and prayers. To my incredible husband Scott, thank you for supporting this goal since the day I quite my job and went back to college. Thank you for working non-stop to support our lives while I went to school. Thank you for putting up with my stress, listening to my fears, encouraging me every step of the way, and loving me through it all. My dearest Amelia, thank you for being my special lab mate throughout this journey, you truly became a MYD group member over the years. Thank you sweet girl for your patience while mommy set up reactions, attended seminar practices (although you always enjoyed the pizza), mounted crystals in the X-ray Laboratory, and thank you for never complaining about the long walk from the lab to the car. We always made our time together special!

My deepest gratitude goes to my parents: my Mom and Craig, and my Dad and Vie. I thank you from the bottom of my heart for your emotional and financial support, your encouragement, your never-ending love, your countless prayers, and always teaching me to do what was right. I am thankful for each of your perspectives, and I could not have made it this far with out each of you in my life. Much appreciation goes to my Mom and Craig for consistently visiting College Station with Alysa to see Amelia, and I truly appreciate the numerous times that they met me in Bastrop to hand off Amelia. Thank you for being our long distance babysitter! Dad and Vie Vie, my prayer warriors, thank you for always having the time to listen to me, to give me advice, and thank you for always understanding what I had on my plate. Furthermore, I would like to thank ALL my family for always believing in me and praying for me!

Sincere thanks go to my church family in College Station and San Antonio for their support and prayers, my loving family at Brazos Christian School, with special thanks to Kelly Rodgers, Mary Woods, Estella Braswell, Lisa Pahl and Carmen Ramirez. Thank you ladies for your friendship, love, and prayers.

The power of prayer is amazing, and I thank the Lord Jesus for always listening. I praise God for giving me the strength, the knowledge and the ability to reach this goal.

TABLE OF CONTENTS

CHAPTER Page

LIST OF FIGURES

FIGURE Page

FIGURE Page

FIGURE Page

FIGURE Page

FIGURE Page

FIGURE Page

FIGURE Page

LIST OF TABLES

TABLE Page

CHAPTER I

INTRODUCTION

Biological Functions of Nickel in Microorganisms

Plants, fungi, archaebacteria and eubacteria utilize nickel ions in a variety of essential metalloproteins which participate in Ni-sensing, uptake, trafficking, storage, regulation and utilization.[1-2] There are nine known Ni-dependent enzymes: urease, [NiFe]-hydrogenase, carbon monoxide dehydrogenase, acetyl-coenzyme A decarbonylase/synthase, methyl-coenzyme M reductase, Ni-superoxide dismutase, Ni-dependent glyoxylase, acireductone dioxygenase and methylenediurease.[1] Nickel can function as a redox cycling agent, a binding site for reactive small molecules (CH_3 or CO) in organometallic transformations, a Lewis acid to promote hydrolysis, or as a regulator of vital response mechanisms.[1-2] For example, nickel ions are essential to the physiology of microorganisms such as *Helicobacter pylori* and *Escherichia coli*. The survival of the bacteria relies on the nickel-containing enzyme urease (comprised of a dinickel active site containing four histidines) which helps maintain a neutral pH within the bacterial cytoplasm, and it depends on the [NiFe]-hydrogenase to supply energy to the cell.[3-5] The pathogenic bacterium *H. pylori*, found in the acidic environment of the stomach of humans, is known to infect more than 50% of the world's population.[6-7] It has been associated with the onset of duodenal or gastric ulcers, gastritis and certain gastric cancers.[8]

This dissertation follows the style of *Journal of the American Chemical Society*.

NikR: A Nickel Regulation Protein

As a surplus of nickel is toxic in biological systems, the control of the intracellular levels of nickel is essential.[9] Nickel homeostasis in *H. pylori* and *E. coli* is controlled by the nickel-responsive transcription factor, NikR.[10-12] The molecular structure of the NikR protein of *E. coli* has been most extensively studied.[2] As shown in Figure I-1, it is a homotetramer containing four high-affinity nickel binding sites (one per subunit) in the Metal Binding Domain (MBD).[13]

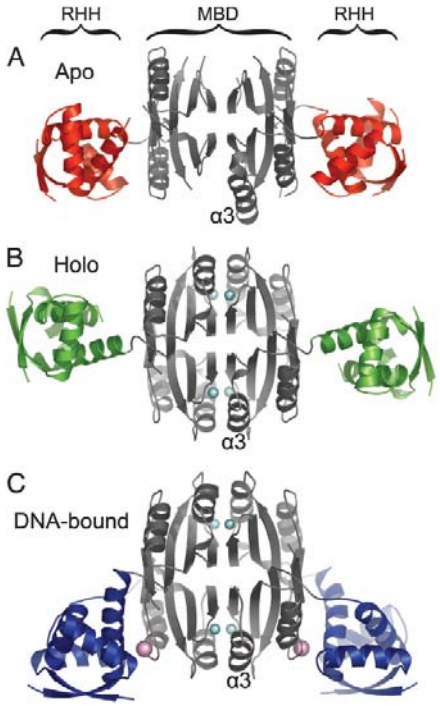

Figure I-1. A. NikR apoprotein highlighting the disordered α3 helix.; B. NikR holoprotein.; C. DNA-bound NikR protein. Adapted from Reference 13.

Each Ni^{II} ion is held in a square-planar arrangement consisting of the side chains of two histidine (His87 and His89) and one cysteine residue (Cys95) from one NikR monomer, and a histidine (His76) from an adjacent monomer (Figure I-2).[13-14] This

cytoplasmic nickel sensor is responsible for repressing the transcription of the nickel membrane transporter, NikABCDE, when ample levels of intracellular nickel are met.[10] The initiation of NikR binding to a 28-bp palindromic operator sequence found in the promoter nikABCDE occurs following the coordination of four nickel ions to the high affinity sites located in the Ni-regulatory domain, i.e. the metal binding domain (MBD).[13]

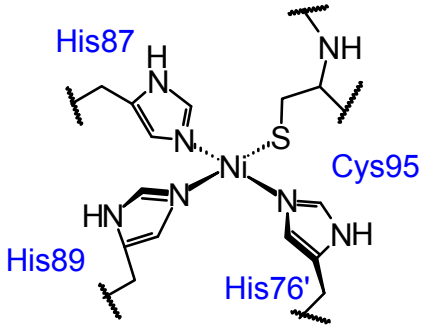

Figure I-2. The nickel binding site of NikR. Adapted from Reference 14.

As Figure I-1 shows, the binding of Ni^{2+} ions in this domain organizes the α3 helix and initiates the protein-DNA communication.[13] The exact DNA-binding response mechanism is still not completely understood. A DNA-complementary surface on the MBD is created from the binding of nickel ions in the high affinity sites in the MBD. Polar interactions between the α3 loop and DNA phosphate backbone are created from the stable conformation of the α3 helix. The localization of the NikR protein to the DNA is promoted by a short-range allosteric effect. The ribbon-helix-helix (RHH) domains extend completely outwards from the MBD and the β-sheets which bind to the DNA major groove point in opposite directions. When the operator base sequence is

recognized by the repressor, a cooperative interaction of both RHH domains ensues. The RHH domains rotate about the interdomain linkers and the anti-parallel β-strands orient to occupy the *nik* operator half-sites in the DNA major groove.[13]

There have been two other metal binding sites proposed in NikR, one of which was observed in the molecular structure of the DNA-bound NikR protein.[13] Drennan and coworkers observed an additional metal binding site bridging the metal binding domain and the DNA binding domain.[13] They proposed this conformation was held in place by a K^+ ion. Still another, a low affinity nickel binding site has been postulated, but not indentified by X-ray crystallography.[2] Studies have established that stoichiometric amounts of nickel induce a nanomolar binding affinity of NikR to DNA.[15-16] However, it has been demonstrated that excess nickel causes tighter binding of the protein-DNA complex. In this case, XAS data suggests a nickel coordinated to N/O donors in an octahedral geometry defines this site.[15] Biomimetic studies of the high affinity nickel(II) binding site have not been reported until now.[131]

Proteins typically bind metal ions in a highly specific manner. Nevertheless, divalent transition metal ion binding studies of the high affinity metal binding site of NikR have demonstrated that metals such as Co^{2+}, Cu^{2+}, Zn^{2+}, and Cd^{2+}, bind with a similar affinity as Ni^{2+}.[15-16] Drennan and Zamble, et al., investigated the structural changes in the NikR protein induced by the binding of Cu^{2+} and Zn^{2+} ions to the high affinity metal binding domain as compared to the Ni^{2+} bound form.[17] The results indicated that both Ni^{2+} and Cu^{2+} ions coordinate to the protein in a similar manner, and both promote the ordering of the α3 helix. In contrast, the α3 helix remains disordered

on the binding of Zn^{2+} ions. Competitive binding between Ni^{2+} and Cu^{2+} ions is however not observed in the cell, since free copper in the 2+ form is not present.[17] Overall, it is important to note that the coordination geometry about the nickel ion in NikR is controlled by the binding preferences of the metal and not induced by the protein superstructure, and this is critical to the function of the protein.

Ni-dependent Superoxide Dismutase (NiSOD)

In contrast to the structural, redox invariant function of the nickel ions found in NikR, a nickel-dependent enzyme in microorganisms in which the nickel ion plays a redox role is superoxide dismutase. Nature has designed superoxide dismutase to defend respiring cells from the cytotoxic effects of superoxide, catalyzing its dismutation reaction to molecular oxygen and peroxide. The reaction proceeds via a two step, ping pong mechanism wherein the metal center is first reduced by one molecule of superoxide producing molecular oxygen and subsequently the metal center is reoxidized by a second molecule of superoxide generating peroxide (Figure I-3).[19-20]

Superoxide is a natural byproduct of aerobic metabolism. Superoxide and its derivatives damage living systems by causing oxidative damage to cellular components. Superoxide has the ability to abstract weakly bound protons producing organic radical species and it can also reduce metals leading to various Reactive Oxygen Species,

$$M^{3+} + O_2^{\cdot -} + H^+ \rightarrow \ M^{2+} + O_2$$

$$M^{2+} + O_2^{\cdot -} + H^+ \rightarrow \ M^{3+} + H_2O_2$$

Figure I-3. Ping pong mechanism of superoxide dismutation.

ROS's. The extremely reactive products generated from cellular reactions with superoxide are more deleterious to the cell than superoxide itself. The damaging reactivity of ROS's include inactivating enzymes, abstracting protons from DNA bases, modifying amino acids and interfering with NO-mediated signaling. Superoxide and reactive oxygen species have been linked to many degenerative conditions, inflammatory diseases, reperfusion injury after ischemia, the process of aging, cell death during infections, advancement of AIDS and amyotrophic lateral sclerosis ("Lou Gehrig's disease").[19-21]

SODs are classified according to their redox active metal center. As shown in Figure I-4, the metal centers of the heterobimetallic Cu, Zn- and the monometallic Fe- or Mn- containing SODs, are coordinated to hard N or O donor atoms. Histidine imidazoles, aspartate carboxylates, and water are the common ligands demonstrated to bind to these metal centers.[22] Two simultaneous studies presented by Getzoff et al.., and Wuerges et al.., revealed the first protein crystal structures of the nickel-containing superoxide dismutase, NiSOD.[23-24] The NiSOD is a relatively small protein consisting of a 117 amino acid sequence and is comprised of a four helix bundle hexamer structure

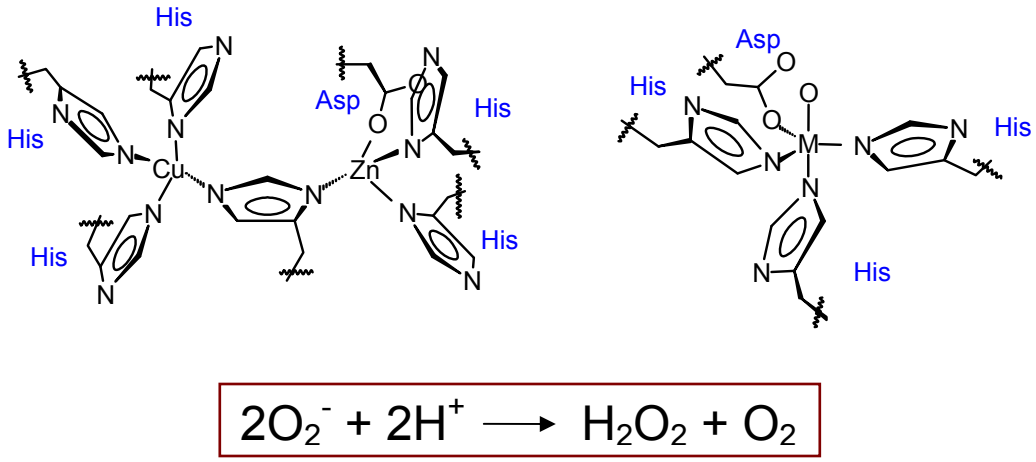

Figure I-4. The Cu,Zn-SOD active site, the Mn-, Fe-SOD active site and the reaction they catalyze.

containing six Ni ions arranged in an octahedral array (Figure I-5). The nickel(II) binding sites were found to incorporate both N-histidine and S-cysteine ligands creating a N_2S_2 binding motif. This distinct SOD coordination environment involving N_2S_2 ligation is a nickel binding pocket which is also observed in the acetyl coA synthase (ACS) metalloenzyme, where a nickel is bound by two S-thiolates and two N-amides from a Cys-Gly-Cys tripeptide motif.[25-27]

Molecular structures of NiSOD suggested that the redox active metal center undergoes conformational changes during the catalytic cycle (Figure I-5).[23] The reduced form of the active site of NiSOD features a square planar geometry about Ni^{II} consisting of the N-terminus amine nitrogen, a carboxyamido N atom, two cysteine thiolates and

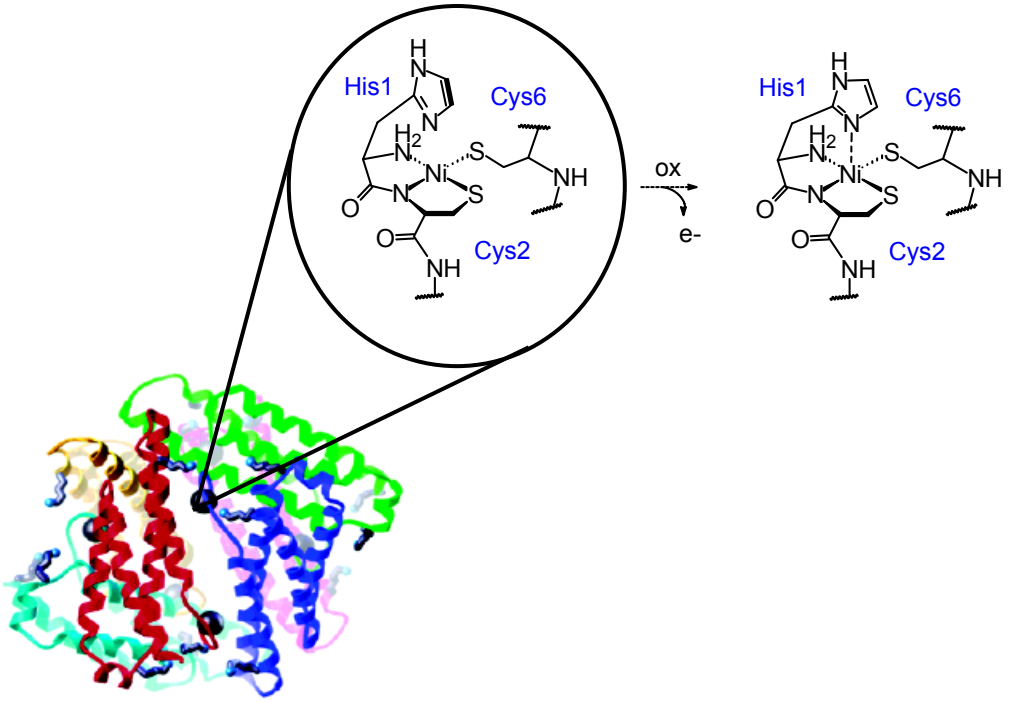

Figure I-5. Molecular structure of NiSOD. NiSOD active site. Left: reduced form; Right: oxidized form. Adapted from Reference 23.

possibly a fifth donor ligand from an axial histidine N atom. The molecular structure of the oxidized form reveals axial imidazole coordination to the Ni metal center resulting in a five coordinate square pyramidal geometry, Figure I-5. The imidazole plane of His1 rotates by ~55° in the course of coordinating the His imidazolate N to the open axial site, achieving a Ni-N distance of ~2.63 Å (Figure 1-6).[23] This is a large movement of the imidazole.

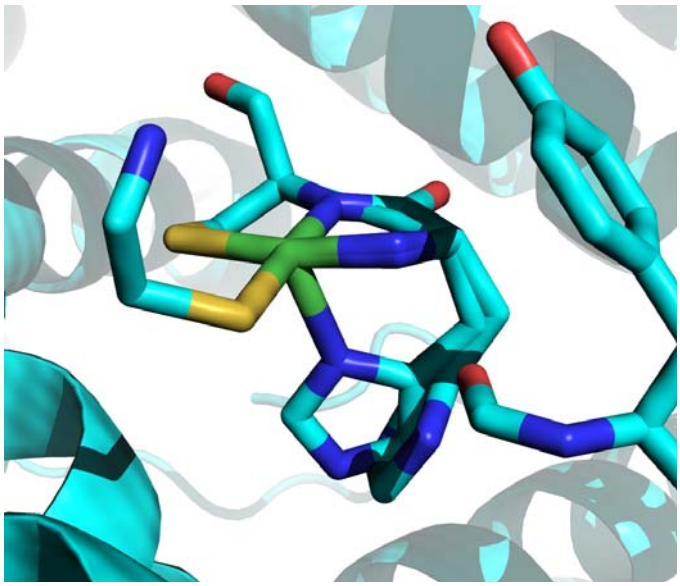

Figure I-6. The NiSOD active site in the reduced state (uncoordinated His) and the oxidized state (coordinated His) highlighting the large movement of the His1 imidazole donor.

This work focuses mainly on the synthesis and structure of nickel coordination environments containing imidazole and thiolate ligation, as inspired by the NikR and NiSOD nickel binding sites. Fundamental issues were discovered during the exploration of these bioinspired complexes, and led my work into the direction of investigating the factors that influence the orientation of heterocyclic monodentate ligands.

Biological Relevance of Imidazole Orientation

Whereas the orientation of histidine donors in nickel-binding sites has not been addressed in structural studies of biomolecules, much effort has been directed to His-iron interactions, using simple imidazoles as mimics of histidine. The axial imidazole

binding geometry in metalloporphrin complexes has been extensively studied by the use of small molecule models and theoretical computations.[28-36] These works have demonstrated that the axial ligated imidazole geometry (orientation of the plane of the imidazole with respect to the Fe-$N_{porphyrin}$ bond vectors, and tilt of the imidazole plane) can influence spectral changes,[28-30,36] shifts in redox properties,[30-31] coordination of substrates[32] and changes in the spin state. [28]

A system to measure the orientation of imidazole ligands in metalloporphyrin complexes was developed by Hoard et al.., Figure I-7.[37] The imidazole bonding geometry is described as the dihedral angle (φ) defined by the angle between the imidazole plane and a plane perpendicular to the N_4Fe framework, which intersects a N-atom bound to the Fe center. When φ equals 0º (maximum steric repulsion), the imidazole plane eclipses the porphyrin nitrogen metal bonds and a φ value of 45º (minimum steric repulsion) corresponds to the imidazole bisecting the $N_{porphyrin}$-M-

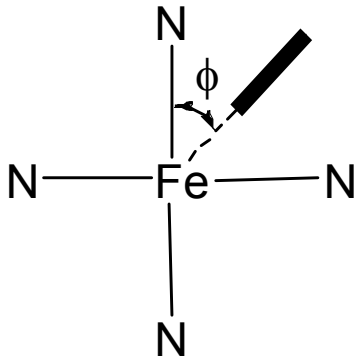

Figure I-7. Definition of φ according to the system developed by Hoard et al. used to measure the orientation of imidazole ligands in metalloporphyrin complexes. Adapted from Reference 37.

$N_{porphyrin}$ angle. An evaluation of reported Fe heme structures by Scheidt and Chapman found that small φ angles (i.e. close to zero) were most often observed.[28] These data implied that non-bonding interactions (steric repulsion) were not the dominating factor in the orientational preference of axial coordinated imidazole ligands in Fe heme complexes. Structural analysis of metalloporphyrins containing two axial coordinated imidazoles found that longer Fe-$N_{imidazole}$ bond distances were associated with imidazole ligands having smaller φ values.

To investigate the electronic effect on ligand orientation, Scheidt and Chapman carried out computational studies on porphyrin type complexes that incorporated metal ions with various oxidation, spin states, imidazole angle.[28] A stabilizing effect was found to be induced from an orientationally dependent small φ angle, which was determined to correspond to a bonding interaction involving a weak p_π imidazole and p_π metal interaction. In all cases, with the exception of a low spin (LS) Fe(III) complex, the resulting conformation of the axial coordinated ligand derived from the opposing forces from p_π imidazole and p_π metal bonding interactions and steric factors, and contributions of d_π orbitals were found to be minimal. In the LS Fe(III) system, the p_π imidazole and d_π metal interactions were shown to influence the value of φ to a greater extent. Furthermore, the π-bonding ability of imidazole ligands in $(CN)_5Fe^{III}(1\text{-}CH_3im)^{2-}$ complexes was examined by Asher and Abola, et al.[38] These studies also found that weak π-bonding interactions between the Fe d_π-Im p_π orbitals of the coordinated imidazole ligand affect the imidazole conformation and the M-imidazole bond distance.

Although a weak contribution from the π-donating properties of the imidazole ligand was suggested in early studies, current research has focused on other factors that affect the orientation of the imidazole ligand. A recent survey of the Protein Data Base (PDB) crystal data base, by Knapp, et al.. found that in the majority of heme complexes the NH group of the axial ligated imidazole pointed in the direction of the propionic acid groups of porphyrin framework.[34] In addition, they identified a second factor which influenced the orientational preference of the axial imidazole donor: the linker atoms of the histidine residue on the imidazole. Both features were interpreted in terms of electrostatic interactions as according to their computational results, and both were considered to be a product of the overall protein environment. A further theoretical study conducted by Knapp and coworkers examined the orientational preferences of axial ligated imidazoles in hemoproteins in the presence of a dielectric medium, such as water or protein environments, and determined that the electrostatic interaction of the total dipole moment of the heme-imidazole system with the solvent reaction field plays a significant role in the conformation of the axial imidazole ligand.[35]

In addition to the stereochemical investigations of imidazole ligands in heme systems, imidazole orientational binding preferences have been studied in square planar platinum complexes and octahedral ruthenium complexes to understand the role of such metal complexes in biological systems, such as their mode of action as anticancer drugs.[39-41] For example, Alessio, Marzilli and coworkers explored octahedral Ru(II) complexes that contained aromatic N-donor, "lopsided" ligands such as 1,5,6-trimethylbenzimidazole, Me_3Bzm, and concluded that opposing forces between steric

and electrostatic interactions affected ligand orientation and observed dynamic processes.[39] The variable temperature ^{1}H NMR spectra of *cis*,*cis*,*cis*-$RuCl_2(DMSO)_2(Me_3Bzm)_2$ found that one Me_3Bzm ligand readily flips between two identified species (each isomer rotated 180º from the another) while the second Me_3Bzm ligand is immobile between -100 and +35 ºC. The preferred, fixed orientation of the latter was attributed to electrostatic interactions between the C-$H^{\delta+}$ of Me_3Bzm and the two *cis* halides. Other investigations by Velder, Reedijk et al. of Ru-N bound substituted imidazoles in dicationic Ru^{2+} complexes that lack coordinated halides established that the observed rotational behavior of the imidazole ligands about the Ru-N_{imid} bond is controlled exclusively by steric interactions.[41]

The orientation and rotational fluxionality of N-heterocyclic carbene (NHC) ligands have also been carefully studied, concluding that rotation of NHCs about the M-C_{NHC} bond is also determined largely, and in most cases solely, by steric effects.[43-51] For square planar d^8 complexes the steric interference of NHC ligands with ancillary ligands dictates the NHC ligand plane to orient nearly perpendicular to the metal ligand plane.[44,50-52]

A final example of the importance of imidazole orientation has been demonstrated in the Cu_A Azurin metalloprotein (Figure I-8). Studies have established that the angular position of the His rings with respect to the Cu_2S_2 core in the active site of Cu_A Azurin modulates the interaction of the axial ligand with the copper ions, and thus fine tunes the structural and electronic properties of the metalloprotein.[53-54]

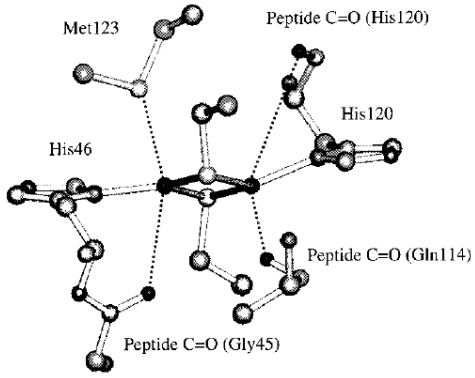

Figure I-8. The active site of Cu_A azurin. Adapted from Reference 53.

As a number of studies demonstrate the effects of subtle changes in imidazole orientation, and the fact that nature commonly employs histidine-rich sites in metalloproteins, further development of understanding the factors which influence the stereochemistry of metal bound His-imidazoles in other coordination geometries is important. The main focus of this dissertation is to expand our knowledge in the coordination chemistry of imidazole ligands bound to nickel centers containing thiolate donors, and to understand the factors which influence the relative orientation of imidazole ligands in such systems. Chapter III describes the electronic and structural effects of the incorporation of an imidazole donor into Ni^{II} square planar complexes containing thiolate ligation as inspired by the nickel binding sites found in NikR, a cytoplasmic nickel sensor protein, and NiSOD, the nickel-dependent superoxide dismutase. The strikingly similar conformation of the imidazole ligand in the continuous tetradentate ($N_2N'S$) and discontinuous (N_2S---N') coordination complexes encouraged

further investigations into the orientational preferences of various types of planar ligands (imidazoles, pyridine and an *N*-heterocyclic carbene), which is discussed in Chapter IV.

A final topic focuses on the coordination chemistry of vanadyl in N_2S_2 ligand sets. Our group has utilized dianionic and tetraanionic N_2S_2 binding motifs to examine the structural and reactivity differences resulting from the incorporation of different metals in such sites. Chapter V describes a synthesis and structural study of vanadyl held within a series of N_2S_2 donor environments. The vanadyl analogues were explored for their reactivity with alkylating agents and $W(CO)_x$.

CHAPTER II

GENERAL EXPERIMENTAL DETAILS

General Procedures

All solvents used were purified and degassed via a Bruker solvent system. Anaerobic techniques, an argon-filled glovebox and standard Schlenk techniques were employed for air sensitive reagents and complexes. Reagents were purchased from commercial sources and used as received unless noted.

General Physical Measurements

Electronic absorption spectra were recorded on a Hewlett-Packard 8453 diode array spectrometer and a Cary1E spectrophotometer using quartz cells (1.00 cm path length). Mass spectrometry (ESI-MS) was performed by the Laboratory for Biological Mass Spectrometry at Texas A&M University. Elemental analyses were performed by Atlantic Microlab, Inc., Norcross, Georgia or by Canadian Microanalytical Services, Ltd., Delta, British Columbia, Canada. Infrared spectra were recorded on a Bruker Tensor 37 Fourier Transform infrared (FTIR) spectrometer. Solution IR spectra were obtained using a CaF_2 cell with a 0.1 mm path length and solid sample analysis was obtained using an attenuated total reflectance attachment equipped with a ZnSe crystal.

^{1}H-NMR spectral measurements were carried out with a Mercury-300 FT-NMR spectrometer. Variable temperature ^{1}H-NMR spectra were acquired on an Inova500 spectrometer operating at 500 MHz. CD_3OD or D_2O were used as solvent and all

resonances were referenced to MeOH (CH_3: 3.31 ppm) or D_2O (H_2O: 4.78), respectively, at all temperatures.

EPR spectra were collected on a Bruker ESP 300 spectrometer equipped with an Oxford ER910 cryostat operating at 10 K. Samples were 1-2 mM in analyte and frozen DMF or MeCN solution. The WinEPR Simfonia program was used to simulate the g and *A* parameters.[55]

Electrochemistry

Cyclic voltammograms and differential pulse voltammograms were recorded on a BAS100W potentiostat under an Ar atmosphere using a three electrode cell, which consisted of a glassy carbon disk (0.071 cm^2) working electrode, a coiled platinum wire counter electrode and $Ag^0/AgNO_3$ reference electrode. Samples were measured in DMF with Bu_4NBF_4 (0.1 M) as the supporting electrolyte and at potential scan rates of 200 mV/s. Ferrocene was added as an internal standard and all potentials are reported relative to the $Ag^0/AgNO_3$ electrode using Cp_2Fe/Cp_2Fe^+ as reference ($E_{1/2}$ = 0.00 V vs. $Ag^0/AgNO_3$ in DMF). The reversibility of the observed redox couples is based on the internal reference (Cp_2Fe/Cp_2Fe^+). The peak-to-peak separations ($Ep_a - Ep_c$) for the complexes studied herein are larger than the 59 mV expected for a reversible one-electron process, but comparable with $Ep_a - Ep_c$ for the Cp_2Fe/Cp_2Fe^+ couple under the same conditions. The ratios of the anodic and cathodic peak currents were close to unity for the assigned reversible systems. Bulk electrolysis was carried out using a BAS 100A potentiostat and BAS bulk electrolysis cell containing 30 mL of DMF which was 1.0

mM in **3** and 0.1 M in Bu_4NBF_4 under an argon atmosphere. The working electrode of the BAS bulk electrolysis cell was reticulated vitreous carbon. Conductance measurements of mmolar concentrations of analyte used an Orion 160 conductivity meter.

X-Ray Diffraction and Analyses

All X-ray diffraction studies were carried out in the X-ray Diffraction Laboratory in the Department of Chemistry at Texas A&M University. Structures were determined with the assistance of Dr. Joe H. Reibenspies. Low-temperature (110 K) X-ray data were obtained on a Bruker SMART 1000 CCD based diffractometer (Mo sealed X-ray tube, Kα = 0.71073 Å) or on a Bruker-D8 Adv GADDS general-purpose three-circle X-ray diffractometer (Cu sealed X-ray tube, Kα = 1.541 84 Å). Space groups were determined on the basis of systematic absences and intensity statistics. Structures were solved by direct methods and refined by full-matrix least squares on F^2. H atoms were placed at idealized positions and refined with fixed isotropic displacement parameters and anisotropic displacement parameters were employed for all non-hydrogen atoms. The following programs were used: data collection, SMART WNT/2000 Version 5.632[56] or FRAMBO Version 4.1.05 (GADDS);[57] data reduction, SAINTPLUS Version 6.63;[58] absorption correction, *SADABS*;[59] cell refinement *SHELXTL*;[60] structure solutions, *SHELXS-97* (Sheldrick);[61] and structure refinement, *SHELXL-97* (Sheldrick).[62] The final data presentation and structure plots were generated in X-Seed

Version 1.5.[63] Experimental conditions and crystallographic data are listed in the Appendix.

Computational Details

All computations were carried out in the Laboratory of Molecular Simulation in the Department of Chemistry at Texas A&M University, and performed by group member Michael Singleton under the direction of Dr. Lisa Perez and Prof. Michael B. Hall. Initial geometries were derived from X-ray structures or deductions based on conformations resulting from fluxional processes in the molecules. In both cases, the conformational space near each of the starting geometries was sampled through simulated annealing calculations in the gas phase using the Cerius^2 software package.[64] The simulated annealing calculations were carried out using the Open Force Field (OFF) module with the Universal Force Field (UFF) for 15 annealing cycles, over a temperature range of 300-5000 K, with ΔT = 50 K. The compounds were minimized after each annealing cycle resulting in 15 conformations. The initial geometry and low energy conformations were then optimized using Density Functional Theory, with the Becke three-parameter exchange functional(B3)[65] and the Lee-Yang-Parr correlation functional(LYP) (B3LYP).[66]

All theoretical calculations, including optimization, frequency and NMR, were performed with the Gaussian 03 suite programs.[67] The Stuttgart-Dresden[68] (SDD) effective core potential and valence basis set were used for nickel. For sulfur, the effective core potential and basis set of Hay and Wadt[69] were used with inclusion of a

modified polarization function developed by Hŏllworth et al.[70] For nitrogen, the correlation-consistent polarized valence double-ζ basis set of Dunning and coworkers[71] (cc-pVDZ) was used. All carbon and hydrogen atoms were represented using the split valence double- ζ basis set of Pople and coworkers with polarization functions on heavy and light atoms[72-74] (6-31g(d',p')).

Transition state geometries were calculated using the synchronous transit-guided quasi-Newton (QST2) method[75-76] with the final optimized geometries for both rotational isomers for each complex used as the initial and final geometries. Relaxed potential energy scans looking at rotation about the Ni – $L_{donor\ atom}$ were accomplished by freezing the S–Ni–$N_{imid/pyr}$–C2 or S–Ni–C_{NHC}–N_{NHC} torsion angles at 5º intervals and then allowing the rest of the molecule to optimize.

CHAPTER III

IMIDAZOLE-CONTAINING (N_3S)-Ni^{II} COMPLEXES RELATING TO NICKEL-CONTAINING BIOMOLECULES*

Introduction

The reactivity of tetradentate N_2S_2 ligands containing nucleophilic S-sites in transition metal thiolate complexes has been extensively explored. In our laboratory, metalation, S-oxygenations, and alkylations have been used to establish reactivity of the neutral (bme-daco)Ni(II) complex, bme-daco = bismercaptoethanediazacyclooctane, the neutral (bme-dach)Ni(II) complex, bme-dach = bismercaptoethanediazacycloheptane, as well as the anionic $[Ni(II)(ema)]^{2-}$ complex, ema = N,N'-ethylenebis-2-mercaptoacetamide.[77-81] Coupled with S-thiolates, such amine, amide, or mixed amine/amide N-donor ligand environments have been proposed by us and others to serve as biomimetics of metalloenzyme active sites.[82-92]

The preparation of histidine/cysteine mixed donor binding sites was first demonstrated in small peptidic complexes by Suguri, et al., as models of blue copper proteins.[93-94] Nickel complexes of -X_{aa}-X_{aa}-His- tripeptide motifs have been studied in detail for their ability to influence DNA damage and cross-linking through oxidative processes.[95-96] To explore the potential oxidative chemistry of cysteine thiolates,

---

*Reproduced with permission from 132. Jenkins, R. M.; Singleton, M. L.; Almaraz, E.; Reibenspies, J. H.; Darensbourg, M. Y. *Inorg. Chem.* **2009**, *48*, 7280-7293.

Burrows and coworkers synthesized the cysteine variants, -X_{aa}-Cys-His- and -Cys-X_{aa}-His-, as possible metal binding sequences.[97-98] It was found that aerobic oxidation of such complexes with cysteine in the second position, -X_{aa}-Cys-His-, led to the rapid formation of disulfide dimers. In this case, other oxidized products such as metallosulfoxides or metallosulfones were not observed. The dimeric disulfide-bridged complex was found to have no further reactivity with oxygen even though Ni^{II} peptides with carboxylate termini are known to spontaneously decarboxylate in air.[97] In contrast, the Ni^{II} derivative of N-terminal -Cys-X_{aa}-His- resulted in the formation of a cysteine sulfinic acid under aerobic conditions.[98] Whether the plethora of possibilities of oxidative products complicate or play fundamental roles in the chemistry underlying biological action is not well understood.

As described in the Introduction, the molecular structures of NikR and NiSOD revealed nickel(II) sites which contain both N-histidine and S-cysteine ligands.[23-24] Their nickel-binding sites are reproduced in Figure III-1 as a reminder of the N/S donor sets needed for biomimetic studies. While biomimetic studies of the NiSOD site are established and on-going, the NikR binding site has received very little attention. This is surprising in that histidine N-binding sites play a major role in Ni-capture both *in vivo* and in technological (His-tag) applications.[1-2,99]

Considerable work has been targeted toward understanding how the NiSOD enzyme avoids S-oxygenation and/or S-oxidation in the presence of the products of SOD, O_2 and H_2O_2. Computational investigations have concluded that the presence of one or two amide donors within the N_2S_2 core promotes metal-based chemistry.[100-101]

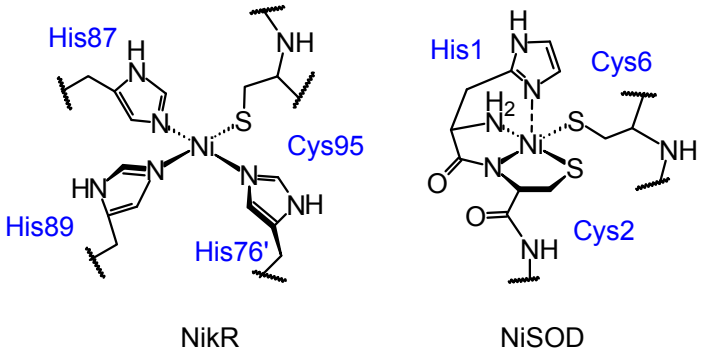

Figure III-1. The metal binding site of NikR and the active site of NiSOD. Adapted from References 13-14 and 23-24.

There has been significant progress in the preparation of synthetic mimics of the NiSOD active site. In particular, a mixed amine/amide donor set in the N_2S_2 core has resulted in a Ni^{II} complex with a ligand environment similar to the reduced state of the native enzyme, and this NiSOD mimic demonstrated enhanced stability toward oxygenation.[102-103] As *cis* dithiolate sulfurs in Ni^{II} complexes have been shown to form stable S-oxygenates in both neutral and dianionic N_2S_2Ni complexes, we have suggested that kinetic control accounts for the lack of S-oxygenates in the enzyme active site of NiSOD.[81]

Jensen and coworkers have utilized "scorpionate" ligands to mimic the nitrogen donors and dithiocarbamates and organoxanthate to mimic the dithiolate ligands of the NiSOD binding motif to obtain a five-coordinate $N_3S_2Ni(II)$ complex.[104] Although synthetic N_2S_2Ni complexes as NiSOD active site mimics have similar spectroscopic features as the native enzyme and quasi-reversible redox couples in the range of SOD dismutation, Shearer and Zhao's model complexes did not produce catalytic activity for

superoxide dismutation.[102-103] Neither did Jensen et al. report SOD activity.[104] Nevertheless, nickel peptide-based models mimicking the amino acid nickel-hook sequence found in the native NiSOD enzyme have been more successful, demonstrating compatible electrochemistry as well as SOD activity.[105] Studies by Shearer and coworkers also suggest that the His imidazole remains ligated throughout SOD catalysis, and this is supported by computational studies of Siegbahn, et al.[106-107]

Very little is known about how the electronic structure of Ni^{II} complexes containing both imidazole and thiolate ligation responds to oxidation and how this might affect SOD catalysis and response to the H_2O_2/O_2 products. To address this, we have prepared two synthetic models containing a continuous and discontinuous $N_2N'S$ donor set. For this study, a dimeric dithiolate bridged Ni^{II} dication and the readily accessed (bme-dach)Ni(II) were used as the precursors to mixed imidazole/thiolate complexes. The work herein reports the synthesis, characterization and molecular structures of both continuous tetradentate ($N_2N'S$) and discontinuous (N_2S-N') synthetic models incorporating simple imidazoles as His mimics. Variable temperature ^1H NMR studies in correlation with DFT calculations have been carried out to further investigate the orientation of the imidazole ligand. The physical properties of the derivatives and precursors and SOD activity are described.

Experimental Details

General Procedures. Isobutylene sulfide,[108] (bme-dach)Ni[79] and 4-(chloromethyl)-5-methyl-1H-imidazole hydrochloride[109] were prepared according to published procedures.

Synthesis of 1-(2-Mercaptoethyl)-methyl-1,4-diazacycloheptane, me-mdach. Similar to the preparation of the N_2S_2 ligand Hmmp-dach,[110] under N_2, *N*-methylhomopiperazine (5 mL, 0.0402 mmol) was dissolved in 50 mL of dry MeCN. With stirring, the solution was heated to 50 °C under N_2 and an excess of ethylene sulfide (8 mL, 0.134 mmol) was added slowly forming a white solid and a light yellow solution. Heating was continued for 20 h after which the solution was anaerobically filtered through Celite giving a light yellow solution. The solvent was removed in vacuo resulting in a yellow oil, 3.33 g, 48% yield. $C_8H_{18}N_2S$ (MW = 174 g/mol) $^+$ESI-MS: *m/z* = 175 $[M+H]^+$. ^{1}H NMR ($CDCl_3$): δ (ppm) = 1.83 (q, 2.0 H), 2.38 (s, 2.9 H), 2.64 (m, 4.2 H), 2.77 (m, 5.2 H), 2.86 (m, 2.6 H).

1-(2-Mercapto-2-methylpropyl)-methyl-1,4-diazacycloheptane, mmp-mdach, was prepared in a similar manner to the above using isobutylene sulfide. A light yellow oil was isolated in 31 % yield. $C_{10}H_{22}N_2S$ (MW = 202 g/mol) $^+$ESI-MS: *m/z* = 203 $[M+H]^+$.

Synthesis of {[1-(2-Mercaptoethyl)-methyl-1,4-diazacycloheptane]nickel(II)} Tetrafluoroborate, $[(me\text{-}mdach)Ni]_2(BF_4)_2$, Complex 1. Under N_2, me-mdach (0.56 g, 3.22 mmol) was dissolved in 20 mL of dry MeOH. A solution of NaOMe (0.17 g, 3.17 mmol) in 10 mL dry MeOH was added via cannula and the mixture was stirred at

room temperature (RT) for 1 h. A solution of $Ni(BF_4)_2 \cdot 6\ H_2O$ (0.75 g, 3.23 mmol) in 25 mL of MeOH was added dropwise via cannula producing a red solution. After stirring at RT for 4 hours the solvent volume was reduced to ca. 5 mL. Addition of 25 mL MeCN resulted in the precipitation of $NaBF_4$ salts, which were separated from the product by filtration in air. The solvent of the filtrate was removed in vacuo resulting in a tacky maroon residue. The residue was dissolved in a minimum of MeOH and a maroon solid was obtained on addition of diethyl ether. Alumina column chromatography was used to purify the crude product using MeCN as the eluent until a light yellow band was removed, followed by an elution mixture of MeOH/MeCN (1:25), which yielded a maroon band of pure $[(me\text{-}mdach)Ni_2](BF_4)_2$ (0.38 g, 37%). X-ray quality crystals were obtained by Et_2O diffusion into a MeCN solution at 5 °C. Elemental anal. for $Ni_2C_{16}H_{34}N_4S_2B_2F_8$ (MW = 638 g/mol) Calcd (found): C, 30.14 (30.40); N, 8.78 (8.65); H, 5.37 (5.25). Absorption spectrum (MeOH): λ_{max} (ε, $M^{-1}\ cm^{-1}$) 524 (817), 452 (775), 354 (2503), 305 (13075), 252 (13675), 229 (21330) nm. $^{+}$ESI-MS (MeCN): *m/z* = 549 $[(me\text{-}mdach)_2Ni_2)]BF_4^{+}$; 231 $[(me\text{-}mdach)_2Ni_2]^{2+}$. Molar conductance at 23 °C: 299 S $cm^2\ mol^{-1}$ (MeCN); 310 S $cm^2\ mol^{-1}$ (H_2O).

Chloro-[1-(2-Mercaptoethyl)-methyl-1,4-diazacycloheptane]nickel(II), [(me-mdach)-NiCl]$_2$, Complex 2. Chloro-[1-(2-Mercaptoethyl)-methyl-1,4-diazacycloheptane]nickel(II), $[(me\text{-}mdach)\text{-}NiCl]_2$, complex **2**, was prepared and purified in a similar manner using $NiCl_2 \cdot 6H_2O$ as the metal source. The complex was purified by alumina column chromatography yielding pure $[(me\text{-}mdach)NiCl]_2$ as a reddish brown solid (31% yield). X-ray quality crystals were obtained by Et_2O diffusion

into an MeCN solution at 5 °C. Elemental anal. for $Ni_2C_{16}H_{34}N_4S_2Cl_2$ (MW = 535 g/mol) Calcd (found): C, 36.0 (37.0); N, 10.5 (10.2); H, 6.41 (6.76). Absorption spectrum (MeOH): λ_{max} (ε, M^{-1} cm^{-1}) 527 (967), 490 (sh), 350 (3307), 307 (7816), 247 (17126), 211 (18002) nm. $^{+}$ESI-MS: *m/z* = 497 $[(me\text{-}mdach)_2Ni_2Cl]^{+}$; 231 $[(me\text{-}mdach)_2Ni_2]^{2+}$. Molar conductance at 23 °C: 124 S cm^2 mol^{-1} (MeCN); 303 S cm^2 mol^{-1} (H_2O).

Chloro-[1-(2-Mercapto-2-methylpropyl)-methyl-1,4-diazacycloheptane]-nickel(II), $[(mmp\text{-}mdach)NiCl]_2$, Complex 2-Me$_2$. Chloro-[1-(2-Mercapto-2-methylpropyl)-methyl-1,4-diazacycloheptane]nickel(II), $[(mmp\text{-}mdach)NiCl]_2$, complex **2-Me$_2$**, was obtained via the above method by using the mmp-mdach ligand. Absorption spectrum (MeOH): λ_{max} (ε, M^{-1} cm^{-1}) 532 (904), 426 (988), 326 (6120), 283 (11940), 244 (21300), 205 (24580) nm. $^{+}$ESI-MS mass spectral analysis for $Ni_2C_{20}H_{42}N_4S_2Cl_2$ (MW = 591 g/mol): *m/z* = 553 $[(mmp\text{-}mdach)_2Ni_2Cl]^{+}$; 259 $[(mmp\text{-}mdach)Ni_2]^{2+}$. Molar conductance at 23 °C: 104 S cm^2 mol^{-1} (MeCN); 299 S cm^2 mol^{-1} (H_2O).

Synthesis of [1-(2-Mercapto-2-methylpropyl)-methyl-1,4-diazacycloheptane]-nickel(II) Imidazole Chloride, [(mmp-mdach)Ni(Im)]Cl, Complex 3. After degassing and under N_2, complex **2,** $[(mmp\text{-}mdach)NiCl]_2$, (0.102 g, 0.173 mmol) and imidazole (0.035 g, 0.514 mmol) were dissolved in 30 mL of dry MeOH, which immediately produced an orange solution. After stirring overnight, the solution volume was reduced to a minimum under vacuum, and Et_2O was added to precipitate the product. The ether was decanted and the product was washed 2 x 25 mL Et_2O to remove excess imidazole. Pure product was isolated as an orange solid (0.092 g,

71% yield). X-ray quality crystals were obtained by Et_2O diffusion into a MeOH solution at -30 °C. $NiC_{13}H_{25}N_4SCl$ Elemental anal. for $NiC_{13}H_{25}N_4SCl{\cdot}H_2O$ (MW = 382 g/mol) Calcd (found): C, 40.92 (40.88); N, 14.68 (14.45); H, 7.13 (7.07). Absorption spectrum (MeOH): λ_{max} (ε, M^{-1} cm^{-1}) 467 (501), 340 (sh), 288 (10767), 211 (21461) nm. $^+$ESI-MS (MeOH): *m/z* = 327 $[(mmp\text{-}mdach)Ni(Im)]^+$. Molar conductance at 23 °C: 89 S cm^2 mol^{-1} (MeOH); 156 S cm^2 mol^{-1} (H_2O).

Synthesis of [1-(5-methyl-1*H*-imidazol-4-yl)methylthio)ethyl-4-mercaptoethyl-1,4-diazacycloheptane]nickel(II) Chloride, [Ni-1'(CH_2-mIm)]Cl, Complex 4. A 100 mL Schlenk flask was charged with (bme-dach)Ni (0.100 g, 0.361 mmol). The solid was degassed and suspended in 25 mL of MeCN. A suspension of 4-(chloromethyl)-5-methyl-1*H*-imidazole hydrochloride (0.060 g, 0.361 mmol) in 25 mL of MeCN was transferred via cannula. As the reaction proceeded, the solids were drawn into solution followed by formation of a light pink precipitate. The mixture was stirred overnight. Filtration yielded a pink solid which was washed 3 x 75 mL MeCN, dissolved in a minimum of MeOH, and recrystallized with Et_2O. The solid was washed 2 x 25 mL Et_2O (45 mg, 31 %). X-ray quality crystals were obtained by Et_2O diffusion into a MeOH solution. Elemental anal. for $NiC_{14}H_{25}N_4S_2Cl{\cdot}H_2O$ (MW = 426 g/mol) Calcd (found): C, 39.50 (40.07); N, 13.16 (13.23); H, 6.39 (6.44). Absorption spectrum (MeOH): λ_{max} (ε, M^{-1} cm^{-1}) 469 (235), 288 (6052), 211 (16983) nm. $^+$ESI-MS: *m/z* = 371 [Ni-1'(CH2-mIm]$^+$. Molar conductance at 23 °C: 103 S cm^2 mol^{-1} (MeOH); 164 S cm^2 mol^{-1} (H_2O).

Synthesis of 1,4-Bis(3-methylimidazol-4-ylmethyl)-1,4-diazacycloheptane nickel(II) Tetrafloroborate, [(bmIme-dach)Ni]$(BF_4)_2$, Complex 5. Synthesis, purification and characterization of 1,4-bis(3-methylimidazol-4-ylmethyl)-1,4-diazacycloheptane penta-hydrochloride hydrate (L-5HCl·H_2O) was executed following the procedure published by Bu, et al.. with 4-(chloromethyl)-5-methyl-1*H*-imidazole hydrochloride used in the place of 4-(chloromethyl)-1*H*-imidazole hydrochloride.[111-112] A solution of $Ni(BF_4)_2$·6 H_2O (1.328 g, 3.903 mmol) in 10 mL of MeOH was added dropwise to a stirring solution of L-5HCl·H_2O (1.100 g, 3.814 mmol) in 15 mL of MeOH, resulting in immediate precipitation of yellow solid. The reaction mixture was stirred overnight at 22 °C under an N_2 blanket. The ensuing green solution and yellow solid were separated via filtration, and the solid was washed with Et_2O and dried in vacuo to yield 0.757 g (1.45 mmol, 38 %). X-ray quality crystals were obtained by slow evaporation from a methanol solution. Elemental anal. for $NiC_{15}H_{24}N_6B_2F_8$ (MW = 521 g/mol) Calcd. (found): C, 34.60 (34.07); H, 4.65 (4.70); N, 16.14 (15.62). Absorption spectrum (MeOH): λ_{max} (ε, M^{-1} cm^{-1}): 449 (29), 280 (sh), 233 (2232) nm. $^{+}$ESI-MS in MeOH: $[M]^{2+}$ *m/z* = 173 $[(bmIme\text{-}dach)Ni]^{2+}$. Molar conductance at 23 °C: 198 S cm^2 mol^{-1} (MeOH); 223 S cm^2 mol^{-1} (H_2O).

Synthesis and Structural Characterization

Synthesis and structure of N_2S bridged thiolate dimers: [(me-mdach)Ni]$_2(BF_4)_2$, 1, and [(me-mdach)NiCl]$_2$, 2. There are many examples of N_2S_2Ni complexes in μ_2S_2-bridged dimers which demonstrate the diverse structural

arrangements encountered by μ-S-thiolate bridging.[84, 87, 90,113-117] Scheme III-1 outlines the synthetic protocol for the N_2S thiolate bridged dimeric complexes **1** and **2** explored

Scheme III-1.

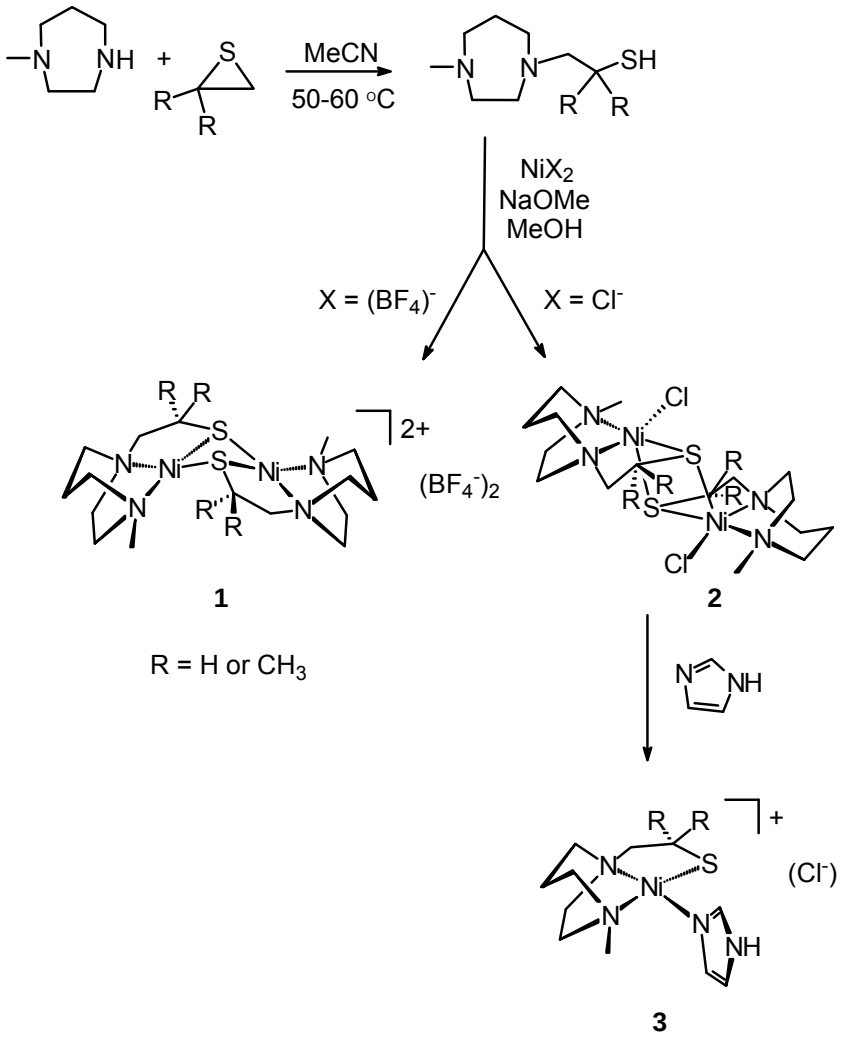

herein. Both are isolated as hygroscopic, air stable solids. Complex **1** is a deep maroon solid that is very soluble in MeCN and H_2O and moderately soluble in MeOH. Complex

2 is isolated as a reddish-brown powder and is very soluble in MeOH and H_2O and moderately soluble in MeCN. The molecular structures of **1** and **2** are shown in Figure III-2 and a selection of metric data is given in Table III-1. The dimeric form of complex **1** involves edged-bridged square planes with symmetry imposed disorder relating to the S to N linkers. The NiN_2S_2 unit is almost perfectly square planar with average standard

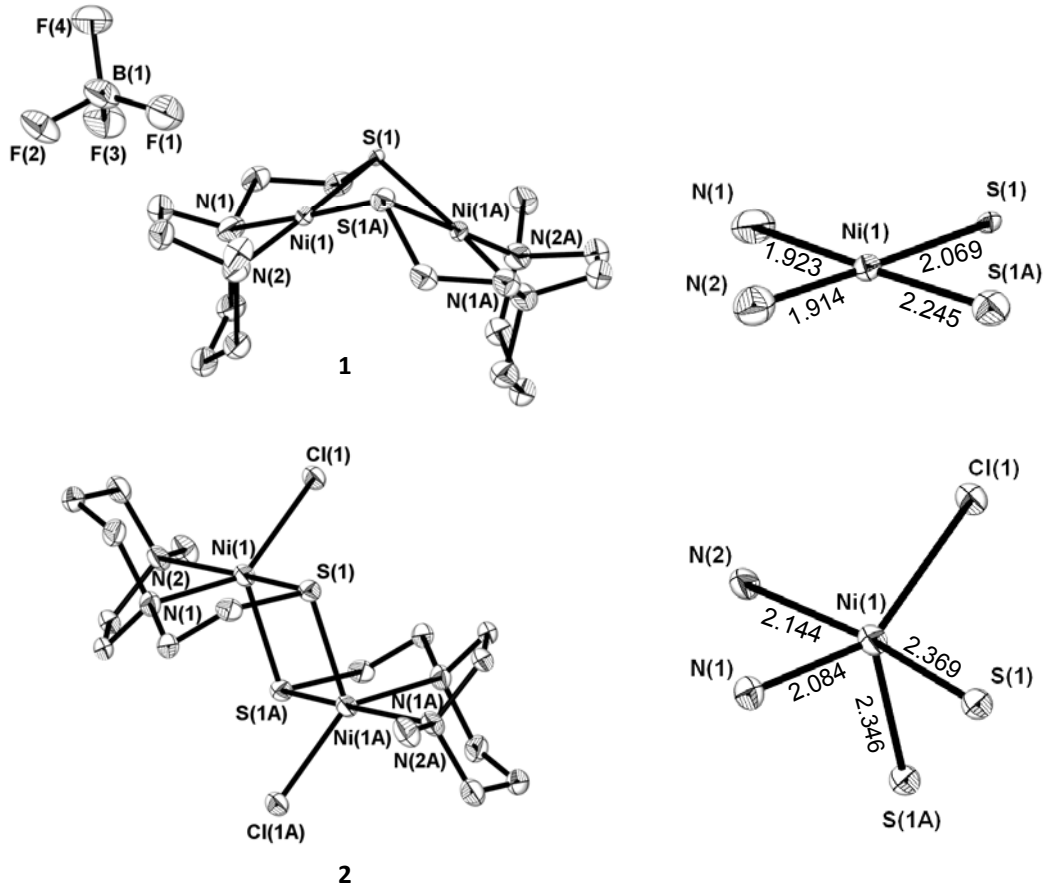

Figure III-2. Molecular structure of complexes $[(me\text{-}mdach)Ni]_2(BF_4)_2$, **1**, and $[(me\text{-}mdach)\text{-}NiCl]_2$, **2**, shown as thermal ellipsoids at 50% probability. First coordination spheres shown at right.

Table III-1. Metric data for complexes [(me-mdach)Ni]$_2$(BF$_4$)$_2$, **1**, and [(me-mdach)-NiCl]$_2$, **2**.

	1	**2**
Ni(1)-S(1)	2.069(19) Å	2.369(17) Å
Ni(1)-S(1A)	2.245(16) Å	2.346(18) Å
Ni(1)-N(1)	1.923(8) Å	2.084(5) Å
Ni(1)-N(2)	1.914(8) Å	2.144(5) Å
Ni(1)···Ni(2)	2.837 Å	3.268 Å
Ni(1)-Cl(1)		2.331(17) Å
N(1)-Ni(1)-N(2)	83.6(3) º	77.3(2) º
N(1)-Ni(1)-S(1)	96.4(5) º	86.7(14) º
N(2)-Ni(1)-Cl(1)		92.9(14) º
S(1)-Ni(1)-Cl(1)		96.6(6) º
S(1)-Ni(1)-S(1A)	79.6(6) º	92.3(5) º
Cl(1)-Ni(1)-S(1A)		114.6(6) º
N(1)-Ni(1)-S(1A)	175.4(5) º	100.6(15) º
N(2)-Ni(1)-S(1A)	100.5(4) º	96.8(15) º
Ni(1)-S(1)-Ni(1A)	82.1(6) º	87.8(5) º

deviation from plane of 0.0038 Å. The "hinge" angle in this butterfly type complex, that is, the dihedral angle between the two N_2S_2 best planes, is 116.7º; the Ni···Ni distance is 2.837 Å. A similar dimer with gem dimethyl groups on the carbon α to the bridging sulfurs has a greater hinge angle of 135.7º and a Ni···Ni distance of 3.034 Å.[110] These distances are compatible with other complexes containing (μ_2-SR)$_2$ bridged Ni_2S_2 rhombs.[84, 87, 113-117] The closest BF_4^- counterion in **1** has an F···Ni distance of 5.031 Å.

In contrast to the μ-SR bridged square planar NiN_2S(μ-S) of **1**, the solid state structure of **2** finds a penta-coordinate Ni^{II} in pseudotrigonal bipyramidal, N_2S(μ-S)Cl coordination (Figure III-2). The equatorial plane in each tbp is comprised of one N-donor atom of the tridentate N_2S ligand, a chloro ligand and a sulfur atom from the adjacent (N_2S)Ni moiety resulting in an Ni_2S_2 diamond core. The S-donor atom and the

trans N-donor atom of the tridentate N_2S ligand make up the axial sites. The $Ni\text{-}S_{axial}$ bond distance of **2** is slightly longer than $Ni\text{-}S_{equatorial}$. As expected, the average Ni-N and Ni-S distances are longer in the penta-coordinate chloride derivative **2** than in **1**, and an increase in the Ni···Ni distance, from 2.837 Å in complex **1** to 3.268 Å in complex **2** is also observed, Table III-1. The N-Ni-N and S-Ni-S angles in complex **1** are acute at 83.6º and 79.6º, while the N-Ni-S angle, within the five-membered ring, is 96.4º. In complex **2**, the N-Ni-N angle contracts to 77.3º, the S-Ni-S opens to 92.3º, and the N-Ni-S angle within the five-membered ring contracts to 86.7º.

The dimeric species, $[(mmp\text{-}mdach)NiCl]_2$, **2-Me$_2$**, is isolated as a hygroscopic, air stable, bright purple powder, which is very soluble in MeOH, H_2O and MeCN. Thus far crystals have not been obtained; however, conductivity and cyclic voltammetry measurements are similar in **2-Me$_2$** and **2**, suggesting similar structures. The **2-Me$_2$** complex was cleaved by imidazole in the preparation of complex **3**.

Synthesis and Structure of [(mmp-mdach)Ni(Im)]Cl, 3 The cleavage of dimeric μ-dithiolato Ni^{II} by monodentate ligands is a fairly common, but not a universally successful approach to mononuclear square planar nickel complexes.[52,110,118-120] As shown in Scheme III-1, addition of excess imidazole to $[(mmp\text{-}mdach)NiCl]_2$ in MeOH results in an orange solid analyzed as complex **3** in high yield. Complex **3** is hygroscopic, soluble in MeOH, H_2O and DMF and crystallizes on layering a MeOH solution with Et_2O. The molecular structure of the imidazole-cleaved complex is shown in Figure III-3 and significant metric parameters are listed in the figure caption. To our knowledge, **3** provides the first molecular structure of a Ni complex containing both

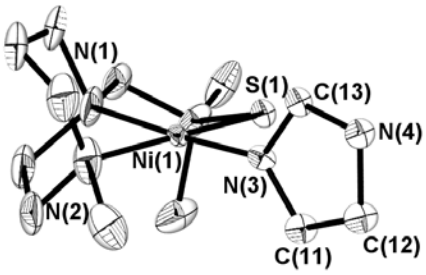

Figure III-3. Molecular structure of the cation of [(mmp-mdach)Ni(Im)]Cl, **3**, shown as thermal ellipsoids at 50% probability. The Cl^- counter ion and MeOH molecule are not shown.

thiolate and imidazole donor ligands. The nickel coordination environment is largely square planar with very slight tetrahedral twist distortion, 7.9°, defined by the intersection of N(1)Ni(1)N(2) and N(3)Ni(1)S(1) planes. The N-Ni-N angle within the dach donor is 81.5º while the S-Ni-N_{imid} angle is 91.4º; the N(2)-Ni(1)-N(3) angle is 97.1º. Notably, the plane of the imidazole ligand is perpendicular to the $N_2N'SNi$ plane, with the amine N(4) in the imidazole ring on the same side of the $N_2N'S$ coordination plane as is the C_3 portion of the dach ring. As in complexes **1** and **2**, the NiN_2C_3 metallodiazacyclohexane ring is in the chair conformation. There is no significant difference in the bond distances of the Ni-N_{amine} and the Ni-N_{imid}. The Ni-S distance of 2.149(3) Å is shorter than any Ni-S distance of complexes **1** or **2**. The extended structure finds a Cl^- and MeOH molecule within the unit cell which appear to create a H-bonding network as seen by the Cl···O distance of 3.568 Å and Cl···N_{imid} distance of 3.119 Å (Figure III-4). The latter is well within the summation of van der Waals' radii of chlorine and nitrogen.

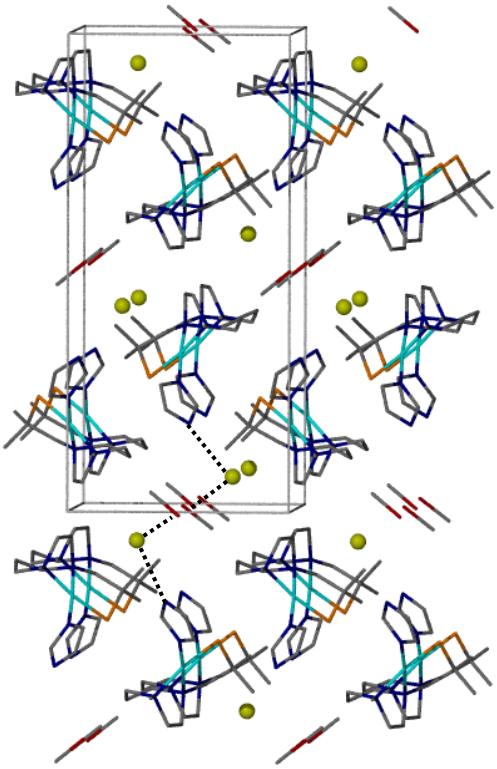

Figure III-4. Packing diagram of complex [(mmp-mdach)Ni(Im)]Cl, **3**.

Synthesis and Structure of [Ni-1'(CH_2-mIm)]Cl, 4. Stoichiometric addition of 4-(chloromethyl)-5-methyl-imidazole·HCl to neutral (bme-dach)Ni in MeOH results in solubilization of the insoluble precursors as S-alkylation occurs, Scheme III-2. The acidic conditions of the reaction sacrifice a portion of the (bme-dach)Ni starting material; however, use of the acid-free imidazole results in poorer yields. Purified complex **4** was isolated as a rose-colored solid in 30% yield. It is hygroscopic and soluble in H_2O, MeOH, and DMF; crystals were grown in a solution of MeOH layered

Scheme III-2

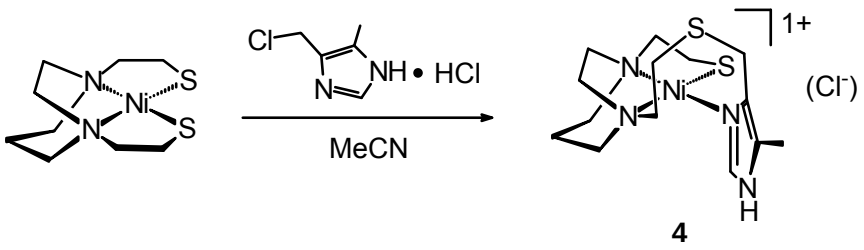

4

with Et_2O. The solid state structure of **4** (Figure III-5) reveals a ($N_2N'S$)Ni square planar binding motif of two amine nitrogens from the dach ring, the imidazole nitrogen and the thiolate sulfur with a slightly larger distortion from planarity, a 13.2° Td twist, than was found in complex **3**.

As given in Figure III-6, angles and bond distances in complex **4** are similar to those of complex **3**. The thioether-S is oriented over the $N_2N'S$ plane, however the Ni-$S_{thioether}$ distance of 3.022 Å is beyond bonding. Although thioethers are weak donors, there are several square planar N_2S_2Ni compounds known in which the sulfur is a thioether within a polydentate ligand or macrocycle.[121-122] In addition, S-alkylation by reagents that provide an additional binding site is known to maintain the tetradentate N_2S_2 bonding and expand the coordination number of N_2S_2Ni complexes.[123-124] The switch of the donor atom from the thioether to the N-imidazole in **4** indicates that the greater binding ability of the imidazole nitrogen over the thioether sulfur overwhelms the favorable chelate effect for the thioether, going from a five-membered ring to a less

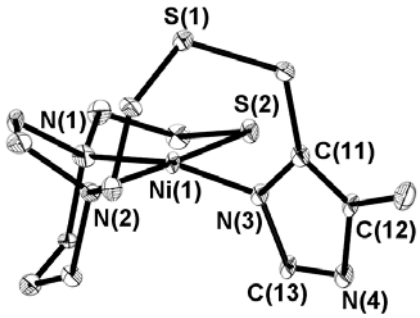

Figure III-5. Molecular structure of the cation of [Ni-1'(CH_2-mIm)]Cl, **4**, shown as thermal ellipsoids at 50% probability. The Cl^- counter ion is not shown.

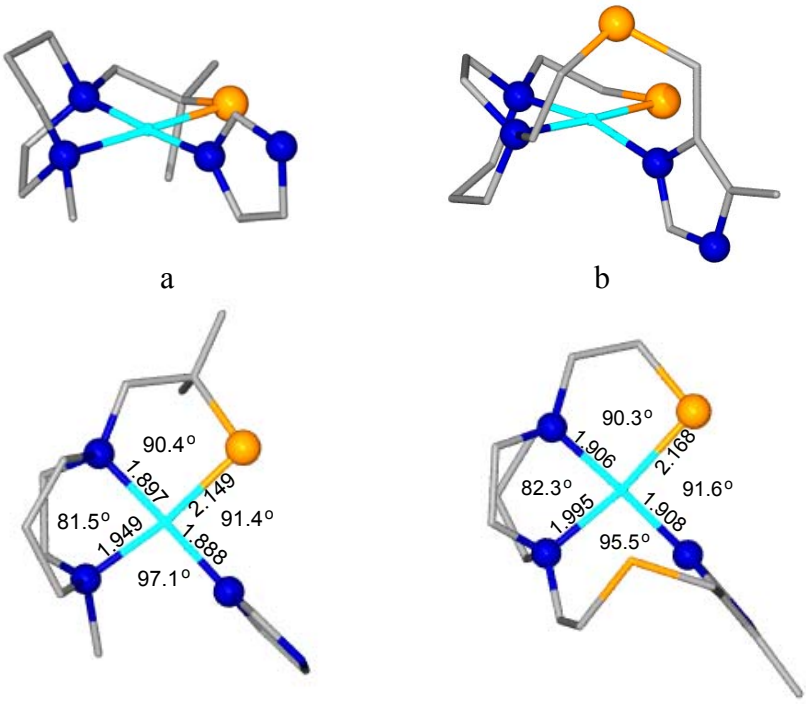

Figure III-6. Ball and stick drawings of (a) [(mmp-mdach)Ni(Im)]Cl, **3**, and (b) [Ni-1'(CH_2-mIm]Cl, **4**. Counter anions are not shown. Top: side view; Bottom: View ⊥ to N_2S plane with selected metric parameters.

Scheme III-3

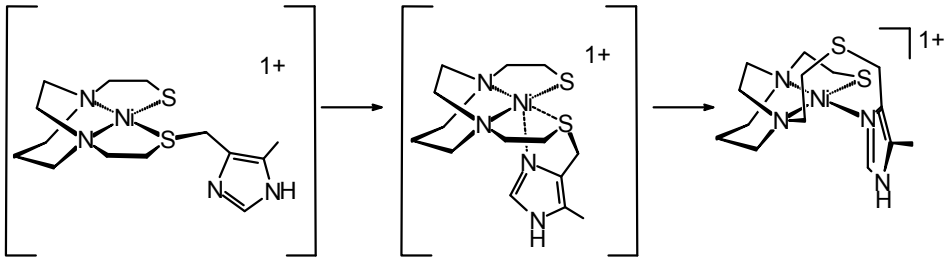

favored eight-membered ring. Scheme III-3 outlines likely intermediates (in brackets) in the reaction pathway; neither of these has thus far been verified.

As was also seen in complex **3**, the orientation of the imidazole plane in **4** is perpendicular to the $N_2N'S$ plane. The N(2)···S(1)···C(11) linker or imidazole tether is sufficiently long so as not to interfere with the optimal binding of the imidazole donor (vide infra). The closest chloride ions in the crystal lattice are located 3.046 Å away from the N of the imidazole ligand (Figure III-7).

Synthesis and Structure of [(bmIme-dach)Ni](BF$_4$)$_2$, 5. Complex **5**, prepared by coworker Elky Almaraz as described in Scheme III-4, is isolated as a gold solid that is soluble in MeCN, MeOH, H_2O and DMF. Figure III-8 displays the thermal ellipsoid plot for complex **5** along with alternate views that highlight the slight staggering of the imidazole rings while the NiN_4 plane (Td twist of 7.9°) is largely coplanar with the imidazole ligand planes. The dihedral angle between the planes of the pendant imidazole rings is 11.4º. An analogue of complex **5,** lacking the methyl group on the

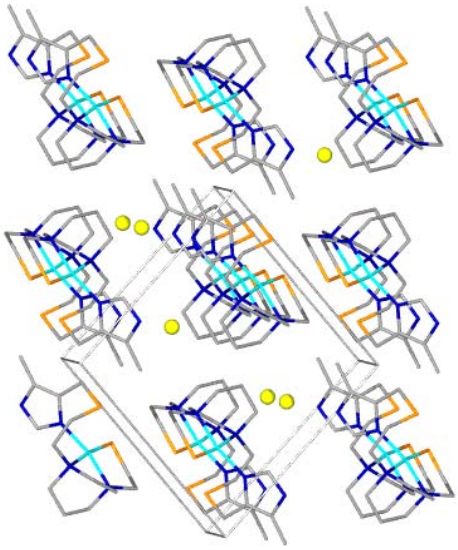

Figure III-7. Packing diagram of [Ni-1'(CH_2-mIm)]Cl, **4**.

Scheme III-4

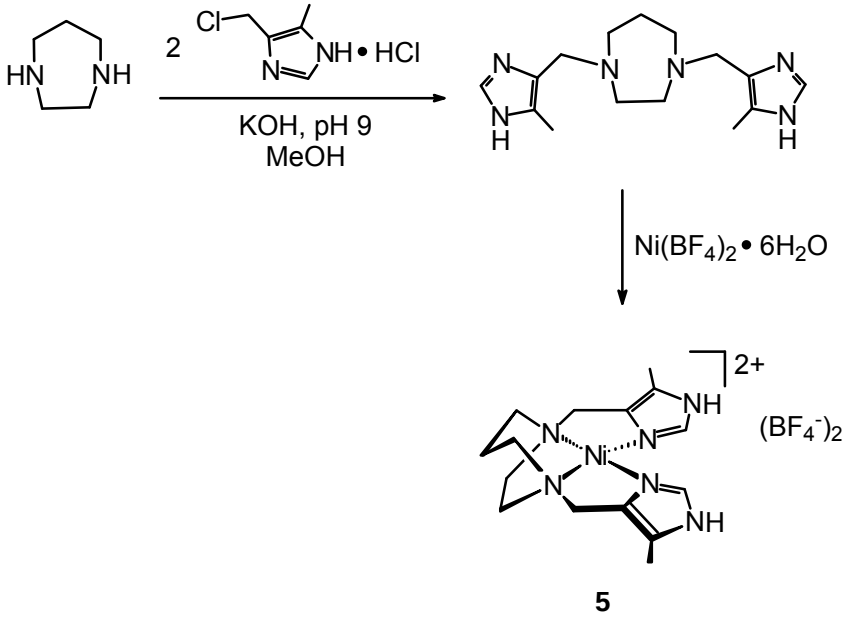

5

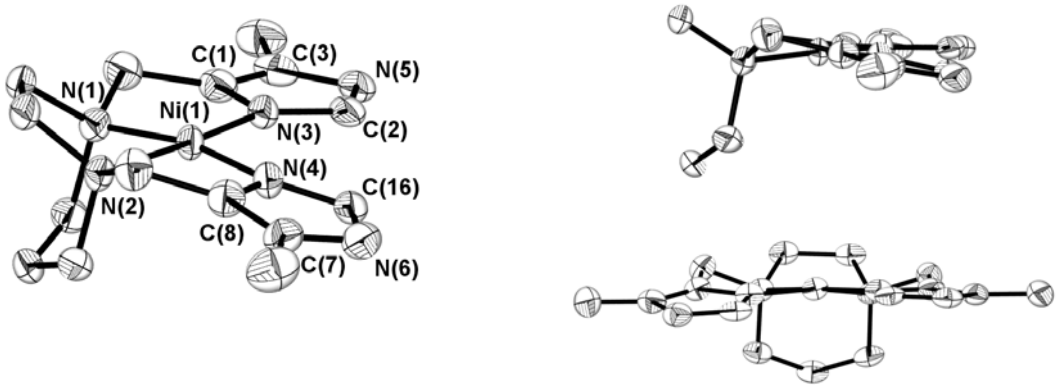

Figure III-8. Molecular structure of the dication of [(bmIme-dach)Ni]$(BF_4)_2$, **5**, shown as thermal ellipsoids at 50% probability. The BF_4 counter ions are not shown.

imidazole and isolated as a perchlorate salt, reported by Bu, et al. has similar metric parameters; however, a smaller dihedral angle exists between the imidazole ring planes (6.1°).[111-112] The extended packing structure of complex **5** shows π-π stacking between imidazole rings as suggested by interplanar distances of 3.432 Å (Figure III-9). In contrast, the crystal structure reported by Bu et al., shows the formation of intermolecular hydrogen bonds between the imidazole N-H and the O atom of the ClO_4^- counterion resulting in a dimeric structure.[111-112]

Despite the differences in the imidazole orientation of the tetradentate $(N_{amine})_2(N_{imid})_2Ni$, complex **5**, and the complexes **3** and **4**, the Ni-N_{imid} bond distances are significantly the same. A final note on the monomeric nickel $N_2N'S$ and $N_2N'_2$ complexes is in regards to angles within the square plane. Figure III-6 shows minor differences in the free imidazole complex **3** and the long tethered imidazole complex **4**.

In complex **5**, the N(1)-Ni-N(2) angle is largely the same as in complexes **3** and **4**, while the angle between donor atoms trans to the diazacycle donors, N(3) and S or N(3) and N(4), opens substantially from 91.4º and 91.6º in **3** and **4**, respectively, to 104º in complex **5.**

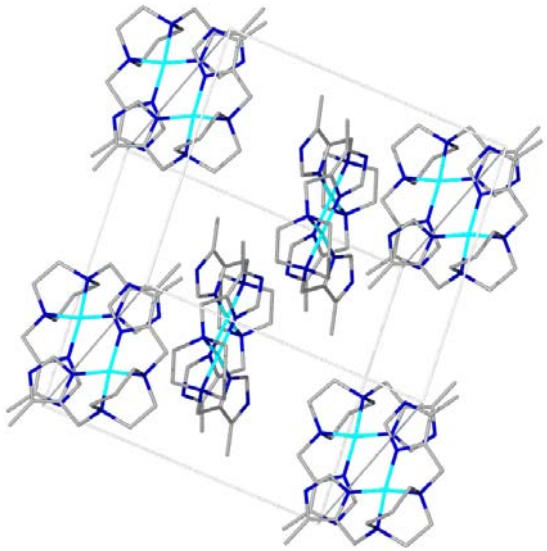

Figure III-9. Packing diagram of [(bmIme-dach)Ni]$(BF_4)_2$, **5**, showing π-π stacking between imidazole rings.

Conductivity Measurements

The results of molar conductivity measurements are listed in Table III-2. As expected, because of the non-coordinating BF_4^- counterion, complex **2** behaves as a 2:1 electrolyte in both MeCN and H_2O solutions, while the Cl^- derivative, complex **1**, is a 1:1 electrolyte in MeCN and acts as a 2:1 electrolyte in H_2O.[125] Note that the conductivity of **2-Me$_2$** follows that of complex **1** with a single Cl^- dissociating in the polar organic solvent; both Cl^- ions dissociate in H_2O. The molar conductance values for

the mononuclear square planar complexes, **3** and **4**, are consistent with a 1:1 electrolyte in both MeOH and H_2O solutions and complex **5** is a 2:1 electrolyte in MeOH and H_2O.

Table III-2. Molar conductivities at 25ºC.

	Λ_M at 10^{-3} M ($cm^{-1}mol^{-1}\Omega^{-1}$)		
Compound	H_2O	MeCN	MeOH
$[(me\text{-}mdach)_2Ni_2](BF_4)_2$, **1**	310	299	
$[(me\text{-}mdach)NiCl]_2$, **2**	303	124	
$[(mmp\text{-}mdach)NiCl]_2$, **2-Me$_2$**	299	104	
[(mmp-mdach)Ni(Im)](Cl), **3**	156		89
[Ni-1'(CH_2·mIm)](Cl), **4**	164		103
$[(bmIme\text{-}dach)Ni](BF_4)_2$, **5**	223		198

Electronic Absorption Spectra

Typical square planar nickel complexes exhibit d-d transitions in the range of 400-600 nm. Higher energy and more intense features can be assigned as ligand-to-metal charge transfer (LMCT) transitions. Nickel complexes with RS^- ligands show such intense absorbances within the 250-350 nm range, which are attributed to $RS^- \rightarrow Ni^{II}$ charge transfer transitions.[126] Table III-3 lists the electronic absorption data for complexes **1-5** and **2-Me$_2$**. The UV-vis absorption spectrum of $[(me\text{-}mdach)Ni]_2(BF_4)_2$, **1**, in which the Ni^{2+} ions are held in a square planar geometry exhibit two d→d bands with λ_{max} at 452 and 524 nm, in addition to high energy LMCT absorptions at 229, 252, 305, and 354 nm (ε values > 10,000 M^{-1} cm^{-1}). In complex $[(me\text{-}mdach)NiCl]_2$, **2**, four intense LMCT absorptions are observed and a broad d→d band is seen at 527 nm with a

shoulder at 490 nm. The absorptions for **2-Me$_2$** are similar to complex **2**. The absorption spectrum of the imidazole cleaved dimer, (mmp-mdach)Ni(Im)](Cl), **3**, displays one d-d band with λ_{max} at 467 nm and two intense ligand to metal charge transfer bands at 211 and 288 nm. Similar absorptions are observed for the square planar complex **4**. In complex **5**, all absorptions are of low intensity.

Table III-3. Summary of electronic absorption spectra.

	UV-Vis: λ_{max} (nm) (ε, $\mathbf{M}^{-1}$ cm^{-1})					
	CT transitions				d→d transitions	
[(me-mdach)$_2$Ni$_2$](BF$_4$)$_2$, **1** [b]	229 (21330)	252 (13765)	305 (13075)	354 (2503)	452 (775)	524 (817)
[(me-mdach)NiCl]$_2$, **2**	211 (18000)	247 (17126)	307 (7816)	350 (3310)	490 (sh)	527 (967)
[(mmp-mdach)NiCl]$_2$, **2-Me$_2$**		244 (21298)	283 (11940)	426 (6115)	426 (988)	532 (904)
(mmp-mdach)Ni(Im)](Cl), **3**	211 (21460)			288 (10767)	340 (sh)	467 (501)
[Ni-1'(CH$_2$-mIm)](Cl), **4**	211 (16980)			288 (6052)		469 (235)
[(bmIme-dach)Ni](BF$_4$)$_2$, **5**		233 (2232)		280 (sh)		449 (29)

[a] Unless specified otherwise, all results were obtained from MeOH solutions. [b] The electronic spectrum of [(me-mdach)$_2$Ni$_2$](BF$_4$)$_2$ was measured in MeCN.

Electronic absorption spectroscopy was used to investigate whether donor switching of the N-imidazole to the S-thioether of Ni-1'(CH$_2$-mIm)](Cl) might occur during incremental addition of acetic acid to a methanolic solution of **4**, with the expectation that protonated imidazole might promote thioether binding. No changes in the absorption spectrum were observed over a pH range of 8.5 to 3.4, indicating that the coordination environment was constant. These results are consistent with density functional theory (DFT) computations which found the crystallographically observed

imidazole bound structure was the isomer of lower energy with an energy difference between the two of 3.34 kcal/mol, Figure III-10.

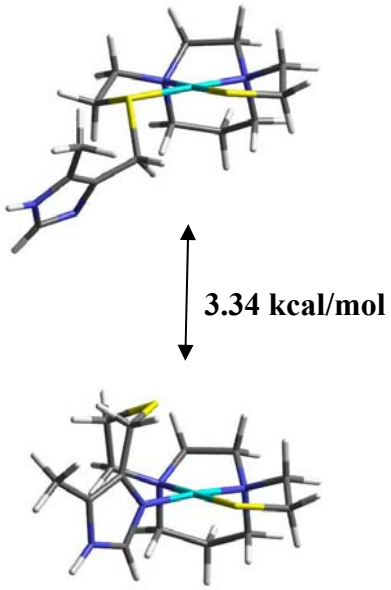

Figure III-10. DFT optimized isomeric forms of [Ni-1'(CH_2-mIm)]Cl, **4**. (top) S-thioether bond (bottom) N-imidazole bound.

Electrochemical Properties

A summary of electrochemical properties of complexes **1**-**5**, **2-Me$_2$** and (bme-dach)Ni are given in Table III-4. All seven complexes show an irreversible oxidation event, which is ascribed to thiolate oxidation in the case of complexes **3**, **4**, and (bme-dach)Ni.

The cyclic voltammograms for the N_2S μ-thiolate bridged Ni dimers, **1**, **2**, and **2-Me$_2$**, are shown in Figure III-11. Two well-defined reduction events are observed in each; the first reduction is reversible when the scan direction is reversed before the

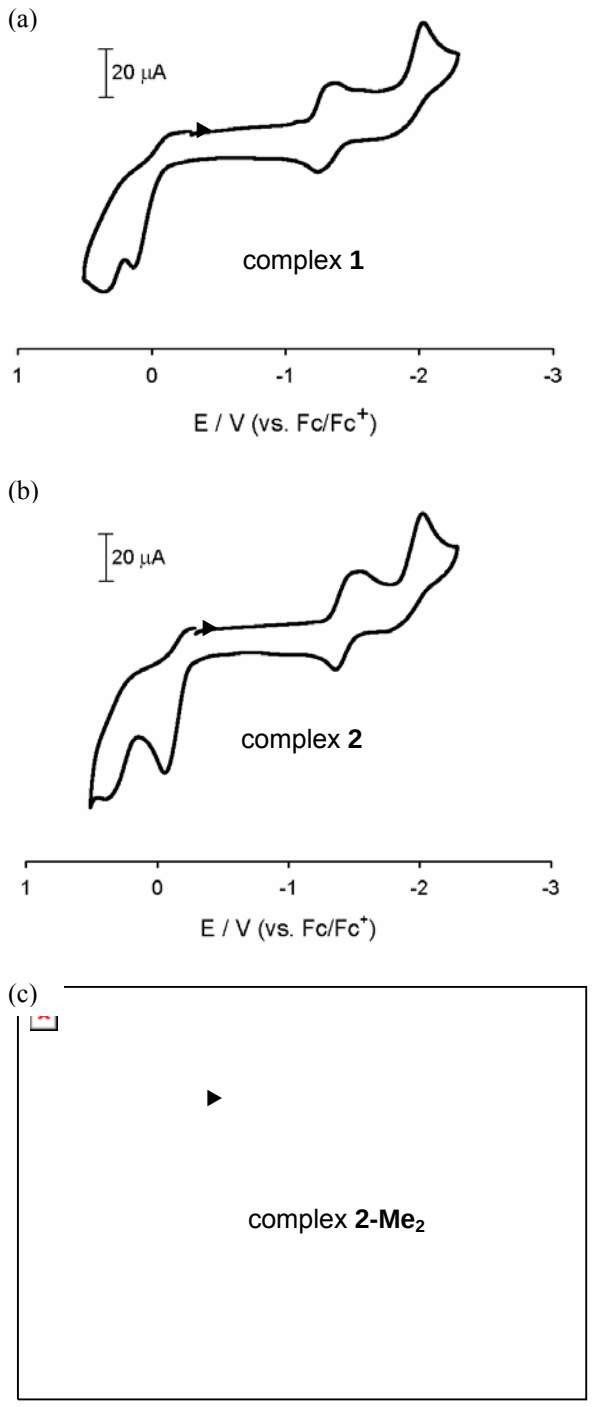

Figure III-11. Cyclic voltammograms of a 2 mM solution of complexes (a) [(me-mdach)Ni]$_2$(BF$_4$)$_2$, **1**; (b) [(me-mdach)NiCl]$_2$, **2**; (c) [(mmp-mdach)NiCl]$_2$, **2-Me$_2$**, in DMF (0.1 M [nBu4N][BF4]) using a Ag/AgNO$_3$ reference electrode, a platinum counter electrode and a glassy carbon working electrode standardized to Fc/Fc$^+$.

Table III-4. Electrochemical data in DMF.

Complex	E_{ox} (V) E_{pa}	E_{red} (V) $E_{1/2}$	E_{pc}
$[(me\text{-}mdach)Ni]_2(BF_4)_2$, **1**	+0.14	-1.30	-2.02
$[(me\text{-}mdach)NiCl]_2$, **2**	+0.06	-1.45	-2.03
$[(mmp\text{-}mdach)NiCl]_2$, **2-Me$_2$**	+0.04	-1.58	-1.91
(mmp-mdach)Ni(Im)](Cl), **3**	-0.07		-1.96 -2.13 -2.31
[Ni-1'(CH_2-mIm)](Cl), **4**	-0.18	-2.50	-1.82
$[(bmIme\text{-}dach)Ni](BF_4)_2$, **5**	+0.77	-1.59	-1.21
(bme-dach)Ni	-0.14	-2.50	

Ar deaerated DMF solution (0.1 M $^nBu_4NBF_4$). All experiments were recorded using a glassy carbon working electrode (A = 0.071 cm^2) referenced to Fc/Fc^+ and a Pt counter electrode at a scan rate of 200 mV/s.

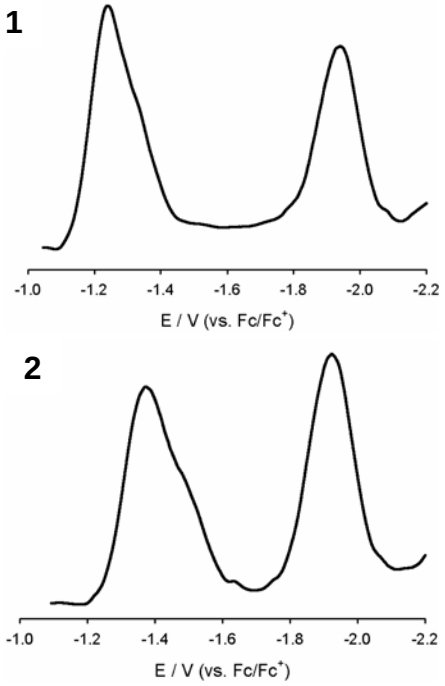

Figure III-12. Differential pulse voltammetry of a 2 mM solution of $[(me\text{-}mdach)Ni]_2(BF_4)_2$, **1**, and $[(me\text{-}mdach)NiCl]_2$, **2**, in DMF (0.1 M [nBu4N][BF4]) using a $Ag/AgNO_3$ reference electrode, a platinum counter electrode and a glassy carbon working electrode standardized to Fc/Fc^+.

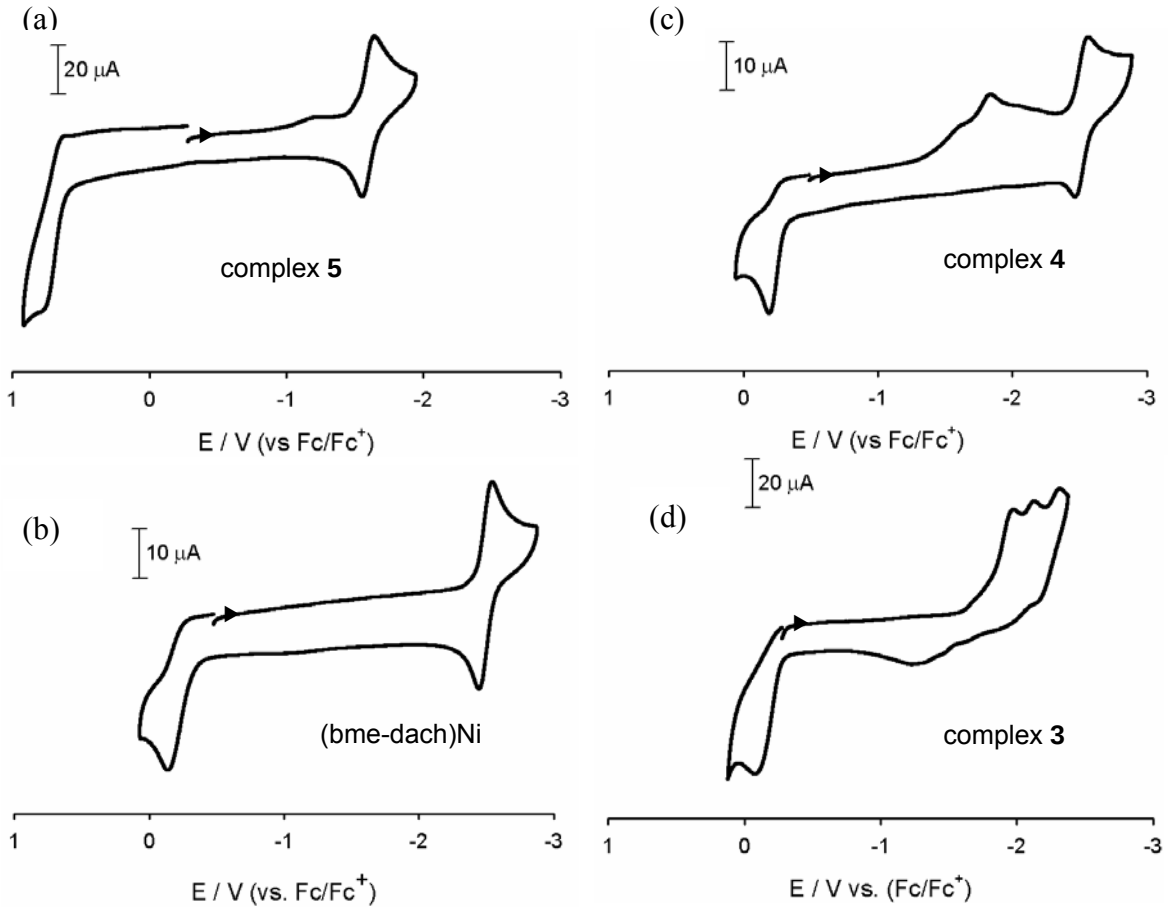

Figure III-13. Cyclic voltammograms of mononuclear square planar Ni^{II} complexes in DMF and referenced to Fc/Fc^{+}. (a) $[(bmIme\text{-}dach)Ni](BF_4)_2$, **5**; (b) (bme-dach)Ni; (c) [Ni-1'(CH_2-mIm)](Cl), **4**; (d) (mmp-mdach)Ni(Im)](Cl), **3**.

second reduction, and is assigned to a $Ni^{II}Ni^{II}/Ni^{II}Ni^{I}$ couple. The second reduction, presumably accessing an unstable $Ni^{I}Ni^{I}$ redox level in the intact dimers, engenders degradation as seen by its irreversibility and also in the differential pulse voltammetry of the first reduction process (Figure III-12). All three dimers display similar electrochemistry in both the anodic and cathodic regimes with differences in potentials relating to the extent of counterion interaction or the presence of gem-dimethyl groups in

2-Me$_2$. Figure III-13 displays the cyclic voltammograms of mononuclear complexes **3**-**5** and (bme-dach)Ni. Figure III-13 (a) and (b) show fully reversible Ni^{II}/Ni^{I} reduction events at -1.59 and -2.50 V for complex **5** and (bme-dach)Ni, respectively. The greater accessibility of the former is a result of the dicationic charge, as well as the differences in donor ability of the imidazole versus the thiolate ligands. For complex **4** a reproducible broad feature (deconvoluting into at least 3 maxima by square wave voltammetry, Figure III-14) is centered at -1.82 V, and a fully reversible reduction is seen at -2.50 V, identical to the Ni^{II}/Ni^{I} couple of the (bme-dach)Ni dithiolate complex, Figure III-13 (b). Multiple scans did not affect the form of the CV, however bulk electrolysis of **4** was informative. A potential of -2.26 V was applied to a solution of pure, crystalline complex **4** dissolved in DMF and stopped when the total charge (Q) approached a calculated value of 3 electrons per molecule. The cyclic voltammogram obtained on this solution showed almost total loss of the broad

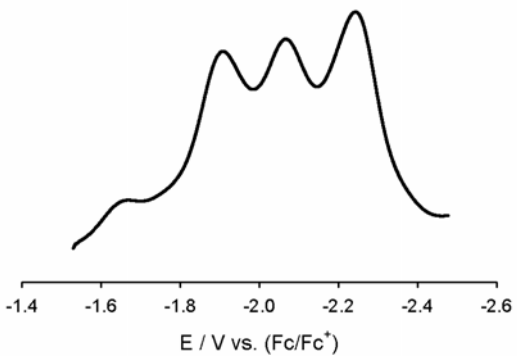

Figure III-14. Square wave pulse voltammetry of a 2 mM solution of [(mmp-mdach)Ni(Im)]Cl, **3**, in DMF (0.1 M [nBu4N][BF4]) using a $Ag/AgNO_3$ reference electrode, a platinum counter electrode and a glassy carbon working electrode standardized to Fc/Fc^+.

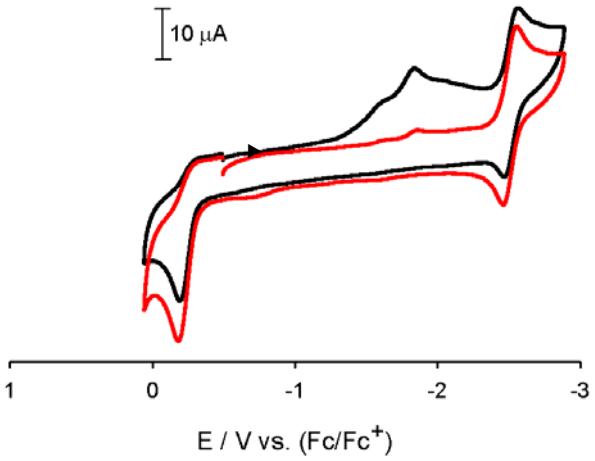

Figure III-15. Cyclic voltammograms before (black) and after (red) bulk electrolysis (-2.26 V) of a 2 mM solution of [Ni-1'(CH_2-mIm)]Cl, **4**, in DMF (0.1 M [nBu4N][BF4]) using a Ag/$AgNO_3$ reference electrode, a platinum counter electrode and a glassy carbon working electrode standardized to Fc/Fc^+.

feature at -1.82 V while the reversible wave at -2.50 V and the oxidation wave at -0.18 V remained unchanged, see Figure III-15. The lack of current increase following bulk electrolysis in the -2.50 V event was of concern. As the addition of excess (bme-dach)Ni did not change the intensity or potential of the CV waves, it may be assumed that the solubility limit of (bme-dach)Ni in DMF was reached. This was confirmed by control experiments with pure (bme-dach)Ni. The low intensity, broad feature centered at -1.82 V in complex **4** and the first two reduction waves in complex **3** (DPV shown in Figure III-16) are tentatively assigned to complexes of different imidazole coordination in number or isomeric form. Consistent with this assignment, on addition of free imidazole to a solution containing complex **3** the multiple events become one broad intense feature centered at ca. -2.05 V (Figure III-17).

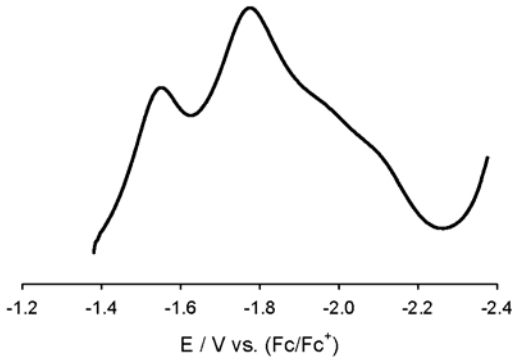

Figure III-16. Square wave voltammetry of a 2 mM solution of [Ni-1'(CH_2-mIm)]Cl, **4**, in DMF (0.1 M [nBu4N][BF4]) using a $Ag/AgNO_3$ reference electrode, a platinum counter electrode and a glassy carbon working electrode standardized to Fc/Fc^+.

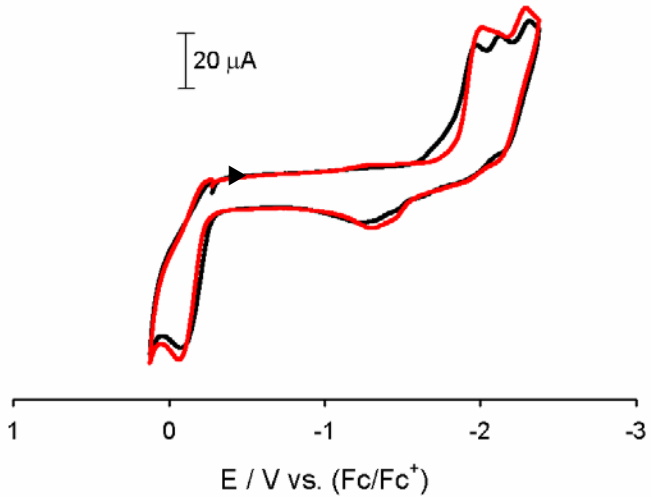

Figure III-17. Cyclic voltammograms before (black) and after (red) bulk electrolysis (-2.26 V) of a 2 mM solution of [Ni-1'(CH_2-mIm)]Cl, **4**, in DMF (0.1 M [nBu4N][BF4]) using a $Ag/AgNO_3$ reference electrode, a platinum counter electrode and a glassy carbon working electrode standardized to Fc/Fc^+.

Computational Studies

DFT computational studies were carried out by group member Michael Singleton with a goal of determining the activation barrier to imidazole rotation about the Ni-N bond. Using the X-ray crystal structures as a starting point, DFT optimized structures accurately reproduced the experimental coordination geometries, see Figure III-18 and Table III-5. Table III-6 lists the energies and compositions of the frontier molecular orbitals of complexes **3** and **4**; the corresponding MO contour plots are shown in Figure III-19.

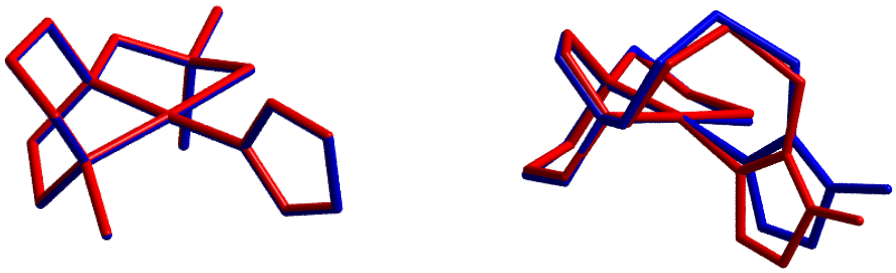

a **b**

Figure III-18. Overlay of experimental structure from X-ray diffraction with DFT optimized structures of (a) [(mmp-mdach)Ni(Im)]Cl, **3**, and (b) [Ni-1'(CH_2-Im)]Cl, **4**.

The highest-occupied molecular orbitals (HOMO) of complexes **3** and **4** both display Ni d_π – $S_{p\pi}$ antibonding orbital character, with electron density from the Ni d_{yz} (12.3%) and $S_{thiolate}$ p_z (58.8%) orbitals of complex **3**; in complex **4**, the distribution is Ni d_{yz} (17.1%) and $S_{thiolate}$ p_z (57.1%). The S-thiolate contribution to the HOMO is slightly more in the untethered imidazole derivative, **3**, as compared to the tethered

Table III-5. Selected experimental and optimized parameters for [(mmp-mdach)Ni(Im)]Cl, **3**, and [Ni-1'(CH_2-Im)]Cl, **4**.

	Calculated	Experimental
Complex 3		
Ni-N_{Imid}	1.922 Å	1.888 Å
Ni-N_{amine}	1.998 Å	1.923 Å
Ni-$S_{thiolate}$	2.179 Å	2.149 Å
Complex 4		
Ni-N_{Imid}	1.930 Å	1.908 Å
Ni-N_{amine}	2.005 Å	1.950 Å
Ni-$S_{thiolate}$	2.192 Å	2.168 Å
Ni-$S_{thioether}$	3.145 Å	3.022 Å

Table III-6. Energies and composition (%) of frontier molecular orbitals of [(mmp-mdach)Ni(Im)]Cl, **3**, and [Ni-1'(CH_2-Im)]Cl, **4**, as obtained from DFT calculations.

MO	E(eV)	Ni	$S_{thiolate}$	$S_{thioether}$	N_{imid}	N-H_{imid}	N_{amine}	Orbital composition
*Complex **3***								
LUMO	-4.56	51.7%	13.1%		5.73%	1.15%	14.8%	Ni(x^2-y^2)
HOMO	-8.19	17.8%	69.0%		0.309%	0.298%	0.838%	S(p_z)
HOMO-1	-9.35	76.6%	14.6%		0.286%	0.187%	1.88%	Ni(z^2)
*Complex **4***								
LUMO	-4.43	52.7%	14.0%	0.238%	5.34%	0.159%	15.3%	Ni(x^2-y^2)
HOMO	-8.02	22.1%	62.3%	4.38%	0.144%	0.020%	0.568%	S(p_z)
HOMO-1	-8.83	60.2%	4.67%	23.5%	0.452%	1.71%	0.319%	Ni(z^2), $S_{thioether}$($p_{x,y,z}$)

imidazole complex, **4**, while the Ni orbital contribution is slightly greater in the tethered imidazole compound. Similarly there are small differences between the orbital makeup of the lowest unoccupied molecular orbitals (LUMO's) in complexes **3** and **4**, which are in the σ-framework of the molecules. The HOMO-LUMO gaps in complexes **3** and **4** are nearly identical at 3.63 eV and 3.59 eV, respectively.

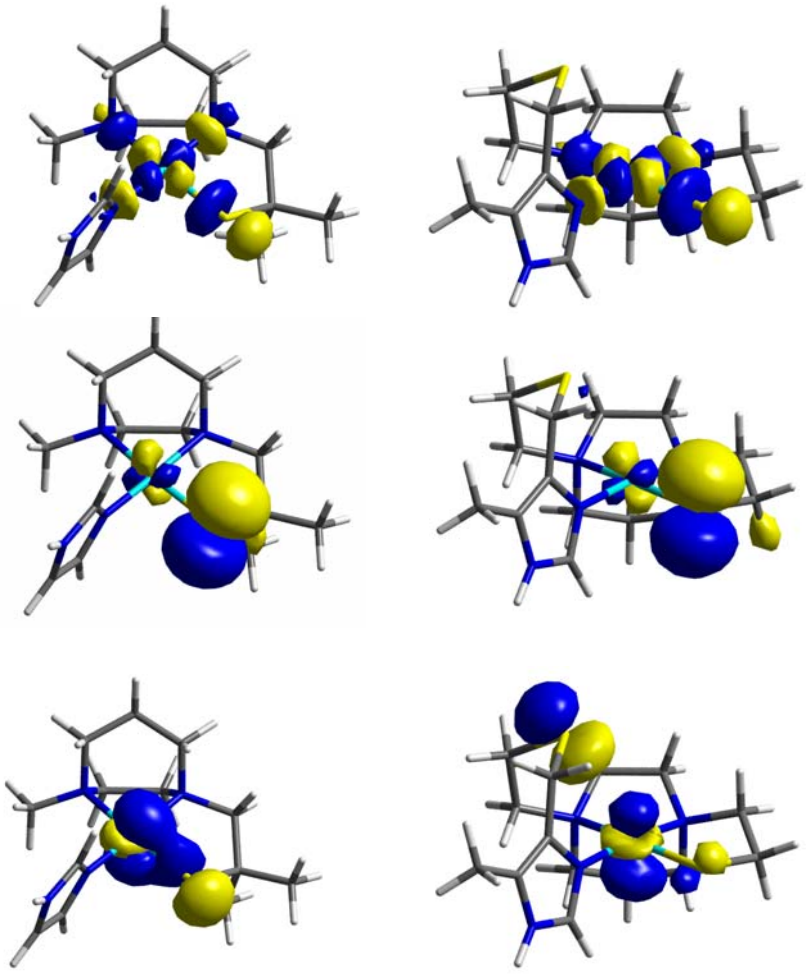

(a) **(b)**

Figure III-19. Frontier molecular orbitals of (a) [(mmp-mdach)Ni(Im)]Cl, **3**, and (b) [Ni-1'(CH_2-Im)]Cl, **4**. In each column, the orbitals descend in the order LUMO, HOMO, and HOMO-1.

The most significant differences in molecular orbitals are observed in the HOMO-1. The HOMO-1 of complex **3** is comprised largely of the overlap of the Ni d_{z2}(54.0%), Ni s (15.5%) and $S_{thiolate}$ p_y (12.4%) orbitals whereas the HOMO-1 of p_π complex **4** shows a large contribution from the $S_{thioether}$ of 23.4% in addition to the Ni d_π– overlap.

As discussed above, the $S_{thiolate}$-Ni interaction dominates the frontier molecular orbitals in complexes **3** and **4**. The $N_{imidazole}$-Ni bonding interaction is seen in lower lying orbitals which show large contributions of Ni and the N-imidazole character for both the ground and the DFT derived transition state for rotation of the imidazole about the Ni-N bond in complex **3,** *vide infra*.

Variable Temperature ^{1}H NMR Studies

As shown in Figure III-6, solid state structures find the orientation of the imidazole ligand plane in both [(mmp-mdach)Ni(Im)]Cl, **3**, and [Ni-1'(CH_2-mIm)]Cl, **4**, to be perpendicular to the $NiN_2N'S$ plane and largely eclipsing the N-Ni-N' vector. In order to further explore the imidazole ligand orientational preference, in collaboration with group member Michael Singleton, the solution phase conformation of the imidazole ligand in complex **3** was investigated via variable temperature ^{1}H NMR spectroscopy. At 23 ºC, the spectrum of **3** in CD_3OD shows three sharp singlets attributed to the C-H hydrogens on the coordinated imidazole ligand positioned at 8.11, 7.33 and 7.12 ppm, Figure III-20. The assignments given in Figure III-20 are in agreement with DFT computations, *vide infr*a (Figure III-21). Upon lowering the temperature, resonances *a* and *b* broaden and by -80 ºC each has split into two signals, indicating the presence of two isomers. Integration shows *a'* and *a''* to be in a ratio of ~1. The resonance due to the proton labeled *c* remains sharp throughout the temperature range and the resonances derived from *b* overlap with *c* and an impurity. Note that impurities are readily seen at room temperature. The lower field impurity is unaffected by temperature changes.

However, the higher field impurity, which has not been identified, undergoes broadening as do the signals of interest.

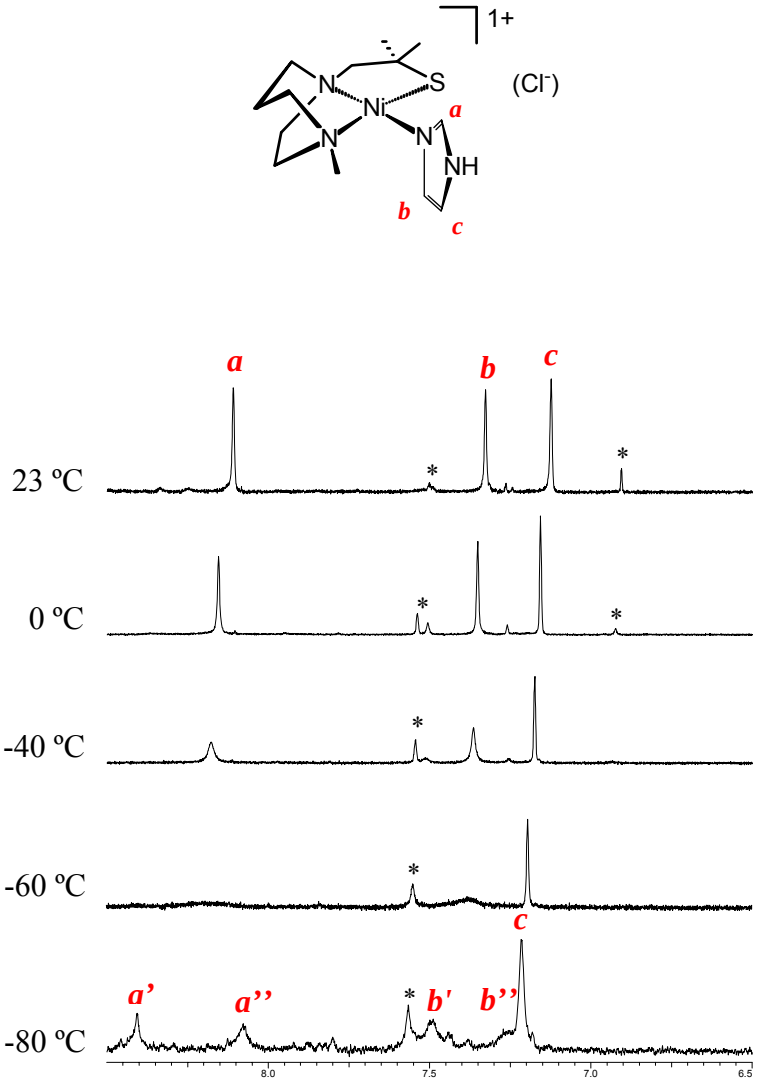

Figure III-20. Variable temperature 400-MHz ^{1}H NMR spectra of [(mmp-mdach)Ni(Im)]Cl, **3**, in MeOH. * = impurity.

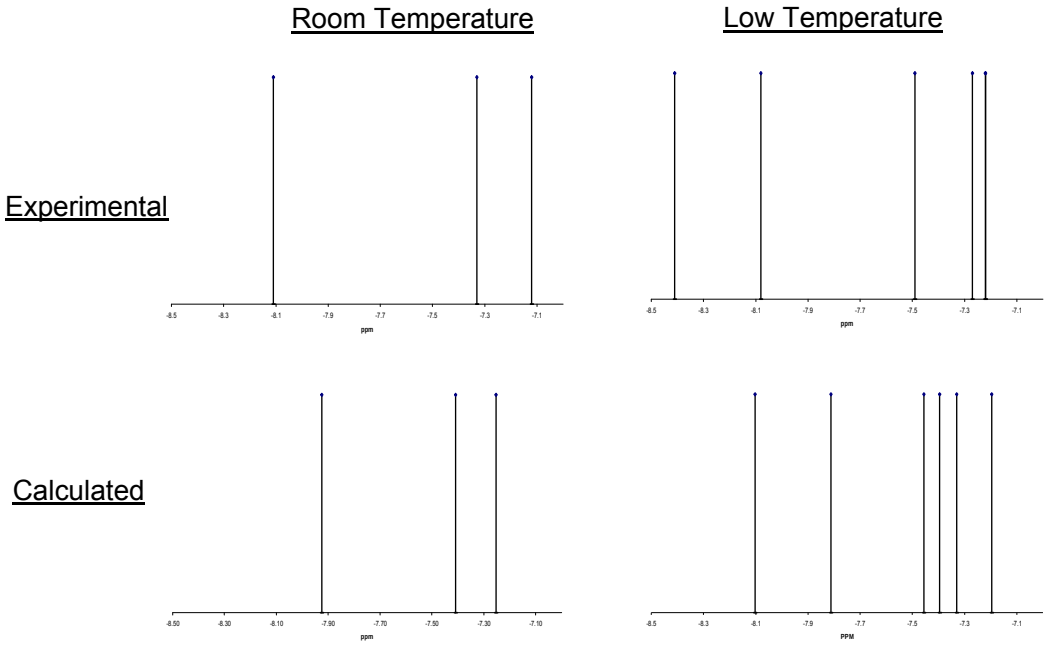

Figure III-21. Experimental ^{1}H NMR resonances and DFT ^{1}H NMR predictions for the imidazole protons of [(mmp-mdach)Ni(Im)]Cl, **3**, calculated at room and low temperature.

Thermodynamic (isomer ratios) and kinetic barriers associated with the fluxional process were obtained by using conventional equations, eqs 1 and 2.

$$\Delta G^{o} = - RT \ln (K_{eq}), \quad K_{eq} = [a']/ [a''] \qquad (1)$$

$$\Delta G^{\ddagger} = - RT \ln (k_T h/ k_b T_{coal}), \quad k_T = (\pi \Delta \nu/ \sqrt{2}) \qquad (2)$$

The ratio of the two isomers (57: 43) at -80 ºC (193 K) resulted in a ΔG^{o} of 0.1 kcal mol^{-1}. From the chemical shift difference of *a'* and *a''* (164.7 Hz) and the coalescence temperature (213 K), eq 2 gives $\Delta G^{\ddagger}$ equal to 8.9 kcal mol^{-1}.

There are four possible isomers of **3** (Figure III-22). Isomer **A** depicts the molecular structure as determined by X-ray crystallography. Isomer **B** leaves the imidazole orientation unchanged but the NiN_2C_3 metallocycloheptane ring is converted

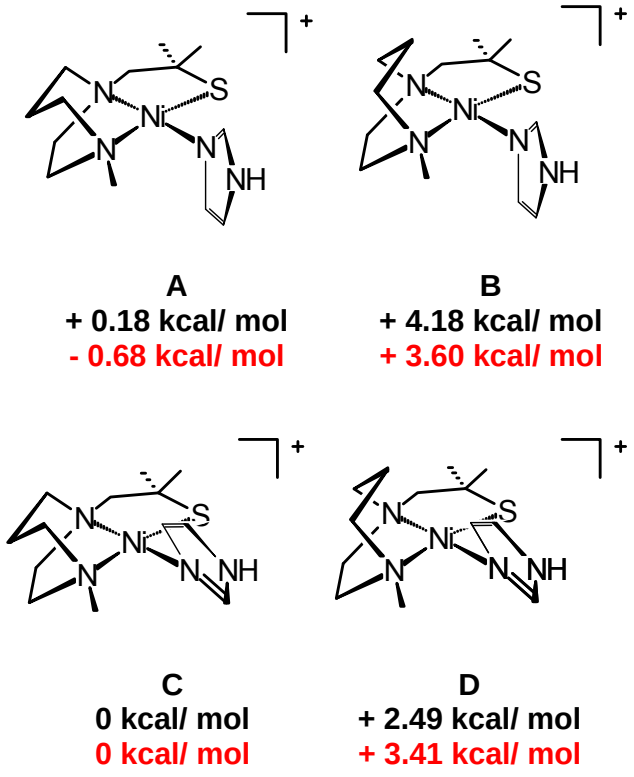

Figure III-22. Four possible conformational isomers of [(mmp-mdach)Ni(Im)]Cl, **3**, and their DFT calculated relative energies (G^o) Black: gas phase; Red: solvent correction in MeOH.

from chair to boat conformation. Isomers **C** and **D** are analogous to **A** and **B**, respectively, but with the imidazole ring inverted. While the lowest energy gas phase DFT-calculated structure is isomer **C**, solvent correction indicates that in MeOH isomer **A**, the experimentally found structure is of lowest energy (more stable than **C** by 0.68 kcal/mol). The stability of **A** in polar solvent over **C** is attributed to the differences in the dipole moments of the two complexes; the dipole moment in **A** is calculated to be 6.59 and in **C** it is 6.11. In both the gas phase and in solvent, the calculated difference in

energy between the two complexes is relatively small. DFT calculations were used to examine activation barriers to proton site equilibration due to the ring flip in the diazacycle backbone (**A** vs **B** or **C** vs **D**) or to rotation of the coordinated imidazole (**A** vs **C** or **B** vs **D**).

Note that the calculated ΔG^{o} value of isomers **A** vs. **B** and **C** vs. **D** would correspond to an isomer ratio of ~33,000:1 and ~700:1, respectively. At these ratios, only one set of signals in the NMR spectra would be observable at low temperatures. On the basis on these values, the fluxional process that most likely corresponds to the signals seen in the NMR spectra is the rotation of the imidazole ring that equilibrates isomers **A** and **C**.

The DFT calculated barriers for the processes that interconvert the four isomers are given in Figure III-23. As shown in Figure III-23(a), starting from the structure of **3** determined crystallographically, isomer **A**, the DFT calculated $\Delta G^{\ddagger}$ for the ring flip in the diazacycle backbone from the chair to the boat conformation, achieving a transition state where the C_3 N to N linker is fairly flat, is 7.02 kcal mol^{-1}. Calculations carried out for the ring flip of the isomer with the imidazole rotated 180º as compared to the solid state structure, isomer **B**, resulted in a $\Delta G^{\ddagger}$ of 6.59 kcal mol^{-1} (Figure III-23(b)). The DFT-calculated $\Delta G^{\ddagger}$ of 8.86 kcal mol^{-1} for the conversion of isomer **A** to **C**, that is, rotation of the imidazole as seen in Figure III-23(c), passing through a transition state where the imidazole plane is roughly within the NiN_2S plane, is strikingly similar to the experimental value obtained from the VT NMR study. Thus, the DFT calculations that aid interpretation of experimental results suggest that the separate isomers seen at low

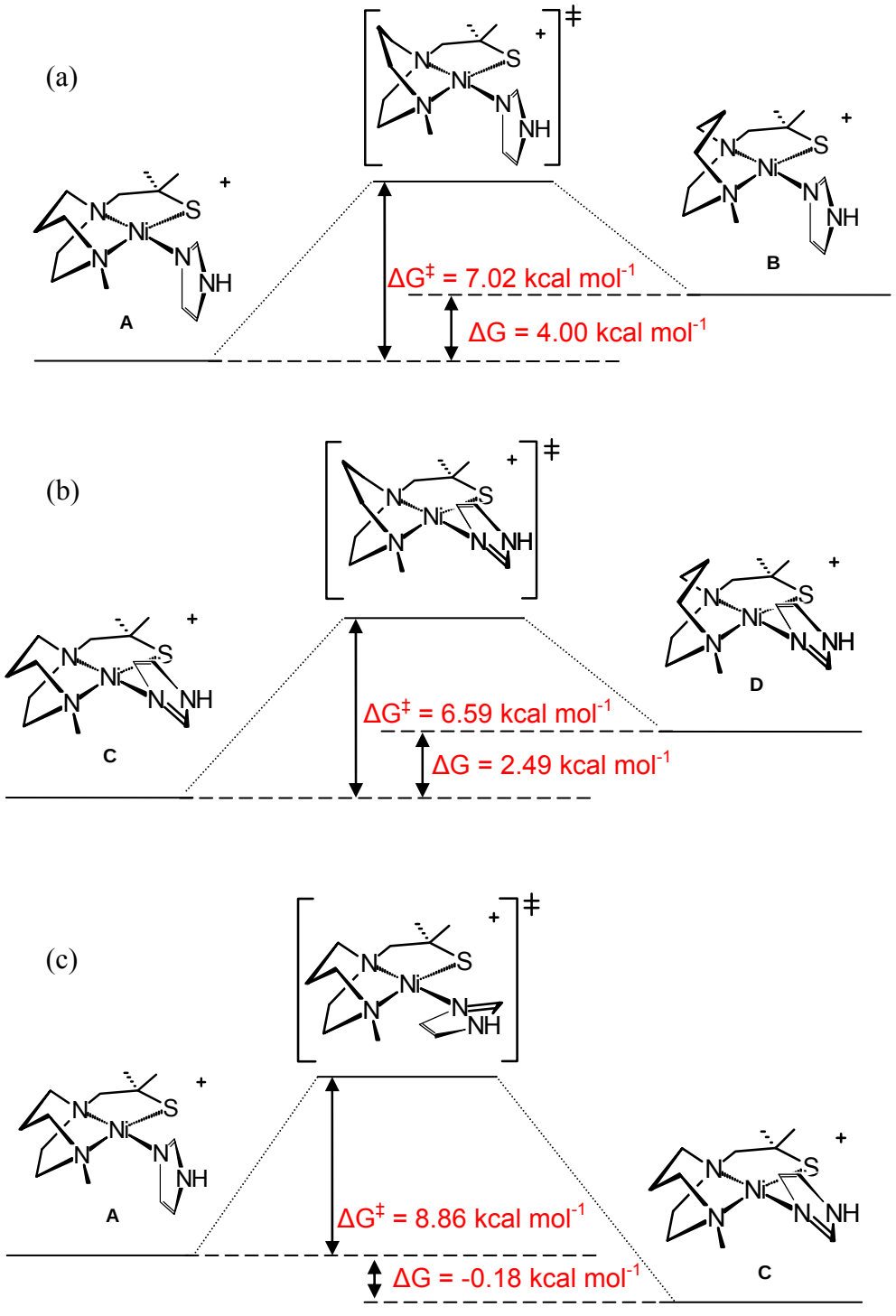

Figure III-23. DFT calculated energies (kcal mol^{-1}): (a) Ring flip calculated with imidazole orientation same as in solid state structure; (b) Ring flip calculated with imidazole orientation 180º rotated as compared to (a); (c) imidazole rotation calculated with NiN_2C_3 ring in chair conformation.

temperature are due to cessation of imidazole rotation about the Ni-N bond. Furthermore, the calculations suggest there is little difference in energy between the two rotational isomers of **3** (<0.2 kcal mol^{-1}), and this is also indicated in the experimental ^1H NMR data which by the ratio of isomers is ca. 1 at -80º C.

Reactivity Studies with Small Molecules (O_2^-, O_2 and H_2O_2)

Complexes **3-5** have been examined for superoxide reactivity using the nitroblue tetrazolium (NBT) assay. This qualitative test based on the reduction of NBT by O_2^- is detected by the change of colorless NBT to the blue formazan (λ_{max} = 580 nm, ~30 000 M^{-1} cm^{-1}; Figure III-24).[127]

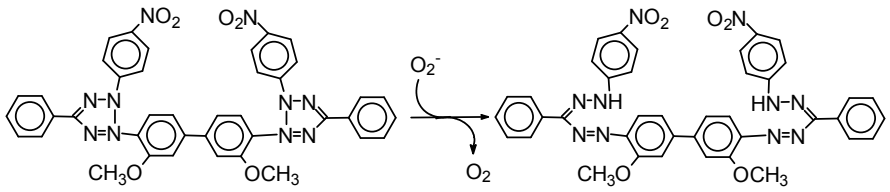

Figure III-24. Nitroblue tetrazolium (NBT) reaction with superoxide to produce formazan.

The presence of an active SOD inhibits the color formation by scavenging the O_2^- radical. Figure III-25 shows the results of addition of solid KO_2 (100 eq. per mole of NBT) to a (61 μM) aqueous NBT solution (phosphate buffer, pH 7.4). Note that the

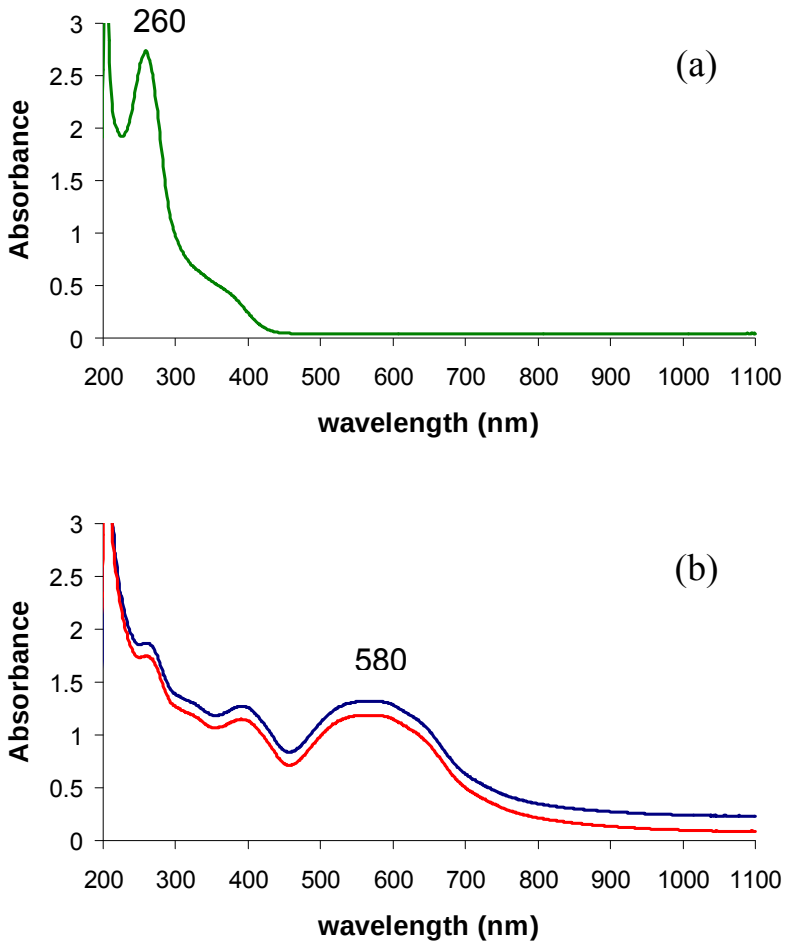

Figure III-25. Electronic spectra of (a) NBT in aqueous phosphate buffer (pH 7.4). (b) Blue - Addition of 100 eq of KO_2; Red – 5 min after addition (formation of insoluble formazan decreases total intensity).

limited solubility of formazan in aqueous solution causes a decrease in the absorbance over time.

Under the same conditions employed in the control experiment and in the presence of complex **3** (69 μM), a 40% decrease in the intensity of the band centered at 580 nm was observed, indicating a decrease in formazan production (Figure III-26a). This result suggests that **3** possesses superoxide scavenging properties that prevent a

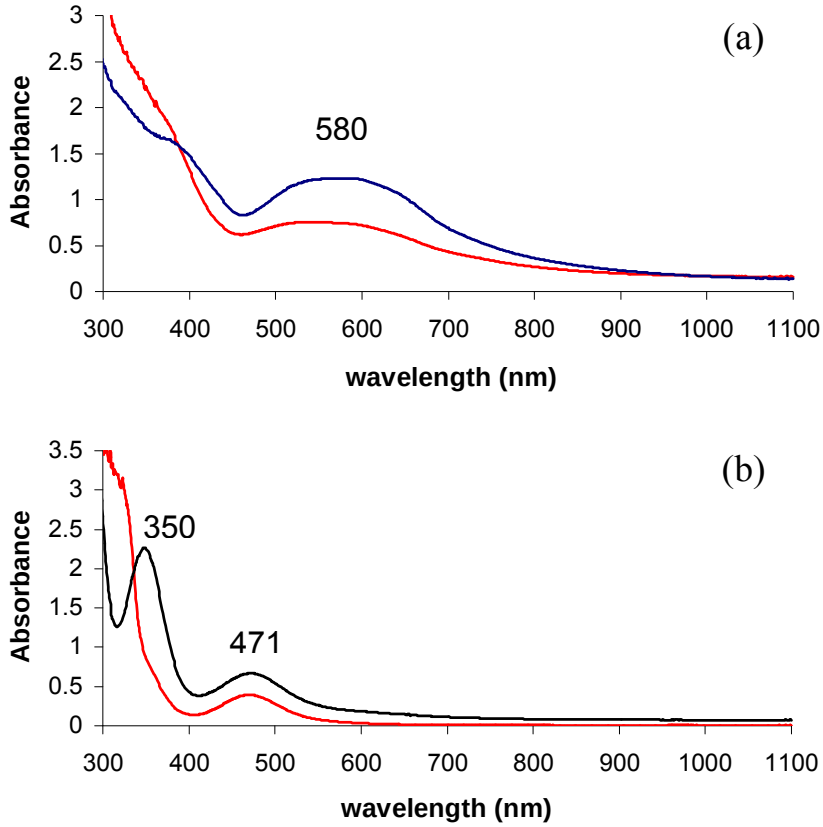

Figure III-26. Electronic spectra of [(mmp-mdach)Ni(Im)]Cl, **3**, in phosphate buffer (pH 7.4) (a): Blue - Addition of 100 eq of KO_2 to NBT (61 μM); Red - Addition of 100 eq of KO_2 to NBT (61 μM) /complex **3** (69 μM). (b): Red – Complex **3** (2.75 mM); Black – Addition of KO_2 to Complex **3** (0.46 mM)/ NBT buffer solution (0.18 mM).

portion of the NBT from reacting with O_2^- and at a rate competitive with NBT. In addition, intense bubble formation, much more than with formazan in the absence of **3**, was observed within the first 30 seconds following KO_2 addition. It should be noted that there is no indication of catalytic O_2^- decomposition. The addition of solid KO_2 to concentrated solutions of complex **3**, resulted in a shift in the d-d band from 464 nm to 471 nm and a new band appeared at 350 nm (Figure III-26b), suggesting that a new nickel species is formed.

The ability of complexes **4** and **5,** and (bme-dach)Ni, as well as $NiCl_2$, to inhibit NBT superoxide reactivity was screened by identical experiments. Under both low and high concentrations, none inhibited the production of formazan.

Complex **3** was screened for reactivity with the products of superoxide dismutation, O_2 and H_2O_2. Molecular oxygen was bubbled through a MeOH solution of complex **3**. No oxygenation products were observed and only the starting material was recovered. Upon addition of H_2O_2 (10 mM) to complex **3** dissolved in MeOH, an immediate color change from orange to yellow was observed. The molecular formulas and predicted isotope envelopes for both the mono-oxygenated and bis-oxygenated derivatives of complex **3** were observed in the ESI-MS spectrum (Figure III-27). These results indicate that complex **3** is stable to aerobic oxidation and only strong oxidants are capable of oxidizing the Ni-bound $N_2N'S$ ligand.

Summary and Remarks

Complexes **3** and **4** presented above are, to our knowledge, the first molecular structures of compounds containing both an S-thiolate and N-imidazole donor atom in the first coordination sphere of Ni^{II}. The use of the (bme-dach)Ni complex and the dimeric dithiolate bridged Ni^{II} dication as precursor reagents in the preparation of the $Ni(N_2N'S)$ complexes resulted in similar solid state structures for complexes containing both tethered and untethered imidazole ligands. That the diazacycloheptane N_2 backbone" plays a stabilizing role in these complexes is highly reasonable. The following salient points are to be noted.

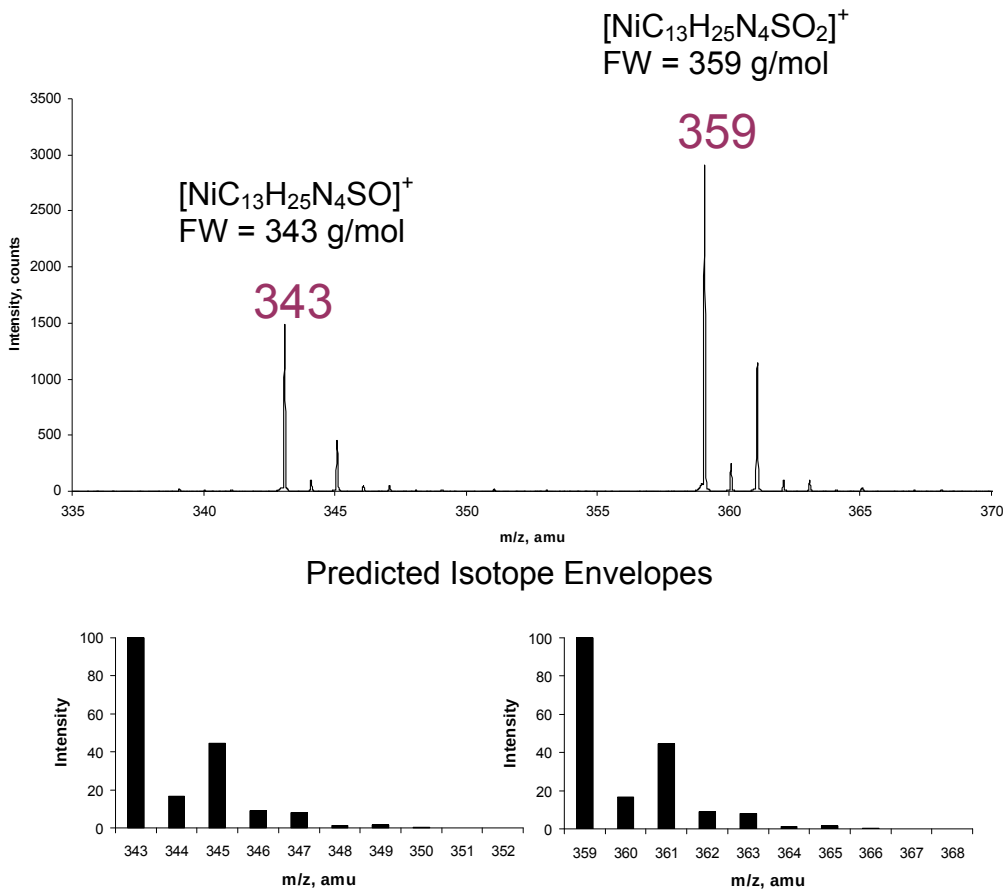

Figure III-27. Positive mode ESI-MS of [(mmp-mdach)Ni(Im)]Cl, **3**, in MeOH after reaction with H_2O_2.

Imidazole Ligand Geometrical Orientation in Square Planar Ni^{II} Complexes. While severe ligand restrictions position the imidazole ligand coplanar with the $N_2N'_2Ni^{II}$ plane of complex **5**, the solid state structures of complexes **3** and **4** revealed a preferred orientation of the imidazole donor ligand perpendicular to the $N_2N'SNi^{II}$ plane. The solution phase VT ^1H NMR study of complex **3** demonstrated that the imidazole ligand freely rotates about the Ni-N_{imid} bond at 22°C, with static structures

appearing between -60 and -80°C. Both the experimental and the DFT computed barriers to rotation are found to be ~9 kcal mol^{-1}. The lowest energy DFT-calculated gas phase structure also found the imidazole plane to orient perpendicular to the $N_2N'S$ plane, but rotated 180° with respect to the crystallographically determined structure. Applying solvent corrections, the DFT lowest energy structure was calculated to be the same orientation as observed in the solid state. Thus the built-in asymmetry of the diazacycloheptane ring provides subtle tuning of ligand orientation preferences.

As discussed in the Introduction, a number of studies have demonstrated that the orientation of imidazole ligands found in metalloenzyme active sites influences structure/function relationships.[28-36,53-54] Furthermore, ligand rotational properties have been shown to contribute to significant factors affecting antitumor properties in platinum and ruthenium antitumor compounds.[42] The DFT computed transition state structure for imidazole rotation about the Ni-N_{imid} bond in complex **3** positions the imidazole ligand roughly coplanar with the NiN_2S plane. In fact, elongation of the $N_{imidazole}$-Ni bond distance by 0.06 Å (from 1.922 in the DFT calculated ground state to 1.982 Å in the transition state) is accompanied by distortion (a Td twist defined by the intersection of the N_2Ni and $SN_{imid}Ni$ planes, of 21.2°), Figure III-28. The preferred orientation may be a product of steric and/or electronic effects, which is the focus of discussion in Chapter IV.

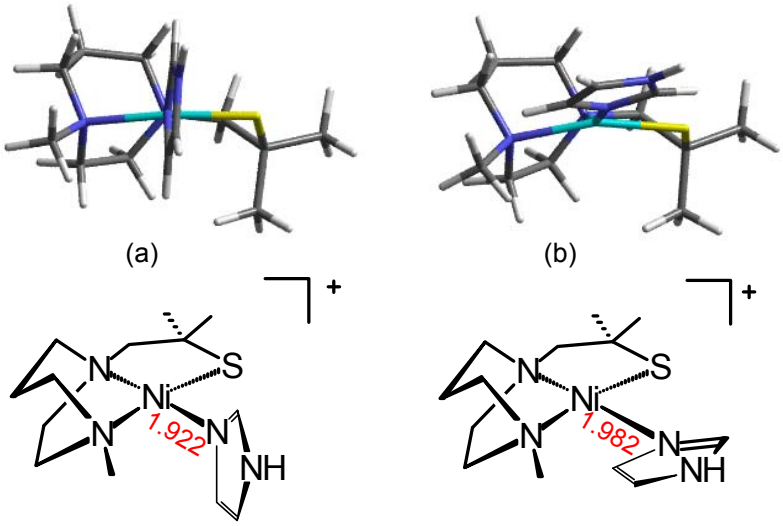

Figure III-28. (a) DFT calculated ground state structure (b) DFT calculated transition state structure.

Superoxide Reactivity. The nickel-imidazole complexes described above are all water soluble and thus their potential for superoxide reactivity could be assessed in aqueous buffer via the NBT assay. Only complex **3** competed with the NBT scavenging of superoxide; complexes **4**, **5**, and (bme-dach)Ni did not and neither did simple salts such as $NiCl_2$. As the NBT assay gives little information regarding the nature of interference from the coordination complex, we can regard these results as preliminary. This data suggests the need for further examination of nickel complexes of various charge and redox properties such as we have in a catalog of such square planar Ni complexes.

Implications to Nickel Containing Biomolecules. An unsuccessful attempt was made to synthesize a NiSOD enzyme active site model complex from alkylation of a thiolate within an $N_2S_2Ni^{II}$ framework by chloromethylimidazole to thus incorporate a

dangling imidazole (His mimic) with the capability of shifting into an axial binding position on oxidation of Ni^{II} to Ni^{III}. The resulting $N_2N'S_{thioether}$ binding motif found for complex **4,** which matched that of complex **3,** was impressive of the good binding ability of imidazole nitrogen and its preference for the square plane of Ni^{II}. In the NiSOD enzyme active site, the axial His binding is governed by the protein superstructure, the position of the His residue next to the N-terminus that provides the amine ligation, the coordination of the strong carboxyamido N and S donors of one cysteine unit, and a second distal S-cysteine donor. This square planar coordination environment creates two favorable 5-membered rings, whereas the His ligand binding in the square plane in place of the N-terminus amine would result in one 5-membered ring and a less-favored 7-membered ring.

Interestingly, the $(N_{imid})_3NiS_{cys}$ "plane" of NikR, Figure III-1, finds a range of N_{imid} plane orientations, canted so as to best accommodate the steric requirements.[23-24] As nickel binding or release, with concomitant long range protein structural changes, is an important feature of this site, specific orientations of the imidazole ligands are likely suspects as triggers of release and binding. Drennan, Zamble and coworkers have demonstrated that other metal ions may bind in this site, however the nickel form is reported to be 250x more active.[13, 15] Our $(N_2N'S)Ni$ complexes are suitable as first coordination sphere molecular models of the Ni-binding site of the NikR protein, and are expected to be useful for selectivity and relative binding affinity studies of physiologically relevant metal ions.

CHAPTER IV

STUDIES OF THE ORIENTATION OF PLANAR MONODENTATE LIGANDS IN SQUARE PLANAR NICKEL COMPLEXES

Introduction

The orientational binding preferences and fluxional processes of ligands in transition metal complexes is an area of fundamental significance relating to catalysis and reactivity.[128-130] In the case of biologically relevant ligands such as imidazole, the study of these processes purports to offer insight into a vast array of biological systems containing metal bound histidine residues. As discussed in Chapter I, much of the effort in this area has been directed toward understanding His-iron interactions through the use of simple imidazoles as mimics of histidine.

Adding to the importance of Fe-$N_{histidine}$ interactions, is a wide range of biological metal-bound histidine complexes that could have orientational consequences, specifically the Ni-containing imidazole metal binding sites found in Ni superoxide dismutase (NiSOD), and the transcription factor, NikR.[13-14,23-24] The orientation of histidine donors in nickel-binding sites in such systems has not thus far been emphasized in structural studies.

Our work has employed diazacycles such as diazacycloheptane (dach) as support for pendant thiolate arms in development of N_2S_2 and N_2S multi-dentate ligands. The dach frame has been particularly amenable to the production of a monothiolate N_2S ligand, which upon reaction with nickel, readily forms a dimeric, dithiolate-bridged Ni^{II}

dication as precursor to monomeric cyano, and as described in Chapter III, imidazole complexes.[110, 131] The $\mu_2(SR)_2$-bridged Ni^{II} dimer/ligand cleavage approach has also been used by Gale, Patra and Harrop to produce monomeric $N_2SS'Ni$ complexes designed as NiSOD analogues,[132] and extensive syntheses based on cleavage reactions of $(S\text{-}N\text{-}S)_2Ni_2$ complexes were recently reported by Huang, Holm et al.[52]

As described in Chapter III, solution phase investigations using ^1H NMR spectroscopy demonstrated that, due to the unsymmetric dach framework, isomers of the $(N_2SN')Ni$ complex **A**, Figure IV-1, existed at low temperatures in nearly equal ratio.[131] The observed equilibration of up/down orientations of the imidazole (with respect to the 6-membered nickel diazacyclohexane ring), isomers **A** and **A',** was assigned to the rotation of the imidazole ligand about the $Ni\text{-}N_{imidazole}$ bond. The rotational barrier, ~8.9

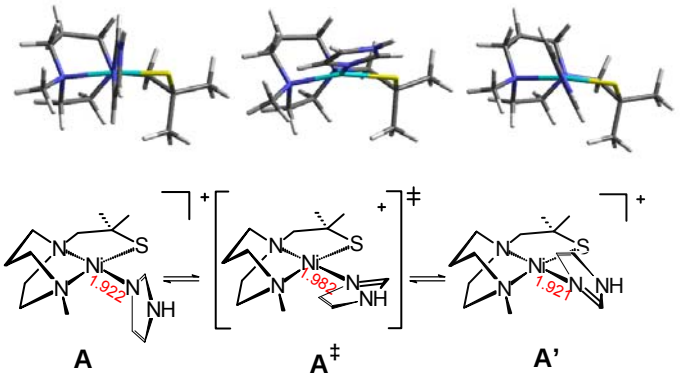

Figure IV-1. Left to right: $[(mmp\text{-}mdach)Ni(Im)]^+$, **A,** DFT-calculated ground state structure of complex **A**; **A**‡, DFT-calculated transition state structure of complex **A** en route to isomer **A'**; Td twist (angle of intersection of N_2Ni and N'SNi planes) of **A** = 7.9 °, of **A**‡ = 21.2°. Adapted from Reference 132.

kcal/mol, was derived from analysis of the VT ^{1}H NMR data. Density Functional Theory (DFT) analysis of the ground state and transition state structures, complexes **A** and $\mathbf{A}^{\ddagger}$, indicated for the latter a 0.06 Å increase in the Ni-N_{imid} bond distance in addition to a significant deviation from square planarity, as shown in Figure 1.[131] To explore the generality of this result and to provide insight into the factors contributing to the ground state imidazole binding orientation and to transition states of dynamic ligand rotational processes, a broader series of $[(N_2S)Ni]_2$ cleavage products containing planar ligands (imidazoles, pyridine and an N-heterocyclic carbene) has been prepared. As the π-accepting/π-donating abilities of the added ligands are insignificant in these strong σ donors, the orientation of the monodentate ligand is dictated largely by minimization of steric interactions of L with the steric constraints of N_2SNi binding site. Nevertheless, electronic effects are seen via DFT computations that suggest an intramolecular donor/acceptor interaction between the imidazole C-H and the thiolate S is operative in determining the stability of the ground state and transition state structures. A structural survey of the solid state structures of ten square planar imidazole Ni complexes of tridentate ONO, ONN, ONS, and NNS Schiff base type ligands shows the importance of this effect in the presence of hard oxygen donors *cis* to the imidazole. [133-141]

Experimental Details

General Procedures. The starting material 1,3-bis(methyl)imidazolium iodide was prepared according to literature procedures.[142] Complexes **1**, **1-H**, and **A** were

prepared as described previously.[110, 131] Lauren A. Leamer, an REU student, assisted with the preparation of complexes **3**-**8**.

[(mmp-mdach)Ni]$_2$[BF$_4$]$_2$, Complex 2. To a solution of 0.050 g (0.085 mmol) of [(mmp-mdach)NiCl]$_2$, complex **1**, in MeOH (20 mL) was added 0.019 g (0.173 mmol) of $NaBF_4$ in MeOH (15 mL); the solution was stirred overnight. Solvent was removed under vacuum, and MeCN (20 mL) was added, precipitating NaCl, and yielding a maroon solution of [(mmp-mdach)Ni]$_2$[BF$_4$]$_2$, complex **2**. The solution was filtered over celite, solvent was removed in vacuo, and 0.055 g (93% yield) of pure complex **2** was isolated as a maroon solid. Absorption spectrum (MeOH): λ_{max} (ε, M^{-1} cm^{-1}) 525 (354), 418 (322), 280 (4138), 244 (7247) nm. $^+$ESI-MS (MeCN): *m/z* = 259 [(me-mdach)Ni]$_2^{2+}$.

[(mmp-mdach)Ni(py)][Cl], Complex 3. A mixture of 0.030 g (0.051 mmol) of **1** in MeOH (25 mL) with 12.0 µL (0.149 mmol) of pyridine was stirred overnight, producing a color change from red wine to yellow-orange. As the solvent was removed in vacuo, the completely dried residue on the sides of the flask turned purple, while the solution changed to a deep orange. An additional 20.0 µL (0.248 mmol) of pyridine was added to the concentrated solution, stirred to mix the residue on the sides of flask, yielding a dark orange solution. Absorption spectrum of the reaction mixture (MeOH): λ_{max} 453, 350 (sh), 290, 255, 231 nm. $^+$ESI-MS (MeOH): *m/z* = 338, [(mmp-mdach)Ni(py)]$^+$.

py-[(mmp-mdach)Ni]$_2$[BF$_4$]$_2$, Complex 4. A mixture of 0.050 g (0.072 mmol) of **2** in MeCN (30 mL) with 21.8 µL (0.253 mmol) of pyridine was stirred for 2 days,

producing a color change from maroon to deep yellow. The solvent was reduced to a minimum followed by Et_2O diffusion (in the presence of a ~ 2.5 equiv excess py) to yield X-ray quality crystals. Pure reddish-orange crystalline product was isolated (0.031 g, 54% yield). Elemental anal. for $Ni_2C_{25}H_{47}N_5S_2B_2F_8$ (MW = 773 g/mol) Calcd (found): C, 38.85 (38.29); N, 9.06 (8.88); H, 6.13 (6.09). Absorption spectrum (MeOH): λ_{max} (ε, M^{-1} cm^{-1}) 502 (sh), 471 (344), 334 (sh), 291 (6976), 244 (8345) nm. ESI-MS (CH_2Cl_2:MeOH): *m/z* = 684, py-[(mmp-mdach)Ni)]$_2BF_4^+$; 338, [(mmp-mdach)Ni(py)]$^+$; 259, [(me-mdach)Ni]$_2^{2+}$.

[(mmp-mdach)Ni(mIm)][BF$_4$], Complex 6. Method A: To a maroon solution of **2**, (0.073 g, 0.105 mmol) in MeOH (30 mL) was added a colorless solution of 1-Methylimidazole, mIm, (30 μL, 0.376 mmol, a 3.5 equiv excess) in MeOH (10 mL), which produced an orange solution. After stirring overnight, the solution volume was reduced to a minimum under vacuum and Et_2O was added to precipitate the product. The ether was decanted and the resulting orange product was dried in vacuo. The solid was dissolved in MeCN (15 mL) and additional mIm (20 μL, 0.251 mmol, ~2 equiv excess mIm) was added. The solution was filtered over celite, the filtrate reduced in volume, and the filtrate was layered with Et_2O. Absorption spectrum (MeOH): λ_{max} (ε, M^{-1} cm^{-1}) 467 (319), 341 (sh), 290 (6534), 225 (8097) nm. $^+$ESI-MS (MeOH): *m/z* = 341 [(mmp-mdach)Ni(mIm)]$^+$. Diffusion of Et_2O into the reaction mixture that contains complex **6** (with 1 equiv of excess py) that gave small yellow-orange needles initially and within two days changed into red-orange block crystals (12 mg, 15%) indentified not as **6** but rather the dinuclear (mIm-[(mmp-mdach)Ni]$_2$[BF$_4$]$_2$, complex **5**.

Method B: To a maroon solution of **2**, (0.035 g, 0.050 mmol) in MeCN (25 mL) was added a colorless solution of mIm (41 μL, 0.514 mmol, a 10-fold molar excess) in MeCN (10 mL), which immediately produced an orange solution. After stirring overnight, the solution volume was reduced to a minimum under vacuum and additional neat mIm (30 μL, 0.376 mmol) was added. The solution was filtered and the filtrate was layered with Et_2O to deposit orange-brown crystalline product (0.018 g, 42% yield) identified as the mononuclear product [(mmp-mdach)Ni(mIm)][BF_4], complex **6**. Elemental anal. for $NiC_{14}H_{27}N_4SBF_4$ (MW = 429 g/mol) Calcd (found): C, 39.20 (39.21); N, 13.10 (12.97); H, 6.34 (6.34). Absorption spectrum (MeOH): λ_{max} (ε, M^{-1} cm^{-1}) 467 (319), 341 (sh), 290 (6534), 225 (8097) nm. $^{+}$ESI-MS (MeOH): *m/z* = 341 $[(mmp\text{-}mdach)Ni(mIm)]^+$. ^{1}H NMR (500 MHz, CD_3OD) δ 8.04 (s, 1H), 7.26 (s, 1H), 7.09 (s, 1H), 3.70 (s, 3H), 1.69 (s, 3H), 1.60 (s, 3H), 1.38 (s, 3H).

[(mmp-mdach)Ni(ipIm)][BF_4], Complex 7. A solution of 2-Isopropylimidazole, ipIm, (0.029 g, 0.264 mmol) in MeCN (10 mL) was added to a stirring maroon solution of **2** (0.061 g, 0.088 mmol) in MeCN (25 mL), resulting in an immediate color change to bright orange. After stirring overnight, the solution volume was reduced to a minimum under vacuum and Et_2O was added to precipitate the product. The ether was decanted, the product was washed Et_2O (3 x 25 mL) to remove excess ipIm, and dried in vacuo to afford the product as an orange solid (0.421 g, 53% yield). X-ray quality crystals were obtained by Et_2O diffusion into a MeCN solution. Elemental anal. for $NiC_{16}H_{31}N_4SBF_4 \cdot H_2O$ (MW = 475 g/mol) Calcd (found): C, 40.46 (40.97); N, 11.79 (11.79); H, 7.00 (6.68). Absorption spectrum (MeOH): λ_{max} (ε, M^{-1} cm^{-1}) 468

(189), 335 (sh), 290 (4190), 223 (4768) nm. $^{+}$ESI-MS (MeOH): *m/z* = 369 [(mmp-mdach)Ni(ipIm)]$^{+}$. ^{1}H NMR (500 MHz, CD_3OD) δ 7.33 (d, 1H), 7.23 (d, 1H), 7.04 (d, 1H), 7.01 (d, 1H).

[(mmp-mdach)Ni(me$_2$NHC)][I], Complex 8. 1,3-bis(methyl)imidazolium iodide (0.044 g, 0.196 mmol) and KOtBu (0.023 g, 0.205 mmol) were mixed and stirred in dry THF (15 mL) for 1 h. The mixture was then added in situ to a slightly soluble purple suspension of complex **1** (0.040 g, 0.068 mmol) in THF (25 mL) and stirred for 18 h. As the reaction proceeded the solution turned orange-red and an orange solid precipitated. The solution was filtered and the solid was washed with hexanes (3 x 25 mL). X-ray quality crystals were obtained by vapor diffusion of Et_2O into a MeCN solution. The bright orange crystalline material was collected yielding 0.030 g (46%). Elemental anal. for $NiC_{15}H_{29}N_4SI{\cdot}H_2O$ (MW = 501 g/mol) Calcd (found): C, 35.95 (35.56); N, 11.18 (11.08); H, 5.82 (6.24). Absorption spectrum (MeOH): λ_{max} (ε, M^{-1} cm^{-1}) 417 (104), 268 (2652), 233 (4148) nm. $^{+}$ESI-MS (MeOH): *m/z* = 355 [(mmp-mdach)Ni(me$_2$NHC)]$^{+}$. ^{1}H NMR (500 MHz, CD_3OD) δ 7.19-7.18 (dd, 2H), 4.37 (s, 3H), 4.38 (s, 3H), 1.92 (s, 3H), 1.62 (s, 3H), 1.39 (s, 3H).

[(mmp-dach)Ni(Im)][BF$_4^-$], Complex 9. To a solution of **1-H** (0.030 g, mmol) in MeOH (30 mL) was added a solution of imidazole, Im, (0.011 g, mmol) in MeOH (10 mL). The color of the solution immediately changed from red to orange. After stirring overnight, the solvent volume was reduced to a minimum and the addition of Et_2O led to an orange precipitate, which was washed with Et_2O (3 x 25 mL). The solid was dissolved in CH_2Cl_2 and filtered over celite, dried in vacuo, yielding 22 mg (61%).

Absorption spectrum (MeOH): λ_{max} (ε, M^{-1} cm^{-1}) 455 (59), 370 (sh), 282 (1319), 215 (3777) nm. $^{+}$ESI-MS (MeOH): *m/z* = 313 [(mmp-mdach)Ni(Im)]$^{+}$. ^{1}H NMR (500 MHz, CD_3OD) δ 7.86 (s, 1H), 7.09 (s, 1H), 7.04 (s, 1H), 1.61 (s, 3H), 1.43 (s, 3H). Slow evaporation of a methanol solution of complex **9** resulted in orange block crystals of a partially cleaved dimer, Im-[(mmp-dach)Ni]$_2$[BF_4]$_2$, complex **10**, (16 mg, 48%).

Scope of the $Ni_2(\mu\text{-}SR)_2$ Cleavage Reactions

Figure IV-2 displays the overall scope of the $Ni_2(\mu\text{-}SR)_2$ cleavage reactions reported herein along with the pK_a values of the attacking ligands (as their conjugate acids) which vary from 5.23 to 23.[143-145] The exogenous ligands are largely planar in the coordination environment closest to the nickel, with steric properties imposed by substituents that flank the donor atom, described further below. The steric character of the nickel binding site is defined by a thiolate sulfur with two α-*gem* dimethyl groups and an N-donor from the diazacycloheptane frame. Given in Figure IV-3 are space-filling models derived from DFT computations, *vide infra*, of ground state structures of the square planar complexes with the monodentate ligands removed so as to display the available binding site in complex **A** and in an analogue, complex **9**, in which the methyl substituent on the dach (mdach) is replaced with hydrogen (dach). While the methyl groups on the carbon α to the S-donor appear to have little steric influence on the ligands that dock into the available site on square planar nickel, the differences between complexes **A** and **9** are more substantial. This was experimentally confirmed by

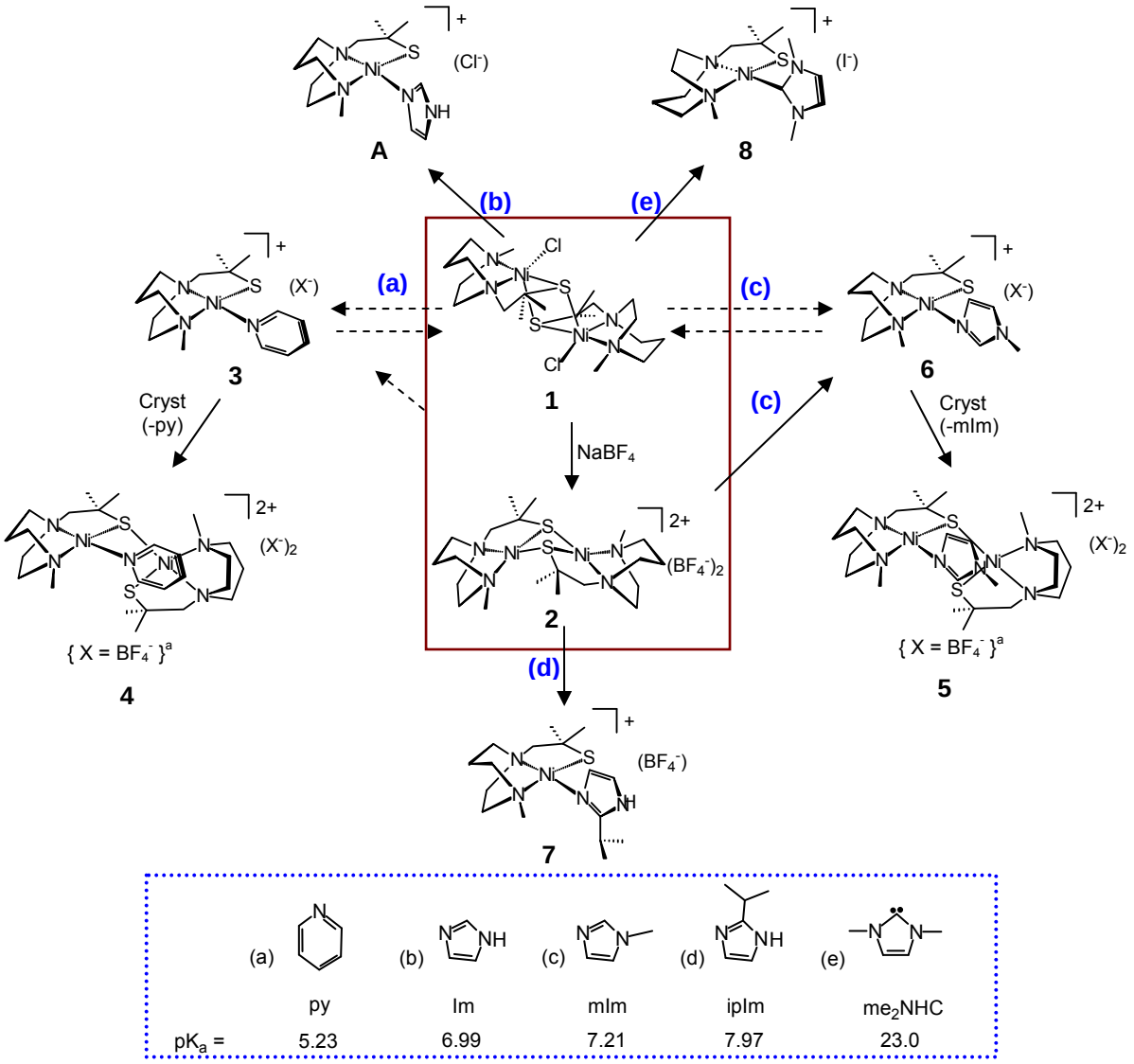

Figure IV-2. A summary of the dimer cleavage reactions of complexes **1** and **2** which yield mononuclear products **3** and **6-8** and monothiolate bridged dinickel complexes **4-5**. [a]Note: With BF_4^- counterion, the dinickel product forms during crystallization. Complex **A** was reported earlier.[131] Identification of ligands with respective pK_a values of the conjugate acids: (a) pyridine (py);[143] (b) imidazole (Im);[143] (c) 1-Methylimidazole (mIm);[144] (d) 2-Isopropylimidazole (ipIm);[144] and (e) dimethyl N-heterocyclic carbene (me_2NHC).[145] See Experimental Section for molar excesses of added ligands and for source of I^- in **8**.

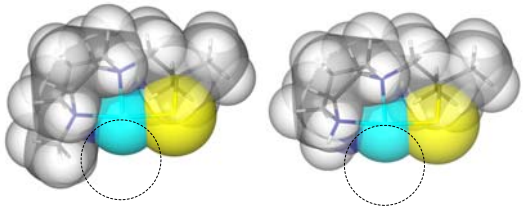

Figure IV-3. Space filling models of complexes $[(mmp\text{-}mdach)Ni(Im)]^{+}$, **A** (left, based on mdach) and $[(mmp\text{-}dach)Ni(Im)][BF_4]$, **9** (right, the dach derivative) in which the monodentate ligand has been removed, displaying the available open site that exists between the N- and S-donor sites.

characterization of complexes **9** and **10** as prepared from dimeric complex **1-H,** Scheme IV-1.

Complexes **4 -8**, **10** and **A** in Figure IV-2 and Scheme IV-1 are represented according to their structures determined by X-ray crystallography. Complexes **3** and **9** are suggested to be analogous to other monomeric complexes consistent with their formulation by positive mode electrospray ionization mass spectrometry ($^{+}$ESI-MS)

Scheme IV-1

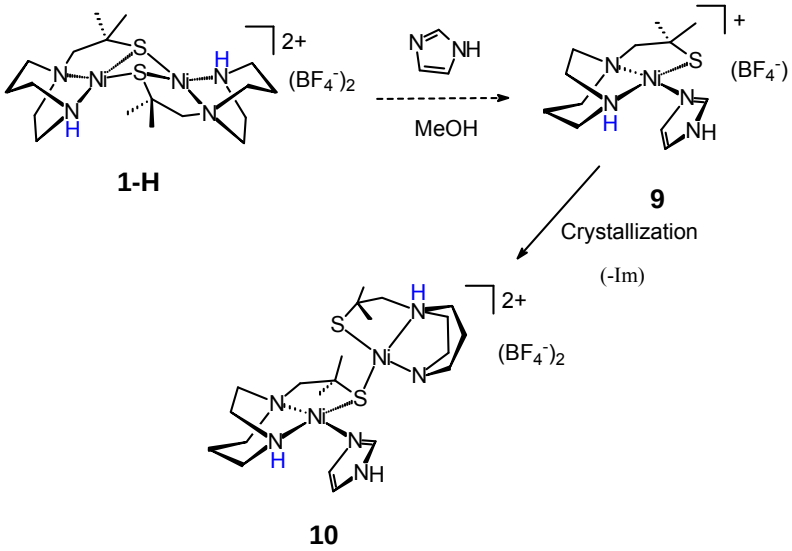

Table IV-1. Summary of electronic absorption spectra.

Complex	UV-Vis: λ_{max} (nm) (ε, $\mathbf{M}^{-1}$ cm^{-1})			
$[(mmp\text{-}mdach)NiCl]_2$, **1**	244 (10161)	283 (5910)	420 (561)	532 (537)
$[(mmp\text{-}mdach)_2Ni_2](BF_4)_2$, **2**	244 (7247)	280 (4138)	418 (322)	525 (354)
[(mmp-mdach)Ni(Py)]Cl, **3**[a]	231 255	290	350 (sh)	453
py-$[(mmp\text{-}mdach)Ni]_2[BF_4]_2$, **4**	244 (8345)	291 (6976)	334 (sh)	471 (344), 502 (sh)
[(mmp-mdach)Ni(mIm)] BF_4, **6**	225 (8097)	290 (6534)	341 (sh)	467 (319)
[(mmp-mdach)Ni(ipIm)] BF_4, **7**	223 (4768)	290 (4190)	335 (sh)	468 (189)
$[(mmp\text{-}mdach)Ni(me_2NHC)]I$, **8**	233 (3387)	268 (1238)		417 (115)
$[mmp\text{-}dach)Ni(Im)]BF_4$, **9**	215 (3777)	282 (1319)	370 (sh)	455 (59)
[(mmp-mdach)Ni(Im)](Cl)[131] **, A**	211 (21460)	288 (10767)	340 (sh)	467 (501)

[a]The molar absorptivity values are not available for complex **3**.

and physical properties (^{1}H NMR and UV-Vis spectroscopies). A listing of all UV-Vis data is given in Table IV-1.

Monothiolate Bridged Dinickel Complexes: Synthesis and Structural Characterization

Syntheses. As implied in Figure IV-2 there are complexities that relate to counterions in the syntheses and isolation of monomeric vs. monothiolate bridged dinickel complexes**.** The dimer cleavage reactions of **1** with py (a) and mIm (c) were initially performed following an identical protocol for complex **A** as described in Chapter III.[131] The addition of excess py to the wine red solution of **1** resulted in an immediate color change

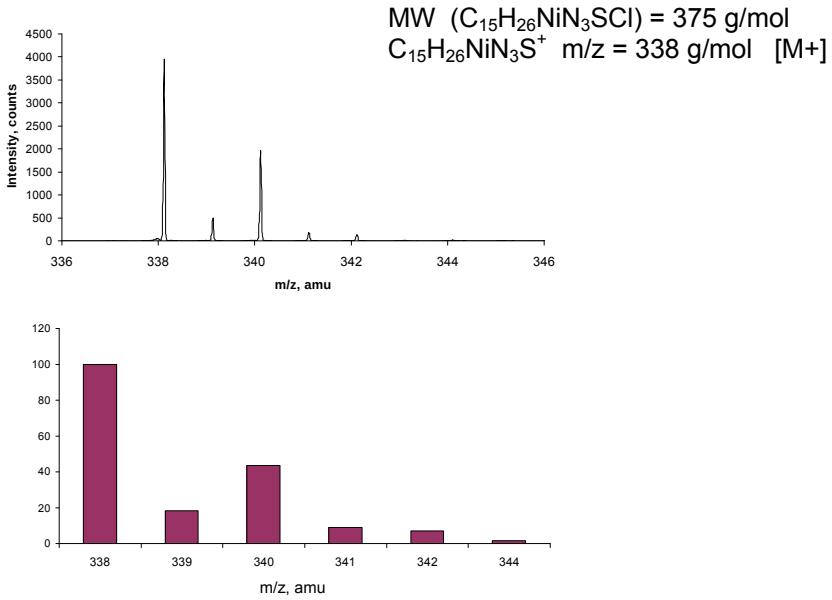

Figure IV-4. Positive mode ESI-MS of the reaction mixture of [(mmp-mdach)Ni(py)][Cl], **3**, in MeOH. Top: Experimental spectrum. Bottom: Predicted isotopic envelope.

to yellow. The $^{+}$ESI-MS of the reaction mixture showed a nickel-containing isotopic bundle at m/z = 338 (Figure IV-4), which corresponds to the predicted pattern for a species having the formula $C_{15}H_{26}NiN_3S^{+}$, i.e., the mononuclear cleaved product, complex **3**. The electronic absorption spectra of the reaction mixture at different concentrations showed the disappearance of the bands that are assigned to complex **1** (λ_{max} = 244, 283, 420 and 532 nm) with new bands appearing at λ_{max} = 231, 255, 290, 350 and 453 nm. Attempts to purify the complex by precipitation with Et_2O resulted initially in a yellow solid which within seconds turned purple. Likewise, on removal of solvent in vacuo, a purple solid was produced. A yellow solution was regained on

subsequent addition of MeOH to the purple solid. That is, the removal of solvent promoted the reformation of complex **1**.

To avoid the competitive binding of Cl^- ions to the mononuclear complex, subsequent cleavage reactions were carried out using the $Ni_2(\mu\text{-}SR)_2$, complex **2**, which contains non-coordinating BF_4^- counter ions. Similar to the cleavage reaction of complex **1** with py, the electronic absorption spectra and $^+$ESI-MS data suggested a fully cleaved product, i.e., complex **3**, which resulted from the treatment of complex **2** with excess py. The slow diffusion of Et_2O into a MeCN solution of this reaction mixture yielded reddish-orange crystals whose X-ray diffraction analysis (*vide infra*) revealed incomplete cleavage of complex **2** and the presence of a Ni-(μ-SR)-Ni dimer, complex **4**. We conclude that aggregation with loss of one py ligand from complex **3** occurs during the crystallization process.

The dimer cleavage reaction of complex **1** using mIm, (c) in Figure IV-2, proceeded with similar complexities during purification as observed when using py as the attacking ligand. While color changes and spectroscopic analyses (Table IV-1 and Figure IV-5) of the reaction mixture from both complexes **1** and **2** suggested complete dimer cleavage, the X-ray quality crystals which were obtained from Et_2O diffusion into a MeCN solution of the reaction mixture and their X-ray diffraction analysis revealed a second partially cleaved dimer, complex **5**.

Complex **1-H** was chosen as a $[(N_2S)Ni]_2$ dimeric precursor to reduce the steric interference between the monodentate ligand and the dach N-donor in the mononuclear

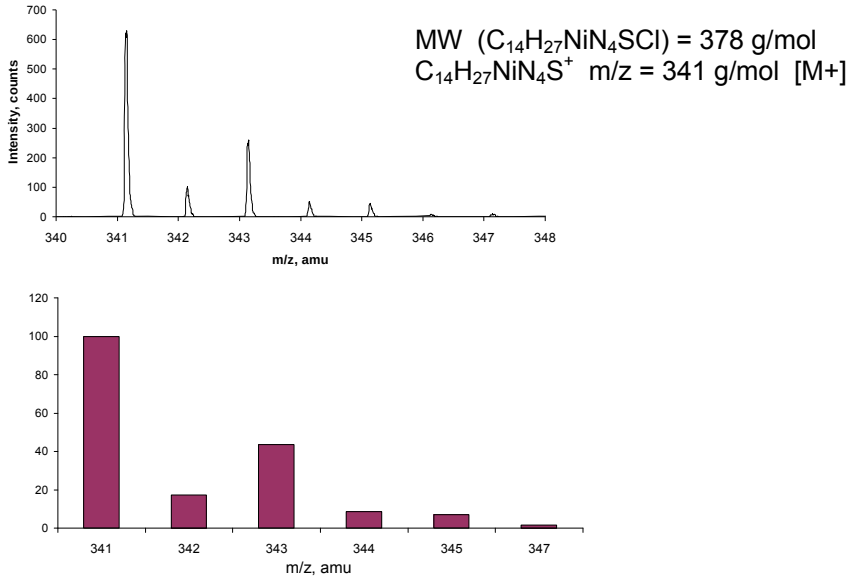

Figure IV-5. Positive mode ESI-MS of the reaction mixture of [(mmp-mdach)Ni(mIm)][BF_4], **6**, in MeOH. Experimental spectrum. Bottom: Predicted isotopic envelope.

product, complex **9** (Scheme IV-1). Under the same conditions as used to produce complex **A**, complex **1-H** (either as its BF_4^- or Cl^- salt) reacted with excess Im in MeOH to yield an orange solid analyzed by $^+$ESI-MS, UV/Vis spectroscopy, and ^{1}H NMR spectroscopy as complex **9**. X-ray quality crystals were obtained by the slow evaporation of complex **9** as its BF_4^- salt in MeOH; however, these crystals analysed as a third partially cleaved dimer, complex **10**.

Molecular Structures of Monothiolate Bridged Dinickel Complexes. Views of the molecular structures of complexes **4**, **5**, and **10** are shown in Figure IV-6, and selected metric data are compared in Table IV-2.

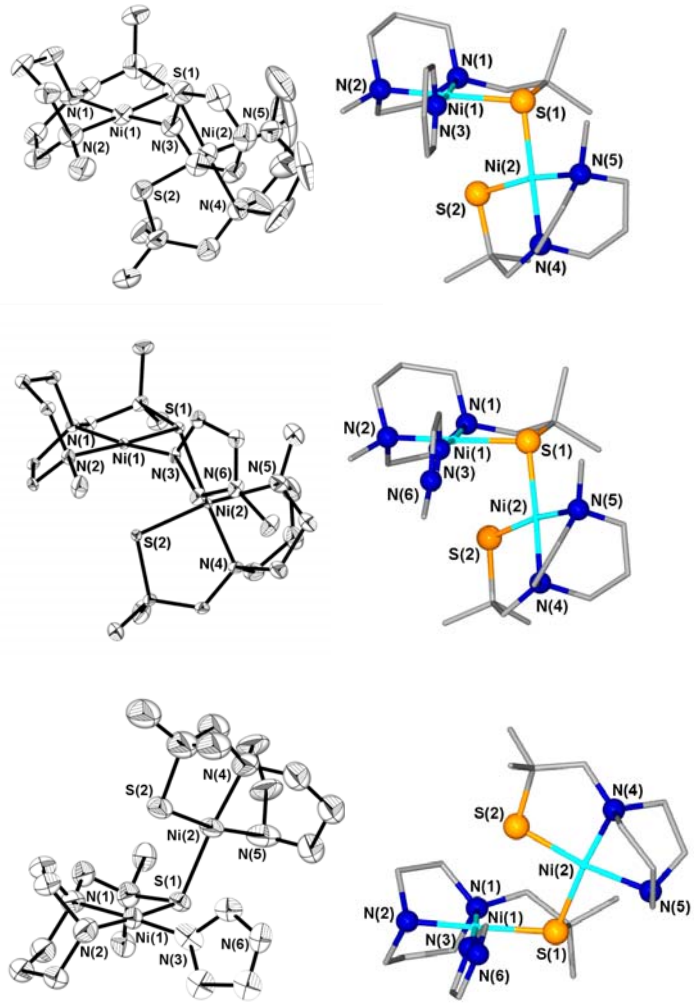

Figure IV-6. Left: Molecular structures of the dications of py-[(mmp-mdach)Ni]$_2$[BF$_4$]$_2$, **4**, (top), mIm-[(mmp-mdach)Ni]$_2$[BF$_4$]$_2$, **5**, (middle), and Im-[(mmp-dach)Ni]$_2$[BF$_4$]$_2$, **10**, (bottom) shown as thermal ellipsoids at 50% probability. The BF_4^- counter ions are not shown. The asymmetric unit of complex **4** contains one MeCN of crystallization. Right: Ball and stick representation of **4** (top) **5** (middle), and **10** (bottom) in different orientation.

Table IV-2. Metric data for complexes py-[(mmp-mdach)Ni]$_2$[BF$_4$]$_2$, **4**, mIm-[(mmp-mdach)Ni]$_2$[BF$_4$]$_2$, **5**, and Im-[(mmp-dach)Ni]$_2$[BF$_4$]$_2$, **10** (distance, Å); angle, deg).

	4	**5**	**10**
Ni(1)-S(1)	2.151(19)	2.166(19)	2.187(4)
Ni(1)-N(1)	1.900(4)	1.922(5)	1.929(11)
Ni(1)-N(2)	1.951(5)	1.961(6)	1.884(11)
Ni(1)-N(3)	1.918(4)	1.905(5)	1.893(12)
Ni(2)-S(1)	2.192(2)	2.214(19)	2.178(4)
Ni(2)-S(2)	2.133(19)	2.140(19)	2.128(4)
Ni(2)-N(4)	1.930(6)	1.925(6)	1.918(12)
Ni(2)-N(5)	1.944(5)	2.026(7)	1.971(13)
Ni(1)···Ni(2)	3.379	3.339	3.534
N(1)-Ni(1)-N(2)	82.6(19)	82.3(2)	82.6(5)
N(1)-Ni(1)-S(1)	92.3(15)	91.2(17)	90.6(4)
N(2)-Ni(1)-N(3)	96.2(19)	97.4(2)	93.6(5)
S(1)-Ni(1)-N(3)	88.9(15)	89.1(18)	93.2(3)
N(1)-Ni(1)-N(3)	173.6(2)	174.4(2)	175.8(5)
N(2)-Ni(1)-S(1)	174.9(14)	173.5(18)	173.2(4)
Ni(1)-S(1)-Ni(2)	102.2(7)	99.34(7)	108.1(17)
N(4)-Ni(2)-N(5)	80.8(2)	80.7(3)	79.6(5)
N(4)-Ni(2)-S(2)	89.9(15)	90.0(18)	91.6(4)
N(5)-Ni(2)-S(1)	97.3(19)	96.4(2)	95.1(4)
S(1)-Ni(2)-S(2)	91.9(8)	92.7(7)	93.7(15)
S(1)-Ni(2)-N(4)	177.5(16)	174.4(18)	174.4(4)
N(5)-Ni(2)-S(2)	170.4(2)	170.3 (2)	171.2(4)

Complexes **4**, **5**, and **10** consist of a Ni(μ-SR)Ni unit, in which both nickels are in a regular square planar geometry. The $N_2S_2Ni(2)$ portion is nearly perfectly square planar with average standard deviation from the N_2S_2Ni plane of 0.0196 Å (maximum and minimum deviation are 0.0259 and 0.0037 Å by N5 and S1, respectively) for **4**; 0.0255 Å (maximum and minimum deviation are 0.0566 and 0.0027 Å by Ni1 and S2, respectively) for **5**; and 0.0168 Å (maximum and minimum deviation are 0.0237 and 0.0082 Å by N4 and Ni2, respectively) for **10**. The average standard deviation in the

$N_2SN'Ni(1)$ portion of **10** is 0.0121 Å (maximum and minimum deviation are 0.0155 and 0.0077 Å by N1 and S1, respectively); of **4**, 0.0520 Å (maximum and minimum deviation are 0.0675 and 0.0404 Å by N1 and Ni1, respectively); and of **5**, 0.0464 Å (maximum and minimum deviation are 0.0603 and 0.0355 Å by N1 and Ni1, respectively). The two square planes intersect with a dihedral angle of 81.4º for **4**, 77.8º for **5**, and 94.7º for **10**. Note that both **4** and **5** show the exogenous N-donor ligand plane is orthogonal to the $NiN_2N'S$ plane, while the imidazole ligand plane in **10** deviates from orthogonality by ~22º. This feature will be discussed later when the structures of the complete series are compared.

The Ni···Ni distances in **4**, **5**, and **10**, 3.379, 3.339, and 3.354 Å, respectively, are significantly longer than typical Ni···Ni distances in $\mu_2(SR)_2$ butterfly complexes (2.7 to 2.9 Å).[110, 113, 131, 146] The distances within the $N_2N'SNi(1)$ plane are nearly identical for complexes **4**, **5**, and **10**, while the distances about Ni(2) show more deviation both between complexes **4**, **5**, and **10**, and as compared to analogous monomeric N_2S_2Ni compounds. As in all diazacycloheptane derivatives, the N-Ni-N angles are pinched to ca. 80º-82º, rendering the S-Ni-S angle or S-Ni-L angle $\geq$ 90 º, as seen here. Overall, metric differences in the first coordination spheres of **5**, **6**, and **10** are minor.

Mononuclear Products: Synthesis and Structural Characterization

Syntheses. Isolation of single crystals of the fully cleaved mIm complex **6** in 42% yield was achieved upon the reaction of **2** with a 10-fold excess of mIm in addition to growing the orange-brown X-ray quality crystals in the presence of a further 5-fold

excess of mIm in MeCN solution layered with Et_2O. A 3-fold excess of ipIm led to the full cleavage of complex **2**, yielding **7**, which was purified by precipitation with Et_2O. Diffraction-quality orange crystals of **7** were isolated from an Et_2O-layered solution of MeCN in 53% yield. The reaction of complex **2** with me_2NHC occurs readily in THF solvent and the pure product precipitated out of solution as the reaction proceeded. Complex **8** was isolated as an air stable, hygroscopic bright orange crystalline solid (46% yield) from the slow diffusion of Et_2O into a MeCN solution.

Molecular Structures of Mononuclear Products. Thermal ellipsoid plots of monocationic complexes **6**, **7**, and **8** are given in Figure IV-7. Salient metric parameters are given within the ball and stick structures shown in Figure IV-8, and, for comparison, those of complex **A** are also given. The Ni-N_{dach} and Ni-S distances, and the N_{dach}-Ni-N_{dach} angles are largely the same in the four structures. The most significant difference is in the Ni-N_{dach} distance trans to the monodentate donor ligand that ranges from 1.890 to 1.947 Å, correlating with basicity of the trans ligand. The Ni-$C_{carbene}$ distance of 1.891 Å in **8** is the same as that reported by Huang, Holm et al. for an NS_2Ni(carbene) complex in which the carbene donor is trans to pyridine. [52]

The critical feature for our study is the dihedral angle defined by the intersection of the exogenous monodentate ligand plane and the Ni complex plane, defined by the best $N_2SNiL_{donor\ atom}$ plane, Table IV-3. For the monomeric complexes, the ligands of greatest steric bulk (ipIm, **7**, and me_2NHC, **8**) are nearest to perpendicular while the mIm derivative, complex **6**, is the furthest from 90º. The torsion angle that is defined in Table IV-3 is required for discussion in the computational section.

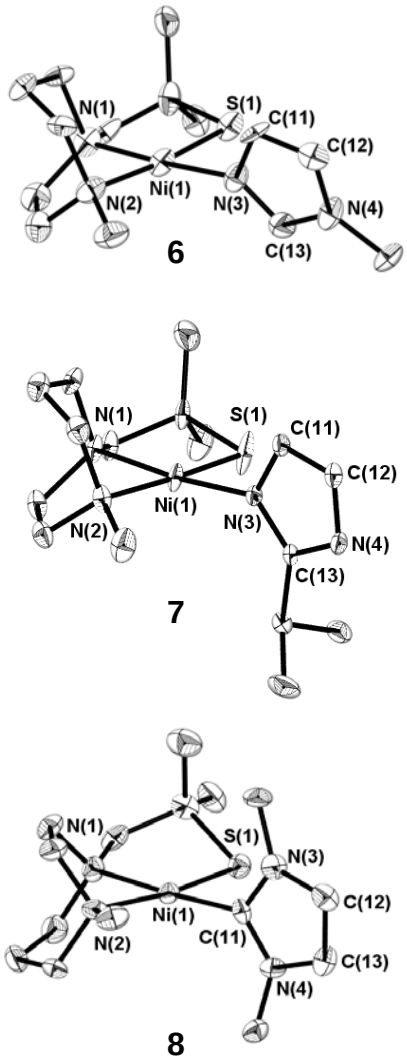

Figure IV-7. Molecular structures of [(mmp-mdach)Ni(mIm)][BF_4], **6**, [(mmp-mdach)Ni(ipIm)][BF_4], **7**, and [(mmp-mdach)Ni(me_2NHC)][I], **8**, shown as thermal ellipsoids at 50% probability. Counter anions are not shown: **6**, BF_4^-; **7**, BF_4^-; and **8**, I^-.

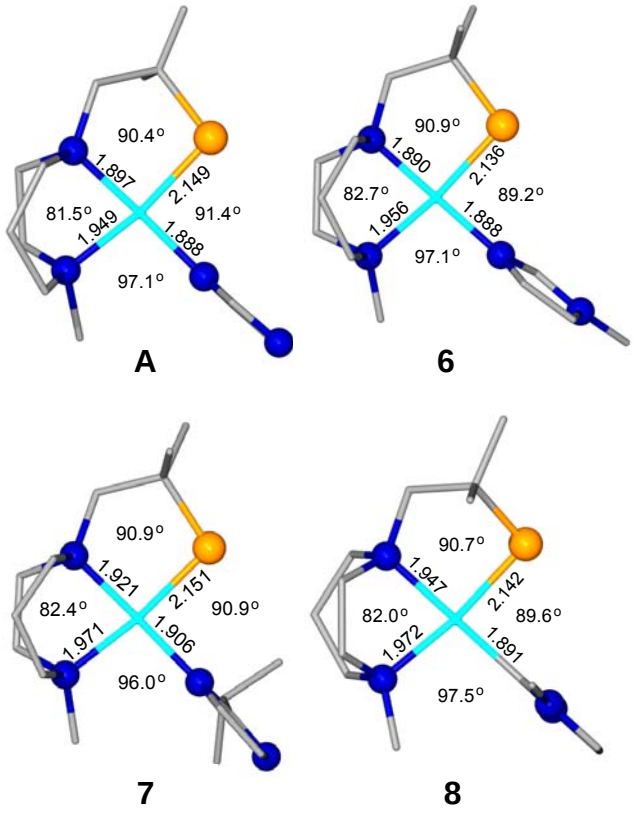

Figure IV-8. Ball and stick drawings with selected metric parameters of [(mmp-mdach)Ni(Im)](Cl), **A**[131]; [(mmp-mdach)Ni(mIm)]BF_4, **6**; [(mmp-mdach)Ni(ipIm)]BF_4, **7**; [(mmp-mdach)Ni(me_2NHC)](I), **8**. Counter anions are not shown. View ⊥ to N_2S plane. Full listings of metric parameters are given in the Appendix.

Table IV-3. Td twist, dihedral angle between the exogenous ligand plane and the N_2SNiL^a plane, and N-Ni-L-C2 torsion angle for complexes **4-8, 10,** and **A**. [131]

complex	**4**	**5**	**6**	**7**	**8**	**10**	**A**
Td twist[b]	6.4 °	5.7	4.1	6.8	4.9	1.7	7.9
Dihedral angle[c]	86.6 °	85.6	76.3	84.8	87.0	68.1	87.8
N-Ni-L-C2[d]	95.4 °	90.6	108.3	93.2	91.1	117.2	95.0

[a]L = N donor atom in complexes **4-7**, **10** and **A,** and L = C donor atom in complex **8**. [b]Td twist defined as the intersection of the N-Ni-N and the S-Ni-L planes. [c]Dihedral angle is defined as the angle between the N_2SNi-L plane and the best ligand plane. For complexes **4** and **8**, [d]C2 = atom α to the donor atom which is on the same side as the ethylene side of the dach backbone. N = nitrogen atom *cis* to L atom.

Defining the Steric and Electronic Contributions of the Ligands

Methods for describing steric and electronic properties of "flat" ligands such as N-heterocyclic carbenes have been well documented.[49, 147] The donor properties of the ligands are typically compared by their effect on υ(CO) values in $LNi(CO)_3$ systems.[147] Due to the lack of spectroscopic reporter groups in our system, as well as the predominately σ donor character N-donors in the N-heterocycles and the C-donor in NHC's, we base the ligand donor ranking in these complexes on the pK_a of the donor atom's conjugate acid in each ligand, Figure IV-2.

The steric bulk of each ligand, was evaluated from features in the experimentally and computationally determined structures by group member Michael Singleton. The ligand width was defined as the widest point closest to the metal center, Figure IV-9. For example, in the ipIm ligand this is the distance between the C5 imidazole proton and the proton on the tertiary carbon atom of the isopropyl substituent. The width as defined at this point on the ligand is more relevant to the steric encumbrance of the ligand within the coordination sphere than the larger width from the C5 proton to the isopropyl CH_3 groups as the latter orients away from the ligand metal system decreasing their steric effect. This effect is comparable to the smaller cone angle in phosphite ligands as defined by Tolman, et al.[148] The ligand wedge angle for flat ligands is defined as the angle made between the atoms that define the ligand width with the vertex being the Ni^{II} ion ($L_{donor\ atom}$-Ni avg. distance = 1.90 Å (exp'tl); 1.92 (calc'd)). This definition is analogous to the A_L parameter described by Nolan and coworkers for comparison of steric properties of N-heterocyclic carbene ligands.[49] Based on these parameters, listed

in Table IV-4, the ligands increase in steric bulk in the order: Im ~ mIm < py < ipIm < me_2NHC.

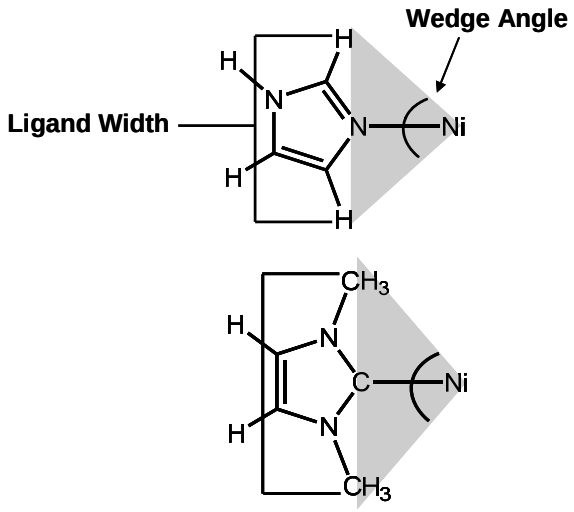

Figure IV-9. Illustration of ligand width and wedge angle used to define the steric bulk for flat ligands such as imidazoles and NHC's.

Table IV-4. Ligand steric parameters taken from DFT calculated structures; Values from the X-ray determined structures are given in parenthesis.

Ligand	Ligand Width (Å)	Wedge Angle (°)
Im, **A**	4.21 (3.94)	83.2 (78.0)
mIm, **6**	4.21 (3.98)	83.2 (79.2)
py, **3**[a]	4.14 (3.94)	91.3 (86.3)
ipIm, **7**	4.76 (4.69)	106.3 (101.6)
me_2NHC, **8**	5.04 (5.28)	121.9 (113.6)

[a]Experimental values were taken from structure of complex **5**.

Defining the Barrier to Rotation about the Ni-L Bond: VT ^{1}H NMR

The VT 1H NMR studies were carried out in collaboration with group member Michael L. Singleton. As was found for complex **A**,[131] the ^{1}H NMR spectra of the mIm analogue, complex **6**, change with temperature, Figure IV-10. In the imidazole C-H region, three ^{1}H resonances are observed at 22°C and assigned according to the structure depicted within Figure IV-10. Resonances *a* and *b* broaden and reach coalescence on

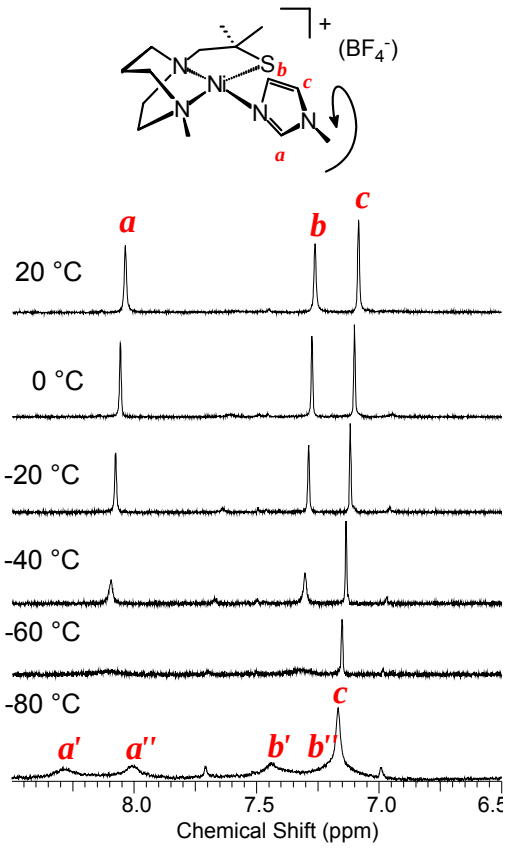

Figure IV-10. VT 500-MHz ^{1}H NMR spectra of [(mmp-mdach)Ni(mIm)][BF_4], **6**, in CD_3OD.

lowering the temperature to -60 ºC, while resonance *c* remains sharp. By – 80 ºC, resonances *a* and *b* reappear as four distinct signals (*a'* and *a''* and *b'* and *b''*), indicating the presence of two isomers. This behavior is almost identical to that of complex **A** and is to be expected as the added steric bulk of mIm is remote from the binding site.[131] Free energy differences were obtained from K_{eq} values based on the isomer ratios at -80 ºC and are calculated as in eqs 1 and 2.

$$K_{eq} = [a']/[a''] = 0.72 \quad (1)$$

$$\Delta G = -RT \ln K_{eq} = 0.14 \text{ kcal/mol} \quad (2)$$

The activation barrier, $\Delta G^{\ddagger}$, is obtained from the chemical shift difference between *a'* and *a''* ($\Delta\nu$ = 145 Hz) and the coalescence temperature (T_{coal} = -60 ºC), eqs 3 and 4.

$$k_T = (\pi\Delta\nu/\sqrt{2}) = 304.7 \text{ s}^{-1} \quad (3)$$

$$\Delta G^{\ddagger} = -RT \ln (k_T h/ k_b T_{coal}) = 9.0 \text{ kcal/mol} \quad (4)$$

The experimental barrier to rotation of 9.0 kcal/mol is, within experimental error, identical to that of complex **A** (8.9 kcal/mol).

The VT ^{1}H NMR spectra for the imidazole region of complex **7**, the ipIm derivative, in CD_3OD are shown in Figure IV-11. Two sets of doublets indicate the presence of two isomers at 20 ºC, of expected structures as shown in Figure IV-11, which on cooling show temperature dependent chemical shifts and some broadening of the signals. From the isomer ratio of a/b to a'/b' observed at room temperature, the ΔG value was calculated to be 0.32 kcal/mol according to eqs 1 and 2. The signal at 6.89 ppm is assigned to unbound ipIm. The increase of temperature to ~60 ºC resulted in

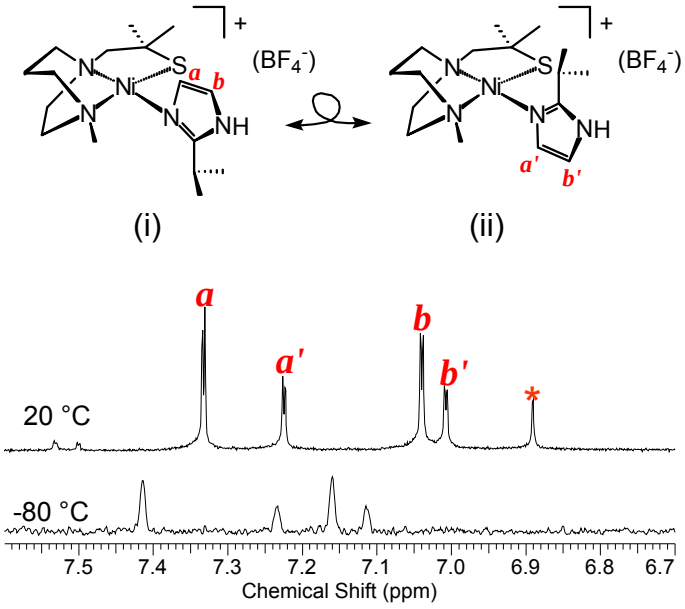

Figure IV-11. Top: Isomers of [(mmp-mdach)Ni(ipIm)][BF_4], **7**; (i) is assigned as in the solid state by X-ray diffraction; (ii) the ipIm ligand is rotated 180º with respect to (i). Bottom: VT 500-MHz ^{1}H NMR spectra of complex **7** in CD_3OD. * = unbound ipIm.

slight broadening of the signals in the imidazole region. An NMR sample of **7** in D_2O solution showed a similar spectrum at 20 ºC as in the CD_3OD solution spectrum, with a more equal distribution of isomers (Figure IV-12). The pairs of singlets (*a* and *b* and *a'* and *b'*) broaden and start to overlap near 100 ºC. The unidentified signal observed at 20 ºC at 7.06 ppm remains visible at 100 ºC, but has shifted downfield (7.70 ppm). On cooling the sample back to 20 ºC the two sets of isomers, *a* and *b* and *a'* and *b'*, reappear, in addition to the unbound ipIm, which is now shifted to 7.16 ppm. Because the observed 'coalescence' temperature is at the experimental high temperature limit, it is unknown whether this change in the spectrum is due to intra- or intermolecular

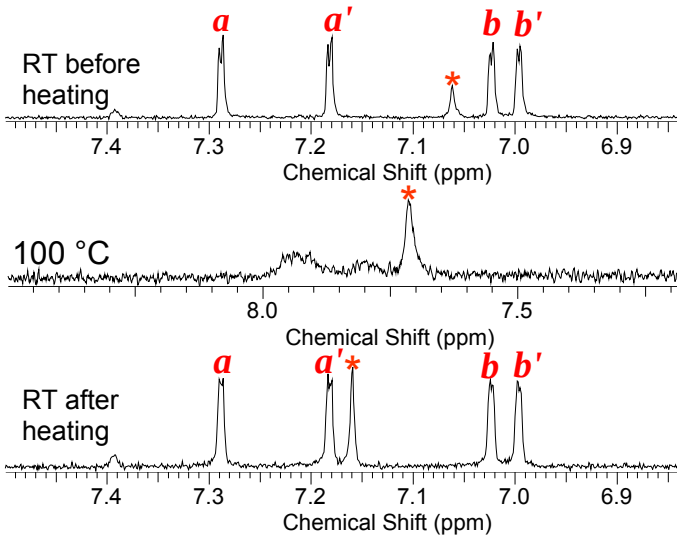

Figure IV-12. VT 500-MHz ^{1}H NMR spectra of [(mmp-mdach)Ni(ipIm)][BF_4], **7**, in D_2O. * = unbound ipIm.

exchange. Evidence for intermolecular exchange in complex **A** in the presence of free imidazole is presented below.

Complex **8**, the me$_2$NHC derivative, in CD_3OD at 20 ºC shows an AB pattern that is centered at 7.18 ppm and assigned to C-H protons on the NHC ligand, and two singlets that are assigned to the NHC methyl groups at 4.37 and 4.38 ppm (Figure IV-13). Upon heating the sample to ~60 ºC or cooling to -80 ºC there are no changes in the spectra except for temperature dependent broadening and shifting (Figure IV-14). This data implies that the NHC ligand does not rotate about the Ni-C bond in the tight confines of the square planar nickel fragment as would be expected for such a sterically hindered ligand of wedge angle = 122°; neither is there isomerization by dissociation/association. A simple representation of the expected transition state for

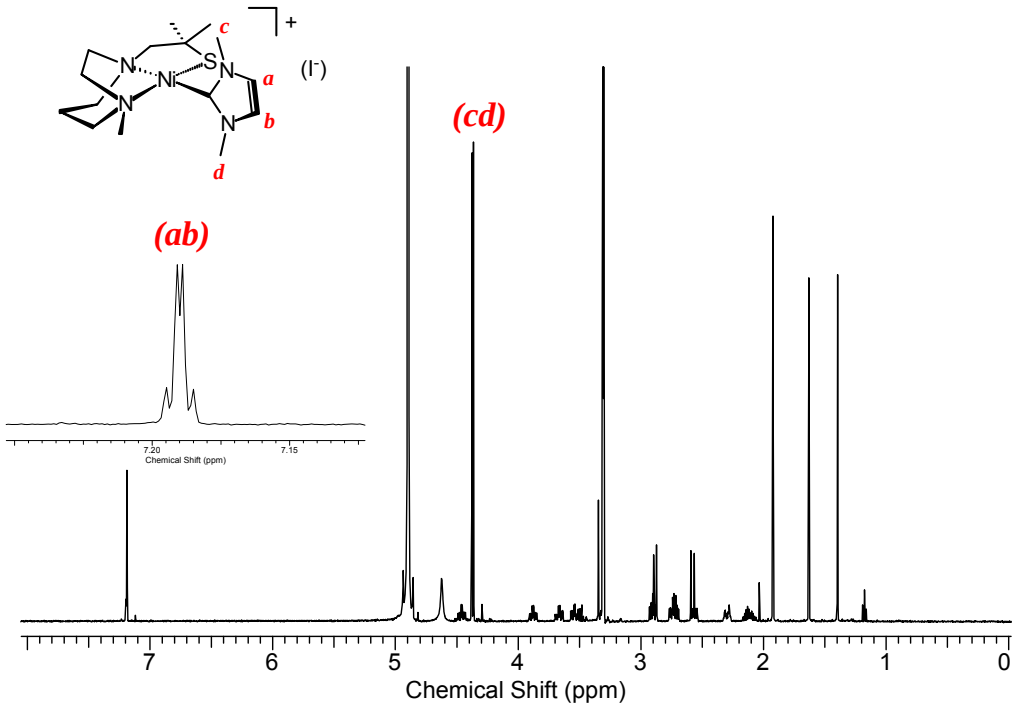

Figure IV-13. 500-MHz ^{1}H NMR spectrum of [(mmp-mdach)Ni(me$_2$NHC)][I], **8** in CD_3OD.

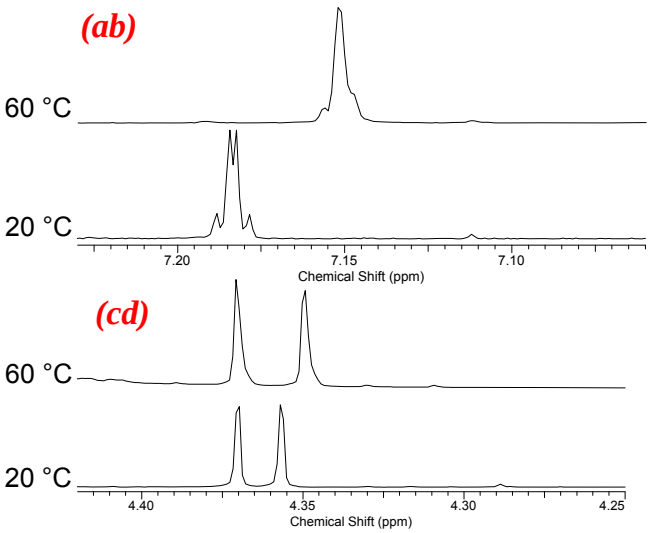

Figure IV-14. 500-MHz ^{1}H NMR spectra of [(mmp-mdach)Ni(me$_2$NHC)][I], **8** in CD_3OD at 20 ºC and 60 ºC. Top: aromatic region; Bottom: NHC methyl group resonances.

rotation in complex **8** is shown in Figure IV-15; a more exact description is presented below in the computational section. Steric repulsion between the NHC methyl group and the S atom as well as the NHC methyl group and the N-dach methyl group is expected to greatly destabilize the coplanar arrangement shown and results in a very high barrier to rotation.

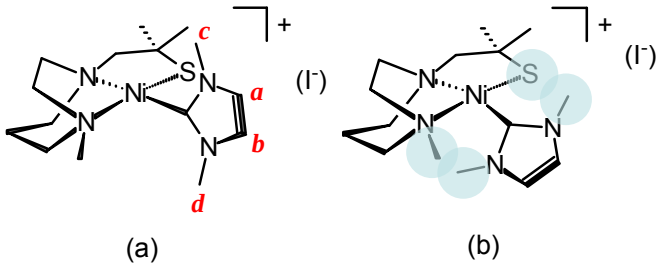

Figure IV-15. (a) Conformation of me_2NHC ligand in complex [(mmp-mdach)Ni(me_2NHC)][I], **8** as observed in the molecular structure; (b) A 90° twist of the me_2NHC as expected for rotational transition state showing the steric repulsion of the NHC methyl groups with the dach-N-methyl and the S atom.

The ^{1}H NMR spectrum of complex **9** at 20 ºC displays three sharp singlets at 7.04, 7.09 and 7.86 ppm (Figure IV-16). These resonances are assigned, consistent with complex **A**, to the C-H protons on the coordinated imidazole ligand. At all temperatures explored (+60 to -80°), these signals remain sharp, but decrease in intensity with lowered temperatures as two additional sets of three singlets, of 1:1:1 ratios, appear. These completely reversible temperature-dependent spectra are shown in Figure IV-16. In view of the complicated dimer cleavage processes encountered during the syntheses,

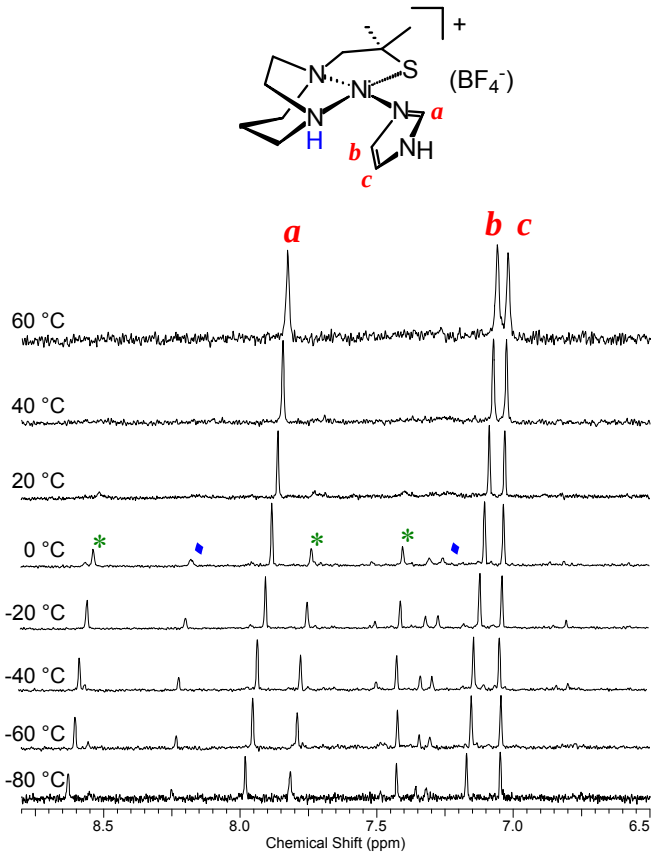

Figure IV-16. VT 500-MHz ^{1}H NMR spectra of [(mmp-dach)Ni(Im)][BF_4], **9**, in CD_3OD.

including monothiolate bridged materials such as those analogous to structures **4, 5** and **10**, the observation of other species is not surprising. While assignments of the other species would be extremely speculative, we can confidently conclude that the primary species is the mononuclear imidazole complex with rapid rotation about the Ni-$N_{imidazole}$ bond at all accessible temperatures. Similar results were noted in the spectra of complex **4** (Figure IV-17); an activation energy barrier was obtained from these spectra; however, assignment to a monomeric or binuclear species is ambiguous.

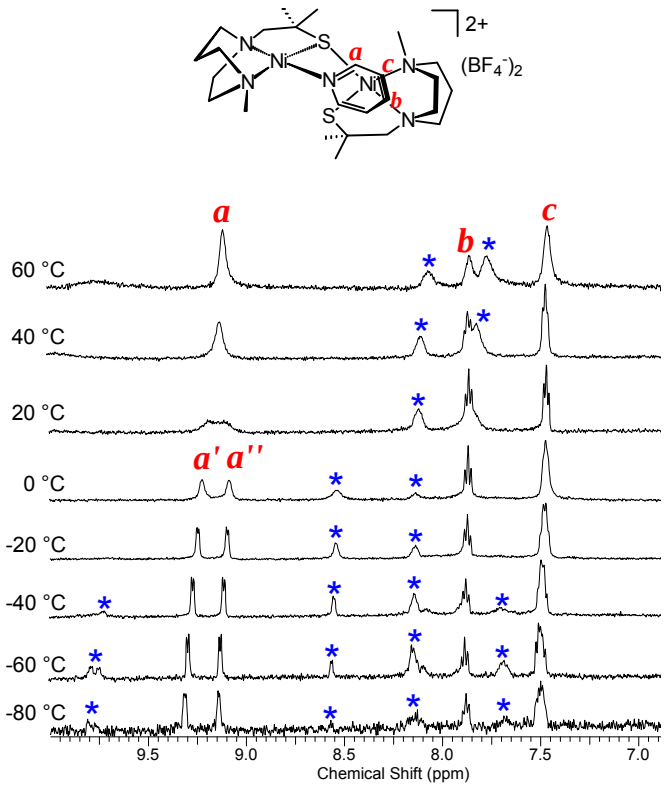

Figure IV-17. VT 500-MHz ^{1}H NMR spectra of py-[(mmp-mdach)Ni]$_2$[BF_4]$_2$, **4**, in CD_3OD. * = unassigned species.

Theoretical Predictions of ΔG and ΔG‡ Values

DFT computations were carried out by group member Michael Singleton to calculate the free energies of (i) and (ii) isomers of complexes **3-4** and **6-9** and to predict the barriers for rotation about the Ni-L bond. Geometry optimizations were performed on each complex using the experimental X-ray molecular structure as the initial

geometry (defined as isomer (i)). The metric data of the optimized structures were in good agreement with the experimentally determined results (Table IV-5). A second

Table IV-5. Selected experimental and optimized parameters for complexes **4** and **6-8**.

	Calculated (Å)	Experimental (Å)		Calculated (Å)	Experimental (Å)
Complex 4			**Complex 7**		
Ni(1)-N_{py}	1.938	1.918	Ni-N_{ipIm}	1.922	1.907
Ni(1)-N_{amine}	2.017	1.951	Ni-N_{amine}	2.046	1.971
Ni(1)-N_{amine}	1.949	1.900	Ni-N_{amine}	1.944	1.922
Ni(1)-$S_{thiolate}$	2.240	2.151	Ni-$S_{thiolate}$	2.175	2.151
Ni(2)-N_{amine}	2.054	1.944			
Ni(2)-N_{amine}	1.979	1.930			
Ni(2)-$S_{thiolate}$	2.187	2.133			
Complex 6			**Complex 8**		
Ni-N_{mIm}	1.919	1.888	Ni-C_{me2NHC}	1.908	1.891
Ni-N_{amine}	2.043	1.956	Ni-N_{amine}	2.042	1.972
Ni-N_{amine}	1.944	1.890	Ni-N_{amine}	1.988	1.947
Ni-$S_{thiolate}$	2.176	2.136	Ni-$S_{thiolate}$	2.178	2.142

optimized structure for each complex was obtained from an initial geometry where the ligand is rotated 180º about the Ni-L bond vector (isomer (ii)). No other energy minima resulting from ligand rotation were found. The initial geometries of the transition state for each complex were located using the synchronous transit-guided quasi-Newton (QST2) method[75-76] utilizing the geometries for isomer (i) and isomer (ii) as the starting points. The transition state geometry of each complex shows the ligand plane to be largely perpendicular to its initial ground state orientation and roughly coplanar with the

N_2SNi plane, Figure IV-18. The lowest energy transition state structure in the imidazole derivatives finds the imidazole C2 directed towards the S atom. To accommodate the transition state structure, the Ni-ligand bonds elongate and there is also a significant increase in the tetrahedral twist of up to 46º (for example, in complex **8**, Td twist in the ground state structure equals 4.8º; in the transition state structure $\mathbf{8}^{\ddagger}$, 51º).

Figure IV-18 shows the computationally determined transition state structures for complexes **3**, **4**, **6-9**, and **A**. In the transition state for complex $\mathbf{6}^{\ddagger}$, the mIm ligand is rotated ~59° from its position in ground-state **6**, with C2 of the imidazole pointed towards the S atom. In order to obtain this orientation the ligand drops out of the N_2S plane towards the ethylene side of the dach frame. This results in a distortion of the square planar geometry around the nickel giving a Td twist of 17°. This distortion is only slightly smaller than that found for complex $\mathbf{A}^{\ddagger}$ (21.2º)[131] and is consistent with the similar experimental barriers for rotation for complexes **A** and **6** (Table IV-6). This further corroborates that the slight difference in electronic character of the mIm over the Im ligand has little effect on the rotational barriers. In contrast, the decreased steric bulk around the Ni in the dach vs. mdach complexes, see Figure IV-3, allows the imidazole ligand of complex $\mathbf{9}^{\ddagger}$ to bind in an orientation that is only 10° from coplanar with the N_2SNi plane, and the complex has a Td twist of only 5.8°. In the transition state structures containing the bulkier ligands, complexes $\mathbf{7}^{\ddagger}$ and $\mathbf{8}^{\ddagger}$, the distortion is much greater: $\mathbf{7}^{\ddagger}$ has a N-Ni-L-$C2_L$ torsion angle of 176.5° and a Td twist of 29.1° while the Td twist of the NHC-containing complex $\mathbf{8}^{\ddagger}$ is 51.0°. The severe distortions required to go through the transition state in both the ipIm and me_2NHC complexes correspond well

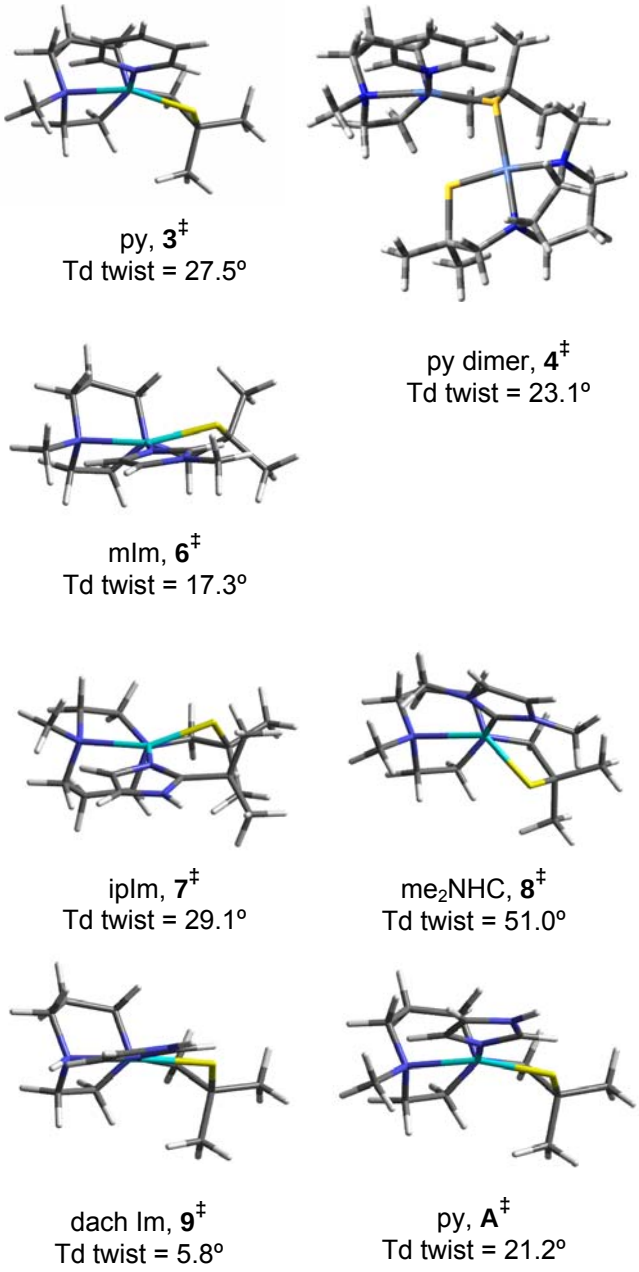

Figure IV-18. DFT optimized structures of the transition state geometries of complexes **3**, **4**, **6-9**, and **A**[131] showing the monodentate ligand planes in their maximum rotation position (ca. 90º from the ground state structure). Td twist values (defined as the intersection of the N-Ni-N and the S-Ni-L_{donor} planes) are given below each structure.

Table IV-6. Experimental and DFT calculated $\Delta G^{\ddagger}$ and ΔG values for complexes **4**, **6-9** and **A** based on the rotation about the Ni-L bond and isomer ratio observed in the ^{1}H NMR resonances.[a]

N_2SLNi L = ligand	$\Delta G_{expt'l}$	$\Delta G_{calc'd}$	$\Delta G^{\ddagger}_{expt'l}$	$\Delta G^{\ddagger}_{calc'd}$
Im(dach), **9**	unknown	0.37	n.a.[b]	3.29
Im(mdach), **A**[131]	0.11	0.18	8.90	8.86
mIm, **6**	0.15	0.13	8.97	8.95
py, **3**	----	----	----	14.04
py dimer, **4**	----	----	11.23	17.82
ipIm, **7**	0.32	0.36	n.a.[b]	21.04
me_2NHC, **8**	----	----	n.a.[b]	29.93

[a]Values reported in kcal/mol. [b]Experimental $\Delta G^{\ddagger}$ value was not determined due to the constraints of the temperature range of the instrument or solvent used.

with the high experimental barriers suggested for these complexes in the VT ^{1}H NMR spectra (Table IV-6).

Because of the possibility of an equilibrium between a monothiolate bridged and a mononuclear species in the case of complex **4**, the transition states for pyridine rotation were calculated for both $\mathbf{3}^{\ddagger}$ (Td twist = 27.5°; N-Ni-L-$C2_L$ torsion angle, where C2 = atom α to the donor atom, which is on the same side as the ethylene side of the dach backbone = 178.3°) and $\mathbf{4}^{\ddagger}$ (Td twist = 23.1º; N-Ni-L-$C2_L$ torsion angle, = 175.6°). Despite these similarities, the energy barrier for Im rotation is calculated to be significantly greater for the dinickel complex **4**, (Table IV-6). However, the disparities between the experimental barrier and the calculated barriers for either the monomer or the dimer indicate that the process observed by NMR spectroscopy may be more complicated than ligand rotation in a single complex.

Table IV-6 lists the experimental and DFT-calculated ΔG and $\Delta G^{\ddagger}$ values for complexes **4**, **6-9**, and **A**. The predicted ΔG of 0.13 kcal/mol and $\Delta G^{\ddagger}$ of 8.95 kcal/mol for complex **6**, the mIm derivative, are consistent with the experimentally determined results and are nearly identical to complex **A**. In complex **7**, the ipIm derivative, the room temperature ^{1}H NMR spectrum indicated the presence of two species. The DFT-calculated ΔG for the two lowest energy conformations was found to be 0.36 kcal/mol, which compares well with the experimental value (based on the observed distribution or K_{eq}) of 0.32 kcal/mol. The large calculated barrier to rotation of 21.04 kcal/mol is due to the steric repulsion that is present when the ipIm ligand is roughly coplanar with N_2SNi plane. Consistently, the experimental $\Delta G^{\ddagger}$ value could not be determined due to the temperature constraints of the solvent used. Likewise, rotation about the Ni-C bond was not observed in complex **8** over the temperature range studied, consistent with DFT-calculated activation barrier of 29.9 kcal/mol. In contrast, DFT predicts a low energy barrier ($\Delta G^{\ddagger}$) of 3.29 kcal/mol and a ΔG of 0.37 kcal/mol for complex **9**, the derivative with least steric hindrance. This barrier to rotation is substantially lower than that for complex **A** and this DFT prediction is consistent with our inability to observe separate rotational isomers by NMR spectroscopy at the lowest accessible temperature. In the case of the pyridine complex the calculated rotational barriers for the monomer and the dinuclear complex were found to be higher than the experimentally determined value of 11.2 kcal/mol by ~3.0 and ~6.5, respectively.

Further evidence for steric control of dynamics is seen in comparisons of complexes **A** and **9**, which differ by the substituent on the terminal N donor of dach in

the N_2SNi binding pocket, Figure IV-3. Relaxed potential energy scans monitor the change in potential energy of complexes **A** and **9** as a function of imidazole rotation, Figure IV-19. Note that two maxima result as the imidazole completes a 360° rotation. The first maximum, occurring as the C2C-H unit passes the thiolate S is slightly lower than the second, resulting from the opposite orientation of the imidazole ligand dipole. This phenomenon is observed for both complexes, but is more dramatic for complex **9**. The large overall difference in the energy barriers for rotation between **A** and **9** is apparent by comparison at each energy maximum, and is consistent with the experimental and computational results for imidazole ligand rotation in **A** and **9**, Table IV-6.

Intermolecular vs. Intramolecular Paths for Isomerization

The VT ^{1}H NMR studies demonstrated that stereoisomers of these complexes may coexist in solution, and according to the good correlation between DFT calculations and the NMR data for complexes **A** and **6** the isomerization process observed in certain N_2SLNi complexes is most reasonably assigned to intramolecular fluxionality, i.e., rotation about the Ni-L bond. Nevertheless intermolecular isomerization processes are of concern, particularly in systems with high activation barriers as is the case of the two complexes containing the ligands of largest wedge angle, complexes **7** and **8**. The NHC ligands are known to be strongly coordinated to metal ions and they show great stability toward thermal degradation in solution.[45, 149]

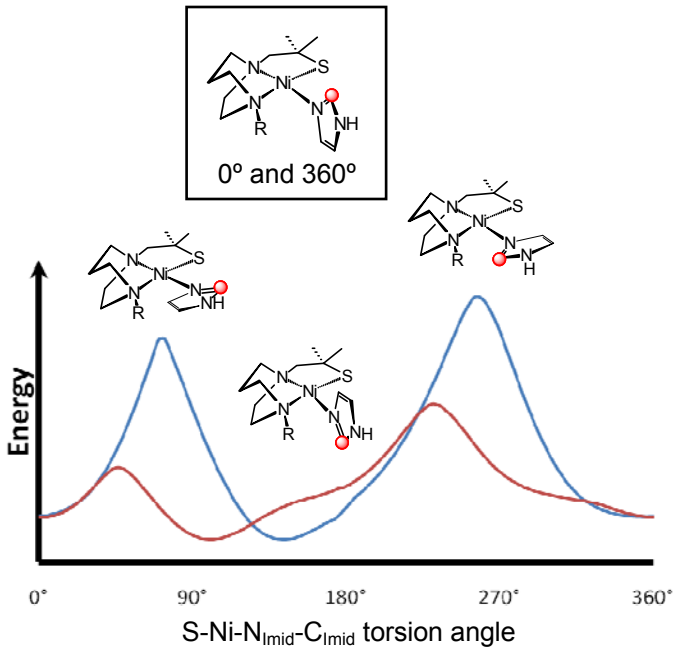

Figure IV-19. Plots of the potential energy of [(mmp-mdach)Ni(Im)]Cl, **A**, (R = CH_3) and [(mmp-dach)Ni(Im)][BF_4], **9**, (R = H) as a function of the S-Ni-N_{Imid}-C_{Imid} torsion angle. Blue: complex **A**; Red: complex **9**. The imidazole rotation starts from the optimized X-ray structure.

As a probe of the possibility of intermolecular exchange, we have monitored the VT ^{1}H NMR spectra of a well-characterized fluxional system, that of complex **A** in the presence of free imidazole. At 20 ºC, the NMR spectrum of pure imidazole in CD_3OD displays two sharp singlets at 7.67 and 7.04 ppm (Figure IV-20). The addition of 1 equiv of imidazole to a sample of complex **A** in CD_3OD at 20 ºC resulted in broadening of the three singlets at 8.11, 7.33 and 7.12 ppm that are assigned to the C-H protons on the coordinated imidazole ligand, *a*, *b*, and *c*. As the temperature is raised above 20 ºC,

a, *b*, and *c* further broaden, completely flat-lining at 60-70 ºC. A decrease in the temperature from 20 ºC results in the sharpening of resonances *a b*, and *c* and singlets for free imidazole appear at 7.07 and 7.73 ppm.

The broad signals observed at temperatures > 10 ºC indicate that the Ni-bound imidazole exchanges with the free imidazole in solution. This intermolecular exchange process is slowed at temperatures below 10 ºC; for example, singlets at 7.07 (free imidazole) and 7.16 ppm (bound imidazole) are observed. The activation energy

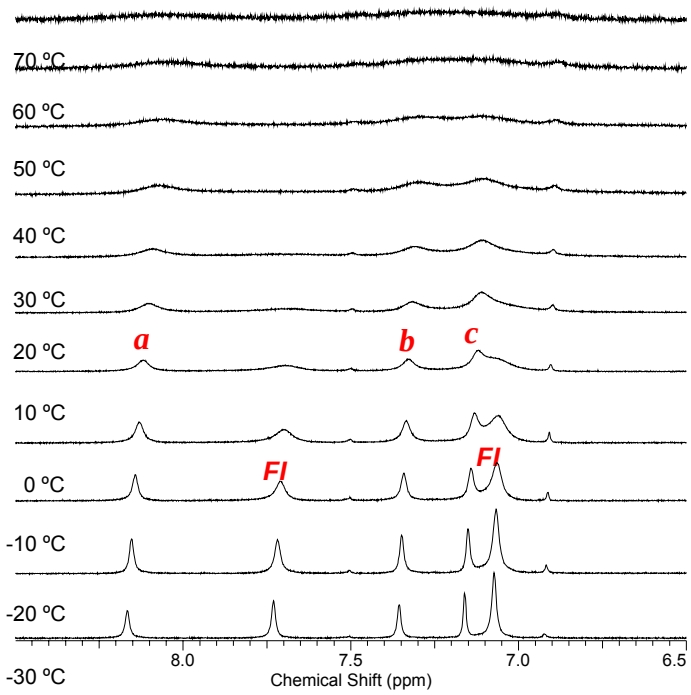

Figure IV-20. VT 400-MHz ^{1}H NMR spectra of the addition of free imidazole to [(mmp-mdach)Ni(Im)]Cl, **A**, in CD_3OD. FI = free imidazole.

parameter ($\Delta G^{\ddagger}$) for the intermolecular exchange of free imidazole with bound imidazole for complex **A** was determined to be 11.3 kcal/mol from the exchange rate constant at coalescence. A comparable $\Delta G^{\ddagger}$ value was determined from the line shape analysis in the slow exchange region ($\Delta G^{\ddagger}$ = 10.8 kcal/mol). The Eyring plots used to derive $\Delta G^{\ddagger}$ for the exchange process are shown in Figure IV-21.

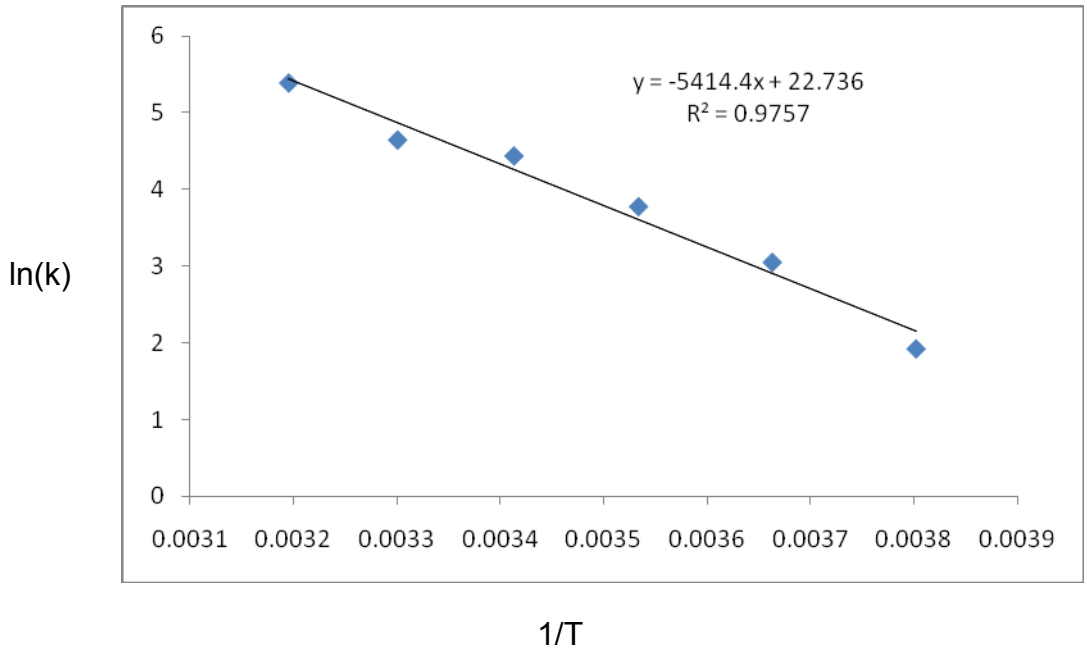

Figure IV-21. Plot of ln(k) versus 1/T for imidazole exchange in complex **A**.

The VT ^{1}H NMR data of pure complex **A**, i.e., without excess imidazole, shows no broadening of signal *c* at temperatures below 0 ºC. In this previously reported VT ^{1}H NMR study,[131] changes were only observed in resonances *a* and *b*, which broaden at -40

ºC, coalesce at -60 ºC, and reappear as two sets of singlets at -80 ºC. In contrast, the VT ^{1}H NMR spectra resulting from the addition of free imidazole to complex **A** displays broadening of resonance *c* at the higher temperatures and begins to separate into two separate signals at ~10 ºC. Comparing the VT ^{1}H NMR parameters for intermolecular exchange of the coordinated imidazole ligand with free imidazole in solution to the VT ^{1}H NMR factors for pure complex **A**, we conclude that the observed fluxional process observed at low temperatures is intramolecular, most reasonably due to the rotation about the Ni-L bond.

Electrostatic Contributions to the Ground State Imidazole Binding Orientation

While the steric bulk of the ligands and interference with ancilliary or spectator ligands likely plays the largest role in the rotational barrier, there are slight deviations from orthogonality in the ground state orientation of the monodentate ligands in the less sterically bulk complexes, **A**, **6**, and **9** that appear to be of electrostatic origin. In all, the C2 position of the imidazole ligands, with its electropositive C-H$^{\delta+}$ tilts towards the thiolate S in both the experimental and DFT calculated structures. This sort of internal electrostatic interaction has been surmised to be important in the orientation of axial coordinated imidazoles in heme systems.[34-35]

Indeed, a computational S/O replacement in complexes **A** and **9** resulted in greater deviation towards coplanarity for the alkoxide analogue of the thiolate. For example the C2 of imidazole orients toward the alkoxide O$^{\delta-}$, resulting in the case of computationally defined **9-(O)** an N-Ni-N$_{imid}$ -C2$_{imid}$ torsion angle of 194°, i.e., *a nearly*

coplanar imidazole/N_2ONiN_{imid} geometry, Figure IV-22. In the case of complex **A**, with more steric hindrance built into the nickel binding pocket by virtue of the methyl group on the dach, the tilt of the imidazole in the N_2ONiN_{imid} is again roughly 40° away from the orthogonal orientation that is observed for the A-(S) derivative both experimentally and in the computations. In this case the Ni-N_{imid} bond lengthens by ca. 0.015 Å, presumably to accommodate the imidazole twist.

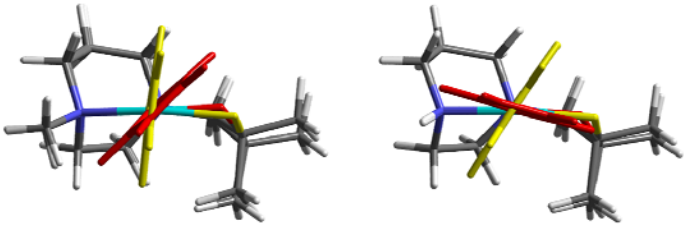

Complex	A-(S)	A-(O)	9-(S)	9-(O)
Ni-N_{imid},Å	1.923	1.938	1.916	1.926
Ni-S/O, Å	2.179	1.815	2.177	1.816
Dihedral Angle[a], °	84.4	41.9	58.5	14.0
N-Ni-N_{imid}-C2, °	102.5	140.8	125.9	194.1
S-Ni-N_{imid}-C2, °	82.8	38.4	58.9	-10.0

Figure IV-22. Overlays of computationally determined structures for (left) [(mmp-mdach)Ni(Im)]$^+$, **A**, as thiolate, (**A-(S)**), and as alkoxide, (**A-(O)**). Similarly (right), complex **9** as thiolate, (**9-(S)**), and as alkoxide, (**9-(O)**). In both overlays, the view is along the N_{imid}-Ni bond vector and shows tilt of the imidazole C2-H unit toward the chalcogen donor. In both overlays, the imidazole is in red for the alkoxide and in yellow for the thiolate derivative. Pertinent metric parameters are given in the table, including dihedral angle of the ligand and complex planes as defined in the text, and torsion angles as noted.

The conclusion that the shift towards coplanarity of imidazole and nickel planes in the N_2ONiN_{imid} virtual complexes is a result of an internal electrostatic interaction is consistent with the experimental structures of a set of square planar Ni^{II} complexes of tridentate, truncated Schiff base units that show greater variation in imidazole ligand orientation with respect to the tridentate ligand-metal plane. Ten such molecular structures are to be found in the Cambridge Crystallographic Data base, six of which are shown in Figure IV-23.[133-141] None were characterized for imidazole fluxionality by VT NMR solution studies as in our study above. The Ni^{II}-Schiff base complexes containing hard O-donors *cis* to the unsubstituted imidazole monodentate ligand, complexes a) and b) in Figure 16, find coplanarity in the nickel complex plane and the plane of the imidazole ligand. Intramolecular H-bonding was reported in the interaction of the C2-H of the imidazole with the O-donor, and intermolecular H-bonding interactions involving the imidazole N-H define a one dimensional assembly in the crystal lattice. The four other structures of this type presented in Figure S9 are also of the co-planar type. With a sterically hindered imidazole ligand, molecular structures such as c) and d) of Figure 16 show substantial displacements of the imidazole ligand plane from the nickel complex square plane inducing dihedral angles of ca. 49º and 87º, respectively. Strong intermolecular H-bonding is seen in the extended molecular structures of both c) and d). In addition, complex c) has an intramolecular C-H$\cdots\pi_{arene}$ interaction involving the ortho C-H group on the phenyl ring of the monodentate ligand and the phenyl ring of the tridentate ligand that is suggested to produce the observed canted orientation of the imidazole plane with respect to the metal square plane.[137] Complexes e) and f) in Figure

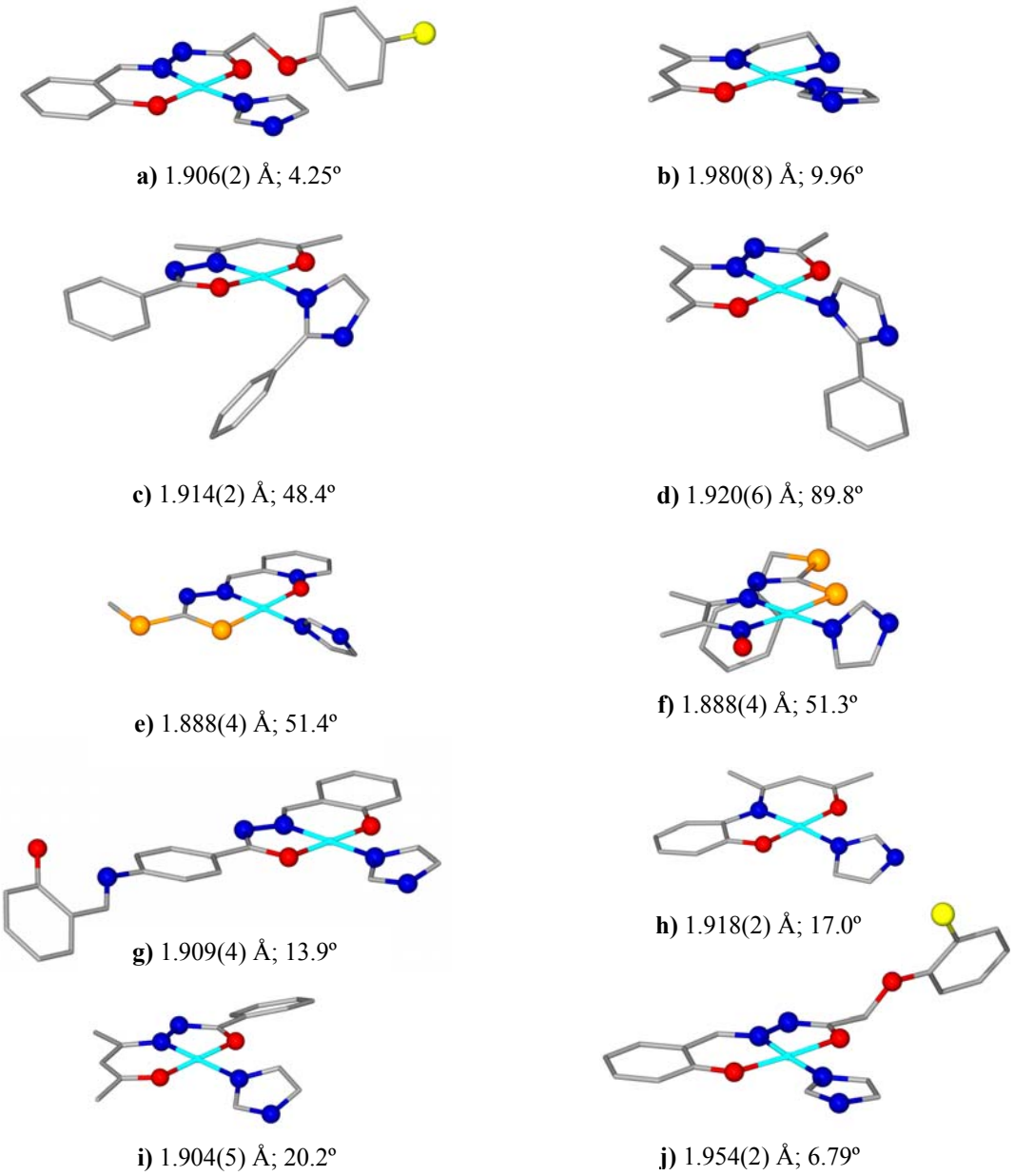

a) 1.906(2) Å; 4.25º

b) 1.980(8) Å; 9.96º

c) 1.914(2) Å; 48.4º

d) 1.920(6) Å; 89.8º

e) 1.888(4) Å; 51.4º

f) 1.888(4) Å; 51.3º

g) 1.909(4) Å; 13.9º

h) 1.918(2) Å; 17.0º

i) 1.904(5) Å; 20.2º

j) 1.954(2) Å; 6.79º

Figure IV-23. A selection of tridentate Schiff base ligand complexes of nickel with imidazoles in the fourth site. Ni-N_{imid} distances and dihedral plane defined as the angle between the best Ni square and imidazole plane given underneath each structure. **a)**: ref. 140; **b)** ref. 135; **c)** ref. 137; **d)** ref. 137; **e)** ref. 141; **f)** ref. 133; **g)** ref. 138; **h)** ref. 139; **i)** ref. 134; **j)** ref. 136. Bond distances and angles are reported as averages for complexes containing more than one molecule in the asymmetric unit.

16 contain anionic S donors *cis* to the imidazole, and have intermediate metal-plane/ligand plane dihedral angles of ca. 50° with, in addition to the intermolecular interactions involving H-bonding of the imidazole N-H to an adjacent complex, an intramolecular interaction that points the C2 of the imidazole in the direction of the S atom of the tridentate ligand.[133, 141]

Summary and Conclusion

Due to the asymmetry of the diazacycle frame in the complexes described above, an opportunity is presented to observe orientational preferences and dynamic rotational barriers that are influenced by the steric constraints of the ligand and the pocket into which flat ligands bind in square planar nickel complexes. While the imidazole ligand has the possibility of intramolecular donor/acceptor interactions, i.e., the C2 $CH^{\delta+}$ with the thiolate $S^{\delta-}$, that would result in a canting of the imidazole towards the negatively charged donor atom, this interaction is very weakly expressed in the structures in our series. Thus we see an orientation of the imidazole plane that is largely orthogonal to the N_2SNi plane in the monomeric complexes, determined principally by the optimization of minimal steric interactions while achieving maximum Ni-N_{imid} σ-bonding.

The structural and dynamic results of our study, using N_2S binding sites, coupled with analysis of literature structures of various square planar nickel imidazole complexes in largely hard donor environment may be correlated as follows:

1) In the Schiff base adducts consisting of N-, O-donor atoms the ground state imidazole binding orientation both reduced steric repulsion in the binding

pocket that flanks the imidazole and significant intramolecular electrostatic interactions between O and the imidazole C2 $CH^{\delta+}$ overwhelm the minimal steric restrictions resulting in coplanarity. In the case of the N_2SNi complexes in the current study, increased steric bulk on either the binding pocket (the secondary and tertiary amines in the N_2S pocket) or on the planar monodentate ligand lead to a nearly perpendicular orientation of the imidazole plane, as intramolecular donor/acceptor interactions that would encourage canting of the imidazole ring towards coplanarity are minimal.

2) While two isomers of the N_2SNi-N_{imid} complexes are seen at room and even higher temperatures for imidazoles with steric hindrance at the C2 site, dynamic interconversions of non-hindered analogues occur with activation barriers experimentally accessible by VT NMR studies. The barriers obtained experimentally and through DFT studies show a correlation between increasing activation barrier and increasing steric hindrance, indicating that the mobility of the monodentate ligands about the Ni-L bond is controlled by the ligand size (width and wedge angle) and the access to nickel as controlled by the ancillary donors.

3) The exchange of free and bound imidazole in complex **A**, occurs with a barrier of ~ 11 kcal/mol and ceases close to 0 ºC, further supporting that the exchange process observed for pure complex **A** at lower temperatures is a result of intramolecular dynamic processes.

4) DFT optimized transition state structures for the interconversion of isomers of $N_2SNi\text{-}N_{imid}$ find a lengthening of the $Ni\text{-}N_{imid}$ bond as rotation about the $Ni\text{-}N_{imid}$ bond pushes the imidazole into coplanarity with the nickel complex plane; distortion from strictly square planar further accommodates the increase in steric repulsion.

The orientation of His-imidazole in biological systems is influenced by many factors. This study has shown two such factors, steric bulk and internal electrostatic interactions, determine the ground state binding orientation and dynamic behavior of N-heterocyclic ligands bound to square planar N_2S nickel sites, such as is found in the nickel responsive transcription factor, NikR.[13-14] The binding of four Ni^{2+} ions, each held in a square planar N_3SNi coordination environment, within the metal binding domain causes conformational changes in the protein superstructure, which initiates the interaction of the protein with DNA.[13] Fundamental model studies such as this one contribute to a delineation of the possible factors that may influence these protein structural and dynamic changes.

CHAPTER V

TETRADENTATE N_2S_2 VANADYL(IV) COORDINATION COMPLEXES: SYNTHESIS, CHARACTERIZATION AND REACTIVITY STUDIES

Introduction

Brief History of Vanadium in Biology. Vanadium chemistry plays a fundamental role in biological systems and industrial applications. Biochemical processes of vanadium span from simple organisms to humans. Vanadium was first recognized as an essential element in living systems in the early 1900's when extraordinary quantities of vanadium were indentified in the blood cells of tunicates (ascidains or sea squirts).[150-151] To date, the functional role of the vanadium in these marine organisms is not well defined, and research in this area has primarily focused on the mechanism of the reduction of the V^{5+} ion from sea water, the oxidation state within the cells, and the transport/storage of vanadium ions.[152-154] In 1931, high concentrations of vanadium were discovered in mushrooms (toadstool), and this vanadium-containing natural product (amavadin) was finally isolated in 1972.[155-156] Although amavadin has been shown to serve as an electron-transfer mediator, the precise mode of action of vanadium in this system is also still unclear, and research is ongoing.[152-154]

The importance of vanadium in biochemistry continues to grow. In 1977, the vanadate ion was indentified as an efficient inhibitor of Na^+, K^+ ATP-ases, and in the 1980's vanadium was established as a biometal in two classes of enzymatic systems,

vanadium-dependent haloperoxidases and vanadium-dependent nitrogenases.[157-160] The discovery of vanadium-containing active sites sparked myriad model compounds and investigations into understanding the coordination chemistry and mode of action of vanadium in biological systems.[152-154]

In humans, vanadium is defined as an ultra trace element (uptake 10-60 μg/day).[161] A clear biochemical function for vanadium in humans has not been identified but the likelihood that it has an essential role is considerable. In fact, vanadium and its aggregates were shown to inhibit many phosphate metabolizing enzymes, even in low concentrations.[154] This inhibition effect is a result of similar structural characteristics between the vanadate, VO_4^{3-}, and the phosphate, PO_4^{3-}, ion which leads to analogous binding in biological environments.[152-154]

Beginning in the early 1980's, much effort has focused on developing and understanding the therapeutic affects of vanadium for treatment of diabetes. The insulin-enhancing properties of vanadium complexes were first discovered by the use of simple inorganic salts of vanadium, such as $[(V{=}O)SO_4]$.[154] Since then, many vanadium compounds in both V^{4+} and V^{5+} states have been synthesized, characterized, and screened for insulin-enhancing properties.[162-163] Numerous studies have established that the oral administration of certain vanadium compounds has positive affects on glucose homeostasis (Figure V-1). In particular, peroxovanadium(V) complexes and vanadium(IV) complexes containing variations of the maltolato ligand have demonstrated the highest insulin-enhancing activity. In fact, BEOV (bis(2-ethyl-3-hydroxy-4-pyronato)oxovanadium(IV)) recently entered phase IIa clinical trials.[164]

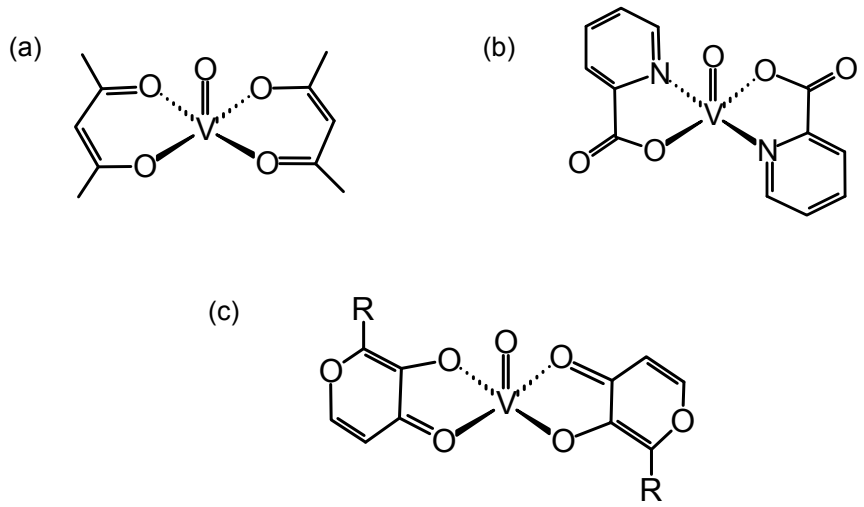

Figure V-1. Structures of vanadium complexes with insulin-enhancing properties.[162-163] (a) bis(acetylaceonato)oxovanadium(IV), $(V{=}O)(acac)_2$; (b) bis(picolinato)oxovanadium(IV), $VO(pic)_2$ or VPA; (c) **1**: bis(maltolato)-oxovanadium(IV), BMOV; **2**: bis(ethylmaltolato)-oxovandium(IV), BEOV.

Considering the complexity of the insulin signaling system, it is not surprising that the precise mode of action of vanadium containing complexes is not completely understood. In the insulin cascade, the binding of insulin to the insulin receptor stimulates tyrosine kinase activity. The resulting autophosphorylation initiates a variety of intracellular signaling pathways, which function in a synergistic manner to regulate glucose metabolism. Studies have demonstrated that the oxovanadium or vanadate insulin-enhancing activity results from the inhibition of phosphotyrosine phosphatase 1B, an enzyme responsible for specifically dephosphorylating the phosphorylated

tyrosine residue on the insulin receptor. It is also important to note that other receptors in the insulin cascade have been shown to be activated by vanadium compounds.[154]

The intact vanadium complex used for the treatment of diabetes is not considered to be the active species in these processes. Recent investigations of BEOV pharmocokinetics in rats established that the vanadyl complexes dissociate after administration, leaving the "free" vanadyl ion to be absorbed and transported by circulatory proteins in the blood.[165-166] Studies established that vanadyl ions bind to both serum albumin and transferrin, and transferrin is accepted as the principal vanadium chaperone.[167] The dissociation of the ligands from orally administered vanadium compounds opens up the possibility of "free" vanadyl ion binding to sites in various proteins and small peptides within the cell.

Vanadium-Sulfur Interactions in Biological Systems. The interaction of vanadium with cysteinyl groups in biological systems is well recognized.[154] For instance, V-S bonding is seen in the active site of vanadium-dependent nitrogenases, and it is known that vanadate inhibits certain phosphate-metabolizing enzymes through binding to cysteinyl residues.[154] Furthermore, the enzyme inhibition properties of vanadium *in vivo* has led to the investigation of oxovanadium(IV) complexes containing S-donor atoms as insulin-enhancing agents.[168] Finally, redox transformations of vanadate to vanadyl occur in the cell through the thiol functional group of glutathione, a tripeptide which can dimerize via oxidative disulfide formation.[167] In fact, several reports suggest complex formation between glutathione and oxovanadium(IV) ions.[169-170] Studies of oxovanadium(IV)-glutathione model compounds demonstrated that two glutathione

coordination modes are observed at different pH ranges, one of which proposes V-$S_{thiolate}$ binding (Figure V-2).[170]

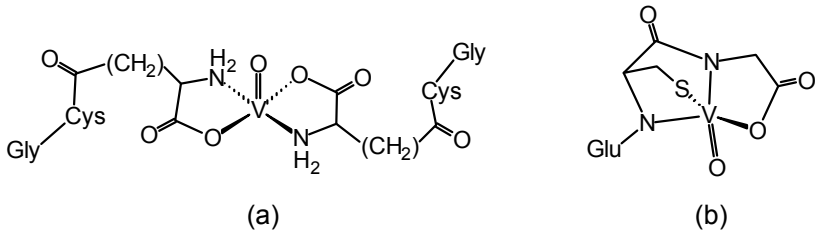

Figure V-2. Proposed structures of $V^{IV}O^{2+}$ bound to glutathione at pH = 5-7 (a) and pH = 7-10 (b).[170]

$N_2S_2(V^{IV}=O)$ Coordination Complexes. In order to understand the coordination chemistry of vanadium in biological systems, simple ligands are commonly used to mimic possible binding sites in biomolecules. The occurrence of thiolates and their interactions with vanadium in nature has encouraged the synthesis and investigation of a manifold of thiolate-bound vanadium coordination complexes in combination with various N,O chelates. In particular, several examples of mononuclear square pyramidal $N_2S_2(V^{IV}=O)$ complexes involving bidentate or tetradentate ligand sets have been examined and only four have been structurally characterized by X-ray diffraction studies. These structurally characterized ($V^{IV}=O$) complexes featuring N_2S_2 coordination spheres include bidentate ligands in *trans* conformations, and tetradentate N_2S_2 ligand sets (Figure V-3).[171-174] These complexes reveal the versatility of the vanadyl ion to accommodate both hard and soft donor atoms, and that such ligand fields can result in stable ($V^{IV}=O$) complexes.

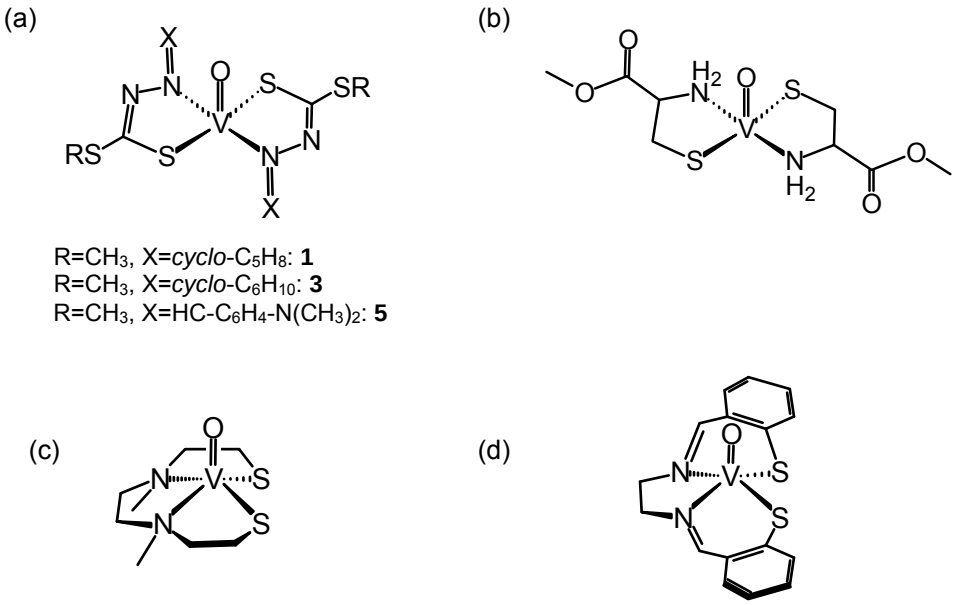

Figure V-3. Examples of mononuclear square pyramidal $V^{IV}O$ complexes containing thiolate ligation. (a) **1**, VO[*cyclo*-C_5H_8=N-NC(-S-)$(SCH_3)]_2$; **3**, VO[*cyclo*-C_6H_{10}=N-NC(-S-)$(SCH_3)]_2$;[172] **5**, VO[4-$(CH_3)_2$N-C_6H_4CH=N-NC(-S-)$(SCH_3)]_2$ (b) vanadyl(IV)-cysteine methyl ester;[171] (c) [$VO(C_8H_{18}N_2S_2)$];[173] (d) $V^{IV}O$(tsalen).[174]

(V^{IV}=O)-amide Coordination Complexes. Chelation through the carboxyamido nitrogen of the peptide backbone, although not a common coordination mode, is observed in certain proteins and enzymes, such as serum albumin, nitrile hydratase, and acetyl coA synthase.[25, 175-177] Vanadium-catalyzed photocleavage has been utilized as a probe to characterize complex protein systems, and there are several examples that suggest the involvement of amide ligands in the photoinduced peptide cleavage process of phosphate binding proteins.[178] A recent survey of the Cambridge data base finds seven square pyramidal (V^{IV}=O) complexes featuring N-amidate binding

(Figure V-4).[179-182] Much work in this area has employed pseudo-peptide complexes utilizing Schiff base adducts or aryl-rich tetradentate ligands to examine the potential for vanadium coordination to deprotonated amide ligands in largely N,O chelate systems. There is only one report of a thiolate donor within the binding pocket.

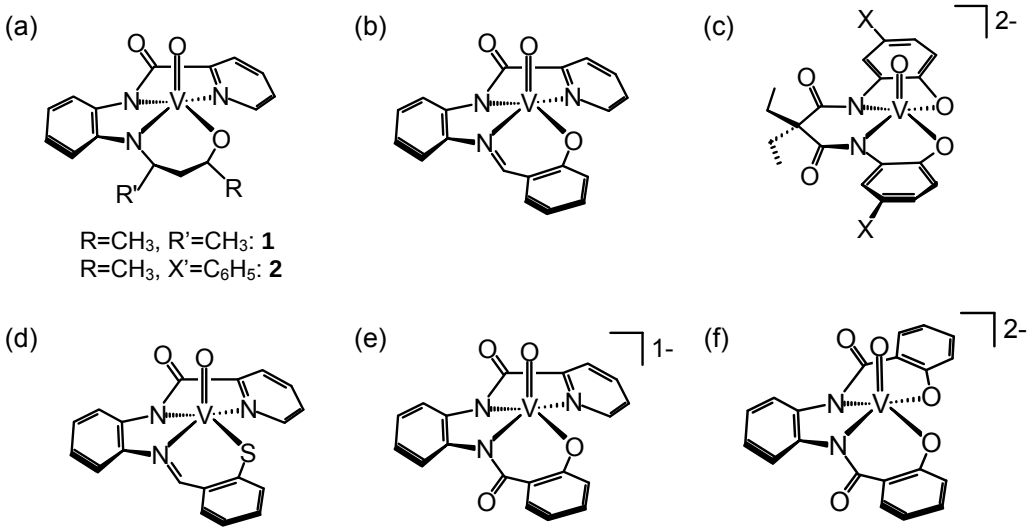

Figure V-4. Examples of mononuclear square pyramidal $V^{IV}O$ complexes containing amide ligation. (a) **1**, [VO(pycac)], **2**, [VO(pycbac)];[179] (b) $V^{IV}O$(PAIS);[180] (c) $\{K_2[VO(depa\text{-}H)]\}\cdot 1.5CH_3CN\cdot H_2O$;[181] (d) $[V^{IV}O(thipca)]$;[182] (e) $Na[V^{IV}O(hypyb)]\cdot 2CH_3CN$;[182] (f) $Na_2[V^{IV}O(hybeb)]\cdot 2CH_3OH$;[182]. Note for (e) the Na ions bind to the carboxyamido oxygen and phenolate oxygen atom, and in (f) the Na ion binds to the carboxyamido oxygen atoms.

Notably, each of these examples involves amide bond(s) extended from aromatic backbones. The incorporation of the amide donor(s) provides a strong σ donating ligand environment resulting in stabilized $V^{IV}=O^{2+}$ complexes. The effect of the amide donor on the ligand field has been noted to lower EPR A_x and A_y parameters relative to amine

donors, and to significantly shift the VO stretching frequency, which ranges from 980-991 cm^{-1} for one coordinated amide and 942-955 cm^{-1} for two ligated amides.[179-182]

Our group has studied a series of metals bound within a dianionic N_2S_2 ligand set utilizing the dach and daco diazacycle frameworks functionalized with ethylene thiolate linkers.[183-185] Furthermore, we recently investigated Cu(II) binding to Holm's tetraanionic N_2S_2 ligand (referred to earlier as ema^{4-}), which contains two aliphatic amide bonds.[82] These studies have now been extended to include vanadyl ions. The work herein examines the structural and electronic changes from the incorporation of $V{=}O^{2+}$ in such dianionic and tetraanionic N_2S_2 binding pockets (Chart V-1). In addition, the vanadyl interaction with the CGC peptide, the biological analogue of the tetraanionic N_2S_2 ligand, has been explored (Chart V-1). As these types of chelating environments are found in nature, the study of $V{=}O^{2+}$ coordination and reactivity of such sites are of much interest.

Experimental Details

Materials. The starting material N,N'-bis(2-mercaptoethyl)-1,5-diazacyclooctane, (H_2-bmedaco),[186] N,N'-bis(2-mercaptoethyl)-1,5-diazacycloheptane, (H_2-bmedach),[187] *N,N'*-ethylenebis(2-mercaptoacetamide), (ema),[82] and *cis*-$[(piperdine)_2W(CO)_4]$[188] were prepared according to literature procedures. Fmoc protected peptides and TentaGel S-RAM® beads were purchased from Advanced Chem Tech. The synthesis of CGC was followed using standard solid-phase peptide techniques.

Chart V-1

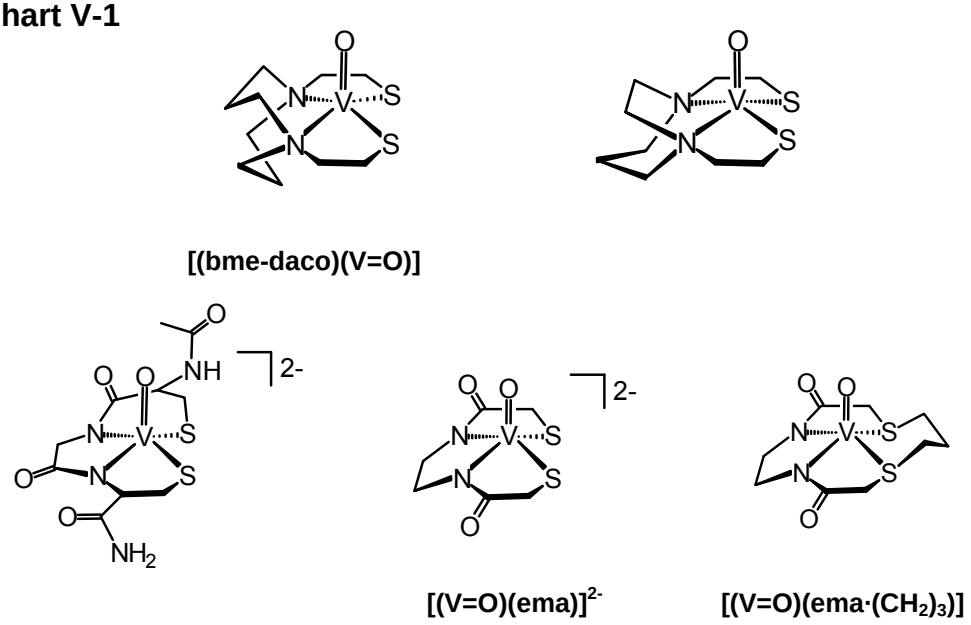

N,N'-bis(2-mercaptoethyl)-1,5-diazacyclooctane oxovanadium(IV), [(bme-daco)(V=O)], Complex 1. As previously prepared by a former group member, Michelle Hatley, the H_2-bmedaco ligand (0.842 g, 3.6 mmol) was dissolved in MeOH (30 mL), and a solution of $(V{=}O)(acac)_2$ (0.868 g, 3.3 mmol) in MeOH (50 mL) was added dropwise.[189] The colorless solution immediately turned green, and upon stirring overnight a green precipitate formed. The mixture was filtered in air, the solid was washed with 30 mL portions of Et_2O, and allowed to dry in air. An analytically pure sample was obtained by recrystallization from warm CH_2Cl_2 to obtain 0.247 mg (25%) of product. Diffusion of Et_2O into a saturated solution of the complex in CH_2Cl_2 produced X-ray quality green needle-like crystals. Elemental anal. for $C_{10}H_{20}N_2S_2VO$

(MW = 299 g/mol) Calcd (found): C, 40.12 (40.12); N, 9.36 (9.25); H, 6.73 (6.55). ATR-FTIR: υ(V=O), 979 cm^{-1}. $^{+}$ESI-MS (CH_2Cl_2): *m/z* = 300 $[(bme\text{-}daco)VO]^{+}$.

N,N'-bis(2-mercaptoethyl)-1,5-diazacycloheptane oxovanadium(IV), [(bme-dach)(V=O)], Complex 2. To a light yellow solution of the H_2-bmedach ligand (0.785 g, 3.56 mmol) in MeOH (20 mL), a solution of $(V{=}O)(acac)_2$ (0.951 g, 3.59 mmol) in MeOH (50 mL) was added dropwise. The solution turned green and a light purple solid precipitated. The reaction was stirred at room temperature for 20 h, the green filtrate was separated from the purple solid. The purple solid was washed with MeOH (3 x 30 mL), then with Et_2O (3 x 30 mL), and dried in air to afford a light purple solid (0.752 g, 74% yield). X-ray quality crystals were obtained from the slow evaporation of the green filtrate under anaerobic conditions. The purple crystalline material was collected yielding 0.031 g (3%) giving total yield of 0.783 g (77%). $C_9H_{18}N_2S_2VO$ Elemental anal. for $C_9H_{18}N_2S_2VO$ (MW = 285 g/mol) Calcd (found): C, 37.89 (37.91); N, 9.82 (9.72); H, 6.36 (6.41). ATR-FTIR: υ(V=O), 976 cm^{-1}. $^{+}$ESI-MS (CH_2Cl_2): *m/z* = 286 $[(bme\text{-}dach)(V{=}O)]^{+}$.

Tetraethylammonium [N,N'-ethylenebis(2-mercaptoacetamide) oxovanadium(IV)], $[Et_4N]_2[(V{=}O)(ema)]$, Complex 3. Under anaerobic conditions, the N,N'-ethylenebis(2-mercaptoacetamide) ligand (0.100 g, 0.344 mmol), KOH (0.079 g, 1.41 mmol) and Et_4NCl (0.114 g, 0.688 mmol) were mixed in MeOH (20 mL) for 30 min resulting in a light yellow solution. A suspension of $(V{=}O)(SO)_4$ (0.051 g, 0.313 mmol) in MeOH (30 mL) was added to the ligand mixture using a plastic cannula. The reaction mixture was heated to 60-65 ºC for 20 hrs yielding a teal blue solution

containing a white precipitate (K_2SO_4). The solution was cooled to RT, filtered over celite, and the solvent was removed in vacuo. MeCN (25 mL) was added to extract the product as a blue solution. The solution was filtered over celite and the solvent reduced to minimum. X-ray quality crystals were obtained by vapor diffusion of Et_2O into the MeCN solution. The blue-purple crystalline material was collected yielding 0.057 g (34%). Compound is extremely hygroscopic. Elemental anal. for $C_{22}H_{48}N_4S_2VO_3 \cdot 2.5\ H_2O$ (MW = 577 g/mol) Calcd (found): C, 37.89 (37.91); N, 9.82 (9.72); H, 6.36 (6.41). ATR-FTIR: υ(V=O), 941 cm^{-1}. $^-$ESI-MS (MeCN): *m/z* = 401 $(Et_4N)[(V=O)(ema)]^-$.

Potassium [(Cysteinyl-glycyl-cysteinecarboxamide) oxovandium (IV)], K_2[(V=O)(CGC)], Complex 4. Method A: The H_4CGC ligand (0.032 g, 0.099 mmol) and KOH (0.011 g, 0.196 mmol) were mixed in DMF (10 mL) and stirred for 30 minutes. A light green solution of $(V=O)(acac)_2$ (0.024 g, 0.091 mmol) in DMF (15 mL) was added dropwise. The reaction was stirred for 16 hrs and a light blue-green solid was obtained after precipitation with Et_2O, yielding 28.1 mg (67 % yield). ATR-FTIR: υ(V=O), 945 cm^{-1}.

[(V=O)(ema·$(CH_2)_3$)], Complex 5. To a blue solution of $[Et_4N]_2$[(V=O)(ema)] (0.031 g, 0.058 mmol) in MeCN (10 mL) was added neat 1,3-dibromopropane (4 µL, 0.039 mmol) resulting in a grey-blue solution with the formation of a white precipitate. After stirring for 30 min, the resulting solution was filtered over celite, the solvent was reduced and layered with Et_2O. Reddish-blue crystals were isolated. ATR-FTIR: υ(V=O), 986 cm^{-1}.

Tetraethylammonium [N,N'-ethylenebis-(2-mercaptoacetamide)-oxovanadium (IV) tungsten tetracarbonyl], $[Et_4N]_2[(V=O)(ema)W(CO)_4]$, Complex 6. A solution of $(pip)_2W(CO)_4$ (0.018 g, 0.039 mmol) in DMF (10 mL) was heated to 40 °C for 10 min under a N_2 atmosphere. To this was added dropwise a blue solution of **3** (0.020 g, 0.038 mmol) in DMF (10 mL). The solution was heated at 40 °C for an additional 20 min producing an amber color. The solution was stirred for 30 min at room temperature. IR in υ(CO) region of the reaction mixture (DMF, cm^{-1}): υ(CO) 1996(w), 1919(w), 1872(s), 1849(m), 1802(m).

Potassium [(CGC)oxovanadium(IV) tungsten tetracarbonyl], $[K]_2[(V=O)(CGC)W(CO)_4]$, Complex 7. In a similar manner for **6**, a light green DMF solution of $K_2[(V=O)(CGC)]$ (0.022 g, 0.047 mmol) was added slowly to a DMF solution of warm $(pip)_2W(CO)_4$ (0.022 g, 0.047 mmol). IR in υ(CO) region of the reaction mixture (DMF, cm-1): υ(CO) 1995(w), 1916(w), 1866(s), 1849(m), 1805(m).

Synthesis and Structural Characterization

Syntheses of neutral [(bme-daco)(V=O)] and [(bme-dach)(V=O)], Complexes 1 and 2. As was earlier performed by a former group member, Michelle Hatley, for the neutral [(bme-daco)(V=O)], the neutral [(bme-dach)(V=O)] was also prepared by ligand displacement on reaction of $(V=O)(acac)_2$ with the H_2-bmedaco or H_2-bmedach ligand in methanol solutions at room temperature (Scheme V-1).[189] The resulting green precipitate (complex **1**) and purple precipitate (complex **2**) were isolated and purified to

Scheme V-1

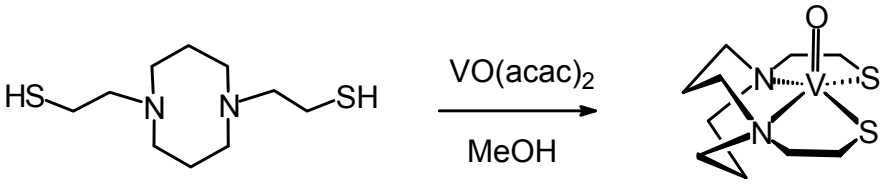

Scheme V-2

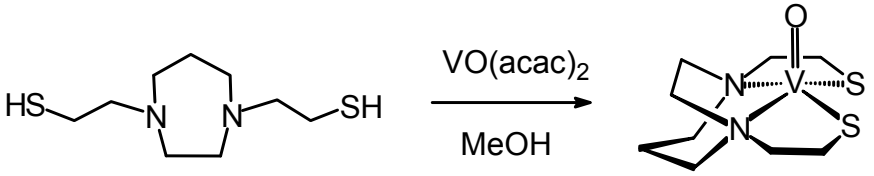

give 25% and 77% yield for **1** and **2**, respectively. These neutral N_2S_2 V^{IV}=O complexes are resistant to aerobic oxidation in the solid state but, slowly (days) decompose in solution, presumably to yield V^{v} species. The neutral complexes are soluble in DMF, H_2O, CH_2Cl_2, and slightly soluble in warm MeOH, where complex **2** was of lower solubility than **1**.

Syntheses of dianionic $(Et_4N)_2$[(V=O)(ema)], Complex 3. The preparation of the dianionic vanadyl complex was accomplished by the addition of $(V{=}O)SO_4$ to the deprotonated form of the ligand in methanol solutions while heating (60 ºC) as outlined in Scheme V-2. The tetraanionic ema ligand was chosen to increase the solubility of the vanadyl-bound complex, and was expected to stabilize the highly oxidized metal center.

Scheme V-2

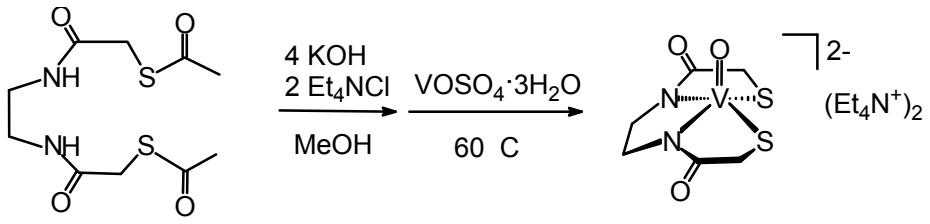

In addition, the N_2S_2 binding pocket of the ema ligand is good synthetic mimic of the CysGlyCys tripeptide motif (vide infra).[190] Raymond and coworkers found that dianionic $N_2O_2(V{=}O)^{2-}$ complexes containing deprotonated amide donors were stable in air in the solid state and in solution.[181] In contrast, the amide-containing dianionic $N_2S_2(V{=}O)^{2-}$, complex **3**, is highly susceptible to oxidation in air in the solid state form and in solution. The exposure of MeCN solutions of complex **3** to air results in a color change from blue to red. X-ray quality crystals obtained by the slow diffusion of Et_2O into a red MeCN solution revealed the commonly observed solution oxidation product, the decavanadate ion $V_{10}O_{28}^{6-}$.[154] Complex **3** is soluble in a wide range of solvents (H_2O, MeOH, MeCN, and CH_2Cl_2).

Synthesis of $K_2[(V{=}O)(CGC)]$, Complex 4. The CysGlyCys (CGC) tripeptide has been complexed with Ni(II) and Cu(II) as metalloenzyme binding site mimics and shown to bind through deprotonated carboxyamido nitrogens and thiolates, producing a tetradentate N_2S_2 coordination environment.[87,183,190] Similar to the $Ni(CGC)^{2-}$ complex, the CysGlyCys peptide derivative of vanadyl was prepared from the displacement of acacH from $(V^{IV}{=}O)(acac)_2$ by the presence of two equivalents of KOH in DMF

solvent. A second method used to prepare by **4** was accomplished by the addition of $(V{=}O)SO_4$ to the deprotonated form of the ligand. Both syntheses yielded a light green solid in ca. 70% yield. Comparable to its synthetic analogue, complex **4** is extremely oxygen sensitive in both the solid and solution state; the light green color changes to red in the presence of oxygen. The dianionic vanadyl peptide complex is soluble in DMF and H_2O. The N_2S_2 coordination environment proposed for the CGC ligand bound to the vanadyl(IV) moiety is based on the comparison of its spectroscopic characterization and reactivity to the synthetic analogue complex **3**.

Description of Molecular Structures of Complexes 1, 2 and 3. Complexes **1**–**3** were characterized by X-ray diffraction analysis and their molecular structures are presented in Figures V-5 and V-6 as thermal ellipsoid plots and salient metric parameters are shown in Table V-1. Full structural reports are given in the Appendix. The crystals of complex **3** exhibit pleochroism (blue/purple). In all complexes, the expected square pyramidal coordination geometry is observed with the N_2S_2 donor set arranged around the basal plane with the vanadyl oxygen at the apex. The vanadium atom is displaced from the basal plane toward the apical oxygen by 0.6525 (**1**), 0.6521 (**2**), and 0.7125 Å (**3**). The N_2S_2 planes are quite regular with average deviation for **1** of 0.0341 Å (maximum and minimum deviation of 0.0365 Å by N2 and 0.0318 Å by S1), for **2** of 0.0481 Å (maximum and minimum deviation of 0.0561 Å by N2 and 0.0402 Å by S1), and for **3** of 0.0674 Å (maximum and minimum deviation of 0.0775 Å by N2 and 0.0572 Å by S1). The V-O bond distances are 1.600(3), 1.605(3), and 1.623(19) Å for complexes **1**, **2**, and **3**, respectively. A distance ranging between 1.56-1.60 is commonly

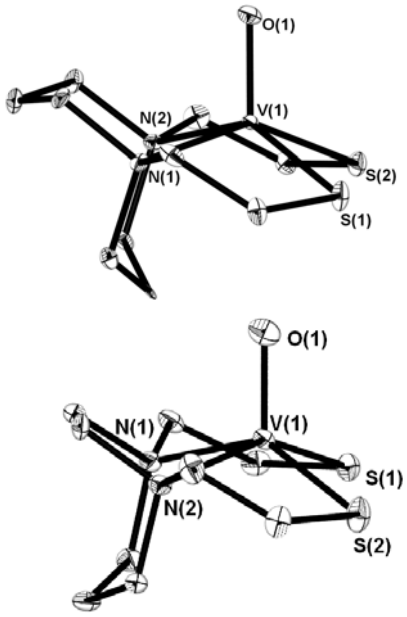

Figure V-5. Molecular structures of the neutral V^{IV}=O complexes [(bme-daco)(V=O)], **1**, (top), and [(bme-dach)(V=O)], **2**, (bottom) shown as thermal ellipsoids at 50% probability.

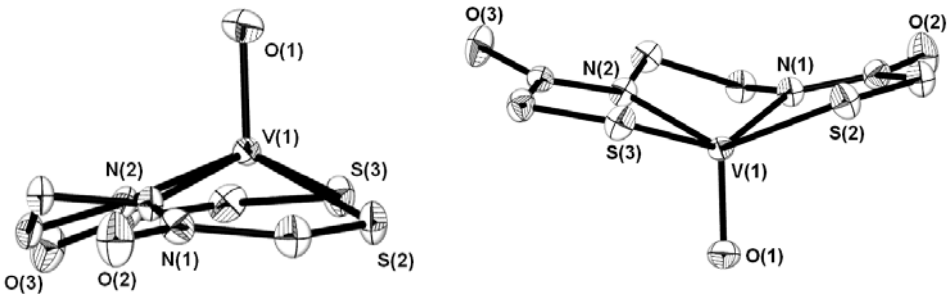

Figure V-6. Molecular structure of the dianionic V^{IV}=O complex $[Et_4N]_2[(V=O)(ema)]$, **3**, shown as thermal ellipsoids at 50% probability in different views. Left: side on as presented for [(bme-daco)(V=O)], **1,** and [(bme-dach)(V=O)], **2**. Right: bisecting the <S-V-S and <N-V-N angles. The EtN_4^+ counter ions are not shown. The asymmetric unit contains one H_2O of crystallization.

Table V-1. Metric data for [(bme-daco)(V=O)], **1**, [(bme-dach)(V=O)], **2**, and $[Et_4N]_2[(V=O)(ema)]$, **3**, (distance, Å; angle, deg).

	1	**2**	**3**
V(1)-O(1)	1.600(3)	1.605(3)	1.623(19)
V(1)-N(1)	2.154(3)	2.122(3)	2.028(2)
V(1)-N(2)	2.159(3)	2.111(3)	2.028(2)
V(1)-S(1)	2.362(17)	2.341(12)	2.369(17)
V(1)-S(2)	2.348(13)	2.346(12)	2.363(15)
N(1)-V(1)-N(2)	84.14(12)	74.35(11)	78.41(10)
S(1)-V(1)-S(1)	88.82(5)	98.20(5)	93.91(6)
N(1)-V(1)-S(1)	84.23(10)	84.50(8)	82.33(8)
N(2)-V(1)-S(2)	83.62(10)	83.34(9)	81.27(8)
N(1)-V(1)-S(2)	144.33(9)	141.09(9)	137.28(7)
N(2)-V(1)-S(1)	148.14(9)	146.39(9)	145.04(7)

reported for the VO distance of vanadyl complexes in square pyramidal geometry; however, longer bond distances (>1.60) have been observed in vanadyl complexes bound in tetra anionic ligand sets. In this series, the longer bond distance observed in complex **3** correlates with the IR data (vide infra).

The V-S distances are comparable to reported square pyramidal vanadyl(IV) complexes and likewise, the $V\text{-}N_{amine}$ and $V\text{-}N_{amide}$ distances are within the normal range of V-N distances. The N-V-N angle in complex **2** is pinched slightly more than that observed for the N_2S_2Ni analogue and this observed constraint is compensated by an increase in the S-V-S angle. Similarly, a restriction in the N-V-N angle resulting in an opening in the S-V-S angle is observed in complex **3**. A molecule of water in the asymmetric unit links two adjacent complexes through hydrogen bonding interactions to the carboxamide oxygens producing a dimer through a closed loop. To our knowledge,

complex **3** represents the first example of square pyramidal vanadyl(IV) complex bound to *cis*-dithiolates and aliphatic diamidates in the basal plane.

In complexes **1**, **2** and **3** the N to S ethylene linkers are eclipsed across the N_2S_2 plane. In **1**, the vanadium diazacyclohexane rings are in chair and boat configurations with the boat opposite to the oxygen side of the vanadyl. In **2**, the single vanadium diazacyclohexane ring is in the chair conformation and opposite to the oxygen side. In this case, the vanadium diazacyclopentane ring is oriented toward the oxo side of the vanadyl.

Infrared Analysis

Complexes **1** and **2** characteristically display a υ(V=O) band in the IR spectrum at ca. 978 cm^{-1}, which is within the range reported for oxovanadium complexes (935-1035 cm^{-1}).[168, 191-195] The most characteristic difference between the IR spectrum of neutral and dianionic vanadyl N_2S_2 complexes is that the vanadyl stretch in the latter is at a lower frequency, ca. 942 cm^{-1}. This significantly lower VO stretching frequency is consistent with the longer V=O bond distance as compared to the neutral N_2S_2(V=O) complexes. Although the lengthening of the V-O bond distance seems to correlate with an increase of sigma donation from the electron rich basal plane ligands, it has been noted by Christou, et al. that a direct relationship between the ligand field in the basal plane and the V-O bond distance cannot be made.[193] In fact, Christou et al. points out that dianionic complexes with electron-rich equatorial planes have similar V-O bond

distances to their neutral ligand sets (<1.6 Å), suggesting the V-O bond distance is influenced by other factors.

Electron Paramagnetic Resonance (EPR) Spectroscopy

Vanadyl complexes are well suited for EPR spectral detection because of the V^{IV}=O d^1 ground state configuration. This spectroscopic tool can provide information on the number and orientations of ligands bound to the vanadyl center. For square pyramidal vanadyl complexes, the unpaired electron is found mainly in a d_{xy} orbital, and complexes of this type exhibit spin Hamiltonian values with $g_z < g_{x,y}$ and $A_z > A_{x,y}$. The most abundant naturally occurring isotope of vanadium is ^{51}V (> 99%), which has a unique nuclear spin, I, of 7/2. The interaction of the unpaired electron with the nuclear spin of vanadium results in a signature eight line hyperfine splitting pattern (2I+1 = 8 lines).

The frozen solution X-band EPR spectra of the neutral N_2S_2(V=O) derivatives, complexes **1** and **2**, were recorded in DMF at 10 K (Figure V-7). The spectra show the distinctive eight line pattern expected for a d^1 V(IV) system. The EPR parameters for the oxovanadium N_2S_2 complexes were determined by computer simulation of the experimental spectra (Table V-2). For comparison, Table V-2 includes EPR parameters reported for complexes with related donor sets.[174, 179-180, 168, 194-195] Overall the g and A values are similar to other square pyramidal V^{IV}=O^{2+} complexes. Complexes **1** and **2** display larger g_x, g_y, and A_z values as compared to other N_2S_2 chromophores containing N-imine donors. The spin Hamiltonian parameters of **1** and **2** better match the values

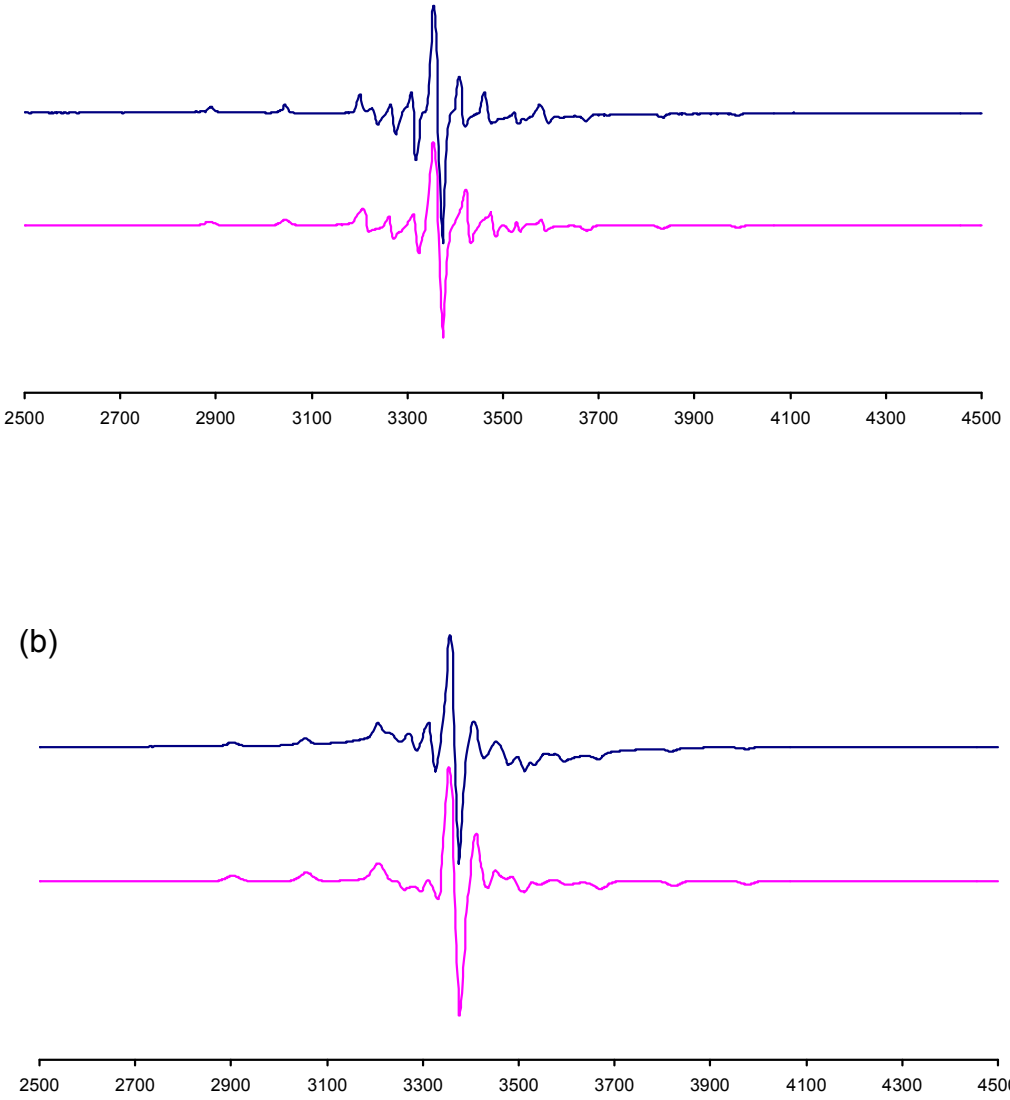

Figure V-7. Frozen solution EPR spectra of neutral $N_2S_2(V^{IV}=O)$ complexes in DMF: (a) [(bme-daco)(V=O)], **1**; (b) [(bme-dach)(V=O)], **2**. Top: experimental spectrum. Bottom: computer simulated spectrum.

Table V-2. EPR parameters for oxovanadium(IV) complexes.[a]

Complex	Donor set	g_Z	g_x	g_y	A_z	A_x	A_y
[(bme-daco)(V=O)], **1**	N_2S_2	1.968	1.991	1.9945	157.40	52.60	42.95
[(bme-dach)(V=O)], **2**	N_2S_2	1.967	1.9915	1.995	153.27	53.67	38
$(Et_4N)_2$[(V=O)(ema)], **3**	N_2S_2	1.970	2.001	2.001	153.27	60	33
$(K)_2$[(V=O)(CGC)], **4**	N_2S_2	1.9695	1.999	1.999	156.41	51.60	42
[(V=O)(ema)·$(CH_2)_3$], **5**[b]	N_2S_2	1.977	2.000	2.000	153.12	49	33
VO(tsalen)[c]	N_2S_2	1.978	1.986	1.986	148	51	51
[VO(tsatln)][c]	N_2S_2	1.966	1.975	1.975	140	37	37
[VO(tsalphen)][c]	N_2S_2	1.967	1.987	1.987	145	51	51
$[VO(mp)_2]^{2-}$[d,e]	O_2S_2	1.975	2.007	1.999	150	40	40
$[VO(mmppt)]_2$[f,g]	O_2S_2	1.958	1.985	1.981	151	42	52
[VO(salen)][h]	N_2O_2	1.955	1.986	1.989	166	56	55
[VO(pycac)][i,j]	N_3O	1.9558	1.9777	1.9811	151.43	53.29	42.46
VO(PAIS)[k,l]	N_3O	1.961	1.986	1.982	154	45	54

[a]In frozen DMF. [b]In frozen MeCN. [c]Reference 174. [d]Measured in frozen CH_2Cl_2/DMF. [e]Reference 194. [f]Measured in frozen CH_2Cl_2/DMF. [g]Reference 168. [h]Reference 195. [i]Reference 179. [j]Measured in chloroform at 120 K. [k]Measured in frozen DMF/EtOH. [l]Reference 180.

reported for O_2S_2 vanadyl complexes. In MeCN, the dianionic $(Et_4N)_2$[(V=O)(ema)], complex **3**, displays the eight line EPR spectra but the signals are very broad (Figure V-8). Identical results are obtained from frozen DMF solutions. The ligand set in complex **3** has a greater ability to delocalize electron density away from the vanadyl center, which may explain the broadened lines in the EPR spectrum. The g-values are quite similar to the neutral N_2S_2 derivative, while the A_x value is slightly larger and the A_y is smaller.

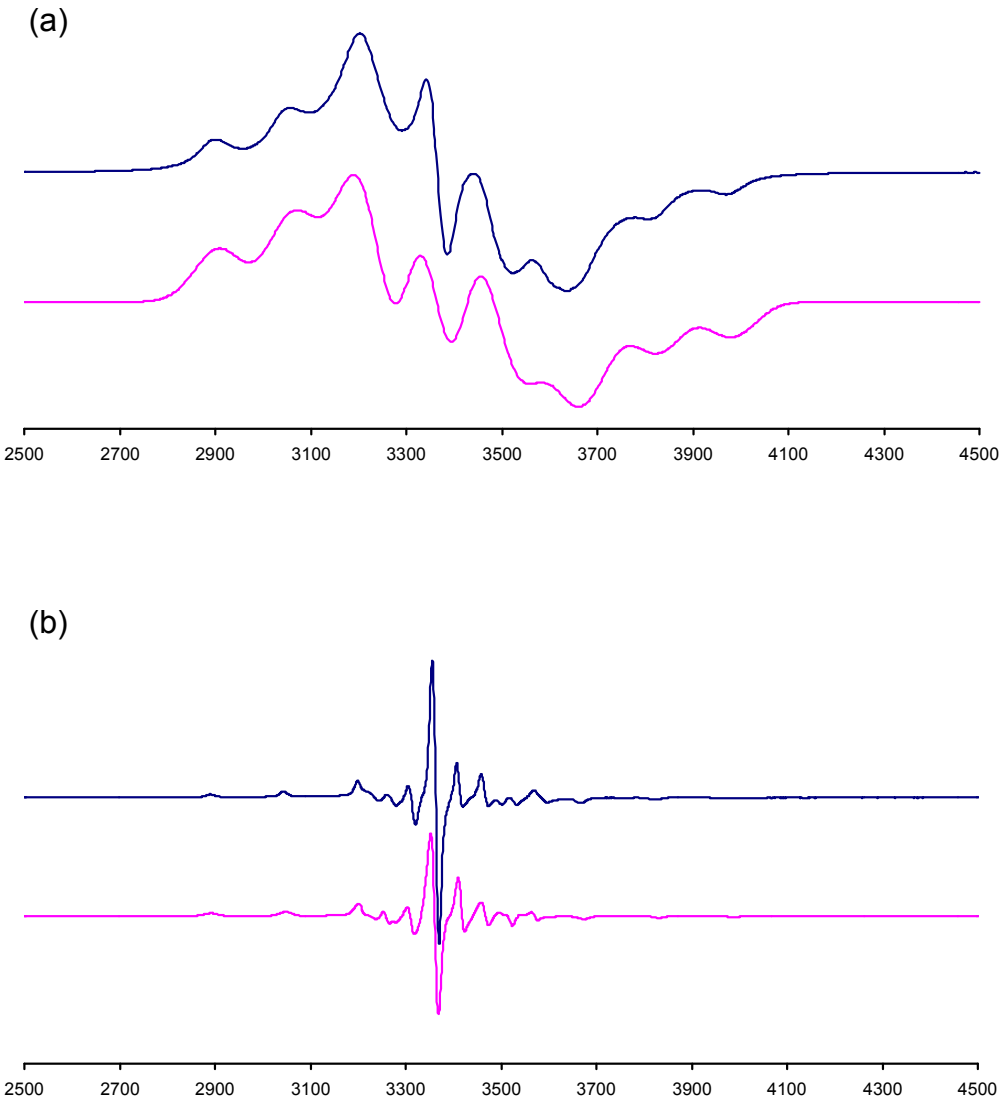
(a)
2500
2700
2900
3100
3300
3500
3700
3900
4100
4300
4500
(b)
2500
2700
2900
3100
3300
3500
3700
3900
4100
4300
4500

The EPR spectra of $(K)_2[(V=O)(CGC)]$, complex **5**, in DMF shows the typical hyperfine splitting and anisotropic line shapes for a $V^{IV}=O^{2+}$ center (Figure V-8). Slight differences in the EPR spectral parameters are observed between **5** and its analogue, complex **4**. The largest difference is seen in the smaller A_x value and larger A_y value in **5** as compared to **4**. In both complexes containing amide donors, the g-values are slightly larger than the complexes with amine donors. From a comparison of the EPR parameters of complex **5** to others in Table V-2, it is clear that **5** contains a $V=O^{2+}$ held in a N_2S_2 coordination sphere.

Overall, the tetradentate square pyramidal $V^{IV}=O$ complexes presented herein fit into the trends observed for square pyramidal oxovanadium(IV) complexes. These general trends show higher g-values and lower A values for basal plane S-donors as compared to their O,N analogues, and higher g-values for dianionic complexes as compared to their neutral counterparts. The most notable difference between the present complexes and others of similar coordination environment is the larger A_z, g_x and g_y parameters.

Reactivity of (V=O)-bound Thiolates

The reactivity of nickel-bound thiolates in neutral and dianionic N_2S_2 complexes has been extensively explored. In fact, reactivity studies of numbers of metal N_2S_2 complexes with M = Ni, Zn, Cu, and Fe have established that the sulfurs are readily alkylated, metallated, or oxygenated.[131, 183-185] The incorporation of the vanadyl ion in

the N_2S_2 donor environment permits the examination of how the electron withdrawing vanadyl unit affects the nucleophilicity of the thiolate donors.

Scheme V-4

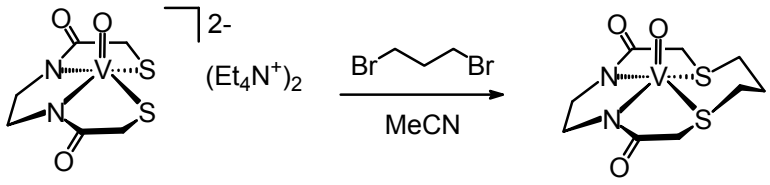

Reactivity with 1,3-dibromopropane. Reaction of neutral $N_2S_2(V{=}O)$ complexes **1** and **2** with 1,3-dibromopropane did not lead to S-alkylated products, even under reflux conditions. However, according to Scheme 4, the addition of neat 1,3-dibromopropane to a blue MeCN solution of complex **3**, $VO(ema)^{2-}$, results in the formation of a white precipitate and a grayish blue solution within 15 minutes. Neutral complex **5**, $[(V{=}O)(ema){\cdot}(CH_2)_3]$, was isolated as X-ray quality crystals following filtration and slow diffusion of Et_2O into a MeCN solution. The $\upsilon(V{=}O)$ frequency in the ATR-FTIR spectrum displays a band at 986 cm^{-1}, which is shifted positively by 41 cm^{-1} compared to the dianionic vanadyl precursor, complex **3**. This shift is consistent with a decrease of electron density in the basal plane. The EPR spectrum of $[(V{=}O)((ema){\cdot}(CH_2)_3)]$ in frozen MeCN shows that the complex contains a paramagnetic $V^{IV}{=}O$ species (Figure V-9). The spectrum differs from the precursor, complex **3**, in that

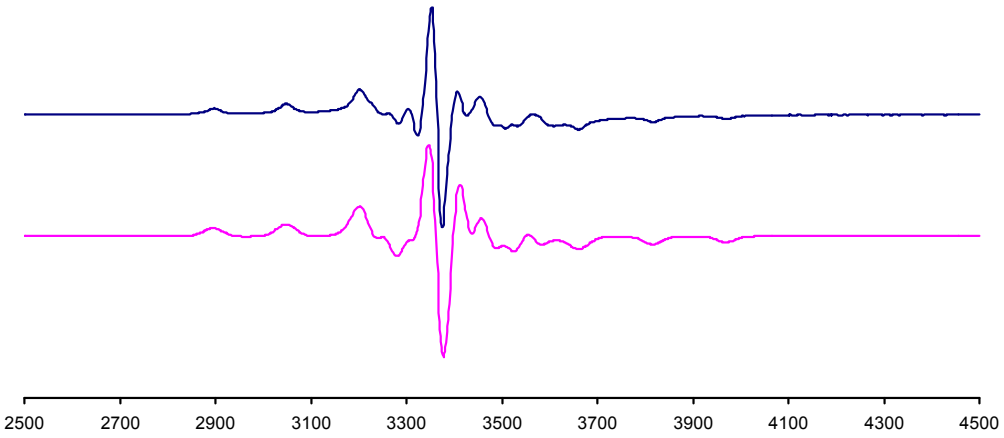

Figure V-9. Frozen solution EPR spectra of neutral complex [(V=O)((ema)·$(CH_2)_3$)], **5**, in MeCN. Top: experimental spectrum. Bottom: computer simulated spectrum.

distinctive sharp hyperfine lines are observed, the g_z value increases, and the A_x parameter decreases. The most significant difference in the EPR parameters of complex **5** as compared to the other complexes in this series is that complex **5** has a larger g_z value.

Reactivity with *cis*-[(piperdine)$_2$W(CO)$_4$]. The tungsten tetracarbonyl derivatives of N_2S_2M (M = Ni or Zn, as $ZnCl^+$) complexes have been used to establish the electron donating ability of the N_2S_2M unit as reported by the CO stretching frequencies.[184-185, 190, 196-198] We carried out analogous studies with the N_2S_2(V=O) derivatives to determine if the S-thiolates were reactive towards $W(CO)_4$ and to gain information regarding their electronic character. While the neutral N_2S_2(V=O)

complexes **1** and **2** showed no tendency to form adducts when exposed to the typical precursor to $W(CO)_4$ derivatives, the dianionic complexes **3** and **4** behaved similarly to the N_2S_2Ni analogues. The preparation of dianionic vanadyl-W derivatives was accomplished via displacement of the labile piperdine ligands from the *cis*-[$(piperdine)_2W(CO)_4$] complex as shown in Schemes 5 and 6. The addition of a DMF solution of **3** (blue) or **4** (green) to *cis*-[$(piperdine)_2W(CO)_4$] in warm DMF

Scheme V-5

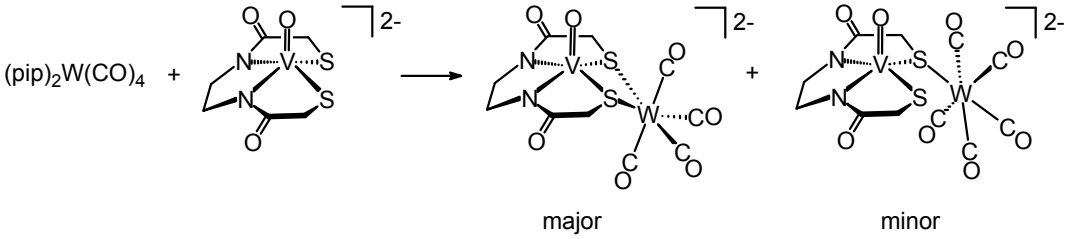

Scheme V-6

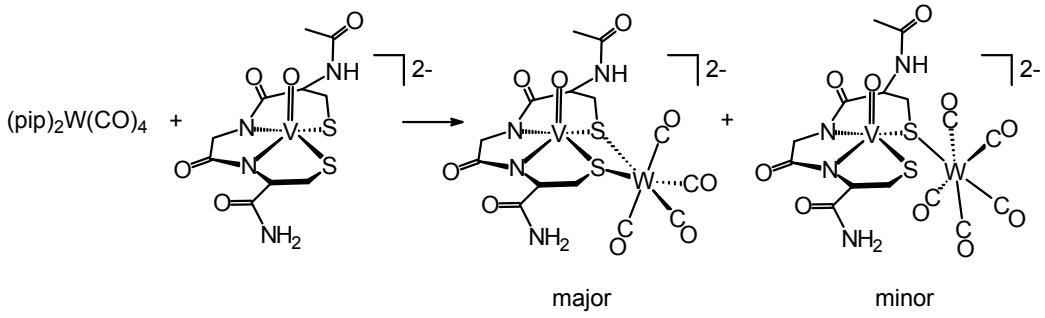

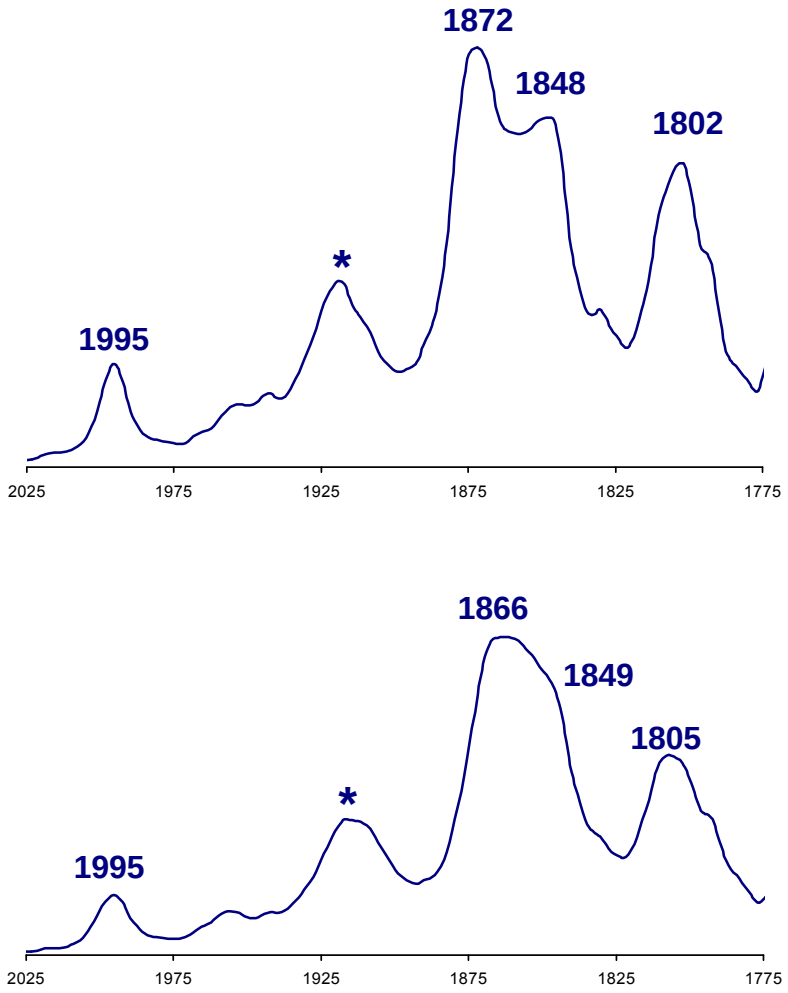

Figure V-10. IR spectra of the υ(VO) region in a DMF solution. Top: $[Et_4N]_2[(V{=}O)(ema)W(CO)_4]$, **5**. Bottom: $[K]_2[(V{=}O)(CGC)W(CO)_4]$, **6**. * = Band at ca. 1919 cm^{-1} indicates the formation of a $(V{=}O)(N_2S_2)$-$W(CO)_5$ adduct.

resulted in a color change to greenish-brown. The reactants were stirred at 40 ºC for 15 min and then stirred at room temperature for an additional 10 min. As shown in Figure V-10, the υ(CO) IR bands indicated quantitative conversion to a new species.

The carbonyl vibrational stretching frequencies are listed in Table V-3; Ni(II) and Zn(II) analogues are included for comparison. For $L_2M(CO)_4$ complexes, four IR bands are observed (assigned to the two A_1, B_1, and B_2 vibrational modes) for idealized C_{2v} symmetry, and three absorptions are expected for $LW(CO)_5$ complexes (assigned to the two A_1 and E vibrational modes) for idealized C_{4v} symmetry.[199] According to the absorptions observed for both complexes **3** and **4**, the formation of a mixture of the tetra- and pentacarbonyl products is a likely conclusion, with the tetracarbonyl adduct as the major species. The presence of the $W(CO)_5$ species has been noted in Ni-W derivatives, and postulated to occur via a CO-scavenging process from the release of a CO from the $W(CO)_4$ precursor or the initial Ni-W adduct, resulting in the thermodynamically stable pentacarbonyl Ni-W product.[184, 190, 196] Scheme 5 and 6 displays the possible (V=O)-W(CO)x (x = 4 or 5) products. While the single X-ray structures of complexes **6** and **7** have not been determined, the vanadyl-W adducts depicted in Schemes 5 and 6 are based on the molecular structure of the pentacoordinate Zn-W analogue.[184]

Previous work in our group established that the $Ni(ema)^{2-}$ and $Ni(CGC)^{2-}$ complexes exhibit similar S-based donor ability as determined by the υ(CO) values of the $W(CO)_4$ adducts of each complex.[190] The position of the infrared υ(CO) bands for the $W(CO)_4$ derivatives of $[(V=O)(ema)]^{2-}$ and $[(V=O)(CGC)]^{2-}$ show that these two complexes are equal in S-based donor ability.

As compared to the dianionic N_2S_2Ni and (CGC)Ni analogue bound to $W(CO)_4$, the υ(CO) values of the $[N_2S_2(V=O)]W(CO)_4$ analogues are shifted positively by ca. 10-20 cm^{-1}. This might be expected due to the electron-withdrawing nature of the vanadyl

Table V-3. CO stretching frequencies (cm^{-1}) and vibrational mode assignments[a] for $W(CO)_4$ and $W(CO)_5$ derivatives of $(V=O)^{2+}$, Ni^{2+} and Zn^{2+} N_2S_2 complexes.[b]

$L_2W(CO)_4$	A_1^1		B_1	A_1^2	B_2
$[VO(ema)]^{2-}$	1995	1919[c]	1872	1848	1802
$[VO(CGC)]^{2-}$	1995	1916[c]	1866	1849	1805
$[Ni(ema)]^{2-}$[d]	1986		1853	1837	1791
$[Ni(CGC)]^{2-}$	1988		1863	1845	1793
[Zn-1'Cl]$^-$[e]	1988		1861	1836	1801
(Ni-1')[f]	1996		1873	1852	1817
(Ni-1*)[f]	1996		1871	1857	1816
piperdine	2000		1863	1852	1809
$LW(CO)_5$	A_1^1	E		A_1^2	
$[Ni(ema)]^{2-}$[g]	2060 (1967sh)	1918		1868	
$[Ni(CGC)]^{2-}$[g]	2061 (1974sh)	1917		1869	
[Zn-1'Cl]$^-$	2063	1920		1869	
(Ni-1*)	2061	1920		1874	

[a]Assignments are based under pseudo-C_{2v} and pseudo-C_{4v} symmetry. [b]Unless otherwise noted, spectra were recorded in DMF solutions. [c]Formation of a $N_2S_2(V=O)$-$W(CO)_5$ species. [d]Reference 190. [e]Reference 184; 1' = [*N*,*N*'-bis(2-mercaptoethyl)-*N*,*N*'-diazacycloheptane]. [f]Reference 196; 1* = [*N*,*N*'-bis(2-mercaptoethyl)-*N*,*N*'-diazacyclooctane]. [g]Reference 190; Recorded in THF solutions.

center, preventing less electron density to be transferred to the $W(CO)_4$ unit. Notably, the υ(CO) values of monoanionic $[(Zn\text{-}1'Cl)W(CO)_4]^-$ are lower that those of the dianionic $[V=O(ema)W(CO)_4]^{2-}$ and $[V=O(CGC)W(CO)_4]^{2-}$ complexes.[184] Despite

the dianionic character of the $N_2S_2(V{=}O)$ moieties, the $\upsilon(CO)$ stretching frequencies are most similar to the values reported for the $W(CO)_4$ derivatives containing neutral N_2S_2Ni units.[196] As mentioned earlier, the neutral $N_2S_2(V{=}O)$ complexes **1** and **2** do not show any reactivity at the coordinated thiolate atoms, whereas the dianionic complexes **3** and **4** demonstrate that the electron withdrawing properties of the vanadyl ion do not quench the nucleophilic nature of the metal-bound thiolate(s).

Conclusions

The synthesis and characterization of five $N_2S_2(V^{IV}{=}O)$ complexes, which incorporate either amine/thiolate, amide/thiolate or amide/thioether donor sets, have been described. The neutral $N_2S_2(V^{IV}{=}O)$ species show stability to aerobic oxidation in the solid state, while the dianionic $N_2S_2(V^{IV}{=}O)$ species complexes are air sensitive. Amide donors in previously reported $V^{IV}{=}O$ complexes are linked to aromatic backbones, whereas the amido nitrogen donors presented herein extend from aliphatic chains, better mimicking amino acid binding sites. Three of the complexes were structurally characterized by X-ray diffraction analysis, the neutral complexes **1** and **2**, and the dianionic complex **3**. In each case, the complexes are five coordinate with square pyramidal geometry, and the V=O moiety is significantly displaced from the basal plane.

The suggested structure for the product of $V{=}O^{2+}$ ion bound to the deprotonated CGC peptide is based on (1) the presence of a strong IR band at 940 cm^{-1}, indicative of a V=O group, and (2) EPR parameters that parallel the complexes within this N_2S_2 series. Although dianionic $[O_2S_2(V^{IV}{=}O)]$ complexes have been shown to display similar V=O

stretching frequencies, the EPR parameters for the $[(V=O)(CGC)]^{2-}$ complex more closely resemble those from $V=O^{2+}$ in a N_2S_2 ligand field.[194] From these similar spectroscopic results, we conclude that the vanadyl ion is bound to an N_2S_2 coordination environment within the CGC peptide. This is consistent with the known N_2S_2 binding of CGC complexes with Cu^{2+} and Ni^{2+}.

The EPR spectra indicate the presence of paramagnetic $V^{IV}=O$ species in all of the complexes presented herein. The g and *Az* values are within ranges typical for N_2S_2 donor sets bound to a oxovanadium centers. The EPR parameters are indicative of strong σ-donation from the basal plane ligands (g-values 1.91-2.0).[181] The replacement of the amine donors with amides results in slightly higher g_x and g_y values, which suggests a slight increase in σ-donation in the basal plane. Specifically, complex **3** displays very broad signals in its EPR spectrum. The absence of sharp hyperfine splitting in complex **3** may be due to the delocalization of the unpaired electron away from the metal center, thus reducing the unpaired electron coupling with the vanadium nucleus. In contrast, the S-alkylated complex **5** displays sharp hyperfine signals in its EPR spectrum. As the electron density on the S-thiolates was shifted from S:→Ni to covalent bond formation with carbon atoms, the electron density becomes localized on the amido donors. This assumption is based on previous NBO analysis and electrostatic potential maps of the Ni^{2+} analogues of complexes **3** and **5**.[190] In the Ni^{2+} systems, the computational results indicated that the electron density is delocalized over the dianionic $[Ni(ema)]^{2-}$ complex (largely on the thiolate S-lone pairs and amido N-lone pairs). The principal resonance structure determined from NBO analysis found covalent bond character in the Ni-S bond

and dative bond character in Ni-N bond. The NBO analysis of the [Ni(ema)]·$(CH_2)_3$ complex derived from alkylation shows that the electron distribution becomes localized on the amido nitrogens resulting in Ni-S dative bond character and Ni-N covalent character. Furthermore, the significantly lower V=O stretching frequencies observed for the dianionic complexes, **3** and **4**, may be a result of the increase in electron richness about the V^{IV}=O center, and upon alkylating **3** to yield **5**, the υ(V=O) band shifts to 986 cm^{-1}. Together these results support our hypothesis that the electronic distribution of complex **3** is delocalized, which in turn affects the interaction of the unpaired electron with the vanadium nucleus. A detailed analysis of the EPR parameters in terms of MO properties in correlation with electronic absorption spectroscopy data would further aid in the interpretation of the affects of the N_2S_2 ligand field on the vanadyl center. In addition, DFT studies (NBO and electrostatic potential analysis) would be beneficial in probing the electron distribution in these $N_2S_2(V^{IV}=O)$ complexes.

There was no evidence of reactivity of the thiolates in the neutral $N_2S_2(V^{IV}=O)$ complexes. However, S-site modification of complexes **3** an **4** was accomplished by the formation of W(CO)x derivatives. Regardless of the electron richness of the N_2S_2 ligand field in complexes **3** and **4**, the S-based donor ability as determined by the υ(CO) values of the $W(CO)_4$ adducts showed that the S-donors bound to the V=O moiety produce a ligand field that is similar to the donor ability of N_2S_2Ni in neutral N_2S_2Ni-$W(CO)_4$ adducts.

The biological relevance of thiolates and amide binding in proteins has been noted in the Introduction. This work adds to the chemistry of oxovanadium binding to

N-amides from aliphatic linkages and S-thiolates, and demonstrates that stable V^{IV}=O complexes can be formed with binding sites that consist of such donors.

CHAPTER VI

CONCLUSIONS

Summary and Perspectives

Much of bioinorganic chemistry is inspired by metal binding sites that involve nitrogen and sulfur-rich coordination environments derived from the amino acid side chains of histidine, methionine and cysteine, as well as the N-terminal amine and the deprotonated carboxyamido nitrogen of the peptide bond. Such N_xS_y binding sites in biomolecules are found in acetyl coA synthase, nitrile hydratase, NikR, and the nickel-dependent superoxide dismutase.[1, 25, 177] Approaches to synthetic analogues of such ligation to transition metals have included a wide variety of ligand sets, but with little emphasis on thiolate/imidazole combinations. Inspired by the metal binding sites in NiSOD and NikR, small molecule models designed to explore the structural and electronic effects of both thiolate and imidazole donors bound to a nickel center were discussed in the first part of this dissertation.

Commonly used as histidine biomimetics are multidentate imidazole type ligands held in rigid settings.[200] For N_3 donor sets that mimic the tri-histidine motif in metalloprotein metal binding sites, the scorpionate ligands, tris(pyrazoyl)borate, (Tp^-), and tris(pyrazol-1-yl)methane, (Tpm), are frequently used (Figure VI-1). These ligand systems are easily synthesized and functionalized. The center boron or carbon anchor can be substituted by another atom or group, and the tripodal arms can be derivatized to

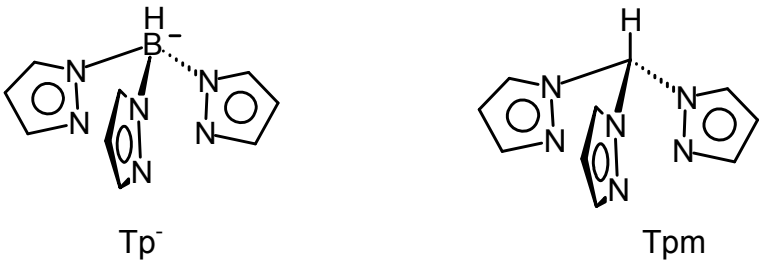

Figure VI-1. Basic tripodal ligand systems: Tp^- and Tpm.

include a variety of different ligand donors. In all such ligand systems, the orientation of the histidine mimic pyrazoyl or imidazole N-donor ligand is controlled by the tripodal arm linker torsion angles. While biomimetics that use such C_3 ligands have most certainly advanced metallobiochemistry, monodentate ligands, such as imidazoles, are expected to more accurately model the flexibility in polypeptide chains and to be more appropriate for square planar coordination geometries.

In my work, simple imidazoles were incorporated into nickel-thiolate complexes to produce N,S coordination environments related to those observed in NiSOD and NikR. During my endeavors, other small molecule models of the NiSOD active site were reported, and these complexes are shown in Figure VI-2.[81, 90, 102-103, 104, 200-201] Research in the area of N_2S_2Ni chemistry has firmly established that electrophilic and oxidative reactivity occurs at the S-thiolates.[202] As predicted by computational studies, the first generation synthetic analogues concentrated on incorporating a mixed amine/amide set into the N_2S_2 coordination sphere in order to suppress reactivity at the nickel bound thiolates and promote nickel-based chemistry.[100-101] The first biomimetic

to incorporate a mixed amine/amide donor set was presented by Shearer et al. (Figure VI-2a).[102-103] This complex exhibited enhanced stability toward oxygenation, but did not show SOD activity. In addition, an amine/amide mixed donor set with an N_2S_2Ni coordination sphere was accessed via dimer cleavage by Harrop et al. (Figure VI-2b).[90] This complex displayed similar spectroscopic properties as did the model by Shearer et al., but also did not exhibit NiSOD chemistry.

Our group investigated thiolate modification by alkylation or S-oxygenation of the $Ni(ema)^{2-}$ complex, which contains two amide and two thiolate donors.[81] In line with our previous studies, we found that such sulfur protection directs reactivity to the nickel. In addition to demonstrating that stable S-oxygenates can be produced from dianionic N_2S_2Ni complexes (Figure VI-2e), we came to the conclusion that the absence of such reactivity in the NiSOD active site was most reasonably due to kinetic control. Subsequent to our reports, Jenson and coworkers presented NiSOD model complexes utilizing the tripodal ligand, hydrotris(3-phenyl-5-methylpyrazolyl)borate ligand ($Tp^{Ph,Me}$), and organoxanthate or dithiocarbamates ligands to produce N_2S_2Ni square-planar and N_3S_2Ni pyramidal complexes (Figure VI-2c and d).[104] As shown for the other model complexes, spectroscopic features were similar to the native active site, but SOD activity was not reported. The synthetic N_3SNi mimic by Grapperhaus et al. shown as f in Figure VI-2 will be discussed below.[201] A final note on NiSOD biomimetics, is that the only functional SOD models that have been reported to date contain nickel centers coordinated within peptidic coordination environments.[203-204] Such constructs have been reported by Shearer and coworkers in which they demonstrated NiSOD catalytic activity

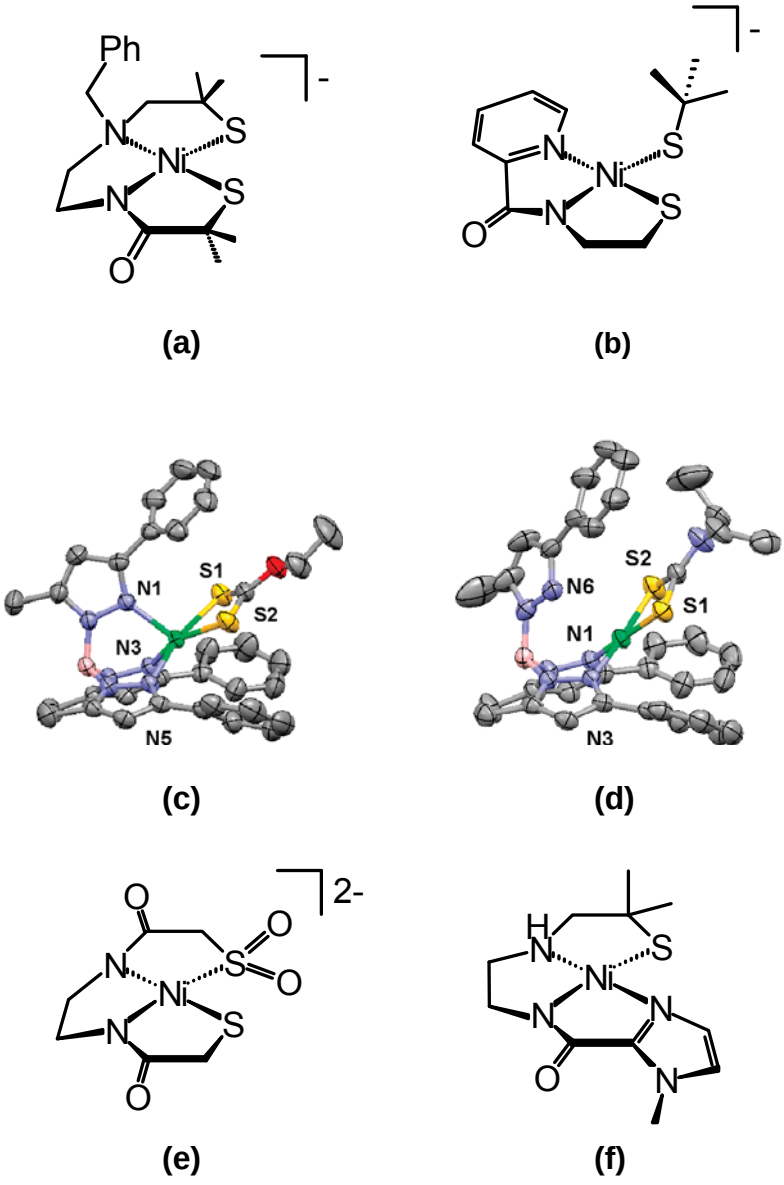

Figure VI-2. Reported NiSOD small molecule models. (a) Adapted from References 102-103; (b) Adapted from Reference 90; (c) Adapted from Reference 104; (d) Adapted from Reference 104; (e) Adapted from Reference 81; and (f) Adapted from Reference 201.

for a nickel(II) ion coordinated to a 12-mer peptide, and by Laurence et al. who has prepared a functional model utilizing a asparagine-cysteine-cysteine tripeptide bound to a nickel(II) center.[203-204]

My original synthetic vision for an ideal NiSOD enzyme active site model complex accessible from known square planar N_2S_2 nickel complexes was to have a dangling imidazole attached from a thiolate or from a thioether sulfur with capability to coordinate in the axial site on oxidation of Ni^{II} to Ni^{III}, see Chapter III. Both plans were reasonable based on prior work. Our group had previously demonstrated that N_2S thiolate bridged nickel dimers could be cleaved with nucleophiles, and we had established that tetradentate N_2S_2 bonding is maintained after S-alkylation by reagents that provide an additional binding site.[109, 122-125] The first plan to include an imidazole linker from a thiolate ligand was to be accomplished by the following reaction:

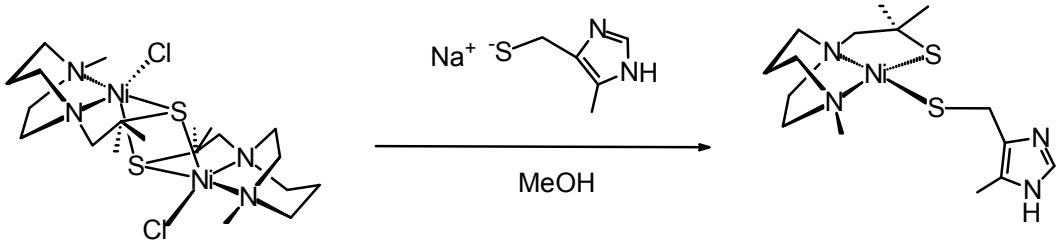

Confirmation of the mononuclear formulation was provided by $^{+}$ESI-MS analysis (m/z = 357) and elemental analysis, and the N_2S_2 coordination was proposed consistent with UV-vis spectral data (λ_{max} = 450, 352, 284, 212 nm). However, the electrochemistry in MeCN did not show a reversible oxidation event in a range that would imply nickel-based chemistry, which would have promoted the axial imidazole binding. Only one

irreversible oxidation event was observed at +24 mV vs. Fc^{+}/Fc and that was assigned to S-oxidation. Attempts to obtain X-ray quality crystals of this complex were unsuccessful, and further study was less promising than other lines of research.

A second plan was carried out to incorporate a dangling imidazole ligand via the alkylation of the thiolate using 4-(chloromethyl)-5-methyl-imidazole·HCl, as shown in Chapter III. In this case, X-ray quality crystals were obtained; however, the molecular structure revealed a preference for N-imidazole binding in the square plane of Ni^{II} over that of the S-thioether donor. Although DFT computations found a difference of only 3.34 kcal/mol between the N-imidazole-bound versus the S-thioether-bound complex, a switch of the donor from the N-imidazole to the S-thioether binding could not be achieved via the protonation of the imidazole ligand. These results demonstrated the strong binding of the imidazole nitrogen. The chain length connecting the imidazole to the diazacycle backbone was the perfect length to promote the imidazole binding in its favored orientation, that is, orthogonal to the NiL_4 square plane.

While the original intent of this work to obtain a NiSOD model with a hemilabile axial imidazole ligand was not achieved, the study of imidazole/thiolate donor combination bound to nickel became, in our opinion, a more significant focus. A second nickel-imidazole complex was designed as a first coordination sphere molecular model of the Ni-binding site of the Nik-R protein and accessed through dimer cleavage reactions using imidazole. This complex differed from the NiSOD model complex in that the N-imidazole ligand was not tethered to the N_2S framework, producing a tridentate and monodentate $N_2N'S$ ligand set. Despite this difference, both molecular

structures revealed that the imidazole plane (tethered or untethered to the N_2S framework) favored a nearly perpendicular orientation with respect to the nickel square plane. In contrast, a bis-imidazole N_4Ni complex, in which both imidazole ligands were connected to the diazacycle backbone by a methylene linkage, was prepared. In this case, the molecular structure found that the imidazole ligands were held roughly coplanar with the nickel square plane. This series of N_xS_yNi imidazole complexes demonstrated the influence of the length of the carbon chain attached to the imidazole ligand; a chain with more flexibility allows the imidazole ligand to orient in an apparently preferred orthogonal position, whereas the shorter carbon chain restricted the imidazole ligand to a planar orientation. Grapperhaus and coworkers synthesized an N_3SNi complex, analogous to my complexes, which contained an amide donor in place of one of the amines (Figure VI-2f).[201] As observed in our bis-imidazole nickel complex, the one carbon linker forces the imidazole plane to orient parallel to the nickel square plane.

Given that the imidazole ligand was not tethered in one of the imidazole $N_2N'SNi$ complexes, we pursued the unique opportunity to investigate the preferred orientation of this imidazole $N_2N'SNi$ complex utilizing VT ^1H NMR spectroscopy. The term "unique" refers to the asymmetry of the $N_2N'SNi$ complex due to the diazacycloheptane ligand which renders one face of the Ni-square plane different from the other. Thus, variable temperature ^1H NMR was used to examine the solution phase conformations and interconversions, and in correlation with these results, density functional theory computations related the orientation of the imidazole with respect to

the $N_2N'SNi$ square plane to the observed fluxionality and activation parameters. Furthermore, the computational studies indicated that the frontier molecular orbitals were predominately derived from the interactions between the S-thiolate and Ni center. While imidazole ligands have the potential to participate in π-donor interactions, the analysis of the ground and the DFT derived transition state computational results showed only σ-bonding orbitals with large contributions from Ni and the N-donor imidazole nitrogen.

Based on this paradigm for imidazole binding in N_2SNi planes, a series of monodentate heterocycles was used to cleave dimeric precursors to produce monomeric square planar $[N_2SNiL]^{n+}$ complexes in order to better understand factors that influence the orientation of imidazole ligands found within a flexible coordination environment. The targeted monomeric square planar $[N_2SNiL]^{n+}$ complexes were designed to encompass different electronic and steric properties. The differences in electronic makeup were governed by the pK_a of the monodentate donor atom's conjugate acid in each ligand. The steric character was altered in two ways: (1) the steric bulk of the monodentate donor atom; and (2), the substituent on the N-donor from the diazacycloheptane frame.

The isolation of the target monomeric square planar $[N_2SNiL]^{n+}$ complexes and characterization by X-ray diffraction analysis revealed that regardless of the electronic or steric makeup, the plane of the monodentate ligand had a preference to orient in a nearly orthogonal position to the nickel square plane. This result suggested that the orientation of the monodentate ligand was dictated largely by minimization of steric interactions of

the monodentate ligand with the steric constraints of N_2SNi binding site that allowed a maximum σ-bonding interaction. Nevertheless, in the case of the imidazole ligands, a slight deviation from orthogonality was observed, and this tilt directed the imidazole C-2 C-H toward the S-thiolate atom. Furthermore, DFT computations suggested a minor electronic contribution between the imidazole C-2 C-$H^{\delta+}$ and the $S^{\delta-}$ influenced the stability of the ground state and in the imidazole rotation process, the transition state structures. The interaction was interpreted as an intramolecular donor/acceptor interaction. This hypothesis was confirmed by computational studies which found that this type of donor-acceptor interaction was magnified in O-analogues, where coplanar arrangements in the ground state of $N_2ON_{imid}Ni$ complexes were predicted.

That imidazoles can be involved in intramolecular donor-acceptor interactions has been previously observed.[133-141] As mentioned in Chapter IV, a survey of the Cambridge data base found ten square planar nickel complexes containing a monodentate imidazole donor, but within different nickel first coordination sphere environments. These compounds were prepared due to their ability to self-assemble in extended arrays originating from intermolecular H-bonding interactions and π-π stacking interactions. The molecular structures of the Ni^{II}-Schiff base complexes containing hard O-donors *cis* to the unsubstituted imidazole monodentate ligand found the imidazole in a nearly coplanar orientation, with the C2 oriented towards the O-donor, consistent with our computational findings.

Overall, our simple $[N_2SNiL]^{n+}$ systems containing imidazole ligands have proved, that much like the protein coordination environment, many factors, such as

steric bulk and internal electrostatic interactions, can affect the imidazole ligand orientation without disturbing the σ-bond between the Ni and the N-imidazole. As described in Chapter I, the ground state binding orientation of the His-imidazole has profound effects on the function of biomolecules particularly well studied. The studies presented in this dissertation have expanded our knowledge of the fundamental coordination chemistry of square planar N_xS_yNi complexes containing imidazole ligands. It is expected that preferences in orientation due to *cis*-O or *cis*-S donor atoms could eventually be recognized as having profound effects in nickel biomolecules/proteins.

REFERENCES

1. Mulrooney, S. B.; Hausinger, R. P. *Microbiol. Rev.* **2003**, *27*, 239-261.

2. Li, Y.; Zamble, D. B. *Chem. Rev.* **2009**, *109*, 4617-4643 and references therein.

3. McGee, D.J.; Mobley, H. L. T.; *Curr. Top. Microbiol. Immunol.* **1999**, *241*, 155-180.

4. Maier, R. J.; Fu, C.; Gilbert, J.; Moshiri, F.; Olson, J.; Plaut, A. G.; *FEMS Microbiol. Lett.* **1996**, *141*, 71-76.

5. Olson, J. W.; Maier, R. J. *Science* **2002**, *298*, 1788-1790.

6. Blaser, M. J. *J. Infect. Dis.* **1990**, *161*, 626-633.

7. Covacci, A.; Telford, J. L.; Del Giudice, G.; Parsonnet, J.; Rappuoli, R. *Science* **1999**, *284*, 1328-1333.

8. Sachs, G.; Weeks, D. L.; Melchers, K.; Scott, D. R. *Annu. Rev. Physiol.* **2003**, *65*, 349-369.

9. Chakrabarti, S. K.; Bai, C.; Subramanian, K. S. *Toxicol. Appl. Pharmocol.* **2001**, *170*, 153-165.

10. De Pina, K.; Desjardin, V.; Mandrand-Berthelot, M. A.; Giordano, G.; Wu, L. F. *J. Bacteriol.* **1999**, *181*, 670–674.

11. Chivers, P. T.; Sauer, R. T. *J. Biol. Chem.* **2000**, *275*, 19735–19741.

12. Dosanjh, N. S.; Michel, S. L. *J. Curr. Opin. Chem. Biol.* **2006**, *10*, 123-130.

13. Schreiter, E. R.; Wang, S. C.; Zamble, D. B.; Drennan, C. L *PNAS* **2006**, *103*, 13676-13681.

14. Scheiter, E. R.; Sintchak, M. D.; Guo, Y. Y.; Chivers, P. T.; Sauer, R. T.; Drennan, C. L. *Nat. Struct. Biol.* **2003**, *10*, 794-799.

15. Bloom, S. L.; Zamble, D. B. *Biochem.* **2004**, *43*, 10029-10038.

16. Wang, S. C.; Dias, A. V.; Bloom, S. L.; Zamble, D. B. *Biochem.* **2004**, *43*, 10018–10028.

17. Phillips, C. M.; Schreiter, E. R.; Guo, Y.; Wang, S. C.; Zamble, D. B.; Drennan, C. L. *Biochem.* **2008**, *47*, 1938-1946.

19. Miller, A.F. *Comp. Coord. Chem. II.* **2004**, *8*, 479-506.

20. Miller, A. F.; Sorkin, D. *Comm. Mol. Cell. Biophys.* **1997**, *9*, 1-48.

21. McCord, J. M. *Methods in Enzymology* **2002**, *349*, 331-341.

22. Noodleman, L.; Lovell, T.; Han, W.; Li, J.; Him, F. *Chem. Rev*. **2004**, *104*, 459˜-508.

23. Barondeau, D. P.; Kassmann, C. J.; Bruns, C. K.; Tainer, J. A.; Getzoff, E. D. *Biochem*. **2004**, *43*, 8038-8047.

24. Wuerges, J.; Lee, J.; Yim, Y.; Yim, H.; Kang, S.; Carugo, K. D. *PNAS*. **2004**, *101*, 8569-8574.

25. Darnault, C.; Volbeda, A.; Kim, E. J.; Legrand, P.; Vernede, X.; Lindahl, P. A.; Fontecilla-Camps, J. C. *Nat. Struct. Biol.* **2003**, *10*, 271-279.

26. Dokov, I. T.; Iverson, T. M.; Seravalli, J.; Ragsdale, S. W.; Drennan, C. L. *Science*, **2002**, *298*, 567-572.

27. Amara, P.; Fonticella-Camps, J. C.; Field, M. *J. Am. Chem. Soc.* **2005**, *127*, 2776-2784.

28. Scheidt, W. R.; Chipman, D. M. *J. Am. Chem. Soc.* **1986**, *108*, 1163-1167.

29. Yatsunyk, L. A.; Dawson, A.; Carducci, M. D.; Nichol, G. S.; Walker, F. A. *Inorg. Chem.* **2006**, *45*, 5417-5428.

30. Walker, F. A.; Huynh, B. H.; Scheidt, W. R.; Osvath, S. R. *J. Am. Chem. Soc.* **1986**, *108*, 5288-5297.

31. Safo, M. K.; Walker, F. A.; Raitsimring, A. M.; Walters, W. P.; Dolata, D. P.; Debrunner, P. G.; Scheidt, W. R. *J. Am. Chem. Soc.* **1994**, *116*, 7760-7770.

32. Menyhárd, D. K.; Keserú, G. M. *J. Am. Chem. Soc.* **1998**, *120*, 7991-7992.

33. Safo, M. K.; Nesset, M. J. M.; Walker, F. A.; Debrunner, P. G.; Scheidt, W. R. *J. Am. Chem. Soc.* **1997**, *119*, 9438-9448.

34. Zaríc, S. D.; Popović, D. M.; Knapp, E-W. *Biochem.* **2001**, *40*, 7914-7928.

35. Galstyan, A. S.; Zaríc, S. D.; Knapp, E-W. *J. Biol. Inorg. Chem.* **2005**, *10*, 343-354.

36. Silvernail, N. J.; Roth, A.; Schulz, C. E.; Noll, B. C.; Scheidt, W. R. *J. Am. Chem. Soc.* **2005**, *127*, 14422-14433.

37. Collins, D. M.; Countryman, R.; Hoard, J. L. *J. Am. Chem. Soc.* **1972**, *94*, 2066-2072.

38. Johnson, C. R.; Jones, C. M.; Asher, S. A.; Abola, J. E. *Inorg. Chem.* **1991**, *30*, 2120-2129.

39. Alessio, E.; Calligaris, M.; Iwamoto, M.; Marzilli, L. G. *Inorg. Chem.* **1996**, *35*, 2538-2545.

40. Alessio, E.; Zangrando, E.; Roppa, R.; Marzilli, L. G. *Inorg. Chem.* **1998**, *37*, 2458-2463.

41. Velders, A. H.; Hotze, A. C. G.; van Albada, G. A.; Haasnoot, J. G.; Reedijk, J. *Inorg. Chem.* **2000**, *39*, 4073-4080.

42. Velders, A. H.; Quiroga, A. G.; Haasnoot, J. G.; Reedijk, J. *Eur. J. Inorg. Chem.* **2003**, 713-719.

43. Doyle, M. J.; Lappert, M. F. *J. Chem. Soc., Chem. Commun.* **1974**, 679-680.

44. Herrmann, W. A.; Gooβen, L. J.; Spiegler, M. *J. Organomet. Chem.* **1997**, *547*, 357-366.

45. Weskamp, T.; Schattenmann, W. C.; Spiegler, M.; Herrmann, W. A. *Angew. Chem. Int. Ed.* **1998**, *37* 2490-2493.

46. Enders, D.; Gielen, H. *J. Organomet. Chem.* **2001**, *617-618*, 70-80.

47. Chianese, A. R.; Li, X.; Janzen, M. C.; Faller, J. W.; Crabtree, R. H. O*rganometallics* **2003**, *22*, 1663-1667.

48. Silva, L. C.; Gomes, P. T.; Veiros, L. F.; Pascu, S. I.; Duarte, M. T.; Namorado, S.; Ascenso, J. R.; Dias, A. R. *Organometallics* **2006**, *25*, 4391-4403.

49. Huang, J.; Schanz, H-J.; Stevens, E. D.; Nolan, S. P. *Organometallics* **1999**, *18*, 2370-2375.

50. Mata, J. A.; Chianese, A. R.; Miecznikowski, J. R.; Poyatos, M.; Peris, E.; Faller, J. W.; Crabtree, R. H. *Organanometallics* **2004**, *23*, 1253-1263.

51. Brissy, D.; Skander, M.; Retailleau, P.; Marinetti, A. *Organometallics* **2007**, *26*, 5782-5785.

52. Huang, D.; Deng, L.; Sun, J.; Holm, R. H. *Inorg. Chem.* **2009**, *48*, 6159-6166.

53. Wang, X.; Berry, S. M.; Xia, Y.; Lu, Y. *J. Am. Chem. Soc.* **1999**, *121*, 7449-7450.

54. Robinson, H.; Ang, M. C.; Gao, Y. G.; Hay, M. T.; Lu, Y.; Wang, A. H.-J. *Biochem.* **1999**, *38*, 5677-5683

55. *WINEPR SIMFONIA version 1.25*, Bruker Analytische Messtechnik GmbH, 1996.

56. *SMART V5.632 Program for Data Collection on Area Detectors*; Bruker AXS Inc.: Madison, WI, 1999.

57. *FRAMBO:FRAME Buffer Operation Version 41.05 Program for Data Collection on Area Detectors*; Bruker AXS Inc.: Madison, WI, 1999.

58. *SAINT V6.63 Program for Reduction of Area Detector Data*; ; Bruker AXS Inc.: Madison, WI, 1999.

59. Sheldrick, G. *SADABS Program for Absorption Correction Area Detector Frames*; Bruker AXS Inc.: Madison, WI, 1999.

60. Sheldrick, G. SHELXTL-PLUS, Version 4.11V, SHELXTL-PLUS Users Manual; Siemens Analytical X-ray Instruments, Inc.: Madison, WI, 1990.

61. Sheldrick, G. *SHELXS-97, Program for Crystal Structure Solution*; Institut fur Anorganische Chemie der Universitat Gottingen: Gottingen, Germany, 1997.

62. Sheldrick, G. *SHELXL-97, Program for Crystal Structure Refinement*; Institut fur Anorganische Chemie der Universitat Gottingen: Gottingen, Germany, 1997.

63. Barbour, L. J. *J. Supramol. Chem.* **2001**, *1*, 189-191.

64. Cerius2, version 4.10; Accelrys Inc.: San Diego, CA, 2007.

65. Becke, A. D. *J. Chem. Phys.* **1993**, *98*, 5648–5652.

66. Lee, C.; Yang, W.; Parr, R. G. *Phys. Rev.* **1988**, *37*, 785–789.

67. All calculations were carried out with the Gaussian 03 program: Frisch, M. J.; Trucks, G. W.; Schlegel, H. B.; Scuseria, G. E.; Robb, M. A.; Cheeseman, J. R.; Montgomery, J. A., Jr.; Vreven, T.; Kudin, K. N.; Burant, J. C.; Millam, J. M.;

Iyengar, S. S.; Tomasi, J.; Barone, V.; Mennucci, B.; Cossi, M.; Scalmani, G.; Rega, N.; Petersson, G. A.; Nakatsuji, H.; Hada, M.; Ehara, M.; Toyota, K.; Fukuda, R.; Hasegawa, J.; Ishida, M.; Nakajima, T.; Honda, Y.; Kitao, O.; Nakai, H.; Klene, M.; Li, X.; Knox, J. E.; Hratchian, H. P.; Cross, J. B.; Bakken, V.; Adamo, C.; Jaramillo, J.; Gomperts, R.; Stratmann, R. E.; Yazyev, O.; Austin, A. J.; Cammi, R.; Pomelli, C.; Ochterski, J. W.; Ayala, P. Y.; Morokuma, K.; Voth, G. A.; Salvador, P.; Dannenberg, J. J.; Zakrzewski, V. G.; Dapprich, S.; Daniels, A. D.; Strain, M. C.; Farkas, O.; Malick, D. K.; Rabuck, A. D.; Raghavachari, K.; Foresman, J. B.; Ortiz, J. V.; Cui, Q.; Baboul, A. G.; Clifford, S.; Cioslowski, J.; Stefanov, B. B.; Liu, G.; Liashenko, A.; Piskorz, P.; Komaromi, I.; Martin, R. L.; Fox, D. J.; Keith, T.; Al-Laham, M. A.; Peng, C. Y.; Nanayakkara, A.; Challacombe, M.; Gill, P. M. W.; Johnson, B.; Chen, W.; Wong, M. W.; Gonzalez, C.; Pople, J. A. Gaussian 03, Revision B.04; Gaussian, Inc.: Wallingford, CT, **2004**.

67. Dolg, M.; Wedig, U.; Stoll, H.; Preuss, H. *J. Chem. Phys.* **1987**, *86*, 866-872.
68. Hay, P. J.; Wadt, W. R. *J. Chem. Phys.* **1985**, *82*, 284–398.
69. Hay, P. J.; Wadt, W. R. *J. Chem. Phys.* **1985**, *82*, 270–283.
70. Hŏllwarth, A.; Böhme, M.; Dapprich, S.; Ehlers, A. W.; Gobbi, A.; Jonas, V.; Köhler, K. F.; Stegmann, R.; Veldkamp, A.; Frenking, G. *Chem. Phys. Lett.* **1993**, *208*, 237–240.
71. Dunning, Jr. T. H. *J. Chem. Phys*. **1989**, 90, 1007-1023.
72. Hehre, W. J.; Ditchfield, R.; Pople, J. A. *J. Chem. Phys.* **1972**, *56*, 2257-2261.
73. Hariharan, P. C.; Pople, J. A. *Theor. Chim. Acta* **1973**, *28*, 213-222.

74. The d',p' functions are the exponents from the 6-311G(d,p) basis set: Krishnan, R.; Binkley, J. S.; Seeger, R.; Pople, J. A. *J. Chem. Phys*. **1980,** 72, 650-654.

75. Peng, C.; Schlegel, H. B. *Isr. J. Chem.* **1993**, *33*, 449–454.

76. Peng, C.; Ayala, P. Y.; Schlegel, H. B.; Frisch, M. J. *J. Comput. Chem.* **1996**, *17*, 49–56.

77. Farmer, P. J.; Reibenspies, J. H.; Lindahl, P. A.; Darensbourg, M. Y. *J. Am. Chem. Soc.* **1993**, *115*, 4665-4674.

78. Musie, G.; Farmer, P. J.; Tuntulani, T.; Reibenspies, J. H.; Darensbourg, M. Y. *Inorg. Chem.* **1996**, *35*, 2176-2183.

79. Smee, J. J.; Miller, M. L.; Grapperhaus, C. A.; Reibenspies, J. H.; Darensbourg, M. Y. *Inorg. Chem.* **2001**, *40*, 3601-3605.

80. Golden, M. L.; Whaley, C. M.; Rampersad, M. V.; Reibenspies, J. H.; Hancock, R. D.; Darensbourg, M. Y. *Inorg. Chem.* **2005**, *44*, 875-883.

81. Green, K. N.; Brothers, S. M.; Jenkins, R. M.; Carson, C. E.; Grapperhaus, C. A.; Darensbourg, M. Y. *Inorg. Chem.* **2007**, *46*, 7536-7544.

82. Kruger, H.-J.; Peng, G.; Holm, R. H. *Inorg. Chem.* **1991**, *30*, 734-742.

83. Sellmann, D.; Prechtel, W.; Knoch, F.; Moll, M. *Z. Naturforsch. (B)* **1992**, *47*, 1411-1423.

84. Wang, Q.; Blake, A. J.; Davies, E. S.; McInnes, E. J. L.; Wilson, C.; Schroder, M. *Chem. Commun.* **2003**, 3012-3013.

85. Hatlevik, O.; Blanksma, M. C.; Mathrubootham, V.; Arif, A. M.; Hegg, E. L. *J. Biol. Inorg. Chem.* **2004**, *9*, 238-246.

86. Grapperhaus, C. A.; Mullins, C. S.; Kozlowski, P. M.; Mashuta, M. S. *Inorg. Chem.* **2004**, *43*, 2859-2866.

87. Krishnan, R.; Riordan, C. G. *J. Am. Chem. Soc.* **2004**, *126*, 4484-4485.

88. Bouwman, E.; Reedijk, J. *Coord. Chem. Rev.* **2005**, *249*, 1555-1581.

89. Chohan, B. S.; Maroney, M. J. *Inorg. Chem.* **2006**, *45*, 1906-1908.

90. Harrop, T. C.; Olmstead, M. M.; Mascharak, P. K. *Inorg. Chem.* **2006**, *45*, 3424-3436.

91. Rauchfuss, T. B. *Science* **2007**, *316*, 553-554.

92. Shearer, J.; Dehestani, A.; Abanda, F. *Inorg. Chem.* **2008**, *47*, 2649-2660.

93. Sugiura,Y.; Hirayama, Y. *J. Am. Chem. Soc.* **1977**, *99*, 1581–1585.

94. Sugiura, Y. *Inorg. Chem.* **1978**, *17*, 2176–2182.

95. Tesfai, T. M.; Green, B. J.; Margerum, D. W. *Inorg. Chem.* **2004**, *43*, 6726-6733.

96. Burrows, C. J.; Perez, R. J.; Muller, J. G.; Rokita, S. E. *Pure Appl. Chem.* **1998**, *70*, 275-278.

97. Ross, S. A.; Burrows, C. J. *Inorg. Chem.* **1998**, *37*, 5358-5363.

98. Van Horn, J. D.; Bulaj, G.; Goldenberg, D. P.; Burrows, C. J. *J. Biol. Inorg. Chem.* **2003**, *8*, 601-610.

99. Hass, K. L.; Franz, K. J. *Chem. Rev.* **2009**, *109*, 4921-4960.

100. Fiedler, A. T.; Bryngelson, P. A.; Maroney, M. J.; Brunold, T. C. *J. Am. Chem. Soc.* **2005**, *127*, 5449-5462.

101. Mullins, C. S.; Grapperhaus, C. A.; Kozlowski, P. M. *J. Biol. Inorg. Chem.* **2006**, *11*, 617-625.

102. Shearer, J.; Long, L. M. *Inorg. Chem.* **2006**, *45*, 2358-2360.

103. Shearer, J.; Zhao, N. *Inorg. Chem.* **2006**, *45*, 9637-9639.

104. Ma, H.; Cattopadhyay, S.; Petersen, J. L.; Jensen, M. P. *Inorg. Chem*. **2008**, *47*, 7966-7968.

105. Neupane, K. P.; Shearer, J. *Inorg. Chem*. **2006**, *45*, 10552-10566.

106. Pelmenschikov, V.; Seigbahn, P. E. M. *J. Am. Chem. Soc.* **2006**, *128*, 7466-7475.

107. Neupane, K. P.; Gearty, K.; Francis, A.; Shearer, J. *J. Am. Chem. Soc.* **2007**, *129*, 14605-14618.

108. Snyder, H. R.; Stewart, J. M.; Aeigler, J. B. *J. Am. Chem. Soc.* **1947**, *69*, 2672.

109. Rosen, T.; Nagel, A. A.; Rizzi, J. P.; Ives, J. L.; Daffeh, J. B.; Ganong, A. H.; Guarino, K.; Heym, J.; McLean, S.; Nowakowski, J. T.; Schmidt, A. W.; Seeger, T. F.; Siok, C. J.; Vincent, L. A. *J. Med. Chem*. **1990**, *33*, 2715-2720.

110. Grapperhaus, C. A.; Bellefuille, J. A.; Reipenspies, J. H.; Darensbourg, M. Y. *Inorg. Chem.* **1999**, *38*, 3698-3703.

111. Du, M.; Guo, Y. M.; Bu, X. H.; Ribas, J.; Monfort, M. *New J. Chem.* **2002**, *26*, 939-945.

112. Guo, Y. M.; Du, M.; Bu, X. H. *Inorg. Chim. Acta* **2005**, *358*, 1887-1896.

113. Colpas, G. J.; Kumar, M.; Day, R. O.; Maroney, M. J. *Inorg. Chem.* **1990**, *29*, 4779-4788.

114. Linck, R. C.; Spahn, C. W.; Rauchfuss, T. B.; Wilson, S. R. *J. Am. Chem. Soc.* **2003**, *125*, 8700-8701.

115. Rao, P. V.; Bhaduri, S.; Jiang, J.; Holm, R. H. *Inorg. Chem.* **2004**, *43*, 5833-5849.

116. Redin, K.; Wilson, A. D.; Newell, R.; DuBois, M. R.; DuBois, D. L. *Inorg. Chem.* **2007**, *46*, 1268-1276.

117. Kruger, H.-J.; Holm, R. H. *Inorg. Chem.* **1989**, *28*, 1148-1155.

118. Mirza, S. A.; Pressler, M. A.; Kumar, M.; Day, R. O.; Maroney, M. J. *Inorg. Chem.* **1993**, *32*, 977-987.

119. Sellman, D.; Prechtel, W.; Knoch, F.; Moll, M. *Inorg. Chem.* **1993**, *32*, 538-546.

120. Sellman, D.; Huabinger, D.; Heinemann, F. W. *Eur. J. Inorg. Chem.* **1999**, 1715-1725.

121. Blinn, E.; Busch, D. H. *J. Am. Chem. Soc.* **1968**, *90*, 4280-4285.

122. Musie, G.; Reibenspies, J. H.; Darensbourg, M. Y. *Inorg. Chem.* **1998**, *37*, 302-310.

123. Goodman, D. C.; Reibenspies, J. H.; Goswami, N.; Jurisson, S.; Darensbourg, M. Y. *J. Am. Chem. Soc.* **1997**, *119*, 4955-4963.

124. Smee, J. J.; Goodman, D. C.; Reibenspies, J. H.; Darensbourg, M. Y. *Eur. J. Inorg. Chem.* **1999**, 539-546.

125. Geary, W. J. *Coord. Chem. Rev.* **1971**, *7*, 81-122.

126. Lever, A. B. P. *Inorganic Electronic Spectroscopy,* 2nd ed.; Elsevier.

127. Greenwald, R. A. *CRC Handbook of Methods for Oxygen Radical Research*, CRC Press, Boca Raton, **1985**, 65-69.

128. Kolb, H. C.; Andersson, P. G.; Sharpless, K. B. *J. Am. Chem. Soc.* **1994**, *116*, 1278-1291.

129. Evans, D. A.; Campos, K. R.; Tedrow, J. S.; Michael, F. E.; Gagné, M. R. *J. Am. Chem. Soc.* **2000**, *122*, 7905-7920.

130. Leitner, A.; Shekhar, S.; Pouy, M. J.; Hartwig, J. F. *J. Am. Chem. Soc.* **2005**, *127*, 15506-15514.

131. Jenkins, R. M.; Singleton, M. L.; Almaraz, E.; Reibenspies, J. H.; Darensbourg, M. Y. *Inorg. Chem.* **2009**, *48*, 7280-7293.

132. Gale, E. M.; Patra, A. K.; Harrop, T. C. *Inorg. Chem.* **2009**, *48*, 5620-5622.

133. Gou, S.; You, X.; Xu, Z.; Zhou, Z.; Yu, K. *Polyhedron* **1991**, *10*, 2659-2663.

134. Mukhopadhyay, A.; Padmaja, G.; Pal, S.; Pal, S. *Inorg. Chem. Commun.* **2003**, *6*, 381-386.

135. Ray, M. S.; Ghosh, A.; Mukhopadhyay, G.; Drew, M. G. B. *J. Coord. Chem.* **2003**, *56*, 1141-1148.

136. Zhang, H.-H. *Acta Cryst.* **2006**, *E62*, m3110-m3111.

137. Mukhopadhyay, A.; Pal, S. *Eur. J. Inorg. Chem.* **2006**, 4879-4887.

138. Chen, P.-K.; Shen, X.-Q.; Ge, C.-Y.; Kou, J.-F.; Zhang, H.-Y.; Hou, H.-W.; Zhu, Y. *Synth. React. Inorg. Met-Org. Nano-Met. Chem.* **2006**, *36*, 603-607.

139. Zhang, Q. L.; Zhu, B. X. *J. Coord. Chem.* **2008**, *61*, 2340-2346.

140. Chen, X.-H. *Acta Cryst.* **2008**, *E64*, m1253.

141. Salem, N. M. H.; El-Sayed, L.; Iskander, M. F. *Polyhedron* **2008**, *27*, 3215-3226.

142. Chu, Y.; Deng, H.; Cheng, J.-P. *J. Org. Chem.* **2007**, *72*, 7790-7793.

143. Lide, D. R. *CRC Handbook of Chemistry and Physics*, CRC Press, Boca Raton, Fl., **2000**, 8-46 to 56.

144. Lenarcik, B.; Ojczenasz, P. *J. Heterocyclic Chem.* **2002**, *39*, 287-290.

145. Amyes, T. L.; Diver, S. T.; Richard, J. P.; Rivas, F. M.; Toth, K. *J. Am. Chem. Soc.* **2004**, *126*, 4366-4374.

146. Fackler, J. P., Jr. *Prog. Inorg. Chem.* **1976**, *21*, 55-90.

147. Gusev, D. G. *Organometallics* **2009**, *28*, 6458-6461.

148. Tolman, C. A. *Chem. Rev.* **1977**, *77*, 313-348.

149. Rodrìguez-Argüelles, M. C.; Ferrari, M. B.; Bisceglie, F.; Pelizzi, C.; Pelosi, G.; Pinelli, S.; Sassi, M. *J. Inorg. Biochem.* **2004**, *98*, 313-321.

150. Henze, M. *Hoppe-Seyler's Z. Physiol. Chem.* **1911**, *72*, 494-501.

151. Smith, M. J.; Kim, D.; Horenstein, B.; Nakanishi, K.; Kustin, K. *Acc. Chem. Res.* **1991**, *24*, 117-124.

152. Rehder, D. *Angew. Chem. Int. Ed. Engl.* **1991**, *30*, 148-167 and references therein.

153. Slebodnick, C.; Hamstra, B. J.; Pecoraro, V. L. *Struct. Bond.* **1997**, *89*, 51-108 and references therein.

154. Crans, D. C.; Smee, J. J.; Gaidamauskas, E.; Yang, L. *Chem. Rev.* **2004**, *104*, 849-902 and references therein.

155. ter Meulen, H. *Recl. Trav. Chim. Pays-Bas.* **1931**, *50*, 491-504.

156. Bayer, E.; Kneifel, H. *Z. Naturforsch.* **1972**, *27*, 207.

157. Cantley, Jr., L. C.; Josephson, L.; Warner, R.; Yanagisawa, M.; Lechene, C.; Guidotti, G. *J. Biol. Chem.* **1977**, *252*, 7421-7423.

158. Josephson, L.; Cantley, C. *Biochem.* **1977**, *16*, 4572-4578.

159. Butler, A.; Walker, J. V. *Chem. Rev.* **1993**, *93*, 1937-1944 and references therein.

160. Eady, R. R. *Vanadium Nitrogenases*. In: Chasteen, N. D. (ed) Vanadium in Biological Systems. **1990**, Kluwer, Boston, p. 99.

161. Nielsen, F. H. *FASEB J.* **1991**, *5*, 2661-2667.

162. Thompson, K. H.; Orvig, C. *Coord. Chem. Rev.* **2001**, *219-221*, 1033-1053 and references therein.

163. Shechter, Y.; Goldwaser, I.; Mironchik, M.; Fridkin, M.; Gefel, D. *Coord. Chem. Rev.* **2003**, *237*, 3-11 and references therein.

164. Thompson, K. H.; Lichter, J.; LeBel, C.; Scaife, M. C.; McNeill, J. H.; Orvig, C. *J. Inorg. Biochem.* **2009**, *103*, 554-558.

165. Thompson, K. H.; Liboiron, B. D.; Sun, Y.; Bellman, K. D. D.; Setyawati, I. A.; Patrick, B. O.; Karunaratne, V.; Rawji, G.; Wheeler, J.; Sutton, K.; Bhanot, S.; Cassidy, C.; McNeill, J. H.; Yen, V. G.; Orvig, C. *J. Biol. Inorg. Chem.* **2003**, *8*, 66-74.

166. Zhang, S.-Q.; Zhong, X.-Y.; Chen, G.-H.; Lu, W.-L.; Zhang, Q.; *J. Pharm. Pharmacol.* **2008**, *60*, 99-105.

167. Kiss, T.; Jakusch, T.; Hollender, D.; Dörnyei, A.; Enyedy, E. A.; Costa Pessoa, J.; Sakurai, H.; Sanz-Medel, A. *Coord. Chem. Rev.* **2008**, *252*, 1153-1162 and references therein.

168. Monga, V.; Thompson, K. H.; Yuen, V. G.; Sharma, V.; Patrick, B. O.; McNeill, J. H.; Orvig, C. *Inorg. Chem.* **2005**, *44*, 2678-2688.

169. Tasiopoulos, A. J.; Troganis, A. N.; Evangelou, A.; Raptopoulou, C. P.; Terzis, A.; Deligiannakis, Y.; Kabanos, T. A. *Chem. Eur. J.* **1999**, *5*, 910-921.

170. Tasiopoulos, A. J.; Troganis, A. N.; Deligiannakis, Y.; Evangelou, A.; Kabanos, T. A.; Woollins, D.; Slawin, A. *J. Inorg. Biochem.* **2000**, *79*, 159-166.

171. Sakurai, H.; Taira, Z.-E.; Sakai, N. *Inorg. Chim. Acta* **1988**, *151*, 85-86.

172. Hazari, S. K. S.; Kopf, J.; Palit, D.; Rakshit, S.; Rehder, D. *Inorg. Chim. Acta* **2009**, *362*, 1343-1347.

173. Farchione, D.; Wedd, A. G.; Tiekink, E. R. T. *Acta Cryst.* **1991**, *C47*, 650-651.

174. Dutton, J. C.; Fallon, G. D.; Murray, K. S. *Inorg. Chem.* **1988**, *27*, 34-38.

175. Margerum, D. W. *Pure Appl. Chem.* **1983**, *55*, 23 and references therein.

176. Laussac, J.-P.; Sarkar, B. *Biochem.* **1984**, *23*, 2832-2838.

177. Nagashima, S.; Nakasako, M.; Dohmae, N.; Tsujimura, M.; Takio, K.; Odaka, m.; Yohda, M.; Kamiya, N.; Endo, I. *Nat. Struct. Biol.* **1998**, *5*, 347-351.

178. Cremo, C. R.; Loo, J. A.; Edmonds, C. G.; Hatlelid, K. M. *Biochem.*, **1992**, *31*, 491-497.

179. Hanson, G. R.; Kabanos, T. A.; Keramidas, A. D.; Mentzafos, D.; Terzis, A. Inorg. *Chem.* **1992**, *31*, 2587-2594.

180. Cornman, C. R.; Zovinka, E. P.; Boyajian, Y. D.; Geiser-Bush, K. M.; Boyle, P. D.; Singh, P. *Inorg. Chem.* **1995**, *34*, 4213-4219.

181. Borovik, A. S.; Dewey, T. M.; Raymond, K. N. *Inorg. Chem.* **1993**, *32*, 413-421.

182. Keramidas, A. D.; Papaioannou, A. B.; Vlahos, A.; Kabanos, T. A.; Bonas, G.; Makriyannis, A.; Rapropoulou, C. P.; Terzis, A. *Inorg. Chem.* **1996**, *35*, 357-367.

183. Green, K. N.; Brothers, S. M.; Lee, B.; Darensbourg, M. Y.; Rockcliffe, D. A. *Inorg. Chem.* **2009**, *48*, 2780-2792.

184. Almaraz, E.; Foley, W. S.; Denny, J. A.; Reibenspies, J. H.; Golden, M. L.; Darensbourg, M. Y. *Inorg. Chem.* **2009**, *48*, 5288-5295.

185. Hess, J. L.; Conder, H. L.; Green, K. N.; Darensbourg, M. Y. *Inorg. Chem.* **2008**, *47*, 2056-2063.

186. Buonomo, R. M.; Goodman, D. C.; Musie, G.; Grapperhaus, C. A.; Maguire, M. J.; Lai, C.-H.; Hatley, M. L.; Smee, J. J.; Bellefeuille, J. A.; Darensbourg, M. Y. *Inorg. Syn.* **1998**, *32*, 89-98.

187. Darensbourg, M. Y.; Font, I.; Pala, M.; Reibenspies, J. H. *J. Coord. Chem.* **1994**, *32*, 39-49.

188. D. J. Darensbourg, R. L. Kump, *Inorg. Chem.* **1978**, *17*, 2680-2682.

189. Hatley, M. L. Masters Thesis "*The Vanadyl Complex of N,N'-bis(2-mercaptoethyl)-1,5-diazacyclooctane"* 1997, pg 16-18.

190. Green, K. G.; Jeffery, S. P.; Reibenspies, J. H.; Darensbourg, M. Y. *J. Am. Chem. Soc.* **2006**, *128*, 6493-6498.

191. Selbin, J. *Chem. Rev.* **1965**, *65*, 153-175.

192. Selbin, J. *Coord. Chem. Rev.* **1966**, *1*, 293-314.

193. Money, J. K.; Huffman, J. C.; Christou, G. *Inorg. Chem.* **1985**, *24*, 3297-3302.

194. Klich, P. R.; Daniher, A. T.; Challen, P. R.; McConville, D. B.; Youngs, W. J. *Inorg. Chem.* **1996**, *35*, 347-356.

195. Jezierski, A.; Raynor, J. B. *J. Chem. Soc., Dalton Trans.* **1981**, 1-7.

196. Rampersad, M. V.; Jeffery, S. P.; Golden, M. L.; Lee, J.; Reibenspies, J. H.; Darensbourg, D. J.; Darensbourg, M. Y. *J. Am. Chem. Soc.* **2005**, *127*, 17323-17334.

197. Phelps, A. L.; Rampersad, M. V.; Fitch, S. B.; Darensbourg, M. Y.; Darensbourg, D. J. *Inorg. Chem.* **2006**, *45*, 119-126.

198. Rampersad, M. V.; Jeffery, S.P.; Reibenspies, J. H.; Ortiz, C. G.; Darensbourg, D. J.; Darensbourg, M. Y. *Angew. Chem., Int. Ed.* **2005**, *44*, 1217-1220.

199. Cotton, F. A.; Kraihanzel, C. S. *J. Am. Chem. Soc.* **1962**, *84*, 4432-4438.

200. Gelinsky, M.; Vogler, R.; Vahrenkamp, H. *Inorg. Chem.* **2002** *41*, 2560-2564

201. Mullins, C. S.; Grapperhaus, C. A.; Frye, B. C.; Wood, L. H.; Hay, A. J.; Buchanan, R. M.; Mashuta, M. S. *Inorg. Chem.* **2009**, *48*, 9974-9976.

202. Kaasjager, V. E.; Bouwnan, E.; Gorter, S.; Reedjik, J.; Grapperhaus, C. A.; Reibenspies, J. H.; Smee, J. J.; Darensbourg, M. Y.; Derecskei-Kovas, A.; Thomson, L. M. *Inorg. Chem.* **2002**, *41*, 1837-1844 and references therein.

203. Shearer, J.; Neupane, K. P.; Callan, P. E. *Inorg. Chem.*, **2009**, *48*, 10560–10571 and references therein.

204. Krause, M. E.; Glass, A. M.; Jackson, T. A.; Laurence, J. S. *Inorg. Chem.* **2010**, *49*, 362-364.

APPENDIX

CRYSTALLOGRAPHIC DATA FOR STRUCTURES

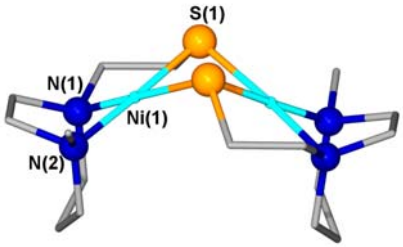

[(me-mdach)Ni]$_2$(BF$_4$)$_2$

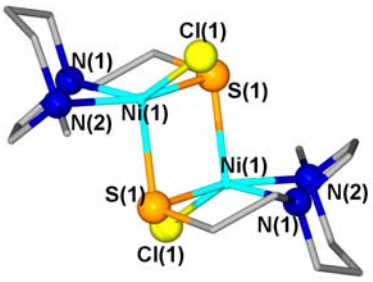

[(me-mdach)-NiCl]$_2$

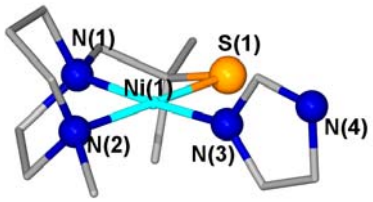

[(mmp-mdach)Ni(Im)]Cl

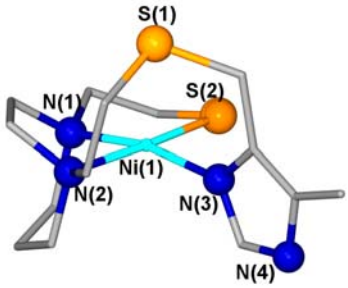

[Ni-1'(CH$_2$-mIm)]Cl

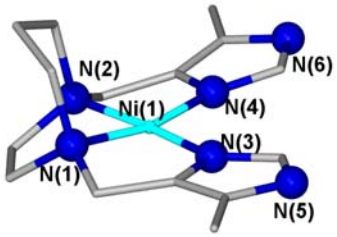

[(bmIme-dach)Ni](BF$_4$)$_2$

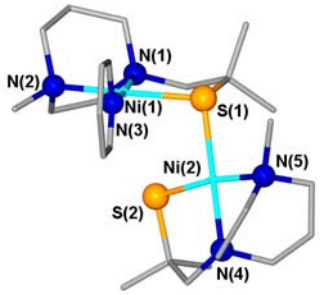

py-[(mmp-mdach)Ni]$_2$[BF$_4$]$_2$

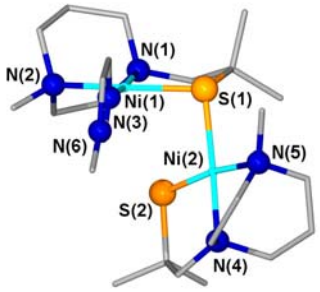

mIm-[(mmp-mdach)Ni]$_2$[BF$_4$]$_2$

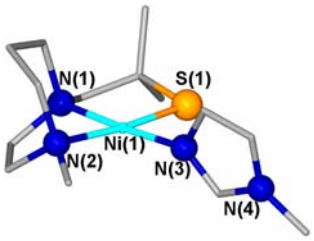

[(mmp-mdach)Ni(mIm)][BF$_4$]

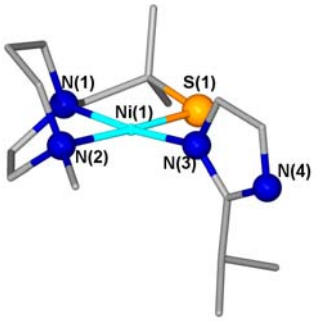

[(mmp-mdach)Ni(ipIm)][BF$_4$]

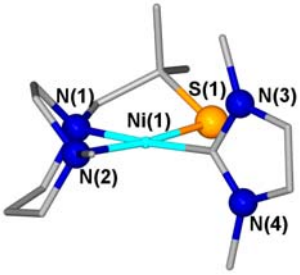

[(mmp-mdach)Ni(me$_2$NHC)][I]

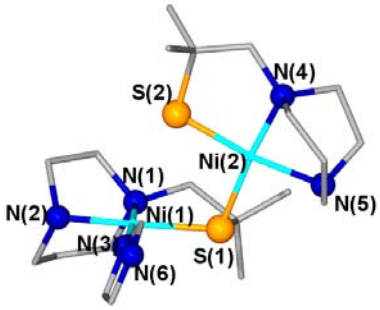

Im-[(mmp-dach)Ni]$_2$[BF$_4$]$_2$

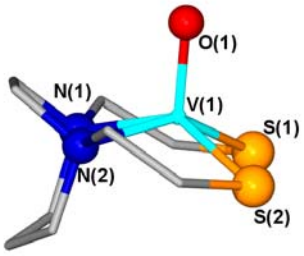

[(bme-dach)(V=O)]

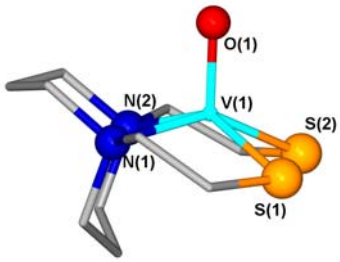

[(bme-daco)(V=O)]

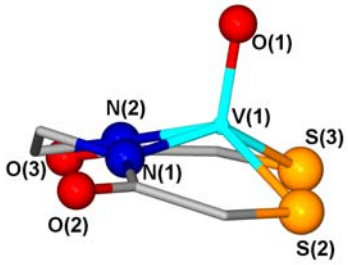

$[Et_4N]_2[(V=O)(ema)]$

Table A-1. Crystal data and structure refinement for $[(me\text{-}mdach)Ni]_2(BF_4)_2$.

Empirical formula	C16 H34 Cl2 N4 Ni2 S2	
Formula weight	534.91	
Temperature	110(2) K	
Wavelength	0.71073 Å	
Crystal system	Monoclinic	
Space group	P2(1)/c	
Unit cell dimensions	a = 7.599(3) Å	α= 90°.
	b = 8.361(3) Å	β = 102.236(6)°.
	c = 17.927(6) Å	γ = 90°.
Volume	1113.1(7) $Å^3$	
Z	2	
Density (calculated)	1.596 Mg/m^3	
Absorption coefficient	2.128 mm^{-1}	
F(000)	560	
Crystal size	0.15 x 0.13 x 0.12 mm^3	
Theta range for data collection	4.02 to 24.99°.	
Index ranges	-9<=h<=9, -9<=k<=9, -21<=l<=21	
Reflections collected	8046	
Independent reflections	1899 [R(int) = 0.0549]	
Completeness to theta = 24.99°	97.0 %	
Absorption correction	Semi-empirical from equivalents	
Max. and min. transmission	0.7843 and 0.7408	
Refinement method	Full-matrix least-squares on F^2	
Data / restraints / parameters	1899 / 0 / 119	
Goodness-of-fit on F^2	1.155	
Final R indices [I>2sigma(I)]	R1 = 0.0597, wR2 = 0.1337	
R indices (all data)	R1 = 0.0690, wR2 = 0.1369	
Largest diff. peak and hole	0.730 and -0.462 $e.Å^{-3}$	

Table B2. Bond lengths [Å] and angles [°] for $[(me\text{-}mdach)Ni]_2(BF_4)_2$.

Ni(1)-N(1)	2.084(5)
Ni(1)-N(2)	2.144(5)
Ni(1)-Cl(1)	2.3315(17)
Ni(1)-S(1)#1	2.3461(18)
Ni(1)-S(1)	2.3693(17)
S(1)-C(1)	1.829(6)
S(1)-Ni(1)#1	2.3461(18)
N(1)-C(2)	1.468(8)
N(1)-C(6)	1.487(8)
N(1)-C(3)	1.491(8)
N(2)-C(8)	1.463(8)
N(2)-C(7)	1.478(7)
N(2)-C(5)	1.505(9)
C(1)-C(2)	1.520(8)
C(3)-C(4)	1.501(9)
C(4)-C(5)	1.523(9)
C(6)-C(7)	1.562(8)
N(1)-Ni(1)-N(2)	77.3(2)
N(1)-Ni(1)-Cl(1)	144.45(15)
N(2)-Ni(1)-Cl(1)	92.91(14)
N(1)-Ni(1)-S(1)#1	100.60(15)
N(2)-Ni(1)-S(1)#1	96.77(15)
Cl(1)-Ni(1)-S(1)#1	114.57(6)
N(1)-Ni(1)-S(1)	86.66(14)
N(2)-Ni(1)-S(1)	162.82(15)
Cl(1)-Ni(1)-S(1)	96.61(6)
S(1)#1-Ni(1)-S(1)	92.25(5)
C(1)-S(1)-Ni(1)#1	104.6(2)
C(1)-S(1)-Ni(1)	96.53(19)
Ni(1)#1-S(1)-Ni(1)	87.75(5)
C(2)-N(1)-C(6)	110.0(5)
C(2)-N(1)-C(3)	111.7(5)

Table B-2 (continuted)

C(6)-N(1)-C(3)	111.4(5)
C(2)-N(1)-Ni(1)	111.6(3)
C(6)-N(1)-Ni(1)	107.1(3)
C(3)-N(1)-Ni(1)	104.7(4)
C(8)-N(2)-C(7)	110.5(5)
C(8)-N(2)-C(5)	109.2(5)
C(7)-N(2)-C(5)	110.2(5)
C(8)-N(2)-Ni(1)	114.0(4)
C(7)-N(2)-Ni(1)	105.8(4)
C(5)-N(2)-Ni(1)	107.0(4)
C(2)-C(1)-S(1)	111.3(4)
N(1)-C(2)-C(1)	111.8(5)
N(1)-C(3)-C(4)	113.7(5)
C(3)-C(4)-C(5)	114.7(5)
N(2)-C(5)-C(4)	112.7(5)
N(1)-C(6)-C(7)	111.6(5)
N(2)-C(7)-C(6)	111.1(5)

Symmetry transformations used to generate equivalent atoms:

#1 -x+1,-y+1,-z+1

Table B-3. Crystal data and structure refinement for [(me-mdach)-NiCl]$_2$.

Empirical formula	C8 H17 B F4 N2 Ni S	
Formula weight	318.82	
Temperature	110(2) K	
Wavelength	1.54178 Å	
Crystal system	Orthorhombic	
Space group	P2(1)2(1)2	
Unit cell dimensions	a = 10.1120(16) Å	α= 90°.
	b = 19.466(3) Å	β= 90°.
	c = 6.0785(9) Å	γ = 90°.
Volume	1196.5(3) Å^3	
Z	4	
Density (calculated)	1.770 Mg/m^3	
Absorption coefficient	4.293 mm^{-1}	
F(000)	656	
Crystal size	0.20 x 0.20 x 0.01 mm^3	
Theta range for data collection	4.54 to 59.96°.	
Index ranges	-9<=h<=11, -20<=k<=21, -6<=l<=6	
Reflections collected	7385	
Independent reflections	1597 [R(int) = 0.1327]	
Completeness to theta = 59.96°	92.2 %	
Absorption correction	Semi-empirical from equivalents	
Max. and min. transmission	0.9583 and 0.4806	
Refinement method	Full-matrix least-squares on F^2	
Data / restraints / parameters	1597 / 268 / 238	
Goodness-of-fit on F^2	1.024	
Final R indices [I>2sigma(I)]	R1 = 0.0650, wR2 = 0.1469	
R indices (all data)	R1 = 0.0927, wR2 = 0.1578	
Absolute structure parameter	0.0(3)	
Largest diff. peak and hole	1.550 and -0.431 e.Å^{-3}	

Table B-4. Bond lengths [Å] and angles [°] for [(me-mdach)-$NiCl]_2$.

Ni(1)-N(2)	1.914(8)
Ni(1)-N(1)	1.923(8)
Ni(1)-S(1')	2.106(17)
Ni(1)-S(1')#1	2.288(17)
Ni(1)-S(1)	2.069(19)
Ni(1)-S(1)#1	2.245(16)
Ni(1)-Ni(1)#1	2.837(3)
S(1)-C(1)	1.800(17)
S(1)-Ni(1)#1	2.245(16)
S(1')-C(1')	1.785(17)
S(1')-Ni(1)#1	2.288(17)
N(1)-C(8')	1.499(18)
N(1)-C(3)	1.503(12)
N(1)-C(6)	1.520(12)
N(1)-C(2)	1.53(2)
N(2)-C(5)	1.464(12)
N(2)-C(8)	1.523(19)
N(2)-C(7)	1.529(11)
N(2)-C(2')	1.542(18)
C(1)-C(2)	1.53(2)
C(1')-C(2')	1.53(2)
C(3)-C(4)	1.552(14)
C(4)-C(5)	1.509(13)
C(6)-C(7)	1.495(14)
B13-F43	1.353(18)
B13-F13	1.359(13)
B13-F33	1.378(16)
B13-F23	1.410(15)
B14-F44	1.354(18)
B14-F14	1.358(14)
B14-F34	1.378(17)
B14-F24	1.409(15)

Table B-4 (continued)

N(2)-Ni(1)-N(1)	83.6(3)
N(2)-Ni(1)-S(1')	95.7(4)
N(1)-Ni(1)-S(1')	177.8(6)
N(2)-Ni(1)-S(1')#1	176.4(5)
N(1)-Ni(1)-S(1')#1	99.7(4)
S(1')-Ni(1)-S(1')#1	81.1(6)
N(2)-Ni(1)-S(1)	178.3(6)
N(1)-Ni(1)-S(1)	96.4(5)
S(1')-Ni(1)-S(1)	84.2(5)
S(1')#1-Ni(1)-S(1)	4.6(8)
N(2)-Ni(1)-S(1)#1	100.5(4)
N(1)-Ni(1)-S(1)#1	175.4(5)
S(1')-Ni(1)-S(1)#1	6.4(9)
S(1')#1-Ni(1)-S(1)#1	76.2(5)
S(1)-Ni(1)-S(1)#1	79.6(6)
N(2)-Ni(1)-Ni(1)#1	129.5(2)
N(1)-Ni(1)-Ni(1)#1	129.3(2)
S(1')-Ni(1)-Ni(1)#1	52.7(5)
S(1')#1-Ni(1)-Ni(1)#1	47.0(4)
S(1)-Ni(1)-Ni(1)#1	51.6(4)
S(1)#1-Ni(1)-Ni(1)#1	46.3(5)
C(1)-S(1)-Ni(1)	96.2(10)
C(1)-S(1)-Ni(1)#1	118.3(10)
Ni(1)-S(1)-Ni(1)#1	82.1(6)
C(1')-S(1')-Ni(1)	96.7(9)
C(1')-S(1')-Ni(1)#1	118.1(11)
Ni(1)-S(1')-Ni(1)#1	80.3(6)
C(8')-N(1)-C(3)	108.1(11)
C(8')-N(1)-C(6)	102.4(10)
C(3)-N(1)-C(6)	112.1(8)
C(8')-N(1)-C(2)	20.6(10)
C(3)-N(1)-C(2)	111.4(14)
C(6)-N(1)-C(2)	117.3(11)

Table B-4 (continued)

C(8')-N(1)-Ni(1)	122.4(9)
C(3)-N(1)-Ni(1)	108.6(6)
C(6)-N(1)-Ni(1)	102.9(6)
C(2)-N(1)-Ni(1)	103.4(10)
C(5)-N(2)-C(8)	118.5(13)
C(5)-N(2)-C(7)	109.6(7)
C(8)-N(2)-C(7)	98.2(10)
C(5)-N(2)-C(2')	107.9(12)
C(8)-N(2)-C(2')	21.8(9)
C(7)-N(2)-C(2')	120.0(10)
C(5)-N(2)-Ni(1)	107.2(6)
C(8)-N(2)-Ni(1)	116.9(12)
C(7)-N(2)-Ni(1)	105.1(6)
C(2')-N(2)-Ni(1)	106.4(9)
C(2)-C(1)-S(1)	101.8(16)
N(1)-C(2)-C(1)	113.2(15)
C(2')-C(1')-S(1')	105.1(13)
C(1')-C(2')-N(2)	114.3(14)
N(1)-C(3)-C(4)	113.8(8)
C(5)-C(4)-C(3)	112.1(9)
N(2)-C(5)-C(4)	117.8(8)
C(7)-C(6)-N(1)	111.5(8)
C(6)-C(7)-N(2)	109.3(8)
F43-B13-F13	112.1(13)
F43-B13-F33	108.2(12)
F13-B13-F33	110.2(12)
F43-B13-F23	108.7(12)
F13-B13-F23	110.0(10)
F33-B13-F23	107.4(12)
F44-B14-F14	111.6(14)
F44-B14-F34	107.9(13)
F14-B14-F34	110.3(13)
F44-B14-F24	108.9(13)

Table B-4 (continued)

F14-B14-F24	110.3(11)
F34-B14-F24	107.8(13)

Symmetry transformations used to generate equivalent atoms:

#1 -x,-y,z

Table B-5. Crystal data and structure refinement for [(mmp-mdach)Ni(Im)]Cl.

Empirical formula	C14 H29 Cl N4 Ni O S	
Formula weight	395.63	
Temperature	110(2) K	
Wavelength	0.71073 Å	
Crystal system	Orthorhombic	
Space group	Pna2(1)	
Unit cell dimensions	a = 9.954(3) Å	α= 90°.
	b = 21.542(8) Å	β = 90°.
	c = 9.090(3) Å	γ= 90°.
Volume	1949.3(11) $Å^3$	
Z	4	
Density (calculated)	1.348 Mg/m^3	
Absorption coefficient	1.246 mm^{-1}	
F(000)	840	
Crystal size	0.30 x 0.10 x 0.10 mm^3	
Theta range for data collection	2.43 to 25.00°.	
Index ranges	-11<=h<=7, -25<=k<=24, -6<=l<=10	
Reflections collected	4018	
Independent reflections	2350 [R(int) = 0.0956]	
Completeness to theta = 25.00°	93.6 %	
Absorption correction	Semi-empirical from equivalents	
Max. and min. transmission	0.8856 and 0.7063	
Refinement method	Full-matrix least-squares on F^2	
Data / restraints / parameters	2350 / 192 / 207	
Goodness-of-fit on F^2	1.020	
Final R indices [I>2sigma(I)]	R1 = 0.0634, wR2 = 0.1046	
R indices (all data)	R1 = 0.1162, wR2 = 0.1205	
Absolute structure parameter	0.00(4)	
Largest diff. peak and hole	0.858 and -0.577 $e.Å^{-3}$	

Table B-6. Bond lengths [Å] and angles [°] for [(mmp-mdach)Ni(Im)]Cl.

Ni(1)-N(3)	1.888(9)
Ni(1)-N(1)	1.897(10)
Ni(1)-N(2)	1.949(10)
Ni(1)-S(1)	2.149(3)
N(1)-C(2)	1.489(15)
N(1)-C(6)	1.517(17)
N(1)-C(3)	1.577(14)
C(1)-C(10)	1.390(17)
C(1)-C(2)	1.528(15)
C(1)-C(9)	1.607(16)
C(1)-S(1)	1.852(12)
N(2)-C(5)	1.337(16)
N(2)-C(7)	1.468(17)
N(2)-C(8)	1.623(17)
N(3)-C(13)	1.342(12)
N(3)-C(11)	1.372(13)
C(3)-C(4)	1.541(5)
N(4)-C(13)	1.326(13)
N(4)-C(12)	1.413(13)
C(4)-C(5)	1.550(5)
C(6)-C(7)	1.611(17)
C(11)-C(12)	1.316(14)
O11-C11	1.679(19)
O12-C12	1.684(19)
N(3)-Ni(1)-N(1)	175.5(4)
N(3)-Ni(1)-N(2)	97.1(4)
N(1)-Ni(1)-N(2)	81.5(5)
N(3)-Ni(1)-S(1)	91.4(3)
N(1)-Ni(1)-S(1)	90.4(3)
N(2)-Ni(1)-S(1)	170.6(4)
C(2)-N(1)-C(6)	120.8(10)
C(2)-N(1)-C(3)	105.6(9)
C(6)-N(1)-C(3)	101.5(9)

Table B-6 (continuted)

C(2)-N(1)-Ni(1)	114.5(7)
C(6)-N(1)-Ni(1)	108.2(8)
C(3)-N(1)-Ni(1)	103.9(7)
C(10)-C(1)-C(2)	112.1(10)
C(10)-C(1)-C(9)	111.0(10)
C(2)-C(1)-C(9)	108.3(10)
C(10)-C(1)-S(1)	114.4(10)
C(2)-C(1)-S(1)	103.0(7)
C(9)-C(1)-S(1)	107.6(8)
C(1)-S(1)-Ni(1)	99.1(4)
C(5)-N(2)-C(7)	123.0(11)
C(5)-N(2)-C(8)	101.1(9)
C(7)-N(2)-C(8)	95.3(10)
C(5)-N(2)-Ni(1)	113.8(10)
C(7)-N(2)-Ni(1)	107.3(8)
C(8)-N(2)-Ni(1)	114.8(8)
N(1)-C(2)-C(1)	115.0(10)
C(13)-N(3)-C(11)	103.7(9)
C(13)-N(3)-Ni(1)	125.1(7)
C(11)-N(3)-Ni(1)	131.1(7)
C(4)-C(3)-N(1)	112.0(10)
C(13)-N(4)-C(12)	106.5(9)
C(3)-C(4)-C(5)	120.0(10)
N(2)-C(5)-C(4)	102.1(11)
N(1)-C(6)-C(7)	111.1(11)
N(2)-C(7)-C(6)	102.5(12)
C(12)-C(11)-N(3)	112.5(10)
C(11)-C(12)-N(4)	105.2(10)
N(4)-C(13)-N(3)	112.0(9)

Table B-7. Crystal data and structure refinement for [Ni-1'(CH_2-mIm)]Cl.

Empirical formula	C14 H25 Cl N4 Ni S2	
Formula weight	407.66	
Temperature	110(2) K	
Wavelength	0.71073 Å	
Crystal system	Triclinic	
Space group	P-1	
Unit cell dimensions	a = 7.409(4) Å	α = 75.918(9)°.
	b = 11.169(6) Å	β= 71.534(9)°.
	c = 11.640(6) Å	γ = 71.494(9)°.
Volume	855.4(8) $Å^3$	
Z	2	
Density (calculated)	1.583 Mg/m^3	
Absorption coefficient	1.535 mm^{-1}	
F(000)	428	
Crystal size	0.16 x 0.08 x 0.02 mm^3	
Theta range for data collection	1.87 to 27.49°.	
Index ranges	-9<=h<=9, -14<=k<=14, -14<=l<=15	
Reflections collected	9125	
Independent reflections	3810 [R(int) = 0.3126]	
Completeness to theta = 27.49°	96.7 %	
Absorption correction	Semi-empirical from equivalents	
Max. and min. transmission	0.9670 and 0.7868	
Refinement method	Full-matrix least-squares on F^2	
Data / restraints / parameters	3810 / 12 / 194	
Goodness-of-fit on F^2	0.907	
Final R indices [I>2sigma(I)]	R1 = 0.0925, wR2 = 0.1609	
R indices (all data)	R1 = 0.1648, wR2 = 0.1886	
Largest diff. peak and hole	1.411 and -1.082 e.$Å^{-3}$	

Table B-8. Bond lengths [Å] and angles [°] for [Ni-1'(CH_2-mIm)]Cl.

Ni(1)-N(1)	1.906(7)
Ni(1)-N(3)	1.908(7)
Ni(1)-N(2)	1.995(5)
Ni(1)-S(2)	2.168(2)
S(2)-C(7)	1.837(9)
S(1)-C(10)	1.815(7)
S(1)-C(9)	1.821(7)
N(3)-C(13)	1.322(8)
N(3)-C(11)	1.378(10)
N(4)-C(13)	1.336(10)
N(4)-C(12)	1.381(9)
N(1)-C(1)	1.500(8)
N(1)-C(5)	1.501(7)
N(1)-C(6)	1.507(10)
C(11)-C(12)	1.324(11)
C(11)-C(10)	1.499(9)
C(8)-N(2)	1.469(10)
C(8)-C(9)	1.528(9)
C(7)-C(6)	1.513(9)
N(2)-C(4)	1.488(9)
N(2)-C(3)	1.498(9)
C(1)-C(2)	1.523(10)
C(5)-C(4)	1.536(11)
C(14)-C(12)	1.485(12)
C(3)-C(2)	1.510(12)
N(1)-Ni(1)-N(3)	166.6(2)
N(1)-Ni(1)-N(2)	82.3(3)
N(3)-Ni(1)-N(2)	95.5(3)
N(1)-Ni(1)-S(2)	90.27(19)
N(3)-Ni(1)-S(2)	91.57(18)
N(2)-Ni(1)-S(2)	172.6(2)
C(7)-S(2)-Ni(1)	98.5(2)
C(10)-S(1)-C(9)	101.9(4)

Table B-8 (continued)

C(13)-N(3)-C(11)	106.7(7)
C(13)-N(3)-Ni(1)	122.0(5)
C(11)-N(3)-Ni(1)	131.0(4)
C(13)-N(4)-C(12)	107.7(6)
C(1)-N(1)-C(5)	110.7(5)
C(1)-N(1)-C(6)	108.9(5)
C(5)-N(1)-C(6)	110.7(6)
C(1)-N(1)-Ni(1)	102.7(5)
C(5)-N(1)-Ni(1)	109.4(5)
C(6)-N(1)-Ni(1)	114.2(5)
C(12)-C(11)-N(3)	109.2(6)
C(12)-C(11)-C(10)	128.6(7)
N(3)-C(11)-C(10)	122.2(7)
N(2)-C(8)-C(9)	116.3(6)
C(6)-C(7)-S(2)	107.2(5)
C(8)-N(2)-C(4)	110.5(5)
C(8)-N(2)-C(3)	107.8(6)
C(4)-N(2)-C(3)	109.3(6)
C(8)-N(2)-Ni(1)	117.2(5)
C(4)-N(2)-Ni(1)	107.8(4)
C(3)-N(2)-Ni(1)	103.9(4)
N(1)-C(1)-C(2)	112.7(6)
N(3)-C(13)-N(4)	109.7(6)
N(1)-C(5)-C(4)	110.4(6)
N(2)-C(4)-C(5)	110.0(5)
C(11)-C(12)-N(4)	106.7(7)
C(11)-C(12)-C(14)	131.8(6)
N(4)-C(12)-C(14)	121.5(7)
C(8)-C(9)-S(1)	116.2(5)
N(1)-C(6)-C(7)	109.5(6)
C(11)-C(10)-S(1)	114.8(5)
N(2)-C(3)-C(2)	112.8(7)
C(3)-C(2)-C(1)	115.3(7)

Table B-9. Crystal data and structure refinement for [(bmIme-dach)Ni]$(BF_4)_2$.

Empirical formula	C15 H22 B2 F8 N6 Ni	
Formula weight	518.72	
Temperature	110(2) K	
Wavelength	0.71073 Å	
Crystal system	Monoclinic	
Space group	P2(1)/n	
Unit cell dimensions	a = 11.8350(19) Å	α = 90°.
	b = 13.9584(19) Å	β= 104.383(7)°.
	c = 13.0506(13) Å	γ = 90°.
Volume	2088.4(5) $Å^3$	
Z	4	
Density (calculated)	1.650 Mg/m^3	
Absorption coefficient	1.015 mm^{-1}	
F(000)	1056	
Crystal size	0.20 x 0.20 x 0.20 mm^3	
Theta range for data collection	2.17 to 25.00°.	
Index ranges	-10<=h<=14, -15<=k<=6, -14<=l<=15	
Reflections collected	4777	
Independent reflections	3370 [R(int) = 0.0275]	
Completeness to theta = 25.00°	91.7 %	
Absorption correction	None	
Max. and min. transmission	0.8228 and 0.8228	
Refinement method	Full-matrix least-squares on F^2	
Data / restraints / parameters	3370 / 20 / 347	
Goodness-of-fit on F^2	1.063	
Final R indices [I>2sigma(I)]	R1 = 0.0550, wR2 = 0.1463	
R indices (all data)	R1 = 0.0640, wR2 = 0.1547	
Largest diff. peak and hole	1.177 and -0.553 $e.Å^{-3}$	

Table B-10. Bond lengths [Å] and angles [°] for [(bmIme-dach)Ni]$(BF_4)_2$.

Ni(1)-N(3)	1.873(3)
Ni(1)-N(4)	1.893(3)
Ni(1)-N(2)	1.904(3)
Ni(1)-N(1)	1.913(3)
N(1)-C(5)	1.485(5)
N(1)-C(12)	1.507(5)
N(1)-C(13)	1.516(5)
N(2)-C(10)	1.490(5)
N(2)-C(14)	1.494(5)
N(2)-C(9)	1.515(5)
N(3)-C(2)	1.332(5)
N(3)-C(1)	1.373(5)
N(4)-C(16)	1.340(5)
N(4)-C(8)	1.386(5)
N(5)-C(2)	1.333(5)
N(5)-C(3)	1.376(6)
N(6)-C(16)	1.343(6)
N(6)-C(7)	1.382(6)
C(1)-C(3)	1.379(6)
C(1)-C(5)	1.489(6)
C(3)-C(4)	1.501(6)
C(7)-C(8)	1.360(5)
C(7)-C(15)	1.500(6)
C(8)-C(9)	1.487(6)
C(10)-C(11)	1.511(6)
C(11)-C(12)	1.512(6)
C(13)-C(14)	1.529(6)
B(1A)-F(3A)	1.376(6)
B(1A)-F(2A)	1.377(6)
B(1A)-F(4A)	1.398(6)
B(1A)-F(1A)	1.399(6)
B(2A)-F(6A)	1.306(10)
B(2A)-F(8A)	1.343(10)

Table B-10 (continued)

B(2A)-F(7A)	1.352(10)
B(2A)-F(5A)	1.410(9)
N(3)-Ni(1)-N(4)	104.07(14)
N(3)-Ni(1)-N(2)	169.62(13)
N(4)-Ni(1)-N(2)	85.92(13)
N(3)-Ni(1)-N(1)	86.48(13)
N(4)-Ni(1)-N(1)	167.01(13)
N(2)-Ni(1)-N(1)	83.25(13)
C(5)-N(1)-C(12)	112.3(3)
C(5)-N(1)-C(13)	111.4(3)
C(12)-N(1)-C(13)	110.3(3)
C(5)-N(1)-Ni(1)	110.6(2)
C(12)-N(1)-Ni(1)	103.8(2)
C(13)-N(1)-Ni(1)	108.1(2)
C(10)-N(2)-C(14)	111.9(3)
C(10)-N(2)-C(9)	111.2(3)
C(14)-N(2)-C(9)	111.4(3)
C(10)-N(2)-Ni(1)	104.3(2)
C(14)-N(2)-Ni(1)	108.3(2)
C(9)-N(2)-Ni(1)	109.4(2)
C(2)-N(3)-C(1)	107.0(3)
C(2)-N(3)-Ni(1)	139.8(3)
C(1)-N(3)-Ni(1)	113.0(2)
C(16)-N(4)-C(8)	106.3(3)
C(16)-N(4)-Ni(1)	140.0(3)
C(8)-N(4)-Ni(1)	112.9(2)
C(2)-N(5)-C(3)	109.5(3)
C(16)-N(6)-C(7)	109.9(3)
N(3)-C(1)-C(3)	109.0(4)
N(3)-C(1)-C(5)	116.2(3)
C(3)-C(1)-C(5)	134.3(4)
N(3)-C(2)-N(5)	109.6(4)
N(5)-C(3)-C(1)	104.8(4)

Table B-10 (continued)

N(5)-C(3)-C(4)	124.7(4)
C(1)-C(3)-C(4)	130.4(4)
N(1)-C(5)-C(1)	106.7(3)
C(8)-C(7)-N(6)	104.6(4)
C(8)-C(7)-C(15)	132.3(4)
N(6)-C(7)-C(15)	123.2(4)
C(7)-C(8)-N(4)	110.2(4)
C(7)-C(8)-C(9)	134.5(4)
N(4)-C(8)-C(9)	115.2(3)
C(8)-C(9)-N(2)	105.6(3)
N(2)-C(10)-C(11)	111.5(3)
C(10)-C(11)-C(12)	116.3(3)
N(1)-C(12)-C(11)	112.3(3)
N(1)-C(13)-C(14)	108.9(3)
N(2)-C(14)-C(13)	110.1(3)
N(4)-C(16)-N(6)	109.1(4)
F(3A)-B(1A)-F(2A)	109.4(6)
F(3A)-B(1A)-F(4A)	110.7(5)
F(2A)-B(1A)-F(4A)	110.4(5)
F(3A)-B(1A)-F(1A)	108.5(5)
F(2A)-B(1A)-F(1A)	110.0(6)
F(4A)-B(1A)-F(1A)	107.7(5)
F(6A)-B(2A)-F(8A)	109.9(11)
F(6A)-B(2A)-F(7A)	107.8(12)
F(8A)-B(2A)-F(7A)	114.3(12)
F(6A)-B(2A)-F(5A)	101.8(10)
F(8A)-B(2A)-F(5A)	108.8(7)
F(7A)-B(2A)-F(5A)	113.4(10)

Table B-11. Crystal data and structure refinement for py-[(mmp-mdach)Ni]$_2$[BF$_4$]$_2$.

Empirical formula	C27 H50 B2 F8 N6 Ni2 S2	
Formula weight	813.89	
Temperature	110(2) K	
Wavelength	1.54178 Å	
Crystal system	Monoclinic	
Space group	C2/c	
Unit cell dimensions	a = 24.647(9) Å	α = 90°.
	b = 10.904(3) Å	β = 113.28(3)°.
	c = 28.217(8) Å	γ = 90°.
Volume	6966(4) Å^3	
Z	8	
Density (calculated)	1.552 Mg/m^3	
Absorption coefficient	3.104 mm^{-1}	
F(000)	3392	
Crystal size	0.10 x 0.01 x 0.01 mm^3	
Theta range for data collection	4.50 to 60.00°.	
Index ranges	-26<=h<=27, -12<=k<=12, -31<=l<=31	
Reflections collected	22435	
Independent reflections	4965 [R(int) = 0.1605]	
Completeness to theta = 60.00°	96.1 %	
Absorption correction	Semi-empirical from equivalents	
Max. and min. transmission	0.9696 and 0.7466	
Refinement method	Full-matrix least-squares on F^2	
Data / restraints / parameters	4965 / 382 / 452	
Goodness-of-fit on F^2	1.244	
Final R indices [I>2sigma(I)]	R1 = 0.0771, wR2 = 0.1534	
R indices (all data)	R1 = 0.2058, wR2 = 0.1709	
Extinction coefficient	0.000033(7)	
Largest diff. peak and hole	0.708 and -0.481 e.Å^{-3}	

Table B-12. Bond lengths [Å] and angles [°] for py-[(mmp-mdach)Ni]$_2$[BF_4]$_2$.

Ni(1)-N(1)	1.900(4)
Ni(1)-N(3)	1.918(4)
Ni(1)-N(2)	1.951(5)
Ni(1)-S(1)	2.1514(19)
Ni(2)-N(4)	1.930(6)
Ni(2)-N(5)	1.944(5)
Ni(2)-S(2)	2.1333(19)
Ni(2)-S(1)	2.192(2)
S(1)-C(1)	1.864(6)
S(2)-C(16)	1.785(7)
N(1)-C(5)	1.465(7)
N(1)-C(3)	1.490(6)
N(1)-C(2)	1.506(7)
N(2)-C(4)	1.491(7)
N(2)-C(8)	1.490(6)
N(2)-C(7)	1.514(7)
N(3)-C(11)	1.332(7)
N(3)-C(15)	1.371(7)
N(4)-C(17)	1.449(7)
N(4)-C(18)	1.491(8)
N(4)-C(21)	1.469(8)
N(5)-C(20)	1.372(9)
N(5)-C(22)	1.539(9)
N(5)-C(23)	1.581(10)
C(1)-C(2)	1.482(7)
C(1)-C(10)	1.518(8)
C(1)-C(9)	1.536(8)
C(3)-C(4)	1.488(7)
C(5)-C(6)	1.498(8)
C(6)-C(7)	1.497(7)
C(11)-C(12)	1.384(7)
C(12)-C(13)	1.375(8)
C(13)-C(14)	1.390(8)

Table B-12 (continued)

C(14)-C(15)	1.349(7)
C(16)-C(25)	1.511(8)
C(16)-C(17)	1.511(8)
C(16)-C(24)	1.554(8)
C(18)-C(19)	1.416(8)
C(19)-C(20)	1.413(10)
C(21)-C(22)	1.656(9)
N(1N)-C(1N)	1.1425(8)
C(1N)-C(2N)	1.5020(7)
B(1)-F(2)	1.316(3)
B(1)-F(3)	1.414(3)
B(1)-F(1)	1.298(4)
B(1)-F(4)	1.444(3)
B(2)-F(5)	1.298(4)
B(2)-F(6)	1.311(4)
B(2)-F(7)	1.425(4)
B(2)-F(8)	1.447(4)
N(1)-Ni(1)-N(3)	173.6(2)
N(1)-Ni(1)-N(2)	82.64(19)
N(3)-Ni(1)-N(2)	96.15(19)
N(1)-Ni(1)-S(1)	92.33(15)
N(3)-Ni(1)-S(1)	88.92(15)
N(2)-Ni(1)-S(1)	174.94(14)
N(4)-Ni(2)-N(5)	80.8(2)
N(4)-Ni(2)-S(2)	89.87(15)
N(5)-Ni(2)-S(2)	170.12(19)
N(4)-Ni(2)-S(1)	177.49(16)
N(5)-Ni(2)-S(1)	97.28(19)
S(2)-Ni(2)-S(1)	91.92(8)
C(1)-S(1)-Ni(1)	99.1(2)
C(1)-S(1)-Ni(2)	111.2(2)
Ni(1)-S(1)-Ni(2)	102.17(7)
C(16)-S(2)-Ni(2)	98.4(2)

Table B-12 (continued)

C(5)-N(1)-C(3)	109.6(4)
C(5)-N(1)-C(2)	112.6(4)
C(3)-N(1)-C(2)	109.8(4)
C(5)-N(1)-Ni(1)	105.0(3)
C(3)-N(1)-Ni(1)	107.4(3)
C(2)-N(1)-Ni(1)	112.2(3)
C(4)-N(2)-C(8)	107.2(4)
C(4)-N(2)-C(7)	111.3(5)
C(8)-N(2)-C(7)	109.6(4)
C(4)-N(2)-Ni(1)	103.5(4)
C(8)-N(2)-Ni(1)	118.1(4)
C(7)-N(2)-Ni(1)	107.1(3)
C(11)-N(3)-C(15)	120.8(5)
C(11)-N(3)-Ni(1)	123.0(4)
C(15)-N(3)-Ni(1)	116.2(4)
C(17)-N(4)-C(18)	112.3(5)
C(17)-N(4)-C(21)	111.4(5)
C(18)-N(4)-C(21)	105.0(5)
C(17)-N(4)-Ni(2)	114.6(4)
C(18)-N(4)-Ni(2)	104.9(4)
C(21)-N(4)-Ni(2)	107.9(4)
C(20)-N(5)-C(22)	118.8(6)
C(20)-N(5)-C(23)	97.5(6)
C(22)-N(5)-C(23)	102.5(5)
C(20)-N(5)-Ni(2)	112.8(5)
C(22)-N(5)-Ni(2)	108.3(4)
C(23)-N(5)-Ni(2)	116.5(5)
C(2)-C(1)-C(10)	116.8(5)
C(2)-C(1)-C(9)	108.8(5)
C(10)-C(1)-C(9)	107.5(5)
C(2)-C(1)-S(1)	107.9(4)
C(10)-C(1)-S(1)	105.8(4)
C(9)-C(1)-S(1)	109.9(4)

Table B-12 (continued)

C(1)-C(2)-N(1)	115.5(4)
N(1)-C(3)-C(4)	110.0(4)
N(2)-C(4)-C(3)	111.3(4)
N(1)-C(5)-C(6)	114.2(4)
C(5)-C(6)-C(7)	113.7(5)
C(6)-C(7)-N(2)	112.2(5)
N(3)-C(11)-C(12)	122.5(6)
C(11)-C(12)-C(13)	116.0(6)
C(14)-C(13)-C(12)	121.8(6)
C(15)-C(14)-C(13)	119.5(6)
N(3)-C(15)-C(14)	119.4(6)
C(25)-C(16)-C(17)	109.6(5)
C(25)-C(16)-C(24)	106.5(5)
C(17)-C(16)-C(24)	113.9(6)
C(25)-C(16)-S(2)	108.9(5)
C(17)-C(16)-S(2)	107.4(4)
C(24)-C(16)-S(2)	110.5(4)
N(4)-C(17)-C(16)	112.5(5)
C(19)-C(18)-N(4)	115.2(6)
C(18)-C(19)-C(20)	129.9(8)
N(5)-C(20)-C(19)	99.0(6)
N(4)-C(21)-C(22)	109.7(5)
N(5)-C(22)-C(21)	103.4(5)
N(1N)-C(1N)-C(2N)	171.74(12)
F(2)-B(1)-F(3)	109.5(3)
F(2)-B(1)-F(1)	120.0(3)
F(3)-B(1)-F(1)	110.2(3)
F(2)-B(1)-F(4)	109.4(3)
F(3)-B(1)-F(4)	100.7(2)
F(1)-B(1)-F(4)	105.3(3)
F(5)-B(2)-F(6)	119.7(4)
F(5)-B(2)-F(7)	109.5(3)
F(6)-B(2)-F(7)	109.6(4)

Table B-12 (continued)

F(5)-B(2)-F(8)	106.3(3)
F(6)-B(2)-F(8)	111.9(3)
F(7)-B(2)-F(8)	97.4(3)

Symmetry transformations used to generate equivalent atoms:

Table B-13. Crystal data and structure refinement for mIm-[(mmp-mdach)Ni]$_2$[BF_4]$_2$.

Empirical formula	C24 H48 B2 F8 N6 Ni2 S2	
Formula weight	775.84	
Temperature	293(2) K	
Wavelength	0.71073 Å	
Crystal system	Triclinic	
Space group	P-1	
Unit cell dimensions	a = 9.967(3) Å	α = 81.848(5)°.
	b = 11.316(3) Å	β = 76.059(5)°.
	c = 16.490(5) Å	γ = 68.849(5)°.
Volume	1680.4(9) Å^3	
Z	2	
Density (calculated)	1.533 Mg/m^3	
Absorption coefficient	1.315 mm^{-1}	
F(000)	808	
Crystal size	0.30 x 0.10 x 0.10 mm^3	
Theta range for data collection	2.24 to 25.00°.	
Index ranges	-11<=h<=11, -13<=k<=13, -19<=l<=19	
Reflections collected	15112	
Independent reflections	5713 [R(int) = 0.0553]	
Completeness to theta = 25.00°	96.4 %	
Max. and min. transmission	0.8797 and 0.6937	
Refinement method	Full-matrix least-squares on F^2	
Data / restraints / parameters	5713 / 332 / 443	
Goodness-of-fit on F^2	1.041	
Final R indices [I>2sigma(I)]	R1 = 0.0759, wR2 = 0.1761	
R indices (all data)	R1 = 0.1044, wR2 = 0.1921	
Largest diff. peak and hole	1.507 and -1.039 e.Å^{-3}	

Table B-14. Bond lengths [Å] and angles [°] for mIm-[(mmp-mdach)Ni]$_2$[BF$_4$]$_2$.

Ni(1)-N(3)	1.905(5)
Ni(1)-N(1)	1.922(5)
Ni(1)-N(2)	1.961(6)
Ni(1)-S(1)	2.1663(19)
Ni(2)-N(4)	1.925(6)
Ni(2)-N(5)	2.026(7)
Ni(2)-S(2)	2.1403(19)
Ni(2)-S(1)	2.2135(19)
S(1)-C(8)	1.850(7)
S(2)-C(22)	1.836(7)
N(1)-C(5)	1.493(8)
N(1)-C(7)	1.498(8)
N(1)-C(1)	1.506(8)
N(2)-C(2)	1.487(9)
N(2)-C(3)	1.504(9)
N(2)-C(6)	1.507(10)
N(3)-C(13)	1.312(9)
N(3)-C(11)	1.353(9)
N(4)-C(15)	1.488(10)
N(4)-C(21)	1.493(9)
N(4)-C(19)	1.505(10)
N(5)-C(17)	1.426(13)
N(5)-C(20)	1.493(12)
N(5)-C(16)	1.569(12)
N(6)-C(13)	1.339(9)
N(6)-C(12)	1.365(10)
N(6)-C(14)	1.479(9)
C(1)-C(2)	1.523(10)
C(3)-C(4)	1.509(10)
C(4)-C(5)	1.514(10)
C(7)-C(8)	1.523(10)
C(8)-C(9)	1.522(10)
C(8)-C(10)	1.537(10)

Table B-14 (continued)

C(11)-C(12)	1.357(10)
C(15)-C(16)	1.522(11)
C(17)-C(18)	1.404(14)
C(18)-C(19)	1.476(12)
C(21)-C(22)	1.524(10)
C(22)-C(23)	1.507(11)
C(22)-C(24)	1.508(11)
B11-F11	1.363(9)
B11-F31	1.371(10)
B11-F21	1.382(10)
B11-F41	1.382(9)
B12-F12	1.363(9)
B12-F32	1.371(10)
B12-F22	1.382(10)
B12-F42	1.382(9)
B13-F13	1.363(9)
B13-F33	1.371(10)
B13-F23	1.382(10)
B13-F43	1.382(9)
N(3)-Ni(1)-N(1)	174.4(2)
N(3)-Ni(1)-N(2)	97.4(2)
N(1)-Ni(1)-N(2)	82.3(2)
N(3)-Ni(1)-S(1)	89.10(18)
N(1)-Ni(1)-S(1)	91.16(17)
N(2)-Ni(1)-S(1)	173.46(18)
N(4)-Ni(2)-N(5)	80.7(3)
N(4)-Ni(2)-S(2)	89.95(18)
N(5)-Ni(2)-S(2)	170.3(2)
N(4)-Ni(2)-S(1)	174.35(18)
N(5)-Ni(2)-S(1)	96.4(2)
S(2)-Ni(2)-S(1)	92.66(7)
C(8)-S(1)-Ni(1)	100.6(2)
C(8)-S(1)-Ni(2)	115.1(2)

Table B-14 (continued)

Ni(1)-S(1)-Ni(2)	99.34(7)
C(22)-S(2)-Ni(2)	101.5(2)
C(5)-N(1)-C(7)	112.0(5)
C(5)-N(1)-C(1)	109.3(5)
C(7)-N(1)-C(1)	109.4(5)
C(5)-N(1)-Ni(1)	107.4(4)
C(7)-N(1)-Ni(1)	112.6(4)
C(1)-N(1)-Ni(1)	105.9(4)
C(2)-N(2)-C(3)	111.0(5)
C(2)-N(2)-C(6)	108.6(6)
C(3)-N(2)-C(6)	108.0(6)
C(2)-N(2)-Ni(1)	104.9(4)
C(3)-N(2)-Ni(1)	108.2(4)
C(6)-N(2)-Ni(1)	116.1(5)
C(13)-N(3)-C(11)	106.2(6)
C(13)-N(3)-Ni(1)	129.4(5)
C(11)-N(3)-Ni(1)	124.0(5)
C(15)-N(4)-C(21)	107.6(6)
C(15)-N(4)-C(19)	109.2(6)
C(21)-N(4)-C(19)	111.6(5)
C(15)-N(4)-Ni(2)	108.6(4)
C(21)-N(4)-Ni(2)	114.2(4)
C(19)-N(4)-Ni(2)	105.6(5)
C(17)-N(5)-C(20)	110.9(7)
C(17)-N(5)-C(16)	111.6(7)
C(20)-N(5)-C(16)	105.8(7)
C(17)-N(5)-Ni(2)	102.9(6)
C(20)-N(5)-Ni(2)	118.8(6)
C(16)-N(5)-Ni(2)	107.0(5)
C(13)-N(6)-C(12)	107.2(6)
C(13)-N(6)-C(14)	126.6(6)
C(12)-N(6)-C(14)	126.2(6)
N(1)-C(1)-C(2)	110.8(5)

Table B-14 (continued)

N(2)-C(2)-C(1)	109.4(5)
N(2)-C(3)-C(4)	112.1(5)
C(3)-C(4)-C(5)	114.9(6)
N(1)-C(5)-C(4)	112.3(6)
N(1)-C(7)-C(8)	115.3(5)
C(9)-C(8)-C(7)	107.9(6)
C(9)-C(8)-C(10)	109.4(6)
C(7)-C(8)-C(10)	114.6(6)
C(9)-C(8)-S(1)	111.4(5)
C(7)-C(8)-S(1)	106.5(5)
C(10)-C(8)-S(1)	107.0(5)
N(3)-C(11)-C(12)	109.7(7)
C(11)-C(12)-N(6)	105.8(6)
N(3)-C(13)-N(6)	111.1(6)
N(4)-C(15)-C(16)	112.0(6)
C(15)-C(16)-N(5)	107.6(6)
C(18)-C(17)-N(5)	114.9(8)
C(17)-C(18)-C(19)	118.5(8)
C(18)-C(19)-N(4)	114.6(7)
N(4)-C(21)-C(22)	113.5(6)
C(23)-C(22)-C(24)	107.0(7)
C(23)-C(22)-C(21)	114.1(6)
C(24)-C(22)-C(21)	109.3(6)
C(23)-C(22)-S(2)	112.1(6)
C(24)-C(22)-S(2)	108.7(5)
C(21)-C(22)-S(2)	105.5(4)
F11-B11-F31	110.1(7)
F11-B11-F21	108.9(6)
F31-B11-F21	109.2(6)
F11-B11-F41	111.5(6)
F31-B11-F41	109.5(6)
F21-B11-F41	107.6(7)
F12-B12-F32	110.0(7)

Table B-14 (continued)

F12-B12-F22	108.9(6)
F32-B12-F22	109.2(6)
F12-B12-F42	111.5(7)
F32-B12-F42	109.5(6)
F22-B12-F42	107.6(7)
F13-B13-F33	110.1(7)
F13-B13-F23	108.9(6)
F33-B13-F23	109.2(7)
F13-B13-F43	111.5(7)
F33-B13-F43	109.5(6)
F23-B13-F43	107.6(7)

Table B-15. Crystal data and structure refinement for [(mmp-mdach)Ni(mIm)][BF_4].

Empirical formula	C14 H27 B F4 N4 Ni S	
Formula weight	428.97	
Temperature	110(2) K	
Wavelength	1.54178 Å	
Crystal system	Monoclinic	
Space group	P2(1)/n	
Unit cell dimensions	a = 11.449(4) Å	α = 90°.
	b = 7.126(3) Å	β = 93.930(14)°.
	c = 22.881(8) Å	γ = 90°.
Volume	1862.3(11) $Å^3$	
Z	4	
Density (calculated)	1.530 Mg/m^3	
Absorption coefficient	2.949 mm^{-1}	
F(000)	896	
Crystal size	0.20 x 0.10 x 0.10 mm^3	
Theta range for data collection	3.87 to 60.00°.	
Index ranges	-12<=h<=12, -7<=k<=7, -25<=l<=25	
Reflections collected	12424	
Independent reflections	2395 [R(int) = 0.2384]	
Completeness to theta = 60.00°	87.0 %	
Absorption correction	Semi-empirical from equivalents	
Max. and min. transmission	0.7569 and 0.5900	
Refinement method	Full-matrix least-squares on F^2	
Data / restraints / parameters	2395 / 0 / 230	
Goodness-of-fit on F^2	1.000	
Final R indices [I>2sigma(I)]	R1 = 0.0603, wR2 = 0.1181	
R indices (all data)	R1 = 0.1733, wR2 = 0.1608	
Largest diff. peak and hole	0.363 and -0.403 $e.Å^{-3}$	

Table B-16. Bond lengths [Å] and angles [°] for [(mmp-mdach)Ni(mIm)][BF_4].

Ni(1)-N(3)	1.888(7)
Ni(1)-N(1)	1.890(7)
Ni(1)-N(2)	1.956(7)
Ni(1)-S(1)	2.136(3)
S(1)-C(1)	1.854(8)
F(4)-B(1)	1.380(12)
F(3)-B(1)	1.376(10)
F(2)-B(1)	1.365(11)
F(1)-B(1)	1.379(13)
N(1)-C(6)	1.486(10)
N(1)-C(2)	1.498(9)
N(1)-C(3)	1.532(9)
N(2)-C(8)	1.464(10)
N(2)-C(7)	1.501(11)
N(2)-C(5)	1.507(9)
N(3)-C(13)	1.318(10)
N(3)-C(11)	1.396(10)
N(4)-C(12)	1.360(10)
N(4)-C(13)	1.358(11)
N(4)-C(14)	1.463(10)
C(1)-C(2)	1.474(12)
C(1)-C(9)	1.519(12)
C(1)-C(10)	1.531(10)
C(3)-C(4)	1.534(10)
C(4)-C(5)	1.501(11)
C(6)-C(7)	1.527(12)
C(11)-C(12)	1.362(11)
N(3)-Ni(1)-N(1)	176.3(3)
N(3)-Ni(1)-N(2)	97.1(3)
N(1)-Ni(1)-N(2)	82.7(3)
N(3)-Ni(1)-S(1)	89.2(2)
N(1)-Ni(1)-S(1)	90.9(2)
N(2)-Ni(1)-S(1)	173.3(2)

Table B-16 (continued)

C(1)-S(1)-Ni(1)	100.7(3)
F(2)-B(1)-F(3)	107.4(8)
F(2)-B(1)-F(1)	109.4(9)
F(3)-B(1)-F(1)	109.2(9)
F(2)-B(1)-F(4)	111.2(9)
F(3)-B(1)-F(4)	109.8(8)
F(1)-B(1)-F(4)	109.9(8)
C(6)-N(1)-C(2)	109.5(7)
C(6)-N(1)-C(3)	110.1(6)
C(2)-N(1)-C(3)	110.6(6)
C(6)-N(1)-Ni(1)	108.8(5)
C(2)-N(1)-Ni(1)	113.6(5)
C(3)-N(1)-Ni(1)	104.1(5)
C(8)-N(2)-C(7)	107.8(7)
C(8)-N(2)-C(5)	108.1(6)
C(7)-N(2)-C(5)	110.7(6)
C(8)-N(2)-Ni(1)	116.9(5)
C(7)-N(2)-Ni(1)	106.3(5)
C(5)-N(2)-Ni(1)	106.9(5)
C(13)-N(3)-C(11)	106.4(7)
C(13)-N(3)-Ni(1)	129.4(6)
C(11)-N(3)-Ni(1)	124.0(5)
C(12)-N(4)-C(13)	108.6(7)
C(12)-N(4)-C(14)	125.3(8)
C(13)-N(4)-C(14)	125.9(7)
C(2)-C(1)-C(9)	116.3(7)
C(2)-C(1)-C(10)	108.6(7)
C(9)-C(1)-C(10)	106.1(8)
C(2)-C(1)-S(1)	107.3(6)
C(9)-C(1)-S(1)	109.4(6)
C(10)-C(1)-S(1)	108.9(6)
C(1)-C(2)-N(1)	115.3(7)
N(1)-C(3)-C(4)	111.8(6)

Table B-16 (continued)

C(5)-C(4)-C(3)	115.7(6)
C(4)-C(5)-N(2)	110.6(6)
N(1)-C(6)-C(7)	109.8(7)
N(2)-C(7)-C(6)	109.9(7)
C(12)-C(11)-N(3)	108.9(7)
N(4)-C(12)-C(11)	106.1(7)
N(3)-C(13)-N(4)	110.0(8)

Table B-17. Crystal data and structure refinement for [(mmp-mdach)Ni(ipIm)][BF_4].

Empirical formula	C15 H28 B F4 N4 Ni S	
Formula weight	441.99	
Temperature	110(2) K	
Wavelength	0.71073 Å	
Crystal system	Monoclinic	
Space group	P2(1)/n	
Unit cell dimensions	a = 7.849(2) Å	α = 90°.
	b = 11.715(4) Å	β = 99.02(3)°.
	c = 23.118(9) Å	γ = 90°.
Volume	2099.4(12) $Å^3$	
Z	4	
Density (calculated)	1.398 Mg/m^3	
Absorption coefficient	1.064 mm^{-1}	
F(000)	924	
Crystal size	0.15 x 0.12 x 0.14 mm^3	
Theta range for data collection	1.78 to 25.00°.	
Index ranges	-4<=h<=6, -13<=k<=5, -25<=l<=27	
Reflections collected	4696	
Independent reflections	2738 [R(int) = 0.0626]	
Completeness to theta = 25.00°	74.0 %	
Absorption correction	Semi-empirical from equivalents	
Max. and min. transmission	0.8154 and 0.8154	
Refinement method	Full-matrix least-squares on F^2	
Data / restraints / parameters	2738 / 222 / 253	
Goodness-of-fit on F^2	1.002	
Final R indices [I>2sigma(I)]	R1 = 0.0713, wR2 = 0.1540	
R indices (all data)	R1 = 0.1145, wR2 = 0.1693	
Largest diff. peak and hole	0.782 and -0.480 $e.Å^{-3}$	

Table B-18. Bond lengths [Å] and angles [°] for [(mmp-mdach)Ni(ipIm)][BF_4]..

Ni(1)-N(3)	1.906(6)
Ni(1)-N(1)	1.921(6)
Ni(1)-N(2)	1.971(6)
Ni(1)-S(1)	2.151(3)
S(1)-C(8)	1.847(7)
F(1)-B(1)	1.388(10)
N(1)-C(5)	1.476(9)
N(1)-C(7)	1.491(9)
N(1)-C(1)	1.536(10)
N(3)-C(13)	1.318(8)
N(3)-C(11)	1.388(9)
F(4)-B(1)	1.381(10)
F(2)-B(1)	1.376(11)
F(3)-B(1)	1.407(12)
C(13)-N(4)	1.342(9)
C(13)-C(14)	1.497(10)
C(12)-C(11)	1.341(10)
C(12)-N(4)	1.353(9)
C(5)-C(4)	1.496(10)
C(14)-C(16)	1.528(11)
C(14)-C(15)	1.544(10)
C(8)-C(9)	1.489(11)
C(8)-C(10)	1.527(10)
C(8)-C(7)	1.545(11)
N(2)-C(3)	1.464(9)
N(2)-C(6)	1.494(9)
N(2)-C(2)	1.496(10)
C(3)-C(4)	1.461(10)
C(1)-C(2)	1.531(10)
N(3)-Ni(1)-N(1)	173.1(2)
N(3)-Ni(1)-N(2)	96.0(3)
N(1)-Ni(1)-N(2)	82.4(3)
N(3)-Ni(1)-S(1)	90.9(2)

Table B-18 (continued)

N(1)-Ni(1)-S(1)	90.9(2)
N(2)-Ni(1)-S(1)	173.16(19)
C(8)-S(1)-Ni(1)	101.3(3)
C(5)-N(1)-C(7)	114.9(6)
C(5)-N(1)-C(1)	108.9(6)
C(7)-N(1)-C(1)	108.5(5)
C(5)-N(1)-Ni(1)	104.3(4)
C(7)-N(1)-Ni(1)	113.2(5)
C(1)-N(1)-Ni(1)	106.5(4)
C(13)-N(3)-C(11)	107.5(6)
C(13)-N(3)-Ni(1)	129.7(5)
C(11)-N(3)-Ni(1)	122.8(5)
N(3)-C(13)-N(4)	108.5(6)
N(3)-C(13)-C(14)	127.1(7)
N(4)-C(13)-C(14)	124.4(7)
C(11)-C(12)-N(4)	106.7(7)
C(12)-C(11)-N(3)	108.0(6)
C(13)-N(4)-C(12)	109.3(6)
N(1)-C(5)-C(4)	115.3(6)
C(13)-C(14)-C(16)	111.2(7)
C(13)-C(14)-C(15)	110.4(6)
C(16)-C(14)-C(15)	110.3(6)
C(9)-C(8)-C(10)	108.7(7)
C(9)-C(8)-C(7)	115.8(7)
C(10)-C(8)-C(7)	105.9(7)
C(9)-C(8)-S(1)	111.6(6)
C(10)-C(8)-S(1)	108.9(5)
C(7)-C(8)-S(1)	105.6(5)
C(3)-N(2)-C(6)	109.1(6)
C(3)-N(2)-C(2)	109.7(6)
C(6)-N(2)-C(2)	107.5(6)
C(3)-N(2)-Ni(1)	106.8(5)
C(6)-N(2)-Ni(1)	116.8(5)

Table B-18 (continued)

C(2)-N(2)-Ni(1)	106.8(4)
C(4)-C(3)-N(2)	114.4(6)
C(3)-C(4)-C(5)	114.2(7)
C(2)-C(1)-N(1)	110.4(6)
F(2)-B(1)-F(4)	110.4(8)
F(2)-B(1)-F(1)	109.2(7)
F(4)-B(1)-F(1)	110.0(7)
F(2)-B(1)-F(3)	108.6(8)
F(4)-B(1)-F(3)	109.3(7)
F(1)-B(1)-F(3)	109.2(8)
N(1)-C(7)-C(8)	114.1(6)
N(2)-C(2)-C(1)	109.4(6)

Table B-19. Crystal data and structure refinement for [(mmp-mdach)Ni(me_2NHC)][I].

Empirical formula	C15 H29 I N4 Ni S	
Formula weight	483.09	
Temperature	110(2) K	
Wavelength	0.71069 Å	
Crystal system	Monoclinic	
Space group	P2(1)/c	
Unit cell dimensions	a = 13.963(5) Å	α = 90.000(5)°.
	b = 12.042(5) Å	β = 110.946(5)°.
	c = 12.364(5) Å	γ = 90.000(5)°.
Volume	1941.5(13) $Å^3$	
Z	4	
Density (calculated)	1.653 Mg/m^3	
Absorption coefficient	2.699 mm^{-1}	
F(000)	976	
Crystal size	0.17 x 0.05 x 0.05 mm^3	
Theta range for data collection	2.54 to 25.00°.	
Index ranges	-16<=h<=15, -14<=k<=13, -14<=l<=14	
Reflections collected	15834	
Independent reflections	3140 [R(int) = 0.1086]	
Completeness to theta = 25.00°	91.6 %	
Absorption correction	Semi-empirical from equivalents	
Max. and min. transmission	0.8769 and 0.6569	
Refinement method	Full-matrix least-squares on F^2	
Data / restraints / parameters	3140 / 0 / 200	
Goodness-of-fit on F^2	0.994	
Final R indices [I>2sigma(I)]	R1 = 0.0472, wR2 = 0.0963	
R indices (all data)	R1 = 0.1030, wR2 = 0.1154	
Extinction coefficient	0.0053(7)	
Largest diff. peak and hole	0.754 and -0.572 $e.Å^{-3}$	

Table B-20. Bond lengths [Å] and angles [°] for [(mmp-mdach)Ni(me_2NHC)][I].

Ni(1)-C(11)	1.891(8)
Ni(1)-N(1)	1.947(6)
Ni(1)-N(2)	1.972(7)
Ni(1)-S(1)	2.142(2)
S(1)-C(1)	1.837(8)
N(1)-C(6)	1.490(10)
N(1)-C(2)	1.495(11)
N(1)-C(3)	1.499(12)
N(2)-C(8)	1.476(11)
N(2)-C(7)	1.490(10)
N(2)-C(5)	1.504(11)
N(3)-C(11)	1.354(10)
N(3)-C(12)	1.389(11)
N(3)-C(14)	1.458(11)
N(4)-C(11)	1.334(10)
N(4)-C(13)	1.383(10)
N(4)-C(15)	1.473(11)
C(1)-C(10)	1.492(14)
C(1)-C(2)	1.530(12)
C(1)-C(9)	1.536(13)
C(3)-C(4)	1.501(13)
C(4)-C(5)	1.464(12)
C(6)-C(7)	1.512(13)
C(12)-C(13)	1.340(13)
C(11)-Ni(1)-N(1)	176.5(3)
C(11)-Ni(1)-N(2)	97.5(3)
N(1)-Ni(1)-N(2)	82.0(3)
C(11)-Ni(1)-S(1)	89.6(2)
N(1)-Ni(1)-S(1)	90.7(2)
N(2)-Ni(1)-S(1)	171.97(19)
C(1)-S(1)-Ni(1)	96.9(3)
C(6)-N(1)-C(2)	113.5(6)
C(6)-N(1)-C(3)	109.4(7)

Table B-20 (continued)

C(2)-N(1)-C(3)	106.4(7)
C(6)-N(1)-Ni(1)	104.4(5)
C(2)-N(1)-Ni(1)	113.5(5)
C(3)-N(1)-Ni(1)	109.6(5)
C(8)-N(2)-C(7)	108.8(6)
C(8)-N(2)-C(5)	108.0(6)
C(7)-N(2)-C(5)	110.5(6)
C(8)-N(2)-Ni(1)	117.8(5)
C(7)-N(2)-Ni(1)	101.7(5)
C(5)-N(2)-Ni(1)	109.8(5)
C(11)-N(3)-C(12)	109.5(7)
C(11)-N(3)-C(14)	124.7(7)
C(12)-N(3)-C(14)	125.9(7)
C(11)-N(4)-C(13)	111.8(7)
C(11)-N(4)-C(15)	125.4(7)
C(13)-N(4)-C(15)	122.7(7)
C(10)-C(1)-C(2)	112.1(8)
C(10)-C(1)-C(9)	109.8(8)
C(2)-C(1)-C(9)	109.3(7)
C(10)-C(1)-S(1)	111.7(6)
C(2)-C(1)-S(1)	105.6(5)
C(9)-C(1)-S(1)	108.3(6)
N(1)-C(2)-C(1)	114.1(7)
N(1)-C(3)-C(4)	112.9(8)
C(5)-C(4)-C(3)	116.4(7)
C(4)-C(5)-N(2)	113.8(7)
N(1)-C(6)-C(7)	109.9(6)
N(2)-C(7)-C(6)	111.6(7)
N(4)-C(11)-N(3)	105.3(6)
N(4)-C(11)-Ni(1)	129.4(6)
N(3)-C(11)-Ni(1)	125.3(6)
C(13)-C(12)-N(3)	107.8(7)
C(12)-C(13)-N(4)	105.6(7)

Table B-21. Crystal data and structure refinement for Im-[(mmp-dach)Ni]$_2$[BF$_4$]$_2$.

Empirical formula	C21 H42 B2 F8 N6 Ni2 S2	
Formula weight	733.77	
Temperature	293(2) K	
Wavelength	1.54178 Å	
Crystal system	monoclinic	
Space group	P2(1)/n	
Unit cell dimensions	a = 10.805(5) Å	α= 90°.
	b = 14.125(7) Å	β= 100.339(19)°.
	c = 20.169(10) Å	γ = 90°.
Volume	3028(3) Å^3	
Z	4	
Density (calculated)	1.609 Mg/m^3	
Absorption coefficient	3.498 mm^{-1}	
F(000)	1520	
Crystal size	0.30 x 0.01 x 0.01 mm^3	
Theta range for data collection	5.36 to 58.82°.	
Index ranges	-11<=h<=11, -15<=k<=14, -22<=l<=22	
Reflections collected	19669	
Independent reflections	3867 [R(int) = 0.4928]	
Completeness to theta = 58.82°	89.2 %	
Max. and min. transmission	0.9659 and 0.4201	
Refinement method	Full-matrix least-squares on F^2	
Data / restraints / parameters	3867 / 210 / 416	
Goodness-of-fit on F^2	1.000	
Final R indices [I>2sigma(I)]	R1 = 0.0752, wR2 = 0.0905	
R indices (all data)	R1 = 0.3079, wR2 = 0.1568	
Largest diff. peak and hole	0.361 and -0.294 e.Å^{-3}	

Table B-22. Bond lengths [Å] and angles [°] for Im-[(mmp-dach)Ni]$_2$[BF$_4$]$_2$.

Ni(1)-N(1)	1.884(11)
Ni(1)-N(1A)	1.893(12)
Ni(1)-N(2)	1.929(11)
Ni(1)-S(1)	2.187(4)
Ni(2)-N(4)	1.918(12)
Ni(2)-N(3)	1.971(13)
Ni(2)-S(2)	2.128(4)
Ni(2)-S(1)	2.178(4)
S(1)-C(7)	1.924(15)
S(2)-C(16)	1.824(18)
N(1)-C(1)	1.510(15)
N(1)-C(4)	1.598(15)
N(1)-H(1C)	0.9100
N(2)-C(6)	1.500(15)
N(2)-C(3)	1.533(15)
N(2)-C(5)	1.551(15)
N(3)-C(13)	1.436(15)
N(3)-C(10)	1.473(17)
N(3)-H(3C)	0.9100
N(4)-C(15)	1.497(17)
N(4)-C(14)	1.514(18)
N(4)-C(12)	1.524(18)
C(1)-C(2)	1.486(16)
C(1)-H(1A)	0.9700
C(1)-H(1B)	0.9700
C(2)-C(3)	1.419(17)
C(2)-H(2A)	0.9700
C(2)-H(2B)	0.9700
C(3)-H(3A)	0.9700
C(3)-H(3B)	0.9700
C(4)-C(5)	1.504(16)
C(4)-H(4A)	0.9700

Table B-22 (continued)

C(6)-C(7)	1.543(18)
C(7)-C(9)	1.486(16)
C(7)-C(8)	1.488(17)
C(10)-C(11)	1.365(18)
C(11)-C(12)	1.491(19)
C(13)-C(14)	1.51(2)
C(15)-C(16)	1.40(2)
C(16)-C(17)	1.370(19)
C(16)-C(18)	1.55(2)
N(1A)-C(1A)	1.349(15)
N(1A)-C(3A)	1.360(16)
N(2A)-C(1A)	1.293(15)
N(2A)-C(2A)	1.314(16)
C(2A)-C(3A)	1.383(18)
B11-F11	1.308(19)
B11-F21	1.349(18)
B11-F41	1.357(18)
B11-F31	1.426(19)
B12-F12	1.308(19)
B12-F22	1.351(18)
B12-F42	1.357(18)
B12-F32	1.427(19)
B13-F13	1.308(19)
B13-F23	1.350(18)
B13-F43	1.357(18)
B13-F33	1.43(2)
N(1)-Ni(1)-N(1A)	93.6(5)
N(1)-Ni(1)-N(2)	82.6(5)
N(1A)-Ni(1)-N(2)	175.8(5)
N(1)-Ni(1)-S(1)	173.2(4)
N(1A)-Ni(1)-S(1)	93.2(3)
N(2)-Ni(1)-S(1)	90.6(4)

Table B-22 (continued)

N(4)-Ni(2)-N(3)	79.6(5)
N(4)-Ni(2)-S(2)	91.6(4)
N(3)-Ni(2)-S(2)	171.2(4)
N(4)-Ni(2)-S(1)	174.4(4)
N(3)-Ni(2)-S(1)	95.1(4)
S(2)-Ni(2)-S(1)	93.73(15)
C(7)-S(1)-Ni(2)	105.4(5)
C(7)-S(1)-Ni(1)	99.7(5)
Ni(2)-S(1)-Ni(1)	108.07(17)
C(16)-S(2)-Ni(2)	99.8(7)
C(1)-N(1)-C(4)	108.6(10)
C(1)-N(1)-Ni(1)	113.0(9)
C(4)-N(1)-Ni(1)	107.2(7)
C(6)-N(2)-C(3)	114.8(10)
C(6)-N(2)-C(5)	109.1(10)
C(3)-N(2)-C(5)	107.8(11)
C(6)-N(2)-Ni(1)	113.6(9)
C(3)-N(2)-Ni(1)	106.8(8)
C(5)-N(2)-Ni(1)	103.9(8)
C(13)-N(3)-C(10)	112.9(13)
C(13)-N(3)-Ni(2)	107.6(10)
C(10)-N(3)-Ni(2)	106.9(10)
C(15)-N(4)-C(14)	108.3(13)
C(15)-N(4)-C(12)	116.0(14)
C(14)-N(4)-C(12)	108.9(12)
C(15)-N(4)-Ni(2)	110.7(9)
C(14)-N(4)-Ni(2)	107.5(10)
C(12)-N(4)-Ni(2)	105.2(10)
C(2)-C(1)-N(1)	108.4(11)
C(3)-C(2)-C(1)	117.1(13)
C(2)-C(3)-N(2)	115.8(12)
C(5)-C(4)-N(1)	105.9(10)

Table B-22 (continued)

C(4)-C(5)-N(2)	111.6(10)
N(2)-C(6)-C(7)	114.0(12)
C(9)-C(7)-C(8)	110.1(12)
C(9)-C(7)-C(6)	109.0(12)
C(8)-C(7)-C(6)	119.2(12)
C(9)-C(7)-S(1)	108.9(9)
C(8)-C(7)-S(1)	106.4(10)
C(6)-C(7)-S(1)	102.7(10)
C(11)-C(10)-N(3)	113.6(15)
C(10)-C(11)-C(12)	117.8(15)
C(11)-C(12)-N(4)	118.2(14)
N(3)-C(13)-C(14)	112.4(14)
C(13)-C(14)-N(4)	106.5(11)
C(16)-C(15)-N(4)	118.8(15)
C(17)-C(16)-C(15)	115.1(18)
C(17)-C(16)-C(18)	101.6(16)
C(15)-C(16)-C(18)	108.9(18)
C(17)-C(16)-S(2)	111.4(14)
C(15)-C(16)-S(2)	110.1(14)
C(18)-C(16)-S(2)	109.3(13)
C(1A)-N(1A)-C(3A)	104.2(12)
C(1A)-N(1A)-Ni(1)	129.0(10)
C(3A)-N(1A)-Ni(1)	126.4(11)
C(1A)-N(2A)-C(2A)	113.2(14)
N(2A)-C(1A)-N(1A)	109.1(12)
N(2A)-C(2A)-C(3A)	102.8(15)
N(1A)-C(3A)-C(2A)	110.5(14)
F11-B11-F21	108.0(15)
F11-B11-F41	116.5(16)
F21-B11-F41	109.1(15)
F11-B11-F31	109.7(15)
F21-B11-F31	105.7(14)

Table B-22 (continued)

F41-B11-F31	107.4(14)
F12-B12-F22	107.8(15)
F12-B12-F42	116.6(17)
F22-B12-F42	108.8(16)
F12-B12-F32	110.1(16)
F22-B12-F32	106.3(15)
F42-B12-F32	106.8(15)
F13-B13-F23	107.9(16)
F13-B13-F43	116.6(17)
F23-B13-F43	109.0(16)
F13-B13-F33	109.8(17)
F23-B13-F33	106.1(16)
F43-B13-F33	107.1(15)

Table B-23. Crystal data and structure refinement for [(bme-daco)(V=O)].

Empirical formula	C10 H20 N2 O S2 V	
Formula weight	299.34	
Temperature	110(2) K	
Wavelength	0.71073 Å	
Crystal system	monoclinic	
Space group	P21/n	
Unit cell dimensions	a = 7.590(3) Å	α = 90°.
	b = 20.689(9) Å	β = 109.55(4)°.
	c = 8.565(3) Å	γ = 90°.
Volume	1267.4(9) $Å^3$	
Z	4	
Density (calculated)	1.569 Mg/m^3	
Absorption coefficient	1.093 mm^{-1}	
F(000)	628	
Crystal size	2.00 x 0.20 x 0.20 mm^3	
Theta range for data collection	1.97 to 25.00°.	
Index ranges	-9<=h<=8, -24<=k<=24, -10<=l<=9	
Reflections collected	11094	
Independent reflections	2159 [R(int) = 0.0584]	
Completeness to theta = 25.00°	96.9 %	
Max. and min. transmission	0.8110 and 0.2185	
Refinement method	Full-matrix least-squares on F^2	
Data / restraints / parameters	2159 / 0 / 145	
Goodness-of-fit on F^2	1.016	
Final R indices [I>2sigma(I)]	R1 = 0.0513, wR2 = 0.1066	
R indices (all data)	R1 = 0.0637, wR2 = 0.1113	
Largest diff. peak and hole	0.432 and -0.604 $e.Å^{-3}$	

Table B-24. Bond lengths [Å] and angles [°] for [(bme-daco)(V=O)].

V(1)-O(1)	1.599(3)
V(1)-N(2)	2.154(3)
V(1)-N(1)	2.159(3)
V(1)-S(1)	2.3482(14)
V(1)-S(2)	2.3617(18)
S(1)-C(1)	1.825(4)
S(2)-C(3)	1.837(4)
N(2)-C(7)	1.499(5)
N(2)-C(4)	1.506(5)
N(2)-C(10)	1.511(5)
N(1)-C(2)	1.493(5)
N(1)-C(5)	1.504(5)
N(1)-C(8)	1.519(5)
C(1)-C(2)	1.519(6)
C(8)-C(9)	1.528(5)
C(3)-C(4)	1.510(6)
C(5)-C(6)	1.507(6)
C(6)-C(7)	1.525(6)
C(9)-C(10)	1.513(5)
O(1)-V(1)-N(2)	102.94(14)
O(1)-V(1)-N(1)	101.26(14)
N(2)-V(1)-N(1)	84.11(13)
O(1)-V(1)-S(1)	112.27(11)
N(2)-V(1)-S(1)	144.33(9)
N(1)-V(1)-S(1)	83.65(10)
O(1)-V(1)-S(2)	110.26(11)
N(2)-V(1)-S(2)	84.23(10)
N(1)-V(1)-S(2)	148.11(9)
S(1)-V(1)-S(2)	88.80(5)
C(1)-S(1)-V(1)	100.53(14)
C(3)-S(2)-V(1)	100.55(13)
C(7)-N(2)-C(4)	106.3(3)
C(7)-N(2)-C(10)	110.7(3)

Table B-24 (continued)

C(4)-N(2)-C(10)	110.8(3)
C(7)-N(2)-V(1)	110.7(2)
C(4)-N(2)-V(1)	108.7(2)
C(10)-N(2)-V(1)	109.6(2)
C(2)-N(1)-C(5)	106.7(3)
C(2)-N(1)-C(8)	110.7(3)
C(5)-N(1)-C(8)	109.9(3)
C(2)-N(1)-V(1)	107.7(2)
C(5)-N(1)-V(1)	110.9(2)
C(8)-N(1)-V(1)	110.8(2)
C(2)-C(1)-S(1)	111.4(3)
N(1)-C(8)-C(9)	111.5(3)
C(4)-C(3)-S(2)	111.4(3)
N(2)-C(4)-C(3)	113.9(3)
N(1)-C(5)-C(6)	114.5(3)
C(5)-C(6)-C(7)	116.6(3)
N(2)-C(7)-C(6)	114.9(3)
C(10)-C(9)-C(8)	117.0(3)
N(2)-C(10)-C(9)	113.3(3)
N(1)-C(2)-C(1)	112.3(3)

Table B-25. Crystal data and structure refinement for [(bme-dach)(V=O)].

Empirical formula	C9 H18 N2 O S2 V	
Formula weight	285.31	
Temperature	293(2) K	
Wavelength	0.71073 Å	
Crystal system	orthorhombic	
Space group	P212121	
Unit cell dimensions	a = 7.2514(18) Å	α = 90°.
	b = 9.816(2) Å	β = 90°.
	c = 16.378(5) Å	γ = 90°.
Volume	1165.8(5) $Å^3$	
Z	4	
Density (calculated)	1.626 Mg/m^3	
Absorption coefficient	1.184 mm^{-1}	
F(000)	596	
Crystal size	0.10 x 0.10 x 0.02 mm^3	
Theta range for data collection	2.49 to 25.00°.	
Index ranges	-8<=h<=8, -6<=k<=11, -19<=l<=13	
Reflections collected	2642	
Independent reflections	1917 [R(int) = 0.0354]	
Completeness to theta = 25.00°	96.5 %	
Max. and min. transmission	0.9767 and 0.8908	
Refinement method	Full-matrix least-squares on F^2	
Data / restraints / parameters	1917 / 0 / 137	
Goodness-of-fit on F^2	1.004	
Final R indices [I>2sigma(I)]	R1 = 0.0363, wR2 = 0.0582	
R indices (all data)	R1 = 0.0476, wR2 = 0.0619	
Absolute structure parameter	0.00(6)	
Largest diff. peak and hole	0.365 and -0.307 $e.Å^{-3}$	

Table B-26. Bond lengths [Å] and angles [°] for [(bme-dach)(V=O)].

V(1)-O(1)	1.605(3)
V(1)-N(2)	2.111(3)
V(1)-N(1)	2.122(3)
V(1)-S(1)	2.3407(12)
V(1)-S(2)	2.3455(12)
S(1)-C(1)	1.841(4)
S(2)-C(3)	1.840(4)
N(1)-C(8)	1.489(4)
N(1)-C(5)	1.489(5)
N(1)-C(2)	1.491(4)
N(2)-C(9)	1.487(4)
N(2)-C(4)	1.490(5)
N(2)-C(7)	1.499(5)
C(1)-C(2)	1.523(5)
C(3)-C(4)	1.513(5)
C(5)-C(6)	1.512(5)
C(6)-C(7)	1.511(5)
C(8)-C(9)	1.553(5)
O(1)-V(1)-N(2)	102.17(13)
O(1)-V(1)-N(1)	105.02(13)
N(2)-V(1)-N(1)	74.35(11)
O(1)-V(1)-S(1)	108.46(10)
N(2)-V(1)-S(1)	146.39(9)
N(1)-V(1)-S(1)	84.50(8)
O(1)-V(1)-S(2)	110.66(10)
N(2)-V(1)-S(2)	83.34(9)
N(1)-V(1)-S(2)	141.09(9)
S(1)-V(1)-S(2)	98.20(5)
C(1)-S(1)-V(1)	99.17(12)
C(3)-S(2)-V(1)	98.23(13)
C(8)-N(1)-C(5)	111.0(3)
C(8)-N(1)-C(2)	111.3(3)
C(5)-N(1)-C(2)	109.8(3)

Table B-26 (continued)

C(8)-N(1)-V(1)	104.8(2)
C(5)-N(1)-V(1)	112.3(2)
C(2)-N(1)-V(1)	107.6(2)
C(9)-N(2)-C(4)	110.9(3)
C(9)-N(2)-C(7)	110.7(3)
C(4)-N(2)-C(7)	109.4(3)
C(9)-N(2)-V(1)	104.8(2)
C(4)-N(2)-V(1)	106.6(2)
C(7)-N(2)-V(1)	114.3(2)
C(2)-C(1)-S(1)	111.2(2)
N(1)-C(2)-C(1)	110.8(3)
C(4)-C(3)-S(2)	112.4(2)
N(2)-C(4)-C(3)	110.1(3)
N(1)-C(5)-C(6)	113.2(3)
C(7)-C(6)-C(5)	114.8(3)
N(2)-C(7)-C(6)	112.4(3)
N(1)-C(8)-C(9)	109.9(3)
N(2)-C(9)-C(8)	109.5(3)

Table B-27. Crystal data and structure refinement for $[Et_4N]_2[(V=O)(ema)]$.

Empirical formula	C22 H50 N4 O4 S2 V	
Formula weight	549.72	
Temperature	293(2) K	
Wavelength	0.71073 Å	
Crystal system	triclinic	
Space group	P-1	
Unit cell dimensions	a = 8.894(5) Å	α = 72.63(5)°.
	b = 12.219(7) Å	β = 79.92(4)°.
	c = 13.832(7) Å	γ = 80.36(5)°.
Volume	1401.9(13) $Å^3$	
Z	2	
Density (calculated)	1.302 Mg/m^3	
Absorption coefficient	0.536 mm^{-1}	
F(000)	594	
Crystal size	0.10 x 0.10 x 0.01 mm^3	
Theta range for data collection	2.00 to 25.00°.	
Index ranges	-10<=h<=10, -14<=k<=14, -16<=l<=16	
Reflections collected	19908	
Independent reflections	4891 [R(int) = 0.0457]	
Completeness to theta = 25.00°	98.9 %	
Max. and min. transmission	0.9947 and 0.9484	
Refinement method	Full-matrix least-squares on F^2	
Data / restraints / parameters	4891 / 0 / 298	
Goodness-of-fit on F^2	1.014	
Final R indices [I>2sigma(I)]	R1 = 0.0397, wR2 = 0.0899	
R indices (all data)	R1 = 0.0561, wR2 = 0.0983	
Largest diff. peak and hole	0.432 and -0.309 $e.Å^{-3}$	

Table B-28. Bond lengths [Å] and angles [°] for $[Et_4N]_2[(V{=}O)(ema)]$.

V(1)-O(1)	1.6229(19)
V(1)-N(1)	2.028(2)
V(1)-N(2)	2.028(2)
V(1)-S(2)	2.3632(15)
V(1)-S(3)	2.3688(17)
S(2)-C(1)	1.828(3)
S(3)-C(6)	1.830(3)
O(2)-C(2)	1.260(3)
O(3)-C(5)	1.256(3)
N(1)-C(2)	1.328(3)
N(1)-C(3)	1.457(3)
N(2)-C(5)	1.333(3)
N(2)-C(4)	1.465(3)
C(1)-C(2)	1.507(4)
C(3)-C(4)	1.531(4)
C(5)-C(6)	1.511(4)
N(3)-C(10)	1.511(3)
N(3)-C(8)	1.520(3)
N(3)-C(11)	1.525(3)
N(3)-C(13)	1.527(3)
C(7)-C(8)	1.509(4)
C(9)-C(10)	1.507(4)
C(11)-C(12)	1.513(4)
C(13)-C(14)	1.505(4)
N(4)-C(19)	1.517(3)
N(4)-C(15)	1.518(3)
N(4)-C(17)	1.521(3)
N(4)-C(21)	1.523(3)
C(15)-C(16)	1.503(4)
C(17)-C(18)	1.513(4)
C(19)-C(20)	1.506(4)
C(21)-C(22)	1.500(4)

Table B-28 (continued)

O(1)-V(1)-N(1)	105.62(10)
O(1)-V(1)-N(2)	109.72(10)
N(1)-V(1)-N(2)	78.41(10)
O(1)-V(1)-S(2)	111.79(8)
N(1)-V(1)-S(2)	81.27(8)
N(2)-V(1)-S(2)	137.28(7)
O(1)-V(1)-S(3)	108.27(8)
N(1)-V(1)-S(3)	145.03(7)
N(2)-V(1)-S(3)	82.32(8)
S(2)-V(1)-S(3)	93.91(6)
C(1)-S(2)-V(1)	98.83(10)
C(6)-S(3)-V(1)	97.51(10)
C(2)-N(1)-C(3)	120.1(2)
C(2)-N(1)-V(1)	126.01(17)
C(3)-N(1)-V(1)	112.86(16)
C(5)-N(2)-C(4)	117.0(2)
C(5)-N(2)-V(1)	125.28(17)
C(4)-N(2)-V(1)	117.59(16)
C(2)-C(1)-S(2)	114.39(18)
O(2)-C(2)-N(1)	125.8(2)
O(2)-C(2)-C(1)	118.8(2)
N(1)-C(2)-C(1)	115.4(2)
N(1)-C(3)-C(4)	107.9(2)
N(2)-C(4)-C(3)	108.3(2)
O(3)-C(5)-N(2)	125.1(2)
O(3)-C(5)-C(6)	119.1(2)
N(2)-C(5)-C(6)	115.8(2)
C(5)-C(6)-S(3)	114.24(18)
C(10)-N(3)-C(8)	112.2(2)
C(10)-N(3)-C(11)	108.1(2)
C(8)-N(3)-C(11)	109.1(2)
C(10)-N(3)-C(13)	107.8(2)
C(8)-N(3)-C(13)	107.7(2)

Table B-28 (continued)

C(11)-N(3)-C(13)	111.8(2)
C(7)-C(8)-N(3)	115.4(2)
C(9)-C(10)-N(3)	115.0(2)
C(12)-C(11)-N(3)	114.4(2)
C(14)-C(13)-N(3)	115.2(2)
C(19)-N(4)-C(15)	106.0(2)
C(19)-N(4)-C(17)	111.2(2)
C(15)-N(4)-C(17)	111.7(2)
C(19)-N(4)-C(21)	111.5(2)
C(15)-N(4)-C(21)	111.0(2)
C(17)-N(4)-C(21)	105.52(19)
C(16)-C(15)-N(4)	115.0(2)
C(18)-C(17)-N(4)	115.5(2)
C(20)-C(19)-N(4)	115.9(2)
C(22)-C(21)-N(4)	115.2(2)

VITA

Roxanne Michelle Jenkins received her Bachelor of Science degree in Chemistry from The University of Texas at San Antonio in 2003, graduating *Magna cum Laude*. She began her graduate studies at Texas A&M University in the Summer of 2004 under the direction of Marcetta Y. Darensbourg and graduated with her Ph. D. in May 2010. Correspondence may be directed to Texas A&M University, Department of Chemistry, c/o Marcetta Y. Darensbourg, Mail Stop 3255, College Station, TX 77843 or marcetta@chem.tamu.edu.